THE UNIVERSITY OF CHICAGO

# A MEASUREMENT OF GRAVITATIONAL LENSING OF THE COSMIC MICROWAVE BACKGROUND USING SPT-3G

A DISSERTATION SUBMITTED TO
THE FACULTY OF THE DIVISION OF THE PHYSICAL SCIENCES
IN CANDIDACY FOR THE DEGREE OF
DOCTOR OF PHILOSOPHY

DEPARTMENT OF PHYSICS

BY
ZHAODI PAN

CHICAGO, ILLINOIS
DECEMBER 2020

# Table of Contents

# List of Figures

# List of Tables

# ACKNOWLEDGMENTS

I was fortunate to work with my advisor John Carlstrom, whose future vision, enthusiasm, and knowledge have guided me through my graduate school years. I have also benefited greatly from my co-advisor Bradford Benson for his guidance on my first hardware project in the group and suggestions on almost all aspects of my research. I want to express my cordial gratitude to Stephan Meyer for the enlightenment of optics and time spent together in the lab. I thank Professor Holz, Professor Paolo for being in my committee and encouraging me through this thesis.

I am deeply indebted to the South Pole Telescope (SPT) Collaboration for the unconditional support, the reservoir of expertise, and the meticulous commitment to scientific excellence, which transformed me. Through the past years, I have benefited a lot from my talented collaborators in the SPT group. Thank Professor Chang and Professor Holzapfel for valuable feedback in detector characterization. Thank Adam Anderson and Amy Bender for their hard work in detectors and readout systems. Without their diligence, the vital hardware systems for SPT-3G won't be ready for another few years, and my thesis too. I am forever thankful to Thomas Crawford, who facilitated the friendly collaboration atmosphere and shared tons of wisdom in data analysis. I offer my sincere gratitude to Kimmy Wu for her patience in all our discussions and advising me through the gravitational lensing data analysis. I am also thankful to Sasha Rahlin and Nathan Whitehorn for their suggestions on software development and data analysis.

Graduate school won't be such a lovely place without my fellow graduate students: Daniel Dutcher, Joshua Sobrin, Wei Quan, Jody Chou, John Hood, Alec Hryciuk, Karia Dibert, and Paul Chichura. I have my special thanks to Daniel Dutcher for being extremely helpful and spending a big chunk of graduate school working with me on detector characterization. Thank Joshua for organizing the preschool outreach program and the Wednesday student hangout, where I had some of the best memories. Thank Wei Quan for his patience and

care in maintaining the lab and data quality monitoring, which improved our working environment. Thank all other newer graduate students for their keen curiosity, intellectual exploration, and for being friends.

Being surrounded by the vibrant mental environment and helpful staff members at Kavli Institute for Cosmological Physics is extremely lucky. Thank Wayne Hu, Scott Dodelson, Bob Wald, Stephan Kent, Fausto Cattaneo, Andrey Kravtsov, Nick Gnedin for great lectures that introduced me to cosmology. Thank Aimee and the organizing committee for great colloquiums and cookies through the past years. Thank Valerie Smith for being our lab assistant in charge of traveling, purchasing, and shipping. My early graduate school work was highly dependent on the machining and fabrication facilities at the Physical Science Division. Thank Helmut and Luigi for guiding me through the lathe, milling machine, and other machining techniques. Thank Gordon Ward and Larry Fiscelli for spending extra hours helping us meet our instrument fabrication deadlines. My later data analysis work won't be possible without all the computing support team here: Judith Stephen, Benedikt Riedel, Valeri Galstev, Lincoln Bryant, and Rob Gardner.

The South Pole Telescope program and my work are supported by the National Science Foundation (NSF) through grant PLR-1248097. Partial support is also provided by the NSF Physics Frontier Center grant PHY-1125897 to the Kavli Institute of Cosmological Physics at the University of Chicago, the Kavli Foundation, and the Gordon and Betty Moore Foundation through grant GBMF 947 to the University of Chicago. Work at Argonne National Lab is supported by UChicago Argonne LLC, Operator of Argonne National Laboratory (Argonne). Argonne, a U.S. Department of Energy Office of Science Laboratory, is operated under contract no. DE-AC02-06CH11357. Work at Fermi National Accelerator Laboratory, a DOE-OS, HEP User Facility managed by the Fermi Research Alliance, LLC, was supported under Contract No. DE-AC02-07CH11359.

The optical characterization work was published in Journal of Low-Temperature Physics

(Pan et al. 2018 [1]). The Fourier transform spectrometer work appeared in two papers, both published in Applied Optics (Pan et al. 2019 [2], Liu, Pan, et al. [3]). The gravitational lensing analysis work is under-preparation for publication.

Finally, I want to thank my family members and friends for supporting me through the hurdles of graduate school. This thesis won't be possible without their support.

# ABSTRACT

Measurements of the cosmic microwave background (CMB) can be used to map the distribution of matter in the universe through gravitational lensing deflections as the CMB photons travel through the large-scale structures of the universe. Gravitational lensing induces correlations between CMB temperature and polarization modes at different angular scales. These correlations can be extracted by lensing quadratic estimators to reconstruct the projected 2D lensing potential and matter distribution. The power spectrum of the lensing potential is a powerful probe of the growth of structure. It can constrain the sum of neutrino masses, dark energy, and the amplitude of matter density fluctuations. Furthermore, the matter distribution from lensing provides a promising source for cross-correlation with surveys at other wavelengths and offers a template for removing lensing-induced contamination in searches for inflationary gravitational waves. The third-generation camera for the South Pole Telescope (SPT-3G) is an excellent instrument for CMB lensing measurements with high-sensitivity from a new multichroic receiver with 16,000 polarization-sensitive detectors, and fine arcminute-scale resolution provided by the ten-meter dish of SPT. A compact Fourier-Transform spectrometer (FTS) was designed and constructed for detector characterization. I review the SPT-3G instrument with particular focus on the detectors and FTS and present measurements of the lensing potential and lensing power spectrum from the 2018 data of the SPT-3G survey.

# CHAPTER 1

# INTRODUCTION

Precise measurements of the cosmic microwave background (CMB) address the most fundamental questions in science, including the origin and composition of the universe, the nature of dark matter and dark energy, and neutrino masses, through their impact on the CMB anisotropy. To enable these science goals, we need to develop sensitive microwave cameras for mapping the CMB and extract cosmological information from the data taken. The third-generation camera for the South Pole Telescope (SPT-3G) is one of the current field-leading CMB instruments with 16,000 polarization-sensitive detectors [4]. I discuss the detector characterization and development for SPT-3G in Chapter 2. An important detector characterization tool is the Fourier-transform spectrometer (FTS), which can be used to measure the spectral bands of the detectors, optical material transmission, and CMB's frequency spectrum. Chapter 3 of my thesis discusses a compact FTS used for SPT-3G, which is also similar to the design of a proposed satellite mission PIXIE [5]. With the SPT-3G instrument, we can make low-noise CMB measurements for both the temperature and polarization. Gravitational lensing from large scale structures (LSS) can deflect CMB photons and correlate CMB temperature and polarization anisotropy across different angular scales. The lensing-induced correlations offer a method to reconstruct the projected LSS in the universe. In Chapter 4, I present a measurement of gravitational lensing using SPT-3G data.

## 1.1 Cosmic microwave background

In standard cosmology, the universe went through an exponential expansion period known as cosmic inflation shortly after the big bang singularity. During inflation, quantum fluctuations are frozen by the expansion when the scales cross the causal horizon. After the inflation,

the quantum fluctuations re-enter the horizon and become primordial seeds that later evolve into structures. At the end of inflation, the inflaton field's potential energy is converted to conventional matter through a process called reheating, starting the universe's radiation-dominated phase. At earlier times, the universe is so dense and hot that baryons and photons are in complete thermal equilibrium. As the universe expands and cools, electrons and protons began to combine into atoms (recombination), which lowered the scattering rate between photons and baryons. After that, photons began free-streaming in the universe, forming the cosmic microwave background (CMB). When we observe the CMB photons today, they appear to have come from a thin spherical shell with the radius being the photons' traveling distance since they last scattered with matter during the epoch of recombination. As a result, we refer to this surface as the last scattering surface.

The CMB is very uniform across the sky, with small anisotropies in the order of 0.001%. The initial adiabatic curvature fluctuations from inflation seeded the anisotropies. The adiabatic nature sets the photon-baryon plasma's initial condition with equal fluctuations for all species, which results in well-established gravitational wells. While the gravitational wells attract the plasma, the radiation pressure from the heat by photon-matter interaction pushes back, creating sound waves with oscillation structures, or "baryon-acoustic oscillations." The baryon-acoustic oscillations leave imprints on the CMB as a series of peaks and troughs in the CMB anisotropy's power spectrum. The first peak in the CMB temperature spectrum corresponds to the mode that just finished a compression or half of the compression-rarefication cycle at recombination. The second peak corresponds to the mode that finished one complete compression-rarefication cycle at recombination. At smaller angular scales, photon diffusion, or Silk damping, suppresses the structures in the CMB [6].

The CMB is also polarized at the 10% level. We can separate the CMB fluctuation into temperature, Stokes Q, U ,and V components. The primordial Stokes V component is zero according to ΛCDM model predictions [7]. Measurements so far have only put upper

limits on the CMB Stokes V component [8, 9]. We can then convert Q and U components into coordinate-independent curl-free E-modes and divergence-free B-modes [10], which have different physical origins. The E-modes are primarily sourced by Thompson scattering off electrons around local quadrupoles associated with gradients in the plasma velocity. The B-modes contain two contributions: Thompson scattering off local quadrupoles sourced by gravitational redshifting [11] and gravitational lensing. The first contribution to the B-modes from gravitational redshifting is a probe of the primordial gravitational waves generated during inflation and will be evidence of inflation once detected. The second contribution from gravitational lensing is the dominant source of the B-modes. Large-scale structures in the universe deflect the CMB photons as they travel through the universe, distorting some of the curl-free E-modes into curl B-modes.

As the CMB travels through the universe, interactions with matter can introduce secondary anisotropies. We can divide the matter interactions into two classes: gravitational interactions and scattering effects [12]. The first class consists of gravitational lensing by large scale structure, traveling through time-varying gravitational potentials (integrated Sachs–Wolfe effect [13]), and traveling through nonlinear gravitational potentials (Rees–Sciama effect [14]). The second class consists of inverse Compton scattering between photons and hot thermal plasma (thermal Sunyaev–Zel'dovich effect, or tSZ [15]) and the scattering off electrons with a net bulk peculiar velocity (kinetic Sunyaev–Zel'dovich effect, or kSZ [16]).

The milestones of CMB measurements include its discovery by Penzias and Wilson in 1965 [17], the frequency spectrum and anisotropy measurement by the Cosmic Background Explorer (COBE) satellite in 1990 and 1992 [18, 19], the measurement of the acoustic peaks and confirmation of ΛCDM cosmology by BOOMERANG (2000, [20]), MAXIMA (2000, [21]), DASI (2002, [22]), and WMAP (2003, [23]), the E-mode detection by Degree Angular Scale Interferometer (DASI) in 2002 [24], the lensing B-mode detection by the South Pole

Telescope (SPT) in 2013 [25], and the degree angular-scale B-mode detection by BICEP2 [26]. Over recent years, ground-based and spaceborne experiments [27, 28, 29, 30, 31, 32, 33] have pushed the CMB measurements' precision and angular scales, bringing us into the era of precision cosmology. The current results are mostly well-described by the standard ΛCDM model. However, with smaller error bars over the years, we began to see discrepancies between the measurements. The most noticeable discrepancy is the different Hubble constant $H_0$ values from lower-redshift measurements and CMB measurements [34, 35]. We also begin to see tensions between CMB measurements at larger and smaller angular scales [36]. For CMB lensing, an inconsistency about the lensing amplitude $A_{\rm lens}$ is that the Planck $A_{\rm lens}$ measured from the peak smoothing is about $2.5\sigma$ higher than from the 4-pt lensing power spectrum [29]. More precise measurements from current and next-generation CMB experiments, including SPT-3G[4], ACTpol[37], Advanced ACTpol[38], Simons Array[39], BICEP3/ BICEP Array[40, 41], the Simons Observatory[42], and CMB-S4[43], will constrain cosmology even better and allow investigation into extended parameters beyond the six parameters in the standard ΛCDM model.

The CMB temperature anisotropies are characterized by a spatial variation on top of the blackbody temperature (2.724 K) and are denoted as $T(\mathbf{n})$, where $\mathbf{n}$ is the direction on the sky. The polarization Stokes parameters $Q(\mathbf{n})$ and $U(\mathbf{n})$ are also defined as a function of $\mathbf{n}$ and can be converted into E and B modes following methods in [10]. The CMB fields are approximately Gaussian random fields, and most of their information can be captured by the two-point correlation function or the power spectrum. For a small patch of sky projected to flat coordinates, the power spectrum calculation is as simple as taking the 2D Fourier transform, multiplying its complex conjugate, and averaging over annuli in Fourier space. We calculate the power spectrum for curved-sky by decomposing the fields into spherical harmonics and averaging the coefficient squares' absolute values at the same angular scales. Figure. 1.1 shows some recent measurements and the theory TEB power spectra with best-

fit parameters from Planck2018 [29]. The model agrees with measured data points well. We can extract the six key parameters for ΛCDM cosmology from the measurements, including the universe's content, the optical depth of reionization, and two other parameters on the universe's initial condition (see Section 1.2). Current data can probe the content of the universe with percent-level precision.

E-modes have a higher peak-to-trough contrast than the temperature and are out-of-phase compared to temperature because E-modes are mostly sourced by the gradient in the velocity field, while temperature measures density fluctuations. E-modes are much weaker than temperature because the local quadrupole sourcing polarization comes from the photon diffusion from different temperatures, which only happens before recombination as the mean-free path increases. At large scales or small $\ell$, the E-mode is small because photons cannot diffuse very far. Lensing-induced B-modes are at the 10% level compared to the E-modes. The inflationary B-modes can be even smaller depending on the amplitude of the tensor-to-scalar ratio and can be buried in the lensing B-modes. Therefore, it's critical to remove the lensing B-mode signal through a process called delensing to obtain a cleaner measure of the inflationary B-modes at all multipoles.

## 1.2 ΛCDM model and cosmological parameters

CMB measurements and other cosmological probes generally match well to a ΛCDM(Lambda Cold Dark Matter) cosmology model, which people also refer to as the standard model of cosmology. The ΛCDM model assumes the universe started from a hot big bang and is composed of 5% baryon matter, 27% dark matter, and 68% dark energy at the current time. The theory of general relativity governs the expansion of space in a homogeneous model of the universe. Specifically, we can write down the Friedmann equation that governs the

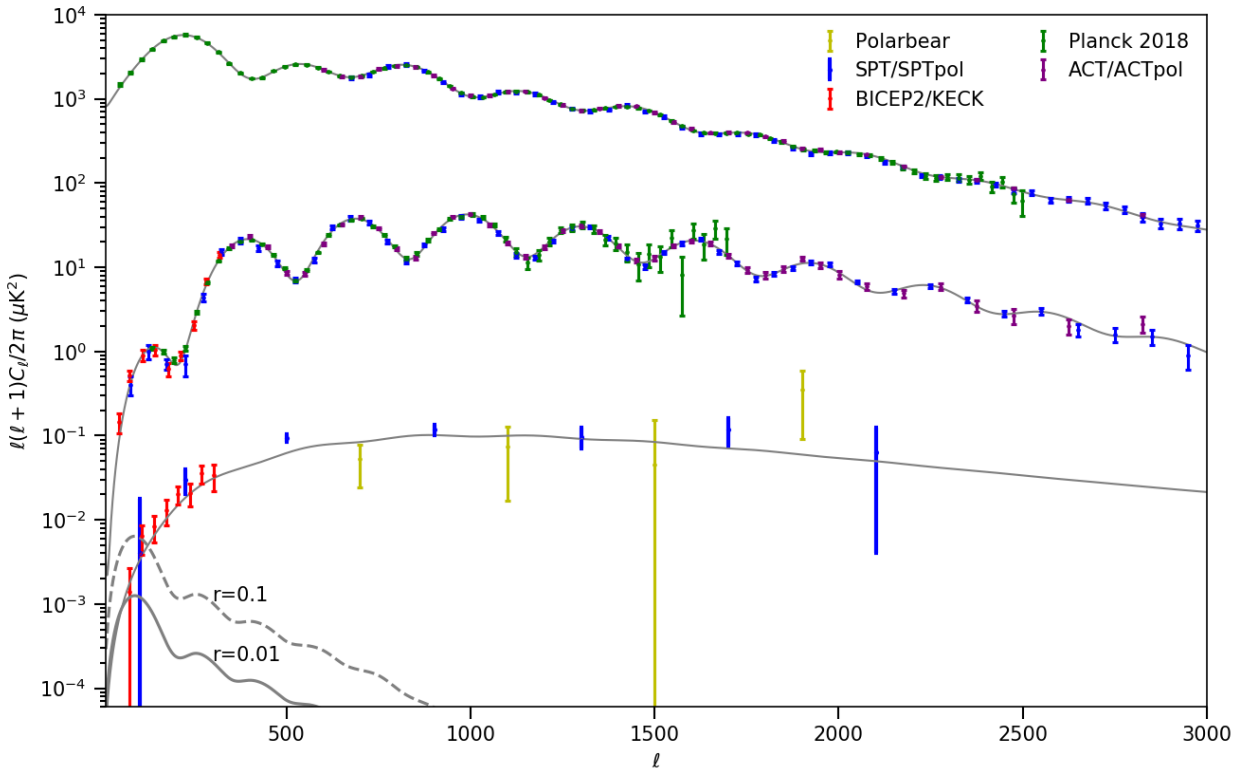


Figure 1.1: The power spectra of T, E, and B-modes. The gray lines are the model spectra with Planck 2018 best-fit parameters. I have also included some recent measurements. The measurements generally agree with each other and the model. Also plotted are the power spectra of inflationary B-modes with the tensor-to-scalar ratio set to $r = 0.1$ and $r = 0.01$. Depending on the tensor-to-scalar ratio, the inflationary B-modes can be much smaller than the lensing B-modes.

universe's expansion with general relativity:

$$H(a) = \frac{\dot{a}}{a} = H_0\sqrt{\Omega_m a^{-3} + \Omega_r a^{-4} + \Omega_K a^{-2} + \Omega_\Lambda a^{-3(1+w)}}, \tag{1.1}$$

where $H$ is the Hubble parameter, $a$ is the scalar factor, $\Omega_m$ is the matter density, $\Omega_r$ is the radiation density, $\Omega_K$ is the spatial curvature density, $\Omega_\Lambda$ is the cosmological constant or vacuum density, and $w$ is dark energy's equation of state. The above densities are defined at the current time where $a = 1$. A flat $\Lambda$CDM model with six cosmological parameters assumes the universe is flat, or $\Omega_K = 0$. The six parameters in $\Lambda$CDM are baryon den-

sity $\Omega_b h^2$, cold dark matter density $\Omega_c h^2$, optical depth $\tau$, the angular size of the sound horizon at recombination $\theta_{\rm MC}$ [1], the amplitude of primordial scalar fluctuation $A_s$, and the spectral index of primordial scalar fluctuation $n_s$. The primordial scalar power spectrum is scale-invariant when $n_s = 1$ (see Eq. 1.2). The CMB temperature spectra measured by the Planck satellite and other experiments generally fit well with the six-parameter ΛCDM model. There are additional parameters beyond ΛCDM that can be probed by the CMB, including curvature of the universe $\Omega_K$, Hubble constant $H_0$, the sum of neutrino mass $\Sigma m_\nu$, the number of relativistic species $N_{\rm eff}$, tensor-to-scalar ratio $r$, and lensing amplitude $A_{\rm lens}$. In the next paragraphs, I will review how the parameters impact the CMB spectra. Much of the content is adapted from Wayne Hu's tutorials [44].

Spatial curvature impacts the CMB power spectra by changing the angular scale of CMB fluctuations. We can parametrize the curvature of the universe using $\Omega_K$. In a closed universe where $\Omega_K < 0$, things look as if they are closer to us, and the same length viewed from the same coordinate distance will appear at a larger angle. Therefore, the features in CMB spectra will shift to larger angular scales or smaller $\ell$. Similarly, for an open universe, the CMB features will move to a higher $\ell$.

Baryon density ($\Omega_b h^2$) changes the relative amplitude between CMB power spectrum peaks. The harmonic feature in the CMB temperature power spectrum is a result of baryon-acoustic oscillation before recombination. As discussed in Section 1.1, the first CMB peak corresponds to the mode that just finished a compression or half of the oscillation cycle during recombination. And the second peak corresponds to the mode that just finished one complete compression-rarefication cycle. If the baryon density increases, the fluid has higher inertia and falls into the potential wells harder, which leads to stronger compressions (odd number of peaks) and weaker rarefactions (even number of peaks).

1. Planck2018 [29] used the CosmoMC theta parameter $\theta_{\rm MC}$ to approximate the acoustic scale $\theta^*$. $\theta^*$ is the ratio of the comoving size of the horizon at the time of recombination, $r_s$, to the angular diameter distance at which we observe the fluctuations, $D_A$. The redshift $z^*$ used for $\theta_{\rm MC}$ is calculated using a quite accurate but non-general fitting formula.

Dark matter can provide the background gravitational potential during the baryon acoustic oscillation for a flat universe. If there is less dark matter or lower $\Omega_c h^2$, the portion of radiation will become larger. For a universe that is photon dominated, the gravitational potential will also be mostly from the photon-baryon fluid instead of the dark matter background. As the fluid finishes the first compression and rarefy, the potential well is less deep. The oscillation amplitude will be much higher because there is less gravity pulling the fluid back. With less dark matter, the oscillation will also be stronger, and the power spectrum amplitude will increase. Since the even number peaks correspond to modes that finish rarefication at the time of recombination, less dark matter will result in higher even number peaks and an overall amplitude increase. On the other hand, a strong third (or odd number) peak compared to the second (or even) ones means more dark matter.

The reionization optical depth ($\tau$) affects the overall amplitude of the measured CMB spectrum and the large-scale polarization-temperature correlation. Free electrons generated during reionization can scatter CMB photons via Thomson scattering. A higher optical depth attenuates the CMB photons more before they can reach us. Rescattering of CMB radiation during reionization can also create a quadrupole temperature anisotropy and a small linear polarization that correlates with the temperature [45]. Therefore, the CMB TE spectrum at low angular multipoles is a sensitive probe for $\tau$.

The amplitude of primordial scalar fluctuation $A_s$ and the spectral index of primordial scalar fluctuation $n_s$ are the initial conditions from primordial fluctuations. They can affect the CMB amplitude and the power spectrum tilt. The CMB structure seeded from adiabatic primordial curvature perturbations

$$P_R(k) = A_s(\frac{k}{k_*})^{n_s-1+\frac{1}{2}\frac{dn_s}{d\ln k}\ln(\frac{k}{k_*})}, \tag{1.2}$$

where $A_s$ is the amplitude, $n_s$ is the spectral index, $k$ is wavenumber, and $k_*$ is the pivot scale. The second-order term in the exponent is the running of the spectral index. $A_s$ will

affect the overall amplitude of the CMB spectra. It's degenerate with optical depth, and $A_s e^{-2\tau}$ can be constrained better than $A_s$ or $\tau$ individually. The $\tau$–$A_s$ degeneracy can be broken using CMB together with CMB lensing or external data on large scale structure, both of which constrain $A_s$. $n_s$ is the spectral index of the fluctuation. It determines the "tilt" of the CMB power spectrum. With a larger $n_s$, CMB spectra is higher above the pivot scale and lower below the pivot scale.

The acoustic angular scale is $\theta_* = r_*/D_M$, where $r_*$ is the comoving sound horizon at recombination, and $D_M$ is the comoving angular diameter distance. The acoustic angular scale is well constrained by the position of the first peak in the CMB angular power spectrum, even independent of cosmology.

CMB can also constrain parameters beyond the standard six parameters in ΛCDM through their effects on the CMB spectra. The effect of the Hubble constant is similar to that of spatial curvature, or $\Omega_K$. With the assumption that the universe is flat ($\Omega_K = 0$), or $\Omega_m + \Omega_\Lambda = 1$, we can break the $\Omega_m$-$\Omega_\Lambda$ degeneracy and obtain a constraint on $H_0$. $A_{\rm lens}$ is the lensing amplitude, which is a made-up parameter for quantifying the amount of lensing. A larger $A_{\rm lens}$ indicates that CMB photons are deflected more. The CMB power spectra are less sharp with more lensing because the CMB power is shoved across different angular scales by lensing-induced mode coupling.

CMB offers a new window into neutrino physics in two ways. 1) The sum of neutrino mass, or $\Sigma m_\nu$, affects the gravitational lensing of the CMB. More neutrino mass suppresses structure growth since neutrinos act like radiation (which suppresses structure growth) at earlier times and dark matter later. More neutrinos will cause less lensing from the large-scale structure. 2) CMB can also be used to constrain $N_{\rm eff}$, which is the number of weakly interacting species that is relativistic at recombination. We can use the $N_{\rm eff}$ parameter to describe radiation-like energy density. The standard model prediction for $N_{\rm eff}$ is 3.046. $N_{\rm eff}$ affects the expansion history and the characteristic scale of CMB fluctuations. On the other

hand, $N_{\rm eff}$ affects sound waves of photon-baryon plasma and change the mean-free-path of photons, or the diffusion scale of the CMB. The ratio of the two scales is precisely measured by the CMB and can constrain $N_{\rm eff}$ [46].

The last parameter I'll mention here is the tensor-to-scalar ratio $r$. Tensor perturbation can generate primordial gravitational waves, which imprint in the CMB as the inflationary B-modes. Inflationary B-mode will increase as the tensor-to-scalar ratio increase.

## 1.3 Gravitational lensing of the CMB

As CMB photons travel through the universe, they are bent by the gravitational potentials from the intervening large-scale-structure through a process known as gravitational lensing. The primordial CMB fields before lensing have well-known statistics and can be approximated by Gaussian random fields. Gravitational lensing distorts the CMB and induces correlations across different angular scales for CMB temperature and polarization. These correlations allow us to reconstruct the lensing potential that deflected the photons' paths by optimally weighting off-diagonal CMB modes across different angular scales [47]. The resulting lensing potential measurement contains information about the projected two-dimensional matter distribution from the last scattering surface($z \sim 1100$) to now. The 2D matter distribution from CMB lensing contains a wealth of information about the growth of structure, which can probe various fundamental physics topics, including matter density fluctuation [48], neutrino mass [49, 50, 51, 52], dark energy [53], and gravity [54, 55, 56].

Lensing induces mode-coupling between CMB modes at different angular scales and smooths the peaks in the CMB power spectra [57]. Multiple experiments have detected the peak smoothing effect using both the temperature and polarization data [58, 27, 29, 59]. The mode coupling enables quadratic-type estimators where one can estimate the lensing signal corresponding to a specific scale in Fourier space by averaging over pairs of CMB modes in Fourier space separated by that scale [60, 47]. Most of the lensing measurements available

now utilize the quadratic estimator, which works optimally at typical current instrument noise levels. So far, there have been measurements on CMB lensing from SPT/SPTpol [61, 62, 63, 64], ACTpol [65, 66, 67], Planck [68, 69, 70], POLARBEAR [71], and BICEP [72]. The most significant lensing amplitude measurement is at $40\sigma$ from Planck 2018 [70], and the most significant polarization-only lensing amplitude measurement is at $10.1\sigma$ from SPTpol [64]. Fig. 1.2 shows the power spectra of lensing measurements from Planck [69], SPT-SZ [63], SPTpol [64], ACTpol [66], as well as the lensing spectrum forecast for the SPT-3G five-year survey. The method for generating the lensing spectrum from a lensing map is similar to that for generating the CMB power spectrum from a CMB map, which is discussed in Section 1.1. From Fig. 1.2, SPT-3G will measure lensing features with larger-than-unity signal-to-noise at angular scales larger than 12 arcmin where the signal curve is above the noise line, thanks to the arcminute resolution and low noise levels of 3.0/2.2/8.8 $\mu$K-arcmin at 95/150/220 GHz [73] provided by the new SPT-3G receiver [4].

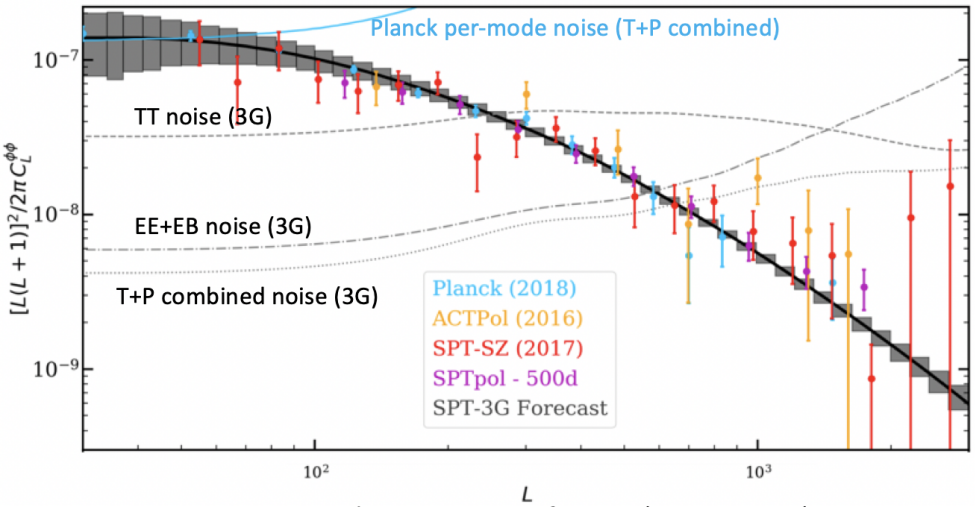


Figure 1.2: The power spectra of lensing measurements from Planck [69], SPT-SZ [63], SPTpol [64], ACTpol [66], along with the lensing forecast for the SPT-3G full survey. The solid cyan line shows the Planck minimum-variance noise curve. The dotted or dashed gray lines show the temperature, polarization, and minimum-variance combined noise curves for SPT-3G. Figure taken from [73]. Credit to Jason Henning.

CMB lensing measures matter distribution in the redshift range between 0 and 1100,

overlapping with the redshift range of all other astrophysical surveys. Owning to the well-known statistics of the CMB as the lensing source, CMB lensing measurements have relatively cleaner astrophysics systematics. As a result, the matter distribution inferred from CMB lensing measurements is an excellent template for cross-correlation studies. It can help constrain systematic effects in other surveys, such as the multiplicative shear bias in optical surveys [74]. Cross-correlation measurements can provide more powerful probes into cosmology and are generally less prone to systematic effects than single surveys [75]. If the other survey contains redshift information, we can use the combination to make a three-dimensional tomographic measurement of the matter distribution [76, 77, 78, 79]. Since the CMB lensing's first detection via cross-correlation [80], there have been cross-correlations with optical surveys [81, 82, 83, 84], far-infrared wavelength [85], infrared wavelength [79], submillimeter galaxies [86, 87], and X-ray [88].

With more precise current and upcoming experiments, we need to build more optimal estimators for various analysis purposes and tackle the lensing biases more carefully. For lensing power spectrum analysis, there are the well-known map-level bias from non-lensing statistical anisotropies in the CMB map (mean-field bias) and the spectrum-level biases from connected and disconnected pieces in the lensing trispectrum [89, 90]. Additionally, we have biases from astrophysical and modeling effects, including polarized [91] and unpolarized [92, 93] foreground emissions, non-Gaussian lensing deflections [94, 95], corrections beyond Born approximations for the lensing deflection [96, 97, 98, 99, 100], lensed foregrounds [101], and baryonic effects [102]. While some of the biases to the lensing power spectrum can be estimated and subtracted, the map-level biases are harder to deal with and are already causing problems at the current instrument sensitivity. For example, some recent cross-correlation analyses are limited by the lensing bias at smaller angular scales caused mostly by the tSZ effect associated with galaxy clusters [103], and the current solution is to cut the contaminated angular scales at the cost of information loss. Recently, some bias-hardened estimators that

are less prone to certain biases have been developed, such as the shear-only estimator [104] and modified quadratic estimator with a tSZ-cleaned map for the gradient leg [105]. Another direction of efforts in lensing estimator development is to build more optimal estimators with lower variance. Quadratic lensing estimators [60, 47] will be less optimal as the CMB noise level approaches 5 $\mu$K-arcmin [106]. Recently, Millea et al. [107, 108] developed an estimator that samples the exact Bayesian posterior of desired cosmological information given the CMB maps. Recent new lensing estimators also include a maximum-a-posteriori CMB lensing reconstruction [109] that iteratively reconstructs the unlensed CMB to improve the signal-to-noise and a gradient-inversion-based approach to improve the smaller-scale lensing reconstruction [110].

Lensing can also convert some primordial curl-free E-modes into curl B-modes by distorting the spatial patterns of the CMB polarizations. A few experiments have measured lensing-induced B-modes [25, 111, 112, 31]. The lensing-induced B-mode is contamination for primordial B-modes imprinted by primordial gravitational waves generated during inflation, and its removal is critical for better constraints on inflation. To remove the lensing B-modes, we can combine E-modes and the lensing potential to get an estimated B-mode template and subtract this template from the measured B-mode power spectrum [113]. While we can estimate lensing potential from the CMB data itself, we can also construct it using other tracers of mass distribution, such as the cosmic infrared background (CIB) [114] and galaxy surveys [115]. For future experiments, the gain of estimating the lensing potential with multiple mass tracers is modest compared to using CMB lensing measurements alone. Removing the lensing B-mode or delensing is also crucial for precise lensing measurements because reconstruction can be improved by an iterative process of delensing and lensing reconstruction [109]. The Bayesian delensing method can also recover the lensing potential and the unlensed CMB modes simultaneously [107, 108]. The South Pole Telescope has high angular resolution and is good at measuring the lensing signal, while the BICEP Array [41]

specializes in measuring the degree-scale B-modes. The delensing from SPT-3G can remove 2/3 of the contamination power from gravitational lensing to large-scale B-modes measured by BICEP Array (Fig. 1.3(a)). The two experiments combined can achieve an uncertainty of $\sigma(r) \sim 0.003$. Without delensing, $\sigma(r)$ is about two times higher (Fig. 1.3(b)).

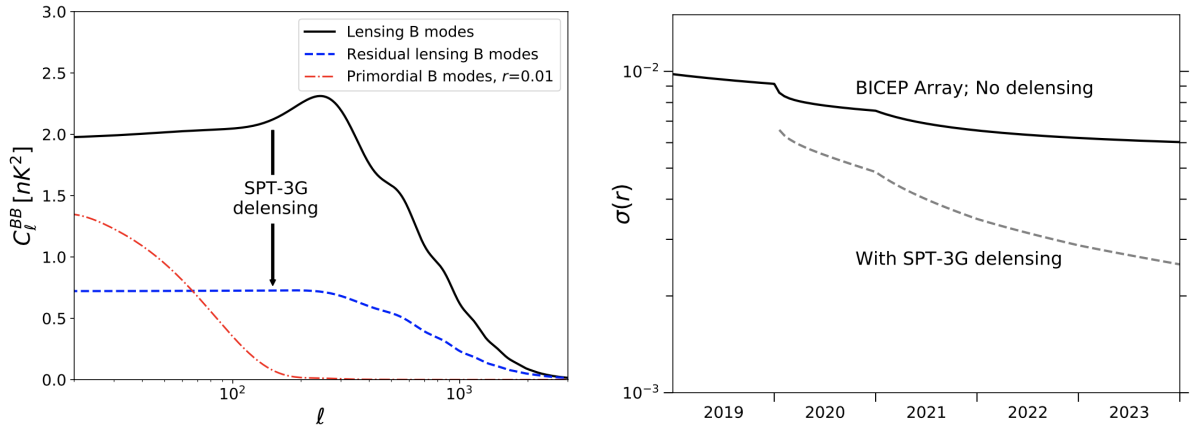


(a) B-mode power spectrum

(b) Constraint on r

Figure 1.3: (a): The power spectrum of the lensing B-modes, primordial B-modes with tensor-to-scalar ratio $r = 0.01$, and the residual B-modes after SPT-3G delensing. If $r = 0.01$, we will be able to detect primordial B-modes with SPT-3G delensing. (b) The uncertainty on tensor-to-scalar ratio as a function of survey year. With SPT-3G delensing, the uncertainty of $\sigma(r)$ can be reduced by a factor of $\sim$2 to be $\sim 0.003$ at the end of the two surveys. Figure taken from [73]. Courtesy of Kimmy Wu.

This work will estimate the lensing potential using the quadratic estimator, which is very close to optimal with our data noise levels. We will estimate map-level biases from masking and non-homogeneous noise and the spectrum-level biases to the zeroth and first order of the lensing power spectrum. Note that most of the higher-order biases discussed in this section are insignificant compared to our error bars with SPT-3G 2018 data's noise level. We can use the reconstructed lensing information to constrain cosmological parameters, including the matter density $\Omega_m$ and the RMS matter mass density fluctuation within an 8-Mpc-diameter comoving sphere, $\sigma_8$.

# CHAPTER 2

# SPT-3G INSTRUMENT

## 2.1 The South Pole Telescope

The South Pole Telescope (SPT) is a ten-meter diameter submillimeter-quality telescope located at the Geographical South Pole [116, 117]. The site is the NSF Amundsen-Scott Research Station on the 2,835 m-elevation Antarctica Plateau. The high elevation and low temperature at the South Pole reduce the precipitable water vapor (PWV) in the atmosphere, reducing the emission and noise fluctuations generated by PWV. The mm-wavelength observation conditions at the South Pole have been extensively measured by [118, 119, 120, 121, 122, 123, 124]. The South Pole has a low winter median PWV of around 0.27 mm [118] and an order of magnitude lower median fluctuation power than Chajnantor [119]. The atmosphere during the six-month-long winter night at the South Pole is remarkably stable compared other sites and is ideal for continuous observation. Even the South Pole summer is excellent compared to many of other sites. The South Pole site also enables access to the same patch of the sky throughout the year.

The telescope was designed to map the faint millimeter-wavelength emission from the CMB with high sensitivity and resolution. The ten-meter primary dish gives the telescope one arcmin resolution at 150 GHz . The primary dish has 20 $\mu$m RMS surface error and can enable future surveys at submillimeter wavelengths[125]. The off-axis Gregorian design with an unblocked primary mirror minimizes ground pickup and maintains a large field-of-view. The optical design also provides an image of the primary dish for a potential Lyot stop. The paraboloidal primary mirror allows changing the focus of the secondary mirror for different receivers. SPT has three generations of receivers over the past ten years. The first generation (2007-2011) was the SPT-SZ receiver with 960 detectors at 95, 150, and 220 GHz optimized for measuring the CMB and the SZ-effect from galaxy clusters

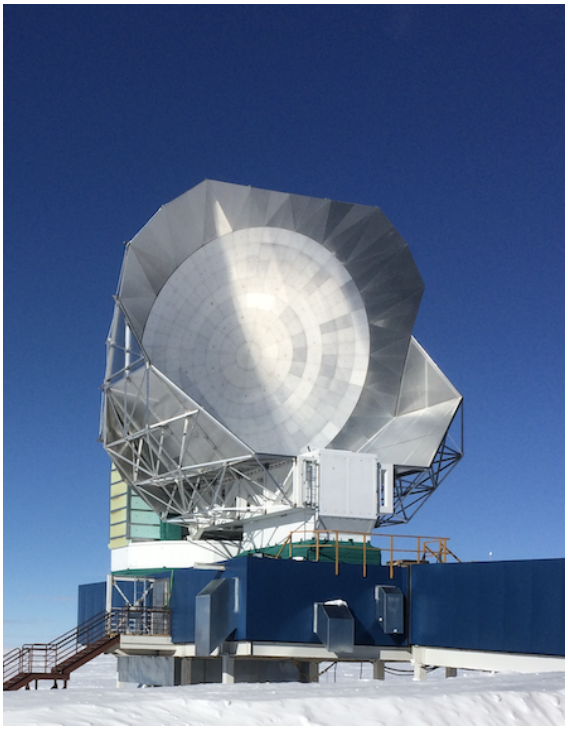

Figure 2.1: The South Pole Telescope. The primary dish is 10 meters in diameter. The white box under the primary dish is the receiver cabin, which was mated to the roof of the blue control room beneath it when the photo was taken. The telescope has ground shields around the primary mirror to prevent stray reflections from the ground.

with high resolution [126, 127]. The second-generation (2012-2016) receiver was the SPTpol receiver with 1500 polarization-sensitive detectors, which enabled the measurement of CMB polarization anisotropy [128, 27]. The currently operating third-generation receiver, SPT-3G [4], was installed in 2017. It has polarization sensitivity and three frequency bands centered at 95, 150, and 220 GHz. The unprecedented detector number of 16,000 and the resulting sensitivity makes SPT-3G a sensitive probe of many fundamental science goals, including B-mode polarization anisotropy, gravitational lensing, inflation constraints (joint with BICEP Array [41]), and the sum of the neutrino masses.

## 2.2 SPT-3G detector overview

To reach the required sensitivity for the SPT-3G science goals, we must push the current technological limits. In particular, the detector number needs to be increased by around 10× compared to SPTpol. Superconducting transition-edge sensor (TES) detectors are the preferred technology for CMB measurements owing to their high sensitivity, excellent fabrication scalability, and compatibility with multiplexing readout technologies. TES detectors were used for SPT-3G. Microwave kinetic inductance detectors (MKIDs) are a competing technology that can detect mm/sub-mm photons and have higher multiplexing factors per readout line due to their higher readout bandwidth. MKIDs do have simpler fabrication, potentially giving them some advantage over TES. However, MKIDs technology is not as mature as the TES technology, which has been demonstrated in many preceding CMB experiments, including SPTpol [129], ACTpol [37], and BICEP2 [130]. MKIDs are promising for future millimeter-wavelength experiments, including CMB experiments. Recently, the microwave-SQUID readout for TES detectors [131] can have similar-to-identical multiplexing factors as MKIDs. Microwave-SQUID readout technology was not chosen for most CMB experiments because it is not well developed but it remains a promising readout technology for the future.

For SPT-3G, TES detectors are used in a bolometer that converts incident optical power into thermal heat, where the TES measures the temperature change from heating. The SPT-3G detector structure uses an antenna to collect the optical signal, a superconductor TES film deposited on a thermal island to measure the power from thermal heat, and a thermal bath weakly coupled to the thermal island to provide a constant reference temperature. Fig. 2.2 is a picture of the bolometer model used by SPT-3G. SPT-3G uses a quad-layer Ti-Au-Ti-Au film as the superconductor sensor [132]. The quad-layer film has advantages of tunable superconducting transition temperature $T_c$ and stable chemical properties. The model in Fig. 2.2 contains a thermal mass called Bandwidth Limiting Interface Normally

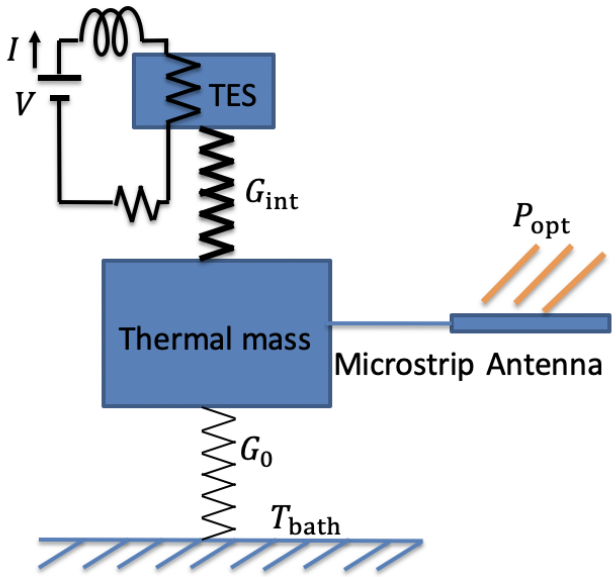


Figure 2.2: Bolometer model. An antenna collects the optical signal and feeds it to a thermal island through a microstrip transmission line. The thermal island is weakly thermally coupled to a thermal bath at a constant temperature. Incident optical power is converted into heat at the thermal island and creates a temperature change at the TES superconductor, and the change is measured by a readout circuit. A thermal mass with a large thermal capacity is often attached to the TES on the same thermal island to control the response speed of the detector.

of Gold (BLING), which is well coupled to the TES for maintaining electrothermal stability (see Section 2.4).

Several detector parameters are defined here: optical power dissipated on the TES ($P_{\text{opt}}$), electrical bias power generated on the TES ($P_{\text{elec}}$), heat capacity of the bolometer ($C$), thermal conductivity to the heat sink ($G$), bolometer temperature ($T_c$), and the heat sink temperature ($T_0$). When the bolometer reaches equilibrium, the total power on the TES equals the power conducted to the heat sink through the weak thermal link: $P = P_{\text{elec}} + P_{\text{opt}} = \int G(T)dT$, where $G(T)$ is the temperature-dependent thermal conductivity. With a power $P$, the thermal gradient between the bolometer and the thermal bath is $\Delta T \approx P/G$ with a thermalization time constant $\tau \approx C/G$. The TES detector is used with a voltage bias, which provides negative feedback and keeps the total power and the temperature on the TES constant. The power generated by a voltage-biased TES is $P_{\text{elec}} = V^2/R$, where $V$ is the bias

voltage on the TES, and $R$ is the TES resistance. When the incident optical power increases, the temperature of the TES increases. If $dR/dT > 0$, the resistance also increases, causing the electrical power $P_{\rm elec}$ to decrease. This process is negative electrothermal feedback [133]. The steepness of the superconducting transition (Fig. 2.3), $\alpha = (T/R)dR/dT$, is proportional to the loopgain of the electrothermal feedback, $\mathcal{L}$, where in the limit of high loop gain, changes in electrical power $\Delta P_{\rm elec}$ perfectly compensate for changes in optical power $\Delta P_{\rm opt}$. In this limit, the measured TES current response $\Delta I = \Delta P_{\rm elec}/V = -\Delta P_{\rm opt}/V$ is close to linear in terms of the change in optical power.

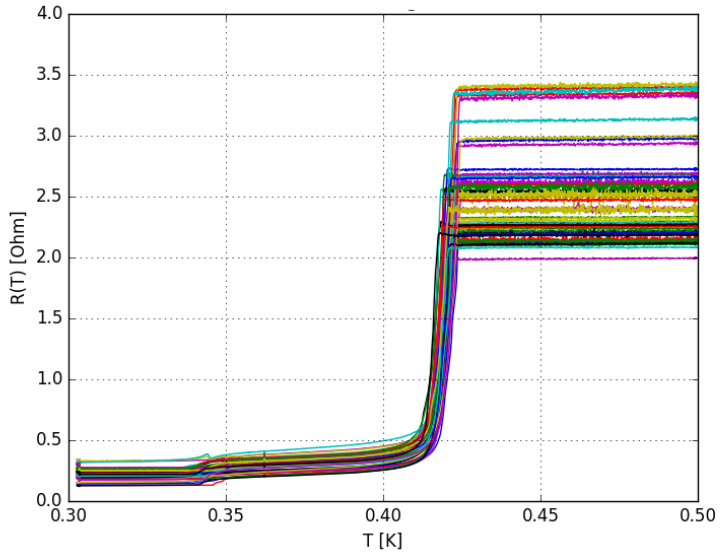


Figure 2.3: Resistance-temperature curves for a deployed SPT-3G wafer. The detectors were operated with a small voltage bias that does not affect their temperature. The thermal bath temperature was swept slowly to ensure the detectors remain in thermal equilibrium with the thermal bath. Detectors' resistances were recorded as functions of the bath temperature. From the curve, most detectors' superconducting transition temperatures are at ∼420 mK. A sharper superconducting transition increases the electrothermal feedback and makes the detector more linear. Courtesy of Tyler Natoli.

## 2.3 Detector structure

TES detectors are now advanced to a stage where they are background limited, which means their detector noise is smaller than the photon noise from optical signals, thanks to the development of sub-kelvin detectors and low-noise readout technology. With background-limited detectors, the only way to increase the CMB mapping speed is to increase the detector number. To improve the packing efficiency of many detectors, SPT-3G uses large arrays of detectors fabricated on six-inch silicon wafers. Each wafer contains 271 pixels, and each pixel has an antenna coupling to six TES detectors (Fig. 2.4). A log-periodic self-complementary sinuous antenna [134] was chosen for its broadband frequency sensitivity, frequency-independent impendence, and dual-polarization sensitivity. The signal collected by the antenna is transferred by niobium microstrip transmission lines and divided into the 95, 150, and 220 GHz frequency bands by three-pole lumped-element triplexer filters. The lumped element filter for one frequency band consists of two parallel plate capacitors and three coplanar waveguide inductors fabricated along the transmission lines. The divided sky signal is coupled to six TES detectors, one for each of the three observing bands and two polarizations.

Fig. 2.5(a) shows the structure of a TES detector. The center island is connected to the thermal bath via four thin legs. Fig. 2.5(b) shows a cut wafer with a dangling thermal island attached to the wafer by two of the four legs. The Nb transmission lines connect to the thermal island via the legs and terminate on a 20 Ohm Ti/Au load resister [136]. The sky signal is converted into thermal energy at the load resistor, which results in a change of island temperature. A superconductor TES film located at the bottom of the thermal island in Fig. 2.5(a) measures the power change. An 850 nm-thick layer of Pd BLING [136] is deposited on the island to slow down the thermal response and stabilize the detectors. Pd was chosen for its high heat capacity at cryogenic temperatures.

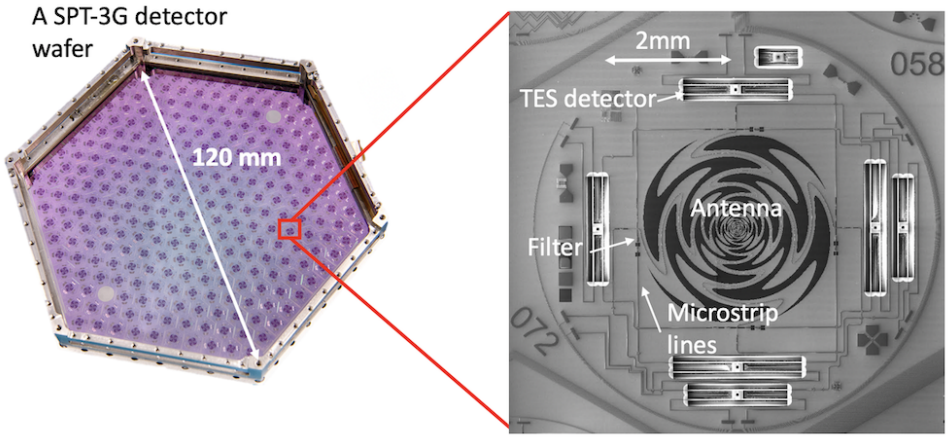


Figure 2.4: A detector wafer and a zoomed-in pixel for SPT-3G (adapted from [135]). The wafer is fabricated from a six-inch silicon wafer and contains 271 individual pixel antennas. The sinuous antenna in the middle of each pixel is sensitive to a broad range of frequencies. Microwave signal collected by the antenna is transferred by the microstrip lines and divided into six detectors by the lumped-element filters.

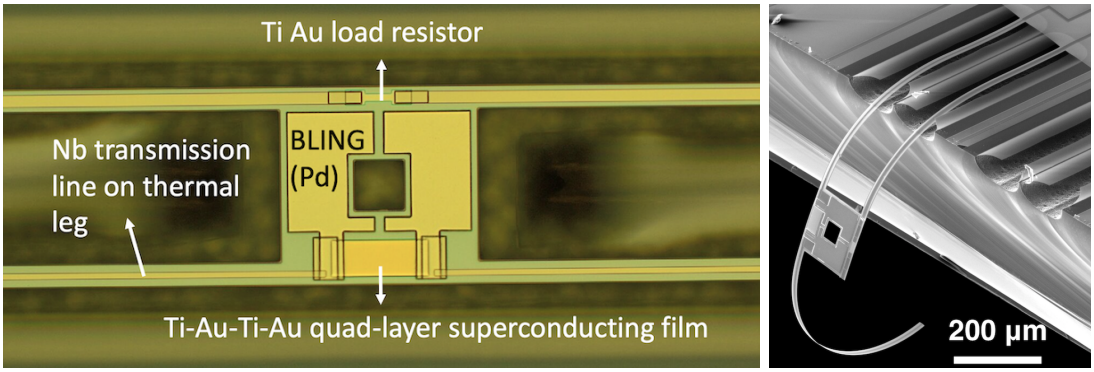


(a) Detector structure

(b) Dangling detector island

Figure 2.5: (a): SEM image of a TES detector. Four legs with a LSN(low-stress silicon nitride)/Niobium/SiOx/Niobium quadruple layer structure[137] connect the TES island to the rest of the wafer. The load resistor is on the top, and the superconductor TES film is on the bottom. (b) shows a dangling detector after dicing. Two legs somehow remain connected to the cut wafer. (b) clearly shows that the detectors are only connected to the wafer by the four legs. Note that the dicing for (b) was non-standard for evaluation purposes and is not how the deployed detectors wafers were diced.

## 2.4 Detector operation and electrothermal feedback

The optical power received by the TES changes its temperature and resistance, causing a modulation in current, and current variation can produce electrical power change, feeding back into temperature. This feedback loop linearizes the detector response vs. deposited optical power and stabilizes the detector. If the model contains multiple thermal elements, such as the BLING, the thermal conduction between different elements and their influences on the temperature need to be considered. For a simple TES detector, which can be treated as a single thermal body connected to a thermal bath Fig. 2.6, we can write down two coupling equations, one from Ohm's law and the other from energy conservation [133, 138]:

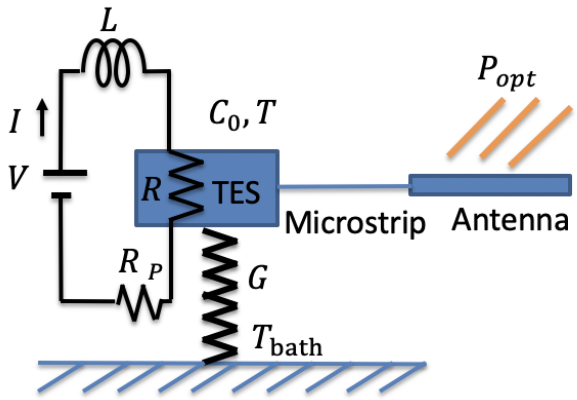


Figure 2.6: Thermal model for a DC biased bolometer. The TES is in a circuit with a DC voltage source, a parasitic resistor $R_p$, and a parasitic inductor $L$. The detector has thermal capacity $C_0$ and is connected to the thermal bath $T_{\rm bath}$ via a thermal link $G$.

$$L\frac{d}{dt}I = V - IR - IR_p, \tag{2.1}$$

where $L$ is the inductance, $I$ is the current, $V$ is the bias voltage, $R$ is the resistance of the TES, and $R_p$ the parasitic resistance in the circuit, and

$$C_0\frac{dT}{dt} = G(T - T_{\rm bath}) + P_{\rm ext} + P_{\rm elec} \tag{2.2}$$

where $C_0$ is the thermal capacity of the TES, $T$ is the temperature of the TES, $T_{\text{bath}}$ is the temperature of the thermal bath, $P_{\text{ext}}$ is the external optical power $P_{\text{opt}}$ or electrical perturbation power, and $P_{\text{elec}}$ is the electrical bias power $I^2R$.

The perturbation from optical power and the subsequent changes are usually small so that we can work with the equations in first-order perturbations. The perturbed electrical power is

$$\delta P_{\text{elec}} = \delta(I^2R) = 2I_0R_0\delta I + I_0^2\delta R \tag{2.3}$$

Resistance change $\delta R$ of the TES superconductor depend on the temperature and current and has the form $\delta(\ln R) = \alpha\delta(\ln T) + \beta\delta(\ln I)$. We put these in $\delta P_{\text{elec}}$ and get

$$\delta P_{\text{elec}} = (2+\beta)I_0R_0\delta I + \mathcal{L}G_0\delta T \tag{2.4}$$

where $\mathcal{L} = \alpha P_{\text{elec}}/GT$, $\alpha = \partial \ln R/\partial \ln T$, $\beta = \partial \ln R/\partial \ln I$.

Also use $\xi = R_p/R_0$, the perturbation equations become:

$$I_0L\frac{d}{dt}\delta I = -G\mathcal{L}\delta T - (1+\xi+\beta)I_0R_0\delta I + I_0\delta V \tag{2.5}$$

$$C_0\frac{d}{dt}\delta T = (\mathcal{L}G - G)\delta T + (2+\beta)I_0R_0\delta I + \delta P_{\text{ext}} \tag{2.6}$$

The two equations can be combined to a matrix form:

$$\frac{d}{dt}\mathbf{v} = \mathbf{A}\mathbf{v} + \mathbf{p}, \tag{2.7}$$

where $\mathbf{v} = \begin{bmatrix} LI_0\delta I \\ C_0\delta T \end{bmatrix}$, $\mathbf{p} = \begin{bmatrix} I_0\delta V \\ \delta P_{\text{ext}} \end{bmatrix}$, and $\mathbf{A} = \begin{bmatrix} -\tau_e^{-1} & -\mathcal{L}\tau^{-1} \\ \frac{2+\beta}{1+\beta+\xi}\tau_e^{-1} & (\mathcal{L}-1)\tau^{-1} \end{bmatrix}$ The thermal and electrical time constants are defined as $\tau \equiv \frac{C_0}{G}$ and $\tau_e \equiv \frac{L}{(1+\beta+\xi)R_0}$.

Note in the general case the thermal conductivity $G$ is temperature dependent. The stability requires the perturbations to be over damped, or Re(Eigenvalues($\mathbf{A}$)) $> \mathbf{0}$ and Im(Eigenvalues($\mathbf{A}$)) $= \mathbf{0}$. The conditions are $\mathcal{L} < (3-\sqrt{2})\frac{\tau}{\tau_e} \approx \frac{1}{5.8}\frac{\tau}{\tau_e}$ from Eq. 2.7. For stability, a Pd BLING was deposited on the thermal island to increase the detector time constant $\tau$.

The response read out from the detector is the current modulated by the incident optical power. One important quantity we are interested in is the current-to-power ($\delta I$ to $P_{\rm ext}$) responsivity $s_I$, which can be calculated by:

$$s_I(\omega) = -\frac{(\mathbf{A}-\mathbf{i}\omega)^{-\mathbf{1}}_{\mathbf{12}}}{LI_0} = -\frac{1}{I_0 R_0}\left(\frac{\mathcal{L}}{\mathcal{L}(1-\xi)+1+\beta}\right)\left(\frac{1}{1+i\omega\tau_{\rm eff}}\right)\left(\frac{1}{1+i\omega\tau_e}\right) \tag{2.8}$$

Here the effective time constant $\tau_{\rm eff} = \frac{\tau}{1+\mathcal{L}\frac{1-\xi}{1+\xi+\beta}}$. The detector response is sped up by a factor of approximately $1+\mathcal{L}$ from the electrothermal feedback. In the limit of large loopgain, the responsivity is $-1/I_0R_0$, or $-1/V_0$ with the electrical and thermal time constant roll-offs.

## 2.5 Detector noise

Detector noise, detector number, and optical efficiency determine the mapping speed of a CMB receiver. Therefore, optimizing the detector noise is a primary goal in detector design and operation. The noise in bolometers and TES sensors have been studied in detail in literature [139, 133]. In this section, I summarize detector noise terms for a typical SPT-3G detector. The noise in detectors is commonly characterized by the noise-equivalent power (NEP), which is defined as the amount of signal power that would have signal-to-noise of one over a one Hz bandwidth range. NEP has contributions from incident photon fluctuation, Johnson noise, phonon (thermal carrier) noise, and readout noise. NEP can be related to the noise-equivalent temperature by NET $= \frac{1}{\sqrt{2}}\frac{dT}{dP}$NEP, where the factor of $1/\sqrt{2}$ comes from the convention that NEP is defined as the power spectrum with just the positive frequencies

while the NET is defined with unit relative to the integration time ($K\sqrt{s}$). One way to understand the $1/\sqrt{2}$ factor is that the noise power spectral density PSD, or NEP$^2$, is conventionally defined only at positive frequencies, and the negative frequency components are folded into the positive frequency part, which effectively doubles the PSD or multiplies the NEP by $\sqrt{2}$ compared to defining them using the full bandwidth. The noise in the CMB maps made from a CMB receiver with multiple detectors is $N_{\rm map} = \frac{\rm NET\sqrt{S_{sky}}}{\sqrt{N_d\, t}}$, where $N_{\rm map}$ is map depth typically in unit of $\mu K$-arcmin, $S_{\rm sky}$ is the sky area, $N_d$ is the number of detectors, and $t$ is the integration time. NEP can also be related to the current noise NEI by NEP = NEI/$s_I$, where $s_I$ is the power-to-current responsivity. In the next sections, different contributions to the noise will be discussed in more detail.

### *2.5.1 Photon noise*

The first significant contribution to the detector noise is the photon noise, which arises from the random exchange of photons with the surrounding environment that leads to fluctuation in temperature. In bolometers, photon noise can be the dominant noise source. Photon noise can be easily calculated for a blackbody illuminating a single-mode diffraction-limited detector. The fluctuation in the number of photons received per second per mode is $\langle \Delta n^2 \rangle = n + n^2$ [140] where $n$ is the received photon number per second per mode. The first term is due to photon shot noise, which can be described by Poisson statistics. The second term is due to photon bunching, which is caused by the Bose-nature of photons. The second term becomes important when the photon number is large. We are interested in the fluctuation of energy received per second, which is [141]

$$\mathrm{NEP}^2_{\rm photon} = 2\int 2Nh^2\nu^2\langle \Delta n^2\rangle d\nu, \tag{2.9}$$

where $N = A\Omega/\lambda^2$ is the number of modes for a detector with an antenna surface area $A$ and a detection solid angle $\Omega$. In the single-mode diffraction limit $N = 1$. The first factor of

2 comes from the two polarizations of a photon, and the second factor of 2 comes from the fact that the bandwidth associated with a 1 s unweighted average is 1/2 Hz (see Section 2.5 for more details). We rewrite the equation as

$$\mathrm{NEP}^2_{\mathrm{photon}} = 2P_{\mathrm{opt}}h\nu_0 + NP^2_{\mathrm{opt}}/\Delta\nu, \tag{2.10}$$

where $P_{\mathrm{opt}} = 2\int Nnh\nu d\nu$ is the total optical power, $\nu_0$ is the band center, and $\Delta\nu$ is the bandwidth. Note that we have used the band center frequency $\nu_0$ to approximate the frequency of the band. For the general case with an extended polarized source, Lamarre [142] calculated the photon noise to be

$$\mathrm{NEP}^2_{\mathrm{photon}} = 2\int h\nu Q_\nu d\nu + (1+P^2)\int \xi(\nu)Q^2_\nu d\nu, \tag{2.11}$$

where $Q_\nu$ is the specific flux in $WHz^{-1}$, and $P$ is the degree of polarization. The first term is approximately $2P_{\mathrm{opt}}h\nu_0$ when we use the band center frequency $\nu_0$ for the frequency band. $\xi(\nu)$ in the second term is the partial coherence factor [142] . In the limit for a point source, $\xi(\nu)$ is 1. In the limit of uniform source extended over a large area, $\xi(\nu)$ is $\lambda^2/A\Omega$, which is one for a single-mode diffraction-limited detector. When the input radiation is unpolarized ($P = 0$) and the detector is single-mode diffraction limited ($\xi(\nu) = 1$), the second term reduces to $P^2_{\mathrm{opt}}/\Delta\nu$. The optical loading for an SPT detector comes from a variety of sources including the atmosphere, the CMB, and various optical elements. Therefore, $\xi(\nu)$ is a factor between 0 and 1.

### *2.5.2 Thermal carrier noise*

Thermal carrier noise can be the second dominant noise source for a typical CMB detector. From thermodynamics, the power flowing from TES to the thermal bath has $\mathrm{NEP}^2_{\mathrm{thermal}} = 4k_BGT^2$ in the classical equilibrium limit [140], where $G$ is the thermal conductance. How-

ever, the thermal conductivity $k(T)$ is usually dependent on temperature. Following a more careful derivation in [139], the analytical result is:

$$\mathrm{NEP}^2_{\mathrm{thermal}} = 4k_B G T^2 \frac{\int_{T_{\mathrm{bath}}}^{T_c} [\frac{tk(t)}{T_c k(T_c)}]^2 dt}{\int_{T_{\mathrm{bath}}}^{T_c} [\frac{k(t)}{k(T_c)}]^2 dt} \tag{2.12}$$

where $T_{\mathrm{bath}}$ is the temperature of the thermal bath, and $T_c$ is the TES's operating temperature. Note that John Mather made the assumption that fluctuation-dissipation theorem at equilibrium with linear elements can describe state variables out of equilibrium with nonlinear elements. [133].

### *2.5.3 TES Johnson noise*

Johnson noise is the electronic noise generated by the thermal agitation of charge carriers inside an electrical conductor at equilibrium[143]. Johnson noise is white noise with power spectrum density

$$\langle E^2 \rangle = 4k_B T R. \tag{2.13}$$

E is the thermally agitated voltage measured in $\mathrm{V}/\sqrt{\mathrm{Hz}}$, and R is the resistance. In a TES, the Johnson noise is suppressed by the electrothermal feedback. The Johnson noise for an AC-biased TES bolometer by [138] is

$$\mathrm{NEP}^2_{\mathrm{Johnson}} = 4k_B T_c P_{\mathrm{bias}} (1 + \omega^2 \tau^2)/\mathcal{L}^2, \tag{2.14}$$

where $P_{\mathrm{bias}}$ is the bias power on the TES, $\omega$ is the angular frequency, $\tau$ is the effective time constant of the TES, and $\mathcal{L}$ is the loopgain.

### *2.5.4 Readout noise*

The readout for SPT-3G is described in Section 2.7. The readout noise can come from the first-stage SQUID amplifier, the Johnson noise of the warm electronics, and the noise of the higher-stage amplifier after the SQUID. Most of the readout noise is generated after the SQUID. For our readout system, we use Digital Active Nulling (DAN) to cancel the current from the bolometer comb so that the SQUID current is smaller. DAN removes the dynamic range limitation of the SQUID amplifier and increases its linearity [144]. Ideally, the DAN feedback can completely cancel the detector signal and only contains the detector signal. But in reality, noise after the SQUID amplifier in the demodulation chain cannot be distinguished from detector signals, and DAN tries to null this noise by sending in a nulling current of the same form. A fraction of the noise in the nulling signal leaks to the detector comb, causing the nuller to increase the feedback amplitude to compensate for it, amplifying the noise by the leaked amount [145]. The amplified noise is called the current-sharing noise and is a large fraction of the readout noise. The solution to reducing this noise is to use lower impedance SQUIDs. With a low SQUID impedance, most of the nuller noise flows through the SQUID instead of the detector comb. The SQUIDs used in the 2017 season have inductance around 300 nH and produce a large impedance comparable to the detector comb at the operating frequency of several MHz. In the following season, we installed new SQUIDs with impedance in the 60-80 nH range, which reduced the current-sharing noise to be below the photon noise for most detectors. To minimize the SQUID noise, we used SQUID arrays, each consisting of 100 individual SQUIDs connected in series. The noise of each SQUID adds incoherently, reducing the SQUID array noise by a factor of $\sqrt{100}$. The readout Johnson current noise $S_{I,\mathrm{Johnson}}$ can be related to the $\mathrm{NEP}_{\mathrm{Johnson}}$ at the detector by $\mathrm{NEP}^2_{\mathrm{Johnson}} = S_{I,\mathrm{Johnson}}/s_I^2 \approx V^2 S_{I,\mathrm{Johnson}} = P_{\mathrm{elec}} R S_{I,\mathrm{Johnson}}$, where $s_I$ is the current-to-power responsivity. So it's advantageous to reduce the electrical power and the resistance of the detectors. The lower limit of the electrical power is designed to be about the same as the

typical optical loading of the detector to allow for some optical loading changes. The lower limit of the resistance needs to be much larger than the stray resistance for the detectors to be properly biased.

## 2.6 Detector characterization

### *2.6.1 Characterization overview*

The properties of the detectors can be divided into two categories: optical properties and electrothermal properties. Optical properties include the detector's optical efficiency, spectral band, and polarization sensitivity. The design and fabrication of the detectors and their coupling optics need to be optimized for these optical parameters. Optical efficiency can be improved by using low-loss microstrip lines to transfer signals on the detector wafer and increasing the coupling optics' transmission efficiency. The frequency bands of the detectors need to align with atmosphere transmission windows where absorption is small. Lumped element filters on the detector chip and the frequency-dependent transmission of the optical elements determine the frequency bandpasses. Polarization sensitivity is essential for measuring CMB polarization signals and is mostly determined by the antenna design and fabrication.

Electrothermal properties include the normal resistance, superconducting resistance, critical temperature, sharpness of the superconducting transition, saturation power, thermal conductivity between the TES island and the bath, thermal capacity of the TES island, time constant, and loopgain. The electrothermal properties affect the operational stability, linearity, and noise level of the detector. A TES's critical temperature is related to its saturation power because more power is required to bring a TES to a higher transition temperature. Decreasing the saturation power reduces the thermal fluctuation noise. For SPT-3G detectors, the estimated optical loadings at 95/150/220 GHz are 5.1/8.7/10.0 pW.

We design our saturation power target to be twice the expected loading, or 10/15/20 pW, to allow for possible loading variations. Low operating resistance is preferred because a higher resistance increases the Johnson noise and the bandwidth per channel, resulting in more crosstalk leakage between neighboring frequency channels. The lower limit of resistance is set by biasing stability requirements and depends on the readout electronics.

The sharpness of the transition, saturation power, and thermal properties determines the loopgain and linearity of the detector. A sharper transition results in a higher loopgain, making the detector more linear with the electrothermal feedback. The higher limit of the loopgain $\mathcal{L}$ is determined by the stability requirement of $\mathcal{L} < (3-\sqrt{2})\frac{\tau}{\tau_e} \approx \frac{1}{5.8}\frac{\tau}{\tau_e}$. The time constant is determined by the thermal capacity of the detector island, the thermal conductivity to the thermal bath, and loopgain. The time constants of the detectors need to be small enough to resolve arcmin-scale structures with a given scanning speed. We can tune the time constants by changing the thermal island's thermal capacity or the thermal link between the TES island and the thermal bath.

Developing TES detectors requires an iterative process of fabrication and lab testing feedback. In total, 120 detector wafers were characterized in-lab for SPT-3G during the development process, though only ten were deployed to the telescope. After the deployment, we did more detector characterizations on-site to validate the achieved integrated performance. A mixture of lab and on-site characterization methods and results are presented in the following sections.

### *2.6.2 Optical efficiency*

The optical efficiency of the detector is measured with a temperature-controlled blackbody source placed in front of the detector array [1]. Fig. 2.7(a) is a computer-aided design (CAD) section view of the blackbody source. The emission source is a radar-absorbing polypropylene-based material with a reflection coefficient of $-40$ dB at 95 GHz purchased

from Thomas Keating Instruments [146]. The emission source is mounted on an OFHC copper plate. Four heaters on the back of the copper plate provide a maximum total heating power of 220 mW for temperature control (Fig. 2.7(b)). Three diode thermometers on the back of the copper plate and one diode on the emission source monitor the system temperature. The copper plate is connected to an aluminum shielding box via four thermally insulating legs made of G10 (Fig. 2.7(a)). A pair of standoff legs on the two sides of the box can bring the source close to the detector array. A PID feedback system can stabilize the blackbody source at a set temperature below 20 K within an hour (Fig. 2.7(d)).

The optical efficiency is calculated by dividing the received optical power by the expected optical power, assuming single-mode beam-filling coupling between the detectors and the blackbody. We measure the electrical bias power of the detector at a fixed point in the superconducting transition as a function of blackbody temperature. The optical power at the detector is the saturation power minus the electrical bias power. Some additional factors complicate the optical efficiency measurements and must be corrected. The first factor is from the detector wafer's thermal heating as the blackbody temperature increases, which will reduce the electrical bias power and bias the optical efficiency high. This effect can be corrected using detectors not coupled to antennas as the reference and subtracting their averaged response before calculating the optical efficiency. The second bias comes from the 0.9 nH wiring inductance in series with the 30 mOhm shunt resistor in parallel with the TES [147]. The optical efficiency measured this way also includes the imperfect transmission of low-pass filters between the detector and source and the loss from lumped element filters in the wafer. With these biases corrected, the optical efficiency measures the detector module's efficiency of converting optical power into measured electrical power. The difference between the measured efficiency and 100% is from the imperfect transmission of the lenslet anti-reflection coating, the antenna loss, and the microwave transmission line loss. The measured optical efficiencies for 95/150/220 GHz are 81%/83%/73% with ∼10% detector-to-detector

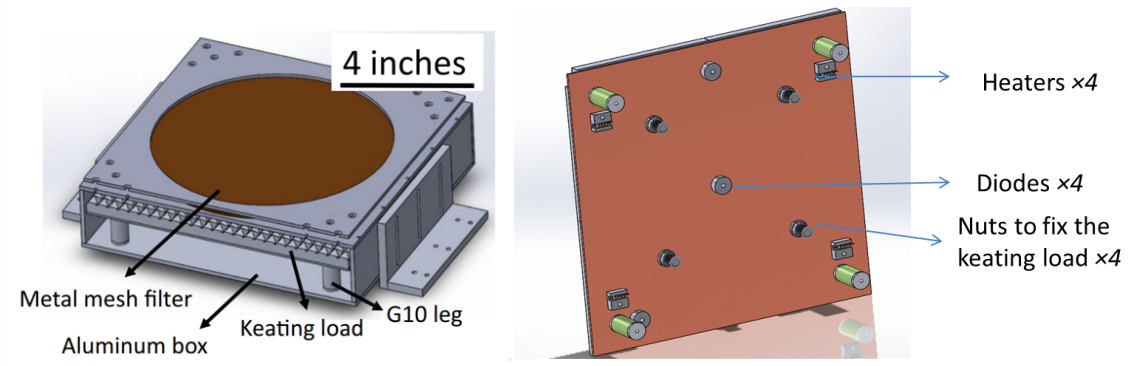


(a) Section view.

(b) Backplate

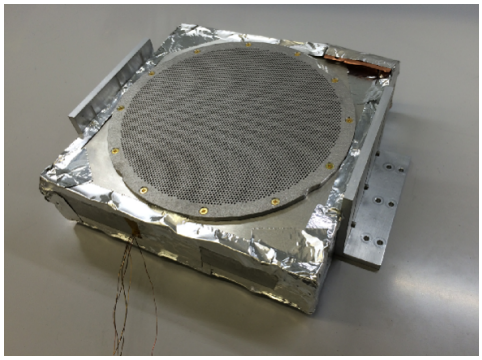

(c) Photo of the source.

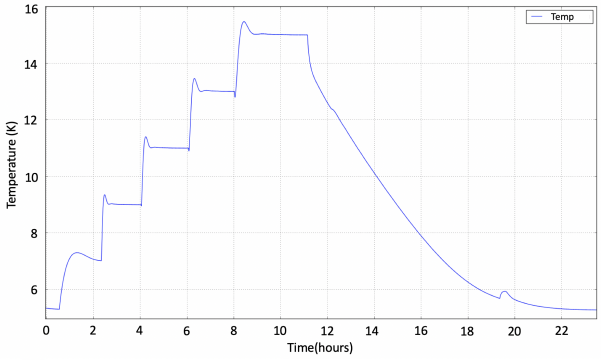


(d) Source temperature vs. time.

Figure 2.7: (a): blackbody source section view. The emission source is a radar-absorbing polypropylene-based material mounted on a piece of OFHC copper plate. The copper plate is weakly thermally coupled to an aluminum shielding box via four G10 legs. (b): the back of the copper plate. Four heaters control the temperature. Three diode thermometers monitor the temperature and provide feedback to the PID temperature control loop. (c): a photo of the blackbody source used for SPT-3G detector characterization. Note that a high pass filter is attached to the front in (c), while the model in (a) has a low-pass filter. Different combinations of low-pass and high-pass filters can be attached to the front of the box to define certain frequency bands. (d): blackbody temperature vs. time in a test run. The temperature can be stabilized by the PID system to a set temperature below 20 K within an hour.

variation for a test wafer [147].

The telescope receiver's end-to-end optical efficiency for an astronomical source includes the atmosphere transmission, the coupling efficiency of the telescope optical system, and the detector module's optical efficiency discussed above. The end-to-end optical efficiency is measured by comparing the detector response to an astronomical source with known

flux, such as RCW38 (a galactic HII region). This process involves converting a calibrated source map into an estimated detector power response, assuming 100% optical efficiency, and comparing it with the recorded detector power response. The measured end-to-end optical efficiency numbers for SPT-3G are 27±4%/45±8%/12±2% for 95/150/220 GHz frequency bands [148]. The measured optical efficiency roughly agrees with model predictions for the 95 and 150 GHz bands. But the 220 GHz efficiency is more than 50% less than the model, probably due to extra scattering or more lens attenuation at 220 GHz.

### *2.6.3 Bandpass*

Ground-based experiments need to look through the atmosphere transmission windows defined by atmosphere absorption lines. The three SPT-3G frequency bands are designed to be 82-105 GHz, 131-162 GHz, and 197-243 GHz to avoid the 60 and 118 GHz oxygen lines and the 183 GHz water line from the atmosphere. The atmosphere transmission is shown in gray in Fig. 2.8(b). SPT-3G uses three-pole lumped-element filters on the detector wafer to define the bands. The detector band shape through the receiver can be affected by other optical elements in the optical path, such as the lenses, Lyot stop, and vacuum window.

We measured the frequency bands of the detectors on-site using a Fourier transform spectrometer (FTS) with symmetric Martin-Puplett design. The same FTS used is also a prototype for the proposed NASA PIXIE mission. The design, characterization, and simulation of the FTS are presented in Chapter 3. For the on-site detector characterization, we used a 1300 K blackbody as the input source and redesigned the output optics to have an f-number of 1.4 to fill the beam of the detector. Two ellipsoidal mirrors and a Mylar reflector replace the original output coupling mirror, directing the beam down to the receiver cryostat. The output from the FTS is focused on the Gregorian focal plane of the receiver, where an equal-sized image of the detector focal plane is formed by three reimaging lenses. The Mylar beam splitter couple only 2% of FTS power to the detectors and redirect 98% of the coupling

onto the sky to avoid saturating the detectors. To further reduce the background optical power, a metal shield surrounds the coupling optics and directs any stray reflections onto the sky. The on-site characterization requires measuring the spectra of thousands of detectors efficiently. To fulfill this goal, we designed an automated measurement setup (Fig. 2.8(a)) and built a suite of controlling software. Since the Gregorian focal plane is an image of the focal plane with a unity magnification ratio, we can predict the position of a detector to be tested and use a 2D linear driver to move the FTS box to the target position automatically. The complete workflow for mapping out the focal plane is

- decide a set of detectors to be tested and their testing order,
- move the FTS to the first target position,
- drop the TES detectors to the superconducting transition,
- scan the FTS and take the measurement,
- overbias the tested detectors above the superconducting transition,
- move the FTS to the next target and repeat the following steps.

The data taken is the time-ordered data of the detectors with the FTS scanning back and forth and contains multiple interferograms. To extract the frequency bands, we first find the center of the interferograms by correlating the time-ordered data with a template. With all interferograms identified, we do FFT for each of the interferograms and average all the FFTs to obtain a low-noise spectrum. The measured spectrum contains the blackbody spectrum, the Mylar's frequency-dependent reflectivity, the transmission of three lenses and the Lyot stop, and the bandpass of the detector. The spectral band of the receiver is the measured band corrected for the blackbody spectrum and the Mylar reflectivity, both of which are proportional to frequency square (in the Rayleigh-Jeans limit). The spectral band of the receiver contains transmission through the alumina lens, the anti-reflection coatings, and the beam's spillover onto the Lyot stop. These factors altered the shape of the measured spectra (Fig. 2.8(b)) from the spectra defined by the on-wafer lumped ele-

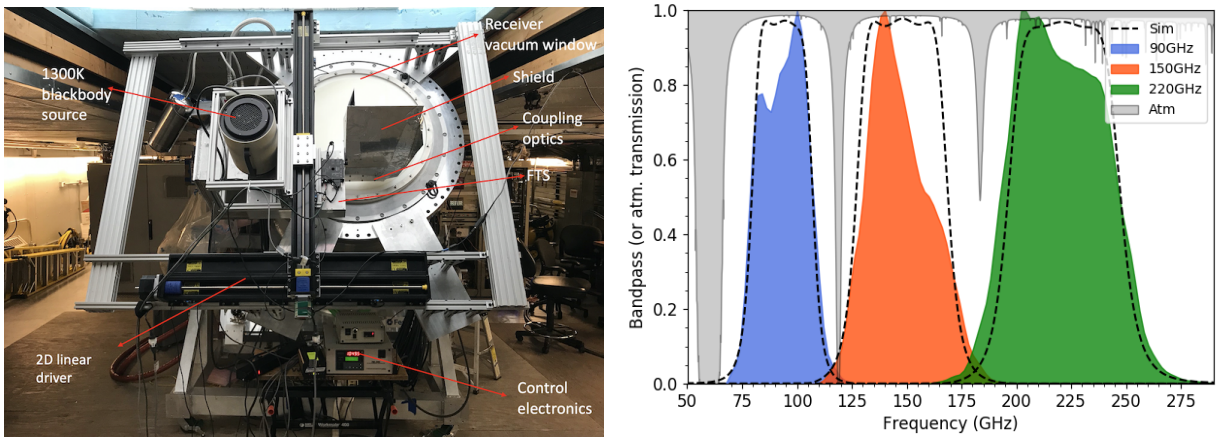


(a) FTS setup

(b) Bandpass

Figure 2.8: (a) a photograph of the testing setup at the South Pole. The FTS is mounted on a 2D linear driver attached to the front of the receiver window. The FTS input is coupled to a 1300 K blackbody source, and the output focal plane is coupled to the detectors within the receiver through three reimaging lenses. The coupling optics can fill the beams of the test detectors. A Mylar beam splitter reflects only 2% FTS power to the detectors. An aluminum shield directs stray reflections onto the sky to further avoid detector saturation. (b): the averaged bandpasses for detectors in the current focal plane. The plot also contains the atmospheric transmission with 0.27 mm water vapor and the Sonnet simulation of the on-wafer lumped-element filters. The measured bandpasses contain attenuation from other optical elements in the optical path and are slightly different from the simulated bands.

ment filters (dashed line). The bands for different detector wafers are very similar. The measured band edges agree with the Sonnet simulations within 5 GHz, and the bands are within the atmospheric window. The difference between the measured band edges and the simulation can be caused by the variation of the dielectric constant of $SiO_2$ over a broad frequency range. The array-averaged band centers calculated using $\int t(\nu)\nu d\nu / \int t(\nu) d\nu$ are 93.5±2.8/146.8±3.5/219.9±3.4 GHz for the three frequency bands, with error bars being the standard deviation across all bolometers. The array-averaged bandwidths are 23.2±4.1/30.7±4.3/46.5±4.5 GHz for the 95/150/220 GHz bands. However, the effective band centers for sources with different frequency spectra are different from the band centers given above, which assumes uniform weighting. The effective band centers for radio sources, dusty sources, and tSZ are 93.5/145.9/213.3, 96.0/150.0/222.8, and 95.7/148.9/220.2 GHz,

respectively. The calculation is in Appendix A.

### 2.6.4 Current-to-power responsivity

The TES detectors have negative electrothermal feedback, which linearizes and stabilizes the detector response. Section 2.4 discussed the electrothermal feedback in the case of a DC-biased TES. The responsivity for an on-resonance AC-biased TES can be derived similarly and has the same format as the DC-biased case (Eq. 2.8) with the electric time constant being $\tau_e = 2L/R_0$ instead of $\tau_e = L/R_0$ [138]. The model is further complicated by adding a Pd BLING, which has a large thermal capacity and is tightly thermally coupled to the detector island to slow down the response. With the BLING, it's useful to define $\eta$ as the thermal capacity ratio between the BLING and the rest of the TES island, and $\gamma$ to be the ratio between TES-to-BLING coupling and BLING-to-bath coupling. Both $\eta$ and $\gamma$ are much larger than one. Martin Lueker [138] calculated the current-to-power responsivity with the presence of a BLING, which is:

$$s_I(\omega) = \frac{\mathcal{L}}{I_0 R_0}\left(\left(\mathcal{L} - \frac{G(\omega)}{G_{\text{eff}}}\right)(1+\xi+\beta)(1+i\omega\tau_e) - \mathcal{L}(2+\beta)\right)^{-1}, \tag{2.15}$$

where most parameters' definitions are the same as in Eq. 2.8. $G_{\text{eff}} = \frac{\gamma}{\gamma+1}G$ is the effective thermal conductivity between the TES and the thermal bath. $G(\omega)$ is the thermal conductivity from TES to the thermal bath at frequency $\omega$ when $\mathcal{L} = 0$ and is

$$G(\omega) = G_0 \frac{\gamma}{1+\gamma} \frac{1 + i\omega\tau + \frac{i\omega\tau}{\eta} + \frac{i\omega\tau}{\eta\gamma} - \frac{\omega^2}{\eta\gamma}\tau^2}{1 + \frac{i\omega\tau}{1+\gamma}} \tag{2.16}$$

Since $\eta$ is large, we can neglect terms proportional to $1/\eta$ when fitting the data, and $G(\omega)$ becomes

$$G(\omega) = G_0 \frac{\gamma}{1+\gamma} \frac{1 + i\omega\tau}{1 + \frac{i\omega\tau}{1+\gamma}} \tag{2.17}$$

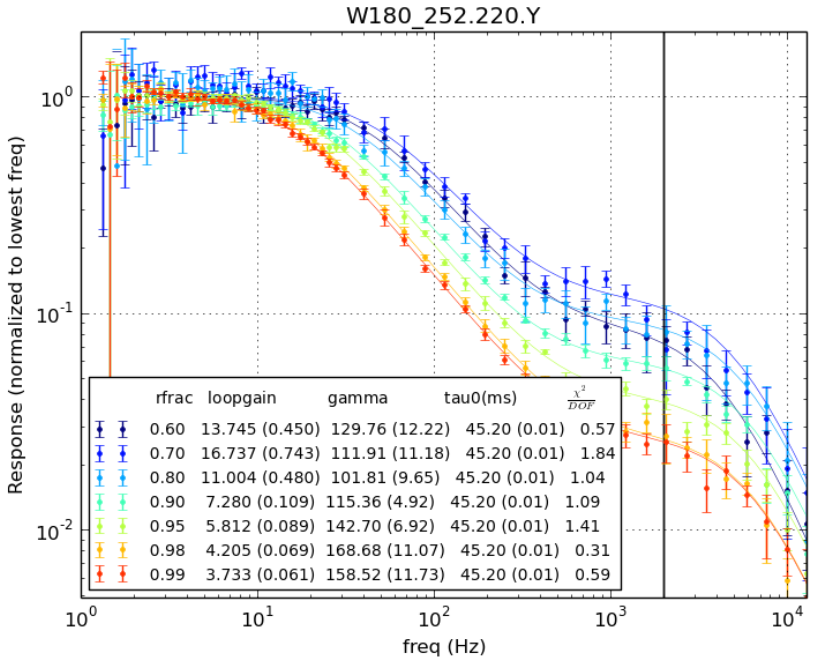


Figure 2.9: Current response vs. perturbation frequency for an SPT-3G detector. Measurements were taken at different depths into the transition. The depth is quantified by the fractional resistance (rfrac), which is the ratio between detector resistance and the normal resistance. As the rfrac decreases, the transition becomes sharper, and the loopgain increases. The black vertical line at 2000 Hz indicates that only data below 2000 Hz was used in the fit because the roll-off above 2000 Hz is from a known electrical time constant.

We adopted a technique from [138] for measuring the current responsivity $s_I$. We apply an AC perturbation signal slightly different from the bolometer's AC bias frequency $\omega$ at $\omega - \Delta\omega$. The perturbation signal beats against the detector bias and creates a power change at $\Delta\omega$. Detector temperature and resistance respond to the power oscillation, resulting in current amplitude modulation at $\Delta\omega$ that produces current signals in both the $\omega - \Delta\omega$ and $\omega + \Delta\omega$ sidebands. The signal in the $\omega + \Delta\omega$ sideband is not contaminated by the input perturbation signal and is a clean measurement of the responsivity $s_I$. Fig. 2.9 is an example measurement for a deployed detector. The X-axis is $\Delta f$ of the perturbation signal, and the Y-axis is the measured current response normalized to the response at the lowest frequency. The detector was dropped into different depths into the superconducting transition with

different transition sharpnesses and loopgains. We fit $\mathcal{L}$, $\gamma$, and $\tau_0$ to the model for every transition depth.

### *2.6.5 Time constants*

The time constant of a detector reflects its responding speed to a varying external (optical) signal. The intrinsic time constant of a detector is $\tau = \frac{C_0}{G}$, where $C_0$ is the thermal capacity of the TES island, and $G$ is the thermal conductivity between the detector island and the thermal bath. With electrothermal feedback in a voltage-biased system, the effective time constant is reduced to $\tau_{\text{eff}} = \tau/(1+\mathcal{L})$, where $\mathcal{L}$ is the loopgain of the detector. The loopgain depends on the bias power, thermal conductivity, TES temperature, and the sharpness of the TES's superconducting transition. The time constant can be adjusted by depositing a Pd BLING with high thermal capacity on the TES island, changing the thermal conductivity, changing the optical loading on the TES island, and tuning the sharpness of the superconducting transition. The time constant needs to be larger than $5.8\tau_e = 5.8(2L/R) \approx 0.35$ ms to ensure the system is overdamped under a perturbation (see Section 2.4), and smaller than ∼20 ms to resolve arcmin-scale features at our scanning speed of 1 deg/second.

The time constants of the detectors are measured regularly in-situ by recording the' data from the detectors while chopping a thermal source behind the telescope's secondary mirror. The calibrator output is placed at the secondary mirror's center and illuminates all detectors through an aperture on the secondary mirror. The structure of the calibrator is shown in Fig. 2.10(a). The calibrator contains two thermal sources: a 1000 K coiled filament and a room-temperature blackbody source. A gold-plated chopper blade is at 45 degrees relative to the optical path. The chopper blade can either reflect the 1000 K filament signal when it is in the optical path or transmit the room-temperature blackbody signal when it is out of the way. The chopper frequency is controlled by an electrical motor with a PID control system and is accurate within 0.002 Hz for set frequencies below 100 Hz. We take detector

data at six chopper frequencies chosen to avoid noise lines in the power spectrum of time-ordered data. The detector in-phase and out-of-phase responses at each chopper frequency are extracted using a phase-locking analysis method. The response vs. frequency data is fit to a single-pole low-pass filter model to extract the time constant.

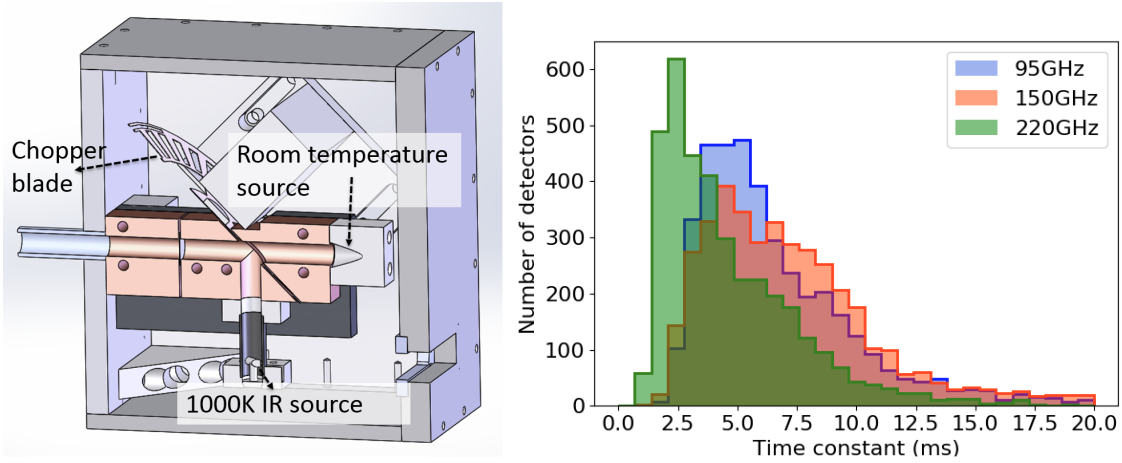


(a) Calibrator image (b) Time constant histogram

Figure 2.10: (a) cross-section view of the calibrator CAD model. The room-temperature source is a cone filled with Eccorsorb HR10 (a microwave absorbing material). The 1000K infrared (IR) source is a 10 W coiled filament. A rotating chopper blade switches between reflecting the radiation from the 1000 K IR source and transmitting the radiation from the 300 K blackbody. The output power is fed into an aperture at the center of the secondary mirror through an optical pipe on the left of the model. (b) is a histogram of the time constants of the detectors divided by their frequency bands. All time constants are above the stability threshold of 0.35 ms, and 98.8% of all detectors are faster than 20 ms.

Fig. 2.10(b) shows the time constant histogram for all detectors in the SPT-3G focal plane separated by their frequency bands. The mean time constant is 6.8±3.9/7.5±4.5/4.7±3.4 ms for 95/150/220 GHz detectors. The errors are the standard deviations for all detectors in that band. The time constants have a wafer-to-wafer variation that is much larger than the variation within the same wafer, resulting in a broad distribution in Fig. 2.10(b). The 220 GHz detectors have the largest bias powers, and thus the shortest time constants. Weather conditions can affect the optical loading and change the time constant. The weather during the South Pole winter season is relatively stable. The day-to-day variation in winter is 10%

to 20% for each detector. During the summer, the day-to-day variation can be as large as ∼50%. We took a time constant measurement with every CMB field scan to track the time-variation in the past year. Despite all the variations discussed above, the values are mostly within the desired range. With extra optical loading, the summer-season time constants can be too large to distort high-resolution features in the CMB maps, such as galaxy clusters. The distortion can be corrected by deconvolving the time-response kernel from the time-ordered data with the recorded time constants.

### *2.6.6 Thermal conductivity*

The thermal conductivity between the TES and the thermal bath can be measured by varying the thermal bath temperature $T_{\rm bath}$ and recording the electrical power needed to bias the detector at a fixed depth in the transition. The thermal conductance $k$ of a material is usually a function of temperature and can have a power-law dependence on temperature: $k = k_0 T^n$. For metal, electrons dominate the thermal transfer, and $k \propto T$ at low temperatures. For semiconductors and insulators, phonons govern thermal conduction and $k \propto T^3$. The saturation power of the detector can be calculated by integrating the conductivity over the thermal link from the thermal bath to the TES.

$$P = \frac{k_0 A}{L} \int_{T_{\rm bath}}^{T_c} k^n dT = K(T_c^{n+1} - T_{\rm bath}^{n+1}), \tag{2.18}$$

where $L$ is the length of the conductor, $A$ is the area, and $K = \frac{k_0 A}{(n+1)L}$ is a constant coefficient determined by the geometry and composition of the four legs connecting the island to the thermal bath. The differential thermal conductivity at the detector is $\frac{\partial P}{\partial T} = (n+1)KT_c^n$. Fig. 2.11 is an example measurement of a detector's thermal conductivity. We measure the saturation power of the detector $P$ vs. thermal bath temperature $T_{\rm bath}$ and fit the data to the model in Eq. 2.18. The thermal conductivity values for the deployed detector wafers are 100±8/123±13/125±16 pW/K for the 95/150/220 GHz frequency bands.

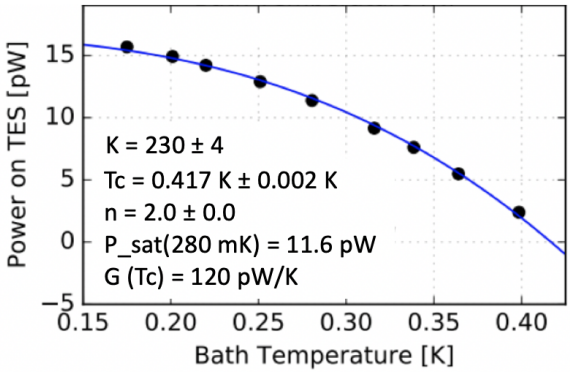


Figure 2.11: Bias power vs. thermal bath temperature for a test detector. Black dots are measurements. The blue line is the fit to $P = K(T_c^{n+1} - T_{\rm bath}^{n+1})$. The fit $K$, $n$, and $T_c$ values are in the figure legend.

Eq. 2.18 shows that the saturation power is dependent on the superconducting transition temperature $T_c$, and the thermal conductivity $G$. The target $T_c$ is chosen at around 450 mK to optimize detector noise and keep the saturation power ∼two times the optical loading. The averaged saturation powers are 12/14/15 pW for the 95/150/220 GHz detectors with a wafer-to-wafer variation of $\sim$ 2 pW. The array-averaged $T_c$ is 453 mK, which is close to the target [148]. The TES's normal resistance is constrained by stability, crosstalk, and noise requirements to be around 1.7 Ohms [132]. The measured averaged resistance is 2.2 Ohms [148].

## 2.7 Readout

We read out the 16,000 detectors in the SPT-3G focal plane using frequency-domain multiplexing (fMux) readout system to reduce the number of readout wires. We connect every detector with a capacitor and an inductor in series, forming an RLC resonance circuit with a resonant frequency of $f_0 = \frac{1}{2\pi}\sqrt{\frac{1}{LC}}$. A total of 66 RLC circuits are connected in parallel and read by one single pair of readout lines (Fig. 2.12). We generate AC biases containing 66 bias frequency tones using digital modulation synthesis and a digital-to-analog converter

operated at room temperature. The AC biases carriers are fed into the RLC combs through the same pair of readout lines, and each RLC circuit picks up one carrier tone at its resonant frequency. Fig. 2.13(a) shows a network analysis of an RLC detector comb, where we sweep the input frequency and record the output current. The network analysis amplitude represents the admittance of the circuit at different input frequencies. Each peak in the diagram corresponds to the resonance of one RLC circuit in the comb. We set the 66 resonant frequencies between 1.6 and 5.2 MHz with sufficient spacing such that the crosstalk between adjacent frequency channels is low.

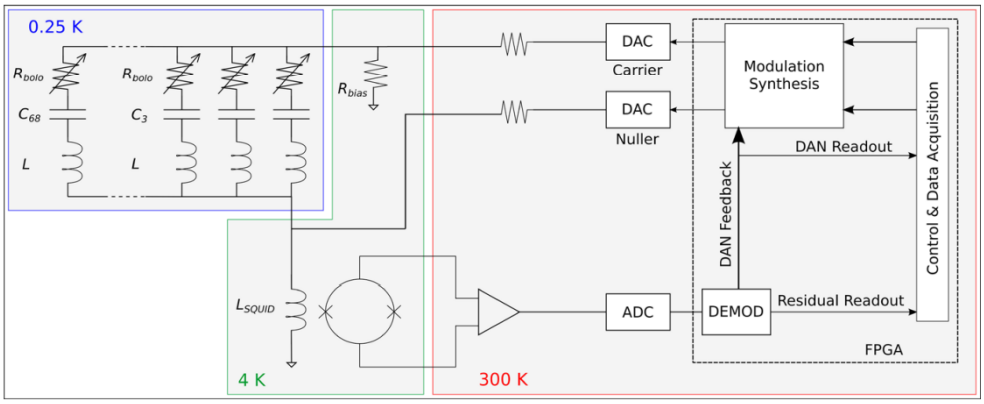


Figure 2.12: The schematics for SPT-3G fMux readout system. Bolometers and the RLC combs are at ∼0.25 K. The SQUID amplifiers are at 4 K. The warm electronics at 300 K generates carrier tones at different frequencies and demodulate the output signal. Figure taken from [149].

The detector we use is a TES bolometer whose resistance can be modulated by sky signal. The resistance change will cause a current amplitude modulation, which creates sidebands around the bias frequency. The sidebands contain sky information measured by the detectors. We collect the amplitude-modulated bias currents from all 66 parallel circuits into one wire and feed the summed current into the first-stage SQUID amplifier. After the amplification, we convert the summed analog signal into a digital signal. We then use a method called digital-active nulling (DAN) [144] to inject a nulling signal that cancels the signal current before the SQUID input coil (Fig. 2.12). DAN reduces the loads on the SQUID input coil

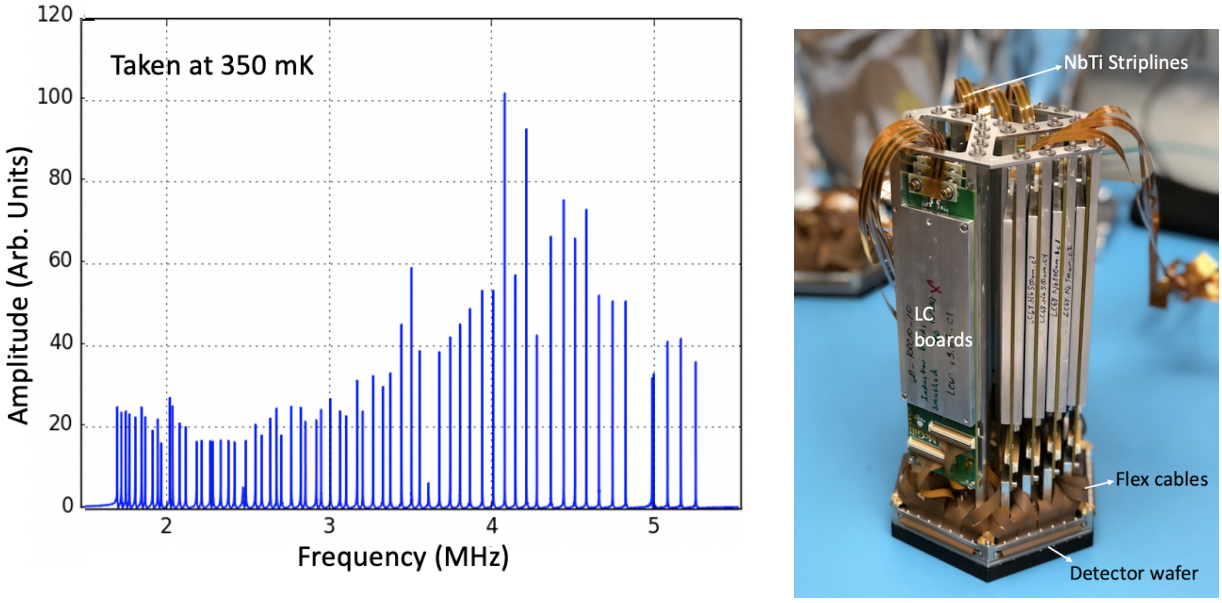


(a) Network analysis

(b) A SPT-3G wafer module

Figure 2.13: Left: network analysis for a SPT-3G detector comb. Every peak corresponds to a detector channel in series with an inductor and a capacitor. The network analysis was taken at 350 mK, where the detectors are superconducting. Right: a SPT-3G wafer module with the detector wafer assembly and the LC boards. Courtesy of Matt Young.

and increases the dynamic range of the SQUID amplifier. We use the nulling current as of the sky signal since it exactly cancels the signal current.

In total, we have 240 detector combs for the ten detectors wafer in the focal plane. Each detector comb has 66 detectors. We connect each detector comb to a lithographed chip with spiral inductors and interdigitated capacitors (LC chip). The LC chips are housed in LC boards shown in Fig. 2.13(b). We use superconducting NbTi cables to connect the LC boards to the SQUID amplifiers. The readout performance is summarized in [149], and we list a few key properties from it below. The achieved readout yield is 94%. The readout noise white noise levels are 10.4/13.0/16.0 pA/$\sqrt{\text{Hz}}$ for 95/150/220 GHz, which are lower than the photon noise level. The low-frequency noise knee (1/f knee) is around 33 mHz, which corresponds to an angular multiple of $\ell = 24$ at the typical telescope scanning speed. The crosstalk level is less than 0.5% for most detector channels.

## 2.8 Optical system

The detector focal plane is coupled to the sky through a high-throughput optical system with 2.8 deg$^2$ field-of-view. The optical system consists of a primary mirror, a secondary mirror, a folding flat, a vacuum window, infrared blockers, a Lyot stop, and three reimaging lenses. The sky signal illuminates the primary mirror and is then reflected by a 1.8 m secondary mirror into a folding flat mirror (Fig. 2.14). The Gregorian focus is formed after the folding flat and in front of the high-density polyethylene (HDPE) receiver cryostat vacuum window with triangular-groove anti-reflective (AR) coating. After the window, multiple layers of polyethylene foam and an alumina plate cooled at 50 K block infrared radiation. Three 0.72 m diameter plano-convex alumina lenses at 4 K reimage the Gregorian focus onto the detector wafers. The three lenses reduce aberrations and enable a large field of view. The lenses are made from low-loss alumina by Coorstek and are AR-coated with 3-layer Teflon [150]. Between the second and third lenses, where the ray bundle diameter is the narrowest, we set a Lyot stop to reduce stray reflections and put a low-pass metal mesh filter to cut the out-of-band optical loading further. Finally, the sky signal is focused by the alumina AR-coated lenslets onto the individual detector antennas. The beam diameter of the detector antenna through the Lyot stop is 30 deg. The beam of the detector angenna is reimaged by the optical system, which gives a $\sim$1 arcmin diameter detector beam on the sky. The field-of-view of the focal plane with all detectors is 2.8 deg$^2$ on the sky.

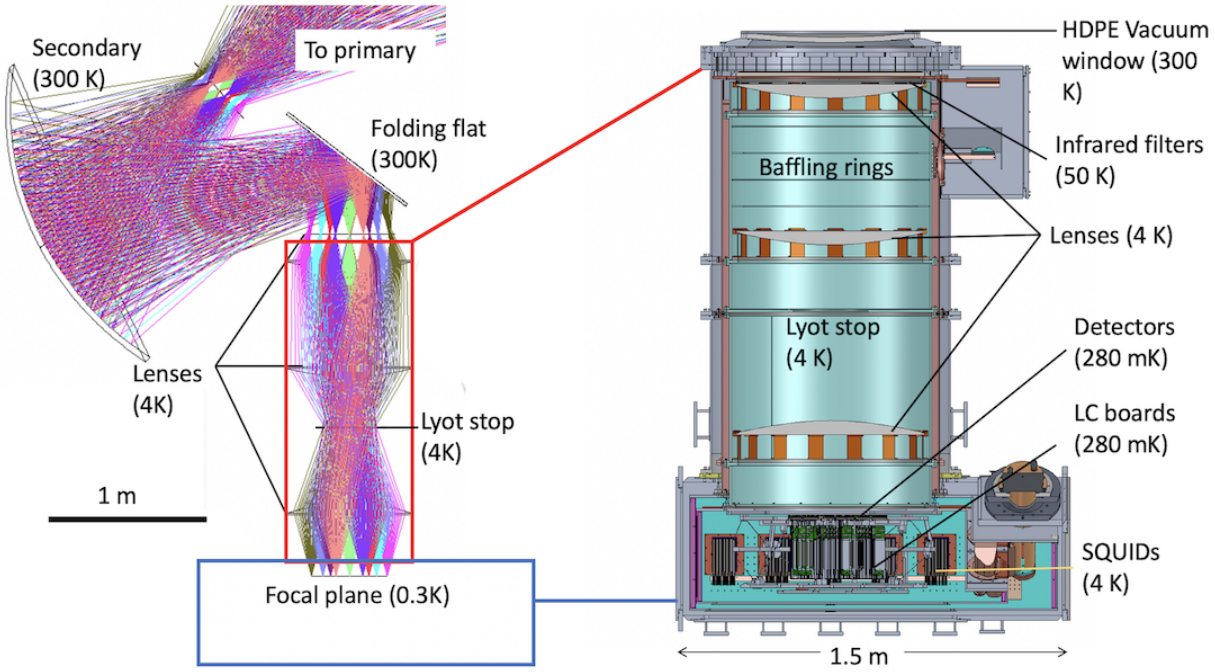


Figure 2.14: Left: ray-tracing diagram of the SPT-3G optical system. We use a primary mirror, an ellipsoidal secondary mirror, a flat tertiary mirror, and three lenses to image the sky onto the detector array. Right: the receiver cryostat of SPT-3G. The cryostat has three aluminum shells at 300 K, 50 K, and 4 K. The 300 K shell supports vacuum pressure, and the other two shells are radiation shielding layers. The optical signal enters the receiver through an HDPE vacuum window. Within the receiver, we use multi-layer polyethylene and an alumina plate at 50 K to block infrared radiation. Three lenses at 4 K reimage the Gregorian focus on the detectors. Some cold readout components, including the LC boards and the SQUID amplifiers, also live within the receiver cryostat.

# CHAPTER 3

# A COMPACT FOURIER TRANSFORM SPECTROMETER

## 3.1 FTS overview

The measurement of SPT-3G detector bandpass is performed with a Fourier-transfer spectrometer (FTS). The core of an FTS is similar to a Michelson Interferometer, which splits the incoming radiation along two light paths and recombines it. The difference is that an FTS creates an adjustable optical delay between the two light paths before recombining them. The intensity of the recombined radiation vs. optical delay is the auto-correlation function of the incoming radiation. The Fourier transform of this autocorrelation function gives the frequency power spectrum of the incoming radiation. Since the FTS measures the power spectrum of the received signal. The measured power spectrum is also sensitive to the frequency-dependent transmission of the optical materials within the optical path and the detector frequency bandpass. An FTS has several advantages over other types of spectrometers at millimeter wavelength, including constructional and operational simplicity, easy systematics control, high throughput, good frequency resolution, broad frequency range, and a small number of detectors required. FTSs have been widely used in astrophysics [151, 152], atmospheric science [153], and many other fields [154, 155, 156] to characterize frequency power spectra of signals. The Far InfraRed Absolute Spectrophotometer (FIRAS) for the COBE satellite is an FTS instrument that firstly measured the spectrum of the CMB. In millimeter-wavelength cosmology, FTSs are used for characterizing detectors and optical elements.

We have constructed an FTS operating at millimeter-wavelength for characterizing the SPT-3G detectors. The same FTS is also a prototype similar to the instrument for a NASA MIDEX mission (PIXIE) [5], which was proposed to measure the CMB's polarization and frequency spectrum in space. PIXIE's primary science goals include detecting the CMB's

spectral distortion from a perfect blackbody, constraining the epoch of inflation and reionization, and measuring the sum of the neutrino masses. The notable features of the FTS are small size (355×260×64 mm), low weight (5.9 kg), and large optical throughput (100 $mm^2$ sr), which are driven by needs of a high-sensitivity CMB space mission. The FTS's operating frequency range of 50-330 GHz and frequency resolution of 4 GHz are chosen to meet detector testing need for SPT-3G and can be adjusted for other applications.

## 3.2 FTS design and structure

### *3.2.1 Design overview*

We modified the polarized Martin-Puplett FTS design [157] to a Mach-Zehnder arrangement to reduce the instrument size and weight while optimizing for high throughput and high efficiency and preserving both polarizations. Our FTS ended up having 2× throughput compared to the COBE FIRAS FTS though the volume is about 10× smaller. The design of the FTS started with the design requirements of the operational frequency range, frequency resolution, and maximum throughput. With the design configuration chosen, specifications for the size of optical elements, mirror move range, and surface roughness are derived from the design requirements. The conflicting design requirements, such as compactness and large throughput, were balanced, resulting in compact FTS that meets specifications. The FTS also features construction simplicity with no optical adjustment needed because the mirrors are machined on the sidewalls. The only moving part during operation is the center mirror that generates optical delay.

The design has two input ports for measuring the differential spectra and two separate output ports to collect redundant signals for systematics control. Input radiation propagates from the input ports through ellipsoidal mirrors, flat moving mirrors, and wire-grid polarizers to the output ports, as shown in Fig. 3.1. The typical Martin-Puplett design has a rooftop

mirror that rotates polarization by 90°, so radiation components initialized separated by a polarizer can later be recombined. Our FTS does not need the rooftop mirrors because the two beam-splitting polarizers are at 90° relative to each other. Four polarizers instead of two for the Martin-Puplett design are needed. However, the design is still compact, thanks to the folded optical paths and the small polarizers. The optical delay in this design is determined by the position of the double-sided center mirror controlled by a linear actuator. The detector placed at the output port measures the power of the recombined radiation from the two light paths modulated by the center mirror. Fig. 3.1 shows a Computer-Aided Design (CAD) of the FTS and two interfering light paths through the FTS. The size is $355 \times 260 \times 64$ mm and is driven by our design parameters, which are a 50 to 330 GHz frequency range, a 1 GHz frequency resolution, and 100 $\text{mm}^2$ sr throughput. Size calculation will be discussed in Section 3.2.2.

The optical paths are folded and are at an angle relative to the box edge to minimize the instrument size and allow all ellipsoidal mirrors to be machined on the sidewalls. As a result of the nonzero incident angle, the recombined beams are further apart when the mirror is displaced away from the center position, causing a reduced interference of the recombined beams. When the displacement is large, the power from the two paths will be added instead of interfering. Another nonideality caused by this angle is the spillover of the beam off the edges of optical elements as the mirror moves. Both effects were carefully characterized and balanced for the required instrument performance.

The ellipsoidal mirrors each reimages the previous mirror onto the next. This design ensures that all light rays reflected by the previous mirror are reimaged within the next mirror and minimizes beam loss. Each mirror's profile is part of the ellipsoid with foci at the last and the following mirror centers. The ellipsoid is a prolate spheroid rotated about its major axis, so there is only one remaining parameter. This parameter is chosen such that the mirrors intersect the inner surface of the box and have the right size to contain the beam.

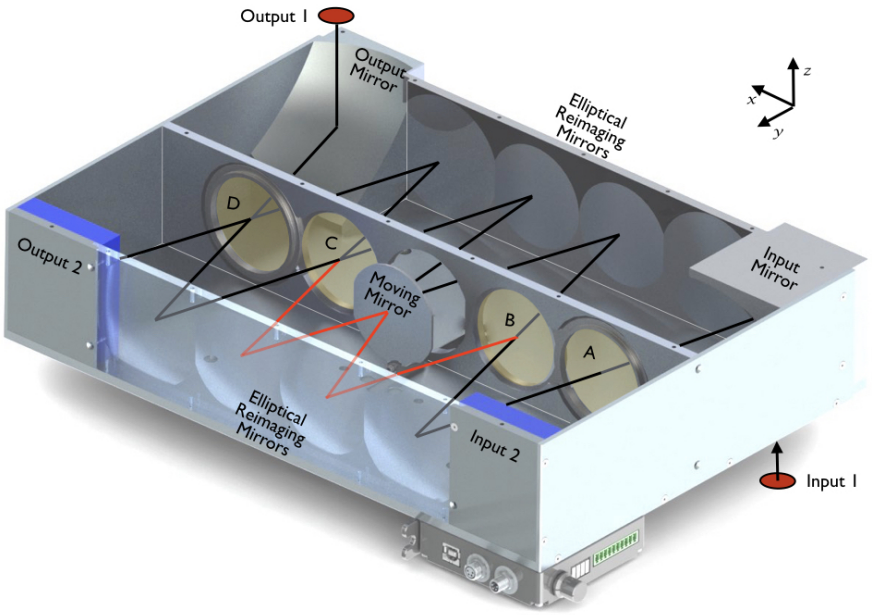


Figure 3.1: Shown is a rendering of a CAD model of the FTS with the near side plate shown transparently. The four polarizers labeled A through D are supported by a center septum. The ellipsoidal input mirror, output mirrors, and reflection mirrors are machined on the side walls. Input and output mirrors focus the beam on focal planes, shown as red disks, which are 38 mm below and above the box's surface. In our configuration, only one input port and output port are coupled to the source and detector. Ambient temperature HR25 absorbers (in blue) cover the other input and output ports. The differential spectrum between the absorber and the source is measured. Each sidewall contains four machined ellipsoidal mirrors. A flat center mirror can be moved by a linear actuator and change the optical delay between the two optical paths. Two interfering light paths are shown in this figure, corresponding to the red lines in Fig. 3.2.

The first and last mirrors are also ellipsoid but have one focus at the input or output port and the other at the neighboring mirror. The input and output mirrors can be redesigned to fit different optical coupling configurations. For our configuration used for SPT detector testing, the output mirror rotates the beam out of the optical plane so the beam could be coupled to the cryostat. In our testing instrument, the input and output ports are 38 mm above or below the box's surface. The incident angle of the chief ray on the center mirror is $\phi = \cos^{-1} 2r/y$, where $r$ is the mirror radius, and $y$ is the box width (see Fig. 3.2). Another advantage of this design is that all mirrors can be machined on the sidewalls and do not need additional alignments.

The optical delay of the FTS is generated by a flat mirror on a linear stage that can scan at a constant speed. The mirror is at the center of the box. Interfering light paths reflect off the mirror's top and bottom surfaces and recombine with an optical delay. The optical delay between the top beam and bottom beam is $d = 4y\cos\phi$, where $y$ is the displacement of the mirror from the center position. When the incident angle is small, the optical delay is nearly four times the mirror displacement, which also helps reduce the instrument size for the same optical delay range. During FTS operation, the center mirror scans along the center axis, and the output power is measured as a function of the mirror delay.

Four polarizers are mounted on a central metal plate, which spans the box's length and has a cutout for mirror translation. The polarizers are wire grids, and their specifications are detailed in Section 3.2.3. In Fig. 3.2, Polarizer A has its wires oriented at 45 degrees to the $z$ axis (pointing out of the page) and divides the incoming radiation into two orthogonal polarizations (red and blue). Polarizer B is at 45 deg relative to polarizer A along the $z$ axis. Therefore, polarizer B transmits and reflects components of the two orthogonal polarizations (solid arrows and dashed arrows, respectively), mixing the radiation initially separated by polarizer A. The center mirror can move and add an optical delay between the radiation reflecting off its upper surface and its lower surface. Polarizer C is placed orthogonal to polarizer B and is along the $x$ axis. It undoes the polarization mixing effect of polarizer B. Light transmitted by B is reflected by C, and the light reflected from B is transmitted by C. Still, due to the center mirror, the components of each recombined polarization have a relative optical delay. Polarizer D is parallel to polarizer A. With no optical delay, the split polarizations after polarizer D behave the same as before polarizer A, and all radiation enters Output 2 (symmetric output port). With an optical delay, the modulated radiation is the sum of two orthogonal linear polarized beams with phase shift, resulting in a modulated elliptical polarization. Polarizer D then splits the elliptically polarized radiation into two linearly polarized portions at the two output ports. The center mirror's movement modulates

both outputs' radiation intensities. The sum of the two ports' powers is constant. Switching the relative orientation of A and D (or B and C) from being parallel to being orthogonal (or the other way) switches the symmetric and antisymmetric output. The set of polarizers can modulate both polarizations 100% with no loss in the ideal case.

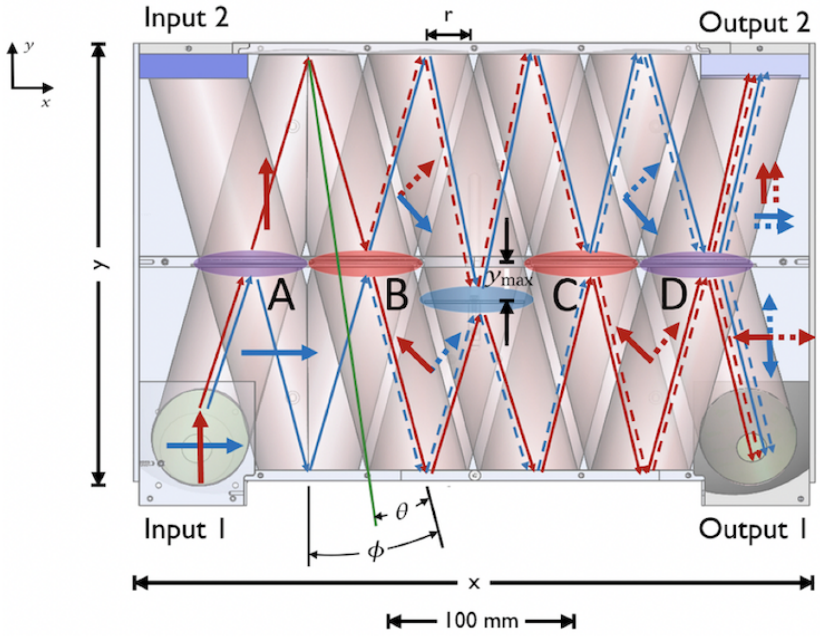


Figure 3.2: Section view of the FTS box with polarization schematic. The input and output ports are labeled. The input radiation enters the FTS box from the bottom left input port. The purple and orange polarizers are fixed on the center septum, and the reflection mirrors are machined on the top and bottom of the box. The center mirror controlling optical delay is in blue. Light paths and polarizations were tracked for the radiation from Input 1. Thin arrows indicate propagating paths, and thick arrows are the polarization directions. Solid and dashed lines are the two orthogonal polarization components of the input radiation. $\theta$ is half of the beam's opening angle, and $\phi$ is the angle between the beam center and the $y$ axis. $y_{\max}$ is the maximum displacement of the mirror, and $r$ is the mirror radius and maximum beam radius at the mirrors.

### *3.2.2 Optical geometry and size calculation*

The FTS design in Fig 3.1 has advantages of large throughput, two separated input and output ports, and construction simplicity with mirrors on sidewalls. The only tuning needed

is the center mirror alignment. Other mirror alignments are fixed after assembling the metal parts with screws. With this geometry selected, the instrument size is defined by the required spectral resolution and the operational frequency range.

The beam's solid angle limits the maximum measurable frequency and the frequency resolution of the FTS because high-angle light rays have different optical delays compared to the central light ray and thus decoheres with higher delay, especially at higher frequencies. The maximum optical delay determines the frequency resolution. The maximum frequency, the frequency resolution, and the throughput together define the size of the mirrors and the FTS box. Assuming a tophat beam profile, Chamberlain calculated the analytic approximation of the wavefront integration over all the beam [158]. For our FTS design, we set the added delay ($b$ in Fig 3.3) for the largest angle light ray to be one wavelength compared to the central ray at the maximum delay for the highest design frequency. This constrains $b = \lambda_{\text{min}} = c/f_{\text{max}}$, where $f_{\text{max}}$ is the highest design frequency. This constraint implies that the beam center and the beam edge have a phase difference of $2\pi$ at the minimum wavelength $\lambda_{\text{min}}$ when the center mirror is at its maximum displacement, reducing the contrast to near zero. The net effect is that the interference or the amplitude of the interferogram decays zero at the maximum optical delay, which effectively multiplies the interference pattern by a window function and limits the frequency resolution. The interferogram scan length is the fundamental limiting factor of the frequency resolution, so having the interference taper to zero at maximum optical delay does not reduce the resolution much.

The size of the FTS is calculated from the design parameters using the decoherence constraint from Fig. 3.3 and assuming the incident angle of the beam ($\phi$ in Fig. 3.2) is small, which turned out to be true after our size calculations. With this assumption, the maximum optical delay $d_{\text{max}}$ is 4 times the center mirror's maximum displacement $y_{\text{max}}$. The maximum optical delay is related to $\Delta f$ by:

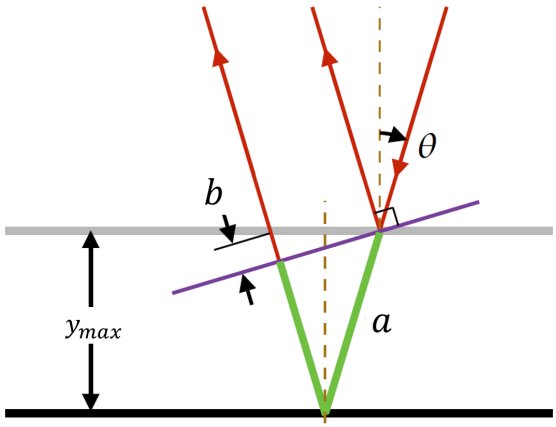


Figure 3.3: The incident light rays when the center mirror is at zero and maximum optical delay of $y_{\max}$. The black and gray lines are the mirror positions at zero and maximum optical delays. The red and green lines are the optical paths of a light ray incident on the mirror at $\theta$ when the mirror is at zero and maximum optical delays. The purple line is the wavefront. Here we assume the incident angle of the central light ray to be zero and compare the path length difference between rays at the center of the beam and the light rays at the edge of the beam with incident angle $\theta_{\max} \sim \sqrt{\Omega/\pi}$.

$$d_{\max} = 4y_{\max} = c/\Delta f. \tag{3.1}$$

Using Fig. 3.3, we can calculate the path difference between the vertically incident central ray and the beam edge incident at angle $\theta$. The path length difference is $\delta = 2y_{\max} - 2a + b$, where $a$ and $b$ are in the figure. Using the geometric relations in the figure, $a$ and $b$ can be related to $y_{\max}$ and $\theta$ by $a = y_{\max}/\cos\theta$ and $b = 2y_{\max}\tan\theta\sin\theta$. With these relations combined, $\delta$ can be written as a function of $y_{\max}$ and $\theta$:

$$\delta = 2y_{\max}\left(1 - 1/\cos\theta + \tan\theta\sin\theta\right) = y_{\max}(2\sin(\theta/2))^2 \tag{3.2}$$

The decoherence constraint requires the path length difference between the central ray and the edge ray to be one wavelength, or $\delta = c/f_{\max}$. This combined with Eq. 3.2 and Eq. 3.1 gives the dependence of $\theta$ on $f_{\max}$ and $\Delta f$:

$$\theta = 2\arcsin(\sqrt{\Delta f / f_{\max}}). \tag{3.3}$$

The beam splitter diameter $r$ is related to the required throughput of the system $A\Omega$, which is the product of the area $A = \pi r^2$ and the solid angle $\Omega = 4\pi(\sin(\theta/2))^2$. The throughput is then $A\Omega = (2\pi r \sin(\theta/2))^2$. This combined with Eq.(3.3) gives:

$$r = \frac{1}{2\pi}\sqrt{\frac{A\Omega f_{\max}}{\Delta f}} \tag{3.4}$$

The length, width, and height of the FTS box can be defined relative to $r$ by $x = 12r$, $y = 2r/\tan(2\theta)$, and $z = 2r$ (Fig. 3.2). Now all size parameters are calculated in terms of of design target parameters $f_{\max}$, $\Delta f$, and $A\Omega$. For our FTS made primarily for SPT-3G detector testing, the design parameters are $f_{\max} = 330$ GHz, $\Delta f = 1$ GHz, and $A\Omega = 100$ mm$^2$sr. The resulting dimensions are $x = 347$ mm, $y = 260$ mm, $z = 58$ mm, $\theta = 6.3$ deg, and $r = 29$ mm. The size of a built FTS is slightly larger ($355 \times 260 \times 64$ mm) due to the thickness of the walls and other practical considerations. See Fig. 3.4 for a built FTS.

### *3.2.3 FTS specifications*

The FTS mirrors and box parts are computer numeric control (CNC) machined from Aluminum 6061, with a precision of $\pm 0.12$ mm. The surface roughness of the machined mirrors is 3.2 $\mu$m Ra. The polarizers are wire grids made of 25-$\mu$m-diameter gold-plated tungsten wires spaced at 100-$\mu$m periods. The linear actuator controlling the motion of the central mirror is a Zaber LSM050B model [159] with a spatial accuracy of 25 $\mu$m and a speed resolution of 0.9 $\mu$m/s. The linear driver's speed can vary between 0.9 $\mu$m/s and 29 mm/s, and its travel range is 50.8 mm, giving an optical delay range of near 400 mm. The metal surfaces of the FTS box that are not optical elements are covered by Eccosorb HR10 [160]

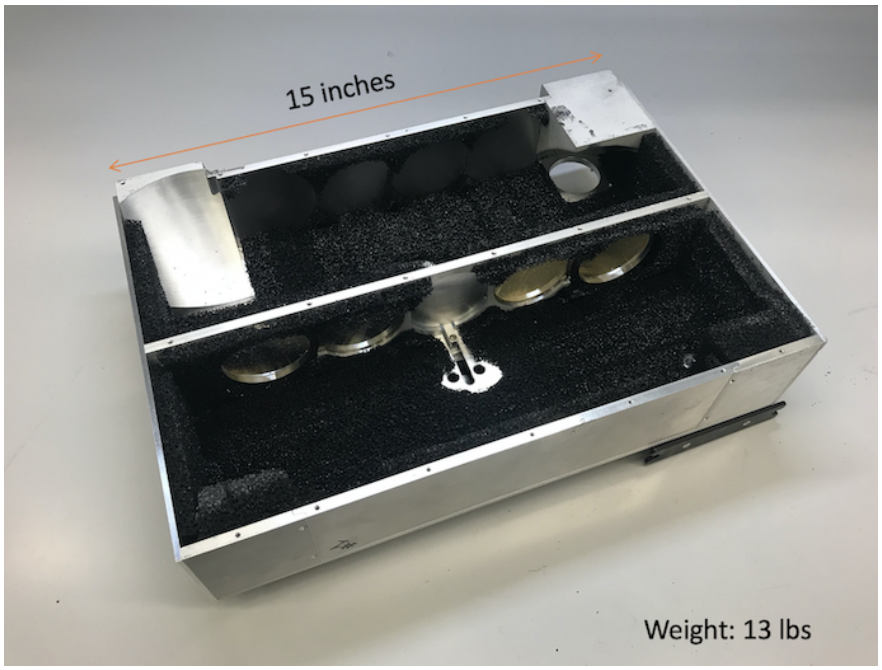


Figure 3.4: This is an FTS built from the CAD drawing in Fig. 3.1. The FTS box is machined from aluminum. The ellipsoidal reflection mirrors were machined on the side walls as part of the box. Metal surfaces that are not in the optical path are covered by black Eccosorb HR10 absorber. The center septum holds four wire grids and has an opening for moving mirror translation. The linear actuator for moving the center mirror is at the bottom of the box.

to reduce stray reflections.

## 3.3 Testing results

### *3.3.1 Testing setup*

The FTS has two input ports and two output ports. In all tests, we put a room-temperature absorber at one input port and the testing source at the other input port, as shown in Fig. 3.1. The differential spectra between the testing source and the room-temperature absorber are measured. An absorber also covers the second output port, which in principle provides the same information as the other output port, because the total power of the two output ports is constant. A monolithic silicon bolometer [161] cooled by a liquid helium dewar is used for

all measurements. The detector has a throughput of 50 $mm^2$ sr, determined by the Winston cone coupling, and a sensitive frequency range of 50-600 GHz, set by the Fluorogold filter placed in front of the Winston cone.

We are interested in both the broadband response and the single-frequency response of the instrument. Therefore, two types of sources were used: an IR-563 blackbody source operating at 1300 K with an adjustable emitting area and tunable single-mode narrow-band Gunn oscillators [162] operating at 90 GHz, 144 GHz, and 295 GHz. The single-mode sources can be treated as point sources because their emitting area is small, and they can be mounted in a 2D stage to move around the focal plane and probe the position-dependent response. Both sources have output beams fully illuminating the first input mirror and can be paired with a chopper for modulating the signal with 100% modulation depth. Fig. 3.5 shows an example measurement setup, where the input couples to a 1300 K blackbody and the output couples to a bolometer (within the gold-colored helium detector dewar). The blackbody source can probe the frequency range of the FTS, whereas the Gunn oscillators with known frequencies can measure the frequency resolution and accuracy of the instrument. The Gunn oscillator is close to a point source. The system's resolution to an extended source with throughput greater than $\lambda^2$ is determined by averaging interferograms of the Gunn oscillator through a grid of source positions.

The only moving part of the FTS is a motorized mirror, which generates optical delay between the two interfering paths. The FTS can operate in two modes: chopped or continuous [163]. In the chopped mode, the output signal for each center mirror position is measured by comparing the input source and a reference source using a chopper. In this mode, only half of the data contains the signal. In the continuous mode, the center mirror is continuously moving while data is taken. This operation mode is susceptible to low-frequency noise, so the center mirror's moving speed needs to be sufficiently high to avoid overlap between the signal frequency and the noise. On the low end, the moving speed is limited by the time constant

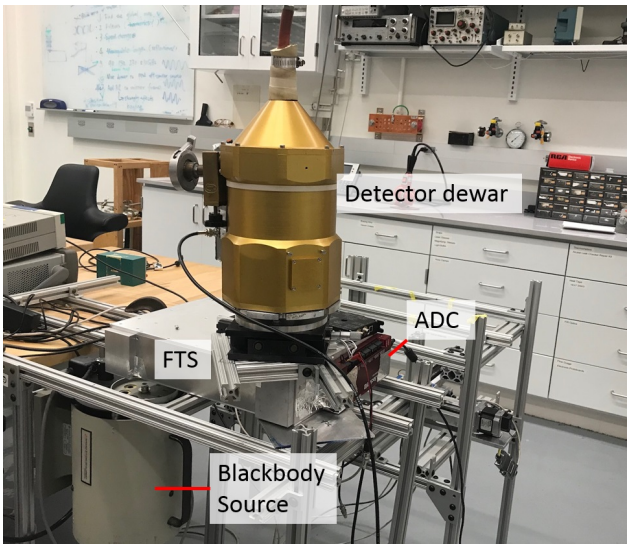


Figure 3.5: Example FTS test setup. The FTS is the aluminum box labeled in the picture. The input port is coupled to a 1300 K blackbody source, and the output port is coupled to a silicon bolometer within the helium dewar. A 2D driver is below the FTS box and can be used to move the Gunn oscillator when a Gunn oscillator is used as the source.

of the detector. The moving speed $v$ is related to the optical speed $v_o$ by $v_o = 4v\cos\phi$ for the beam center (Fig. 3.2). The optical speed is the speed of the optical delay and is chosen between 1 mm/s and 10 mm/s in our applications. The maximum optical delay is selected based on the desired frequency resolution.

The sampled bolometer data needs to be synchronized with the moving mirror's position. However, the bolometer output voltage was sampled asynchronously with the mirror motion during the operation. To correct this, we use a hardware-derived white light fringe indicator sampled at the same rate as the bolometer data to determine the mirror position. The data was oversampled by more than five times above the Nyquist frequency and above the post-detection bandwidth of the detector to avoid aliasing. We set the white light fringe indicator by chopping the source and finding the optical delay with the minimum optical power (center of the white light fringe for antisymmetric output port). The software we have developed for the operation includes linear driver-controlling software and ADC data-taking software. The codes are publicly available [164].

### *3.3.2 Measurements of sources with different bandwidths*

We started our characterization by measuring the power spectra of a few sources with different bandwidths and coherence lengths. Their interferograms and spectra are in Fig 3.6 and 3.7. We tested three types of sources: a 1300 K broadband blackbody source, the same 1300 K blackbody source with a bandpass filter, and a 295 GHz narrow-band source, which is a 98 GHz Gunn oscillator combined with a frequency tripler. The properties of these sources are known so that we can compare the expected spectra with the measurement.

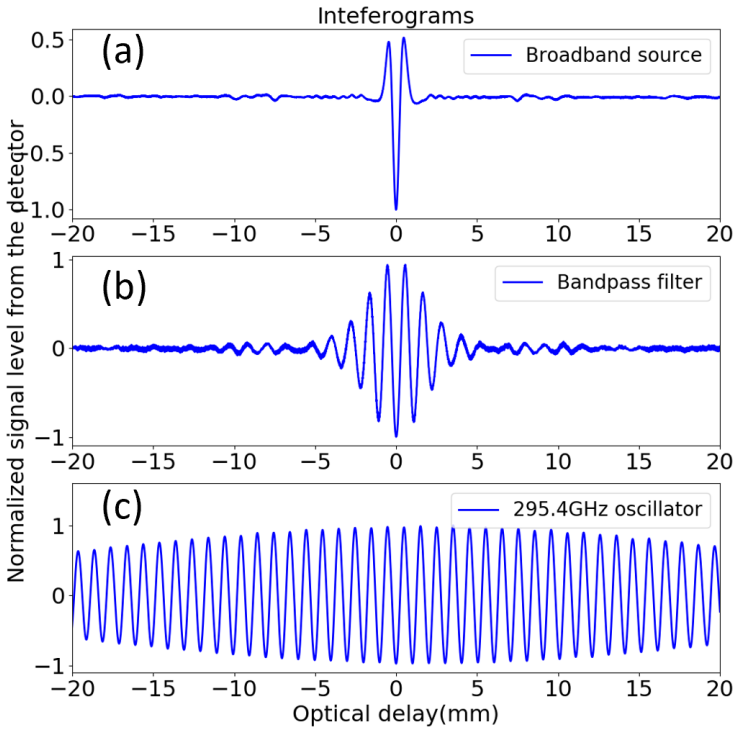


Figure 3.6: Normalized interferograms for three types of sources. The input sources for (a), (b), and (c) are a 1300 K source at one input, the same thermal source as (a) with an additional bandpass filter centered at 280 GHz, and a 295 GHz spectrally unresolved source, respectively. The detector has an absorptive low-pass filter placed in front of it inside the detector dewar to eliminate high-frequency thermal infrared emission in all three cases.

The data taken is the detected power vs. optical delay or the interferogram, and its Fourier transform is the frequency spectrum (Wiener-Khinchin theorem). The three sources have increasing coherence length, in order of a) to c), so the interferograms decay to zero

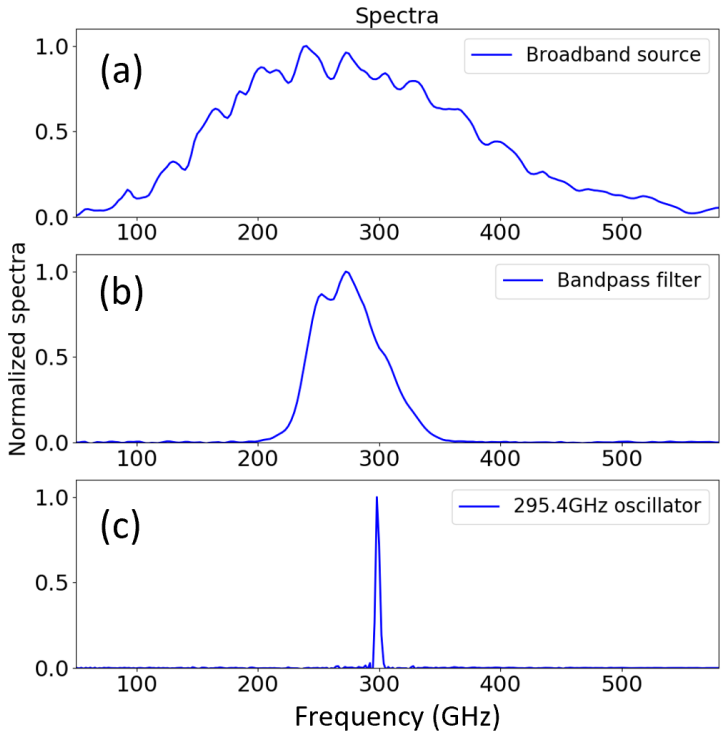


Figure 3.7: Normalized power spectra corresponding to the interferograms of Fig. 3.6. The spectra are Fourier transforms of the interferograms.

at increasing optical delays (Fig. 3.6). The corresponding spectra's bandwidths, therefore, decrease from a) to c) (Fig. 3.7). Fig. 3.6a and Fig. 3.7a shows the interferogram and spectrum of the blackbody with the atmospheric absorption spectrum and the response of the detector. The spectrum grows at low frequencies quadratically following a blackbody spectrum with the Rayleigh-Jeans approximation. The spectrum tapers at high frequencies because the cryogenic low-pass absorptive filter reduces the power in the receiving detector. The dip around 557 GHz corresponds to the water vapor's absorption line. Fig. 3.6b is the measured interferogram of the same 1300 K blackbody source with a bandpass filter in the optical path. The coherence length is longer with a narrower frequency band. Fig. 3.7b is the corresponding frequency band, which is mostly defined by the bandpass filter's transmission spectrum. The interferogram in Fig. 3.6c is taken with a Gunn oscillator. The Gunn oscillator has a <1 MHz bandwidth centered at 295.4 GHz with a long coherence

length beyond the maximum optical delay of the instrument, so the spectral resolution or full-width half-maximum (FWHM) in Fig. 3.7c is the resolution of the FTS and will be discussed in Section 3.3.6. The interferograms and the corresponding spectra agree with the source properties and the water absorption line's position, confirming our FTS covers the desired frequency range and can measure a wide range of spectra.

### *3.3.3 Transfer efficiency*

A small fraction of optical power is lost when transferring through the FTS system due to scattering from the surface roughness of the mirrors and spillover off the edges of optical elements. The transfer efficiency is lower at higher optical delays because the incident beam is not parallel to the mirror motion. The ratio between the optical power that goes through the FTS box and the total input optical power is defined as the transfer efficiency of $\eta$. The transfer efficiency was determined by dividing the detector response viewing chopped thermal source through the FTS by the detector response of the same chopped source illuminating the detector through a reference optical system with only two coupling mirrors. The two coupling mirrors in the reference optical system has one focus coupled to the detector or the thermal source and the other focus coupled to the other mirror. The two mirrors are spaced by $y/(\cos\phi)$, where $y$ is the width of the box, and $\phi$ is the beam's tilt angle, so the two mirrors are at each other's second foci. The ratio of the two responses is an estimate of the transfer efficiency of the FTS relative to a system with the same input and output geometry but no internal optics. The center mirror is at a small optical delay where the interferences are negligible, so the power measured at one of the two input ports is roughly half of the total output power. We multiplied the output power by a factor of two to account for this effect. The measured transfer efficiency is $\eta = 92\% \pm 5\%$ when the optical delay is small. The transfer efficiency is not a strong function of frequency because power loss is mostly caused by spillover, which only depends on the geometry. A high transfer efficiency indicates that

the FTS can couple most of the input power to its outputs. As the mirror moves to higher optical delays, the transfer efficiency is lower because more of the beam misses the moving mirror(Fig.3.10a).

### *3.3.4 Modulation contrast*

The useful signal of the FTS is the power modulation from interference. We define the modulation contrast to be the modulated optical power divided by all the transferred optical power. Several factors can reduce the interference between different optical paths, including non-ideal polarization efficiency of the wire grid, non-uniform optical delays for light rays within the same beam, and the spatial separation of diffraction patterns transferred along different optical paths. The loss of modulation contrast is worse at higher source frequencies because the phase non-uniformity is more significant and the spatial overlap of Airy diffraction patterns is smaller as frequency increases.

The amplitude of the interference-modulated power is the interference amplitude of an interferogram. To measure the total power vs. mirror positions, we operated the FTS at low speed and modulated the source by closing and opening the source aperture alternatively with a chopper. An interferogram with chopper modulation is in Fig. 3.8. The source is a 1300 K blackbody with a bandpass filter, the same as that used for Fig. 3.7b. The unresolved dense blue oscillation is the chopper modulation signal, the depth of which corresponds to the total optical power from the source. The envelope of the blue region is the interferogram. An FFT of this chopped signal has the source spectrum as AM sidebands of the chopper frequency. The modulation depth at a large delay ($I_\infty$) is a measure of the total optical power without interference, while the modulation depth at zero delay ($I_0$) measures how much radiation can interfere. For the antisymmetric port we used, an ideal interferogram would have destructive interference at zero delay with no optical power and zero chopper modulation depth. The contrast at a small optical delay is defined as $C = I_0/I_\infty - 1$ and

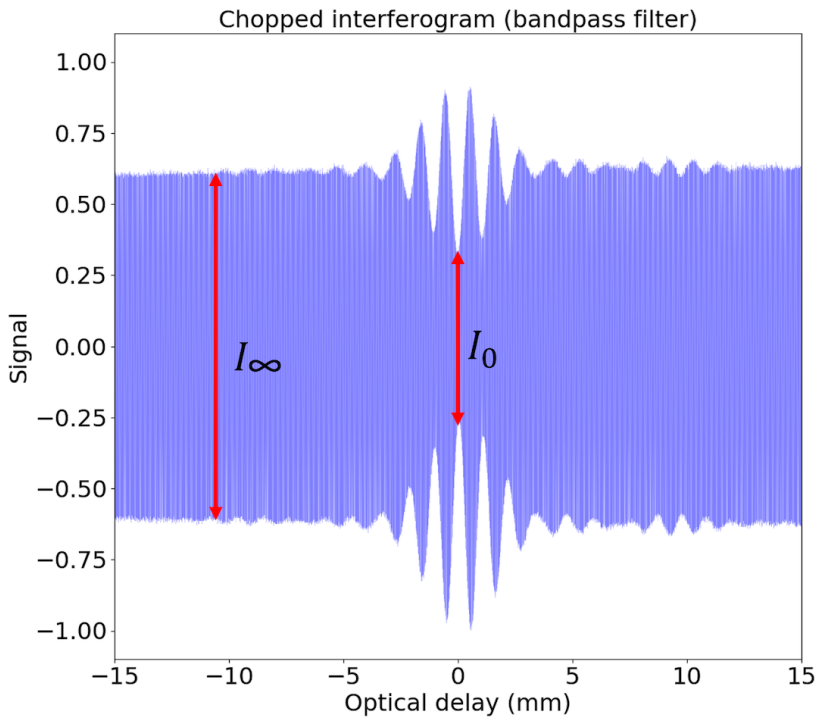


Figure 3.8: Chopper-modulated interferogram for a broadband source. The blue region is unresolved chopper modulation at a much higher frequency than the interference pattern, which is the blue region's envelope. The measured chopped depth at the output, or the vertical span of the blue area, is proportional to the output intensity. $I_0$ and $I_\infty$ are intensities at zero and infinite optical delays.

depends on the source frequency. For an ideal interferogram where all power interferes, the modulation contrast is -100% for the antisymmetric output port or 100% for the symmetric output port. The measured modulation contrast for the 1300 K blackbody source (Fig. 3.7a) and the same blackbody with a bandpass filter (Fig. 3.7b) are $C = -33 \pm 1\%$ and $-55 \pm 3\%$, respectively. The source with a broader bandwidth has a worse contrast because of the nonidealities stated earlier in this section. The contrast is also worse at higher optical delays due to the spatial separation of the recombined beams.

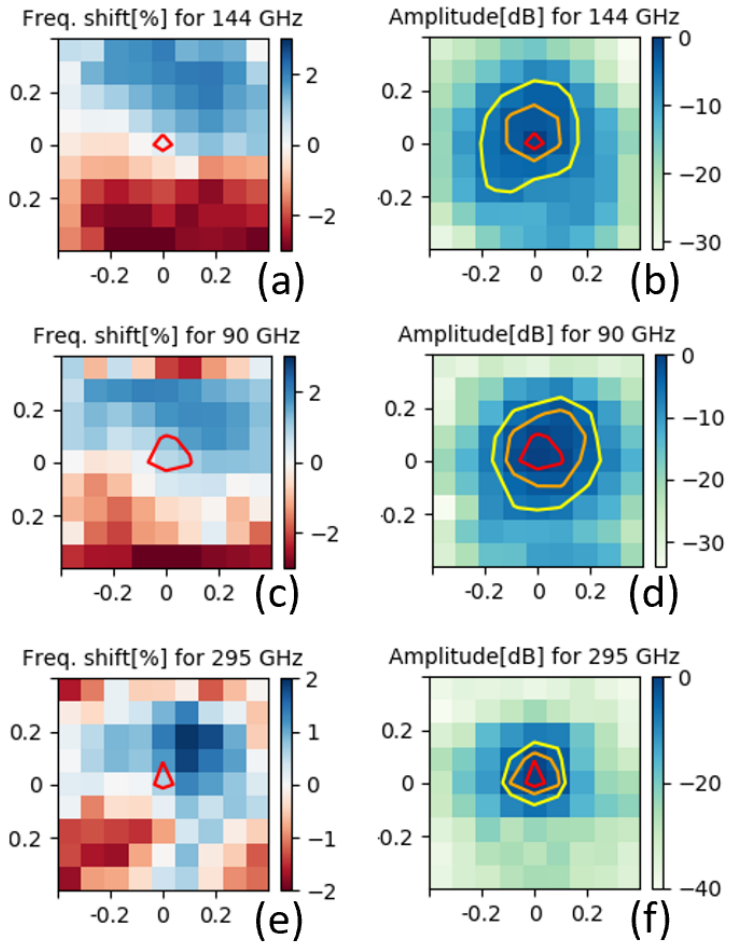


Figure 3.9: (a) is the fractional difference between FTS-determined frequency and the known frequency for a $144.3 \pm 0.1$ GHz Gunn oscillator source as the source is scanned in a grid across the input focal plane. X and Y axes are coordinates on the input focal plane in inches. The effective frequency shift is found by weighting these shifts by the intensity map in b). (b) shows the intensity map for the same source used in (a). The intensity map is the amplitude of the interferogram as the source is moved across the grid. The maximum intensity is normalized to one. The intensity is plotted in dB, with red, orange, and yellow contours indicating -1, -3, and -6 dB (or 79%, 50%, and 25%) relative to the maximum power respectively. The Middle and bottom are similar plots for a $90.4 \pm 0.1$ GHz and a $295.4 \pm 0.1$ GHz Gunn oscillator. The intensity pattern decays faster for the 295 GHz source, and the corresponding frequency shift measurement is noisier towards the sides. The -1 dB contours in amplitude are over-plotted in the frequency shift maps. The frequency within the -1 dB contours is weighted the most for an extended source.

### *3.3.5 Frequency shift*

The first step of FTS data analysis is to convert the mirror position into the optical delay, which depends on the accurate modeling of the FTS hardware. For an extended source with a wide beam, the light paths are different for different photons, resulting in different optical delays for the same mirror position. In our analysis, we use an approximation ($d = 4y\cos\phi$) to calculate the optical delay based on the motorized actuator's location for all the étendu, which is correct for the chef ray but inaccurate for all the light paths. We can do better in modeling by integrating the delay over different light paths using a ray-trace simulation. Another way of quantifying this effect is to calibrate the frequency shift and its dependence on the source's position through measurements, which is useful for understanding the frequency accuracy and can be used to estimate and correct the frequency shift.

The frequency shift's location-dependence was measured by moving a Gunn oscillator point source across the input focal plane and determining the source's frequency using the $d = 4y\cos\phi$ approximation. The determined frequency will be different from the actual frequency, and the difference provides an approximation of the correction factor. Fig. 3.9a shows an example of frequency shift measurement. In this plot, X and Y are the Gunn oscillator coordinates on the input focal plane. The Gunn oscillator's actual frequency is measured by a spectrum analyzer to be $144.3 \pm 0.1$ GHz. The FTS determined frequency depends on the source location and can shift between $-2.5\%$ and $2.5\%$ across a $\pm 0.4 \times \pm 0.4$ in the area of the input focal plane relative to the actual frequency. The FTS determined frequency is accurate at the (0,0) location and deviates as the source is away from the center, which is expected because our modeling of the optical delay assumes a point source at the center of the input plane. The pattern of the frequency shift is a sensitive function of the alignment of the polarizers and the center mirror, according to the simulation results (Section 3.4.3). We performed similar measurements for a 90 GHz and a 295 GHz source and found similar frequency shift patterns scaled by their frequency. The formula we use

for the optical delay ($d = 4y\cos\phi$) neglects the beam divergence and assumes that the full beam's delay is the same as the chief ray. The accurate optical delay for a general light ray is $d = 4y\cos\psi\cos\phi'$, where $\psi$ is the angle relative to the x-y plane, and $\phi'$ is the angle relative to the y-axis in the projected x-y plane. The optical delay for the full beam is the weighted average for all the light rays over the entire solid angle and source area. We also explored ways to correct for the inaccurate optical delay via simulation in Section 3.4.3.

The frequency shift has two effects. It reduces the spectral resolution when using an extended source, and it changes the beam weighted average frequency from that using the simple formula ($d = 4y\cos\phi$) for the optical delay. Fig. 3.9a shows that the measured source frequency could be shifted by 2.5%, depending on the source position. However, the center position of the input focal plane gets the most weight with a higher coupling efficiency (Fig. 3.9b). The coupling amplitude maps in Fig. 3.9b are the total modulated power of the interferograms with the same grid pattern as that used in Fig. 3.9a. The weighted average frequency shift for a source with an extended area is much less. We calculated the coupling weight map by normalizing the intensity map (Fig. 3.9b), so the sum of all pixel weights is one, with pixel values converted to percent from dB. After weighing the frequency shifts (Fig. 3.9a) by the coupling weights, the FTS-determined source frequency is 144.4 GHz, which differs from the known Gunn oscillator frequency of 144.3±0.1 GHz by only ∼0.1 GHz. The FWHMs of the intensity maps for the 90, 144, and 295 GHz sources in Fig. 3.9 are 0.4 in, 0.3 in, and 0.2 in, respectively. The FWHM of the intensity map indicates limits of the source area that can couple through the FTS.

### *3.3.6 Frequency resolution*

The resolution of the FTS is the FWHM of the spectral response to a single-mode source. The resolution is inversely proportional to the interferogram's length because the spectrum is related to the interferogram by an FFT. It is convenient to define delay window function here,

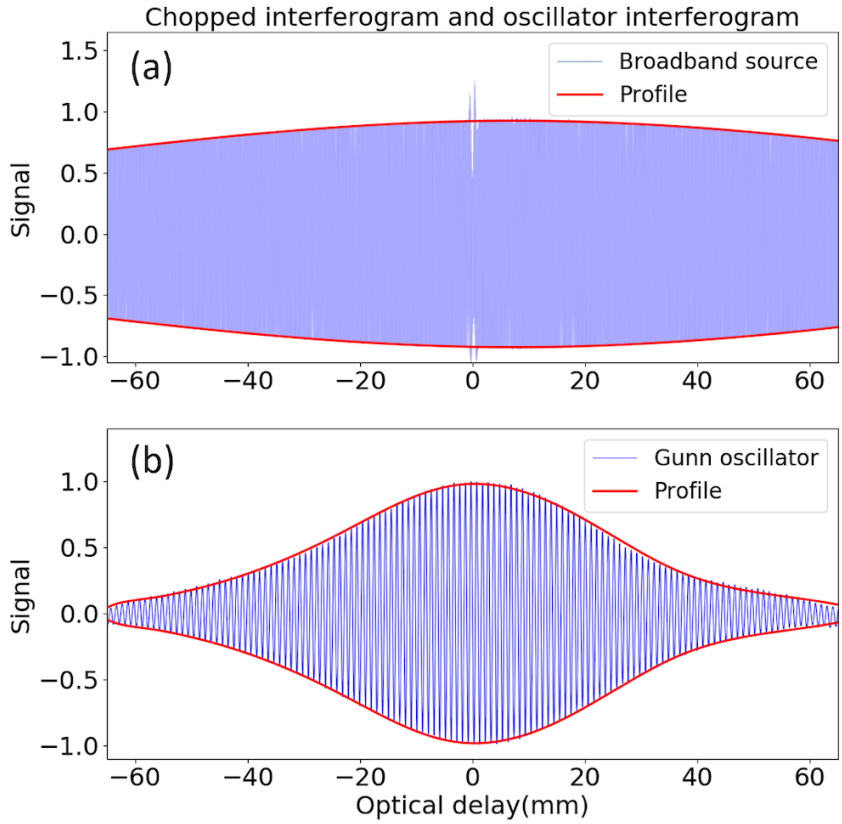


Figure 3.10: (a): An interferogram of a broadband source with the source power 100% modulated by a chopper. The wiggles around zero delay are the interferogram, which decays fast due to the short coherence length. The rest of the plot is a measure of the total power transferred through the FTS box. The blue region is unresolved oscillating chopper modulation, the envelope of which is proportional to the transfer efficiency. The center of the spline is normalized to the transfer efficiency at a small optical delay measured in Section 3.3.3. The transfer efficiency decreases as the mirror delay increases because more beam is lost. (b): An interferogram for an unmodulated 295 GHz Gunn oscillator. It uses the same data for Fig. 3.6c but covers a larger range of optical delay. The oscillation is the interference pattern and is not from chopper modulation. The interferogram tapers faster as the optical delay increases compared to (a) due to modulation contrast loss in addition to the power loss in (a). The shape tapers to zero at the maximum optical delay, which agrees with our design of zero contrast at 330 GHz (Section 3.2.2).

which is the envelope of a spectrally unresolved source's interferogram. With this definition, the spectral resolution is the FWHM of the delay window function's FFT. Several factors limit the width of the delay window function. The first is the interferogram scan range, or

the maximum optical delay when the mirror is at its maximum displacement [165]. The delay window function is also limited by the effects described in the previous sections: the delay-dependent transfer efficiency, the reduction of contrast (decoherence) at high optical delays, and the averaging of the frequency shift due to the effects of an extended source. These nonidealities make the achieved spectral resolution worse than the 1 GHz target, which was inferred from the interferogram scan range.

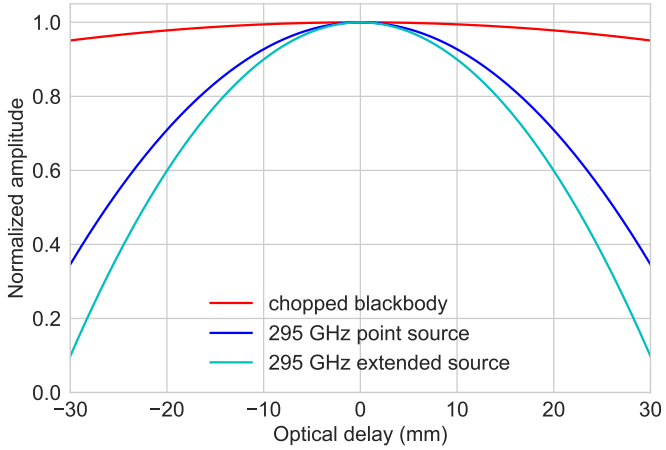


Figure 3.11: Three effects limit the frequency resolution: 1) the delay-dependent transfer efficiency, 2) the reduced coherence at high optical delays, and 3) the average of shifted frequencies for an extended source. The red curve is the transfer efficiency, or effect 1), measured with a chopped blackbody. The blue curve is the delay window function for a 295 GHz point-like Gunn oscillator, which is the envelope of Fig. 3.10b and includes effect 1) and 2). The cyan curve is the delay window function for a 295 GHz extended source obtained by averaging interferograms through a grid of source positions. The cyan curve includes effects 1), 2), and 3), so it decays the fastest. We took the local maxima of the oscillations in the interferogram and fitted them to a second-order polynomial. These parabolas were then normalized to one. The full scan range is -87 to 87 mm, which is not shown here.

We can quantify the nonidealities' effect on the resolution by measuring their impact on the delay window function. Fig. 3.10a is the interferogram of a broadband source (the same as Fig. 3.7a) with a chopper turning on and off the source aperture at a high frequency. We fit the local maxima of the oscillating curve to a spline to get the envelope, which is proportional to the transfer efficiency. Note that interference only happens at the center portion of

the interferogram, and the rest is just a measure of the transferred power. Fig. 3.10b is the interferogram of a 295 GHz source without chopper modulation. The envelope of the interference tapers faster due to delay-dependent decoherence. Fig. 3.11 shows the fit envelope of these two situations and a third, which is the envelope of a weight-averaged interferogram through a grid of source positions (Section 3.3.5). The FFT FWHMs of the three envelopes in Fig. 3.11 are 2, 4, and 6 GHz, respectively. The three widths are the frequency resolutions for cases with 1) transfer efficiency loss only, 2) efficiency loss and decoherence, and 3) average of frequency shift, efficiency loss, and decoherence.

## 3.4 FTS simulation

The FTS design requires optimizing design targets of a large étendu, high spectral resolution, compact size, and operational simplicity. These targets conflict with each other and need to be balanced. To study how hardware configurations affect the achieved performance, we have developed a ray-trace-based simulation, which is detailed in [3]. The simulation can trace the radiation transfer of the light rays and study the interference through the geometry of the FTS as the optical delay changes. The FTS geometry and the resulting interference pattern affect the instrument's transfer efficiency and frequency resolution, but the effects are hard to evaluate analytically. The ray-trace simulation can model these effects and can be used to cross-check with the experimental results, which helps understand the systematic effects and assist FTS design optimization.

In the simulation, light rays are launched at the source plane with positions and angles following the source's area and beam profile. The rays propagate through the FTS optics with their complex phase, polarization, and amplitude information tracked. The interaction with optical elements uses laws of reflection and assumes all mirror surfaces to be perfect, and all polarizers have 100% polarizing efficiency. All the light paths are tracked until they reach the output focal plane or lost if they fall beyond optical elements' edges. At the

detector plane, the detector is modeled as a single-mode perfect power absorber. The power measured by the detector is calculated with the amplitude and phase information of the collected light rays. Fig. 3.12 shows the ray-tracing through the FTS box for a point source.

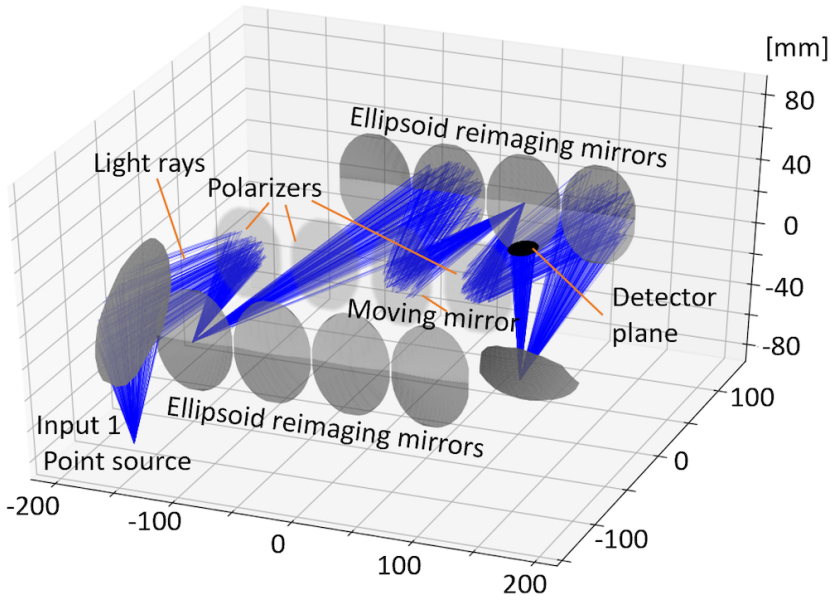


Figure 3.12: An example ray-trace for a point source. The source is placed at the source plane in the lower left, and its emitting beam pattern approximates the beam of a Gunn oscillator. The mirrors are shown in grey on the top and bottom of this plot. The polarizers and the moving mirror in light grey are along the center of the FTS. This image is rotated 180 degrees from Fig. 3.1 about the $z$ (vertical) axis. All rays in this image are linearly polarized, so they all reflect from polarizer A. Rays reflecting from polarizer B are not shown for clarity. The ray trace also illustrates the mirror design in Section 3.2.1. Each mirror images the previous optical element on the next one, so the beam converges to a single point at every other ellipsoidal focusing mirror. In this optical configuration, the image at the detector plane is not an image of the source, but an image of the first mirror.

The simulation provides flexibility in studying effects from hardware configurations that can not be easily tested by experiments, such as the effect of alignment errors, shifted optical element positions, non-ideal polarization efficiency, and the detector and source geometry. Understanding these effects can help set the construction requirements with the given design targets. The simulation can study almost all effects in the experiment section. The light rays' positions enable us to calculate the portion of light rays falling off edges of the optical

elements and calculate the transfer efficiency as a function of optical delay. With the light ray positions, we can also measure the recombined beam's spatial separation and study the recombined beams' spatial coherence. The distances that the light rays traveled can be used to construct an accurate relationship between the optical delay and mirror position, which will correct the frequency shift caused by assuming $d = 4y\cos\phi$ for all the light rays within the étendu. The light rays' phase information can help model the interference, and the polarization information can help study effects caused by imperfect polarizer angles.

The simulation also has limitations. We assume a single-mode detector with a perfect lens collecting all the light rays at the detector plane in our simulation. Horn-coupled single-mode detectors can also be modeled since the phase arriving at the detector can be calculated. However, the simulation cannot model multi-mode detectors due to the ray-tracing nature of the simulation. Also, the ray-trace cannot model diffraction because ray-trace assumes the accurate position of each light ray is known, whereas diffraction means every photon's wave function spread over the surface area of the optical elements. As the center mirror moves, the diffraction patterns for different interfering paths have less overlap and become more different in their phases, resulting in a reduced coherence level. The simulation pipeline cannot model this effect. However, it can track the spatial separation of the recombined beams, which can be used to estimate spatial decoherence with a given diffraction pattern. The right way to model diffraction and decoherence is to propagate the fields by doing Fourier transforms of the aperture fields, which is beyond the scope of our simulation.

### *3.4.1 Simulation implementation*

The simulation starts with a distribution of light rays that can well sample the input source's spatial shape, beam profile, and polarization distribution. Each initial light ray has its launch position, direction vector, and linear polarization assigned according to the source properties. The initial light rays' distances traveled are set to zero, and their initial intensities are the

same. The light rays have their phase and traveled distance tracked as they travel through the optics towards the output port. In total, nine quantities were stored and updated for every light ray, including the position ($p = [x, y, z]$), direction ($\vec{v} = [v_x, v_y, v_z]$), distance traveled ($D$), polarization angle ($\theta$), and intensity ($I \propto E_0^2$).

The FTS model in the simulation assumes all metal surfaces are perfect, and all polarizers are perfect. In the simulation, the ellipsoidal mirror surfaces and polarizer surfaces agree with the CAD drawing for the FTS hardware. Light rays interact with the optics by reflecting at mirror surfaces and reflecting and transmitting at polarizer surfaces. When the light ray meets an optical element, its position, direction vector, and distance traveled will be updated according to laws of reflection and polarizer properties. After reflecting off an ellipsoidal mirror, the light ray's direction vector is modified as $\vec{v}_f = \vec{v}_i - 2(\vec{v}_i \cdot \hat{n})\hat{n}$, where $\hat{n}$ is the unit normal vector of the tangent plane at the intersection, and $\vec{v}_i$ and $\vec{v}_f$ are unit direction vectors before and after the reflection. The distance travelled $D$ is updated as $D_f = D_i + d(p_i, p_f)$, where $D_f$ and $D_i$ are the distance before and after the interaction, and $d(p_i, p_f)$ is the distance between the previous tracked position and the intersection point with the mirror. The polarization angle after the reflection $\theta_f$ is modified as $\theta_f = \theta_i + \pi$. When interacting with a wire grid, an incident ray $R_i$ is split into a reflected light ray and a transmitted light ray. The incident light ray's electric field vector is decomposed into two vectors polarized along the wire grid direction and its orthogonal direction. The electric field of the reflected light ray is along the wire grid direction, and the electric field of the transmitted light is in the orthogonal direction. The reflection at a polarizer is treated in the same way as the reflection at the mirrors. The transmission is simpler, with the direction vector unchanged and only traveled distance and position updated.

The radiation transfer through the FTS is simulated by propagating all light rays through the box to the detector focal plane. Each light ray will interact with four polarizers and either transmit or reflect at each polarizer, resulting in $2^4$ different light paths for every initial ray.

Half of these paths end up at the detector plane, and half arrive at the other output port covered by an absorber. If a light ray falls beyond the optical element edge during the transfer, it will be removed. The ratio of the number of rays that reach the detector to the total number is the transfer efficiency. When the center mirror moves in the simulation, a different number of rays will be lost, and a delay-dependent transfer efficiency can be simulated. The motion of the center mirror also causes a difference between the traveled distances of different light paths, which leads to different interference amplitudes as the rays sum up at the detector.

At the detector plane, we assume a single-mode detector and add the electric field of all light rays and square it. This method can also model a feedhorn-coupled single-mode detector with a flat phase front. The electric field for every single light ray can be decomposed into x and y axes at the output plane:

$$\vec{E} = e^{i\omega t}[E_x e^{i\phi}\hat{x} + E_y e^{i\phi}\hat{y}] \tag{3.5}$$

Here $\phi$ is the phase of each light ray, and $E_x$ and $E_y$ are the x and y components of the electric field calculated using the relative angle between the light ray polarization and the coordinate axes. The phase $\phi$ is derived from the distance that a light ray has traveled: $\phi = 2\pi D/\lambda$. The total power of all the rays is modeled by

$$P_{\text{tot}} = \left(\sum_k E_{x,k}\right)^2 + \left(\sum_k E_{y,k}\right)^2. \tag{3.6}$$

where index $k$ goes over all the collected light rays.

The distribution of rays in the simulation represents the probability function of a single photon from a source with a large emission beam and a finite limiting angle. The initial rays have identical initial phase and source point approximating a spherical phase wavefront. The polarization of all rays is set along the +x direction to match the Gunn oscillator used

in the tests. The Gunn oscillator is used with a waveguide antenna or a horn antenna, which produces nearly spherical phase fronts at the input mirror. The detector in the simulation is assumed to be a single-mode detector with zero phase error, which is a good approximation for feedhorn-coupled single-mode detectors. The power at the detector is calculated by summing the electric field of all light rays with no additional phase added. This power summing method, however, is not accurate for a multi-mode detector.

### *3.4.2 Efficiency loss simulation*

The efficiency loss is caused by the beam falling beyond optical elements. The transfer efficiency can be simulated by tracking the number of rays within the optics and dividing it by the total number of all rays launched at the source. The percentage of rays that can reach the detector as a function of the optical delay is just a simulation of delay-dependent transfer efficiency shown in Fig. 3.10a. We compare the simulation result with the measurement in Fig. 3.13 and found them to agree well. The small difference between the measurement and the simulation can be caused by a small optical configuration difference between the actual FTS hardware and the perfect modeling of the FTS optics assumed in the simulation.

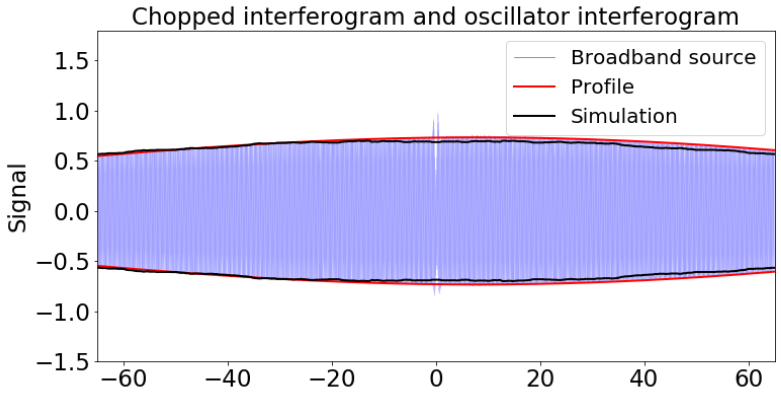


Figure 3.13: Shown in blue is the modulated interferogram of a broadband source the same as in Fig. 3.10a. The red envelope of the interferogram is proportional to the power transferred through the FTS or the transfer efficiency. The simulated transfer efficiency is the black line, which agrees with the measurement.

### *3.4.3 Frequency shift simulation*

The frequency shift is a geometric effect originating from the discrepancy between the optical delay for the chef ray used in the data analysis and the actual optical delay for the full beam, which can be estimated using the travel distance of all light rays in the simulation. In the simulation, the distribution of the initial rays agrees with the beam shape of the Gunn oscillator used for the experiment in 3.3.5. The position of the source can be moved in the simulation to study the location-dependent frequency shift. With the simulation, we can get a more accurate relationship between the optical delay and the center mirror position by averaging the optical delay over light rays within the beam. Simulation results show that the alignment of the polarizers and mirrors needs to be better than 0.3 deg for the frequency shift to be within 1%. Our prototype FTS was not built to this tolerance. However, this can be easily improved. The simulation does not have the same configuration as the hardware and cannot fully correct for the frequency shift pattern in Fig. 3.9. The alignment accuracy of 0.3 deg is unnecessary for our current applications of characterizing detectors and materials. If such accuracy is needed, the wire grid polarizer mounts will need to be improved. The wire grids now sit on a layer of glue used to fix the wires to the frame. The glue layer has an inhomogeneous thickness. With better mounts and better alignment of the instrument, we will be able to use the simulation to correct the frequency shift.

### *3.4.4 Coherence and frequency resolution*

As discussed in Section 3.3.6, loss of coherence reduces the interference level, especially at high optical delays, resulting in a narrower delay window function and reducing the frequency resolution of the FTS. One dominant source of decoherence in our system is the divergence of light rays traveling along interferring optical paths at the source plane (referred to as spatial decoherence). This effect is present because the beam incident angle at the moving mirror is nonzero; thus, as the mirror moves away from the center, the two light paths are shifted

from each other. A more classical system with a mirror that travels along the optical path does not have this effect but will result in a non-compact design. The spatial decoherence is worse at higher frequencies because the Airy diffraction patterns through the optics are smaller and have less overlap and less interference. The simulation pipeline cannot simulate diffraction and model this effect properly, but it can measure the spatial divergence of the recombined beams. With an estimated size of the Airy diffraction pattern, we could estimate the overlap of the recombined beams and their interference level as a function of optical delay. The divergence of the recombined beam vs. optical delay is in Fig. 3.4.4. Points in the same color are from interfering optical paths with the same mirror position, and different-colored points have different mirror delays. As the mirror moves further, the separation between the recombined point pairs also increases, leading to a decrease of spatial coherence and a reduction of interference amplitude at larger optical delays.

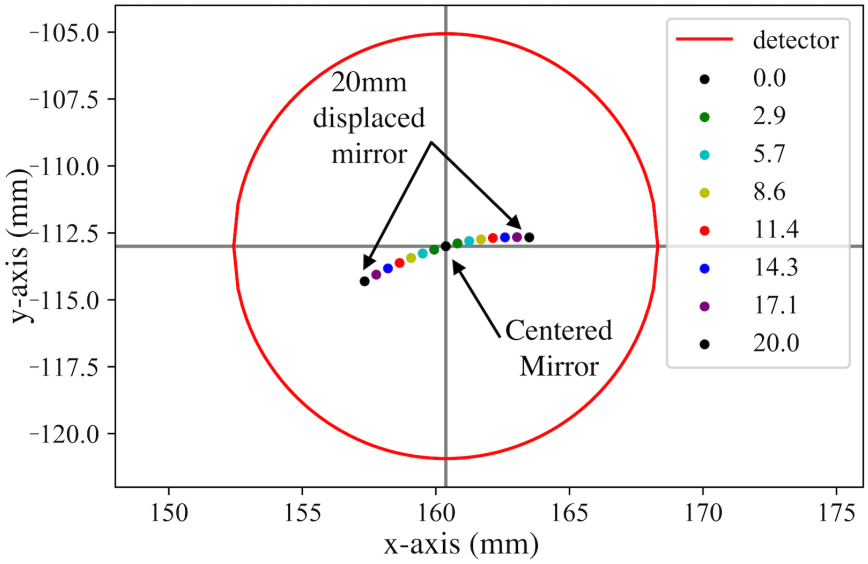


Figure 3.14: The intersection points between the interfering beams and the detector plane as a function of the center mirror position. The intersection points for interfering light paths are in the same color. When the mirror delay is zero, the recombined beams along different paths land in the same spot at the detector plane. When the mirror displaces, the recombined positions become further apart, leading to less interference. The detector area is the red circle.

Another decoherence source is the large solid angle of the beam, which results in length

differences for light paths within the same beam (referred to as phase coherence). The non-uniform phase front at the detector plane causes the beam not to add up coherently and reduce the coherence level. When the mirror is displaced far enough from the center position, the beam center's phase and the beam edge cancels the interference completely. The optics' size needs to be balanced against the coherence requirements to maintain a high throughput with a large solid angle and a high interference level at the same time. To reduce this nonideality, we can make the optical elements larger while reducing the solid angle to get the same throughput, but this will increase the instrument size. The phase decoherence is a geometric effect and can be estimated with ray-tracing simulation.

Equipped with the tools, we simulated the detected power vs. optical delay, or the interferogram, and compared with the experimental results. The experimental results are from a 144 GHz spectrally unresolved Gunn oscillator. We moved the Gunn oscillator across a 0.8 inch by 0.8-inch grid at the input plane to probe the position-dependence of the interferogram. The 81 interferograms taken across the grid were added together to approximate that of an extended source. The simulation was done similarly. For each source position, 500 light rays were launched from the source point with direction vectors following the beam profile. We moved the source over the same grid pattern as the experiment and obtained an interferogram for each grid position. A typical source coupled to the FTS has a finite area. We sum up all 81 interferograms with their coupling efficiency as weights for both the simulation and the experiment to approximate a wholly illuminated source plane. The resulting interferograms are in Fig. 3.15a and Fig. 3.15b for the simulation and experiment, respectively. The spectra from the interferograms are in Fig. 3.15c and Fig. 3.15d. The FWHM of the spectrum is the frequency resolution for an extended source. The resolution for the experiment is 7.1 GHz, which is different from the 6 GHz resolution for an extended source reported in Section 3.3.6 due to a different source frequency and an extra Hanning apodization window used in our analysis. Section 3.3.6 used a cosine window function only

at the edges of the interferogram because the 295 Ghz interferogram already tapers at high optical delays due to reduced coherence. The simulated resolution from adding all 81 simulated interferograms is 6.7 GHz, close to the experimental result. The small difference is caused by extra scattering and diffraction that is not captured by the simulation. The simulation provides a method to predict the resolution of an FTS with a given geometry and will be useful for optimizing FTS designs.

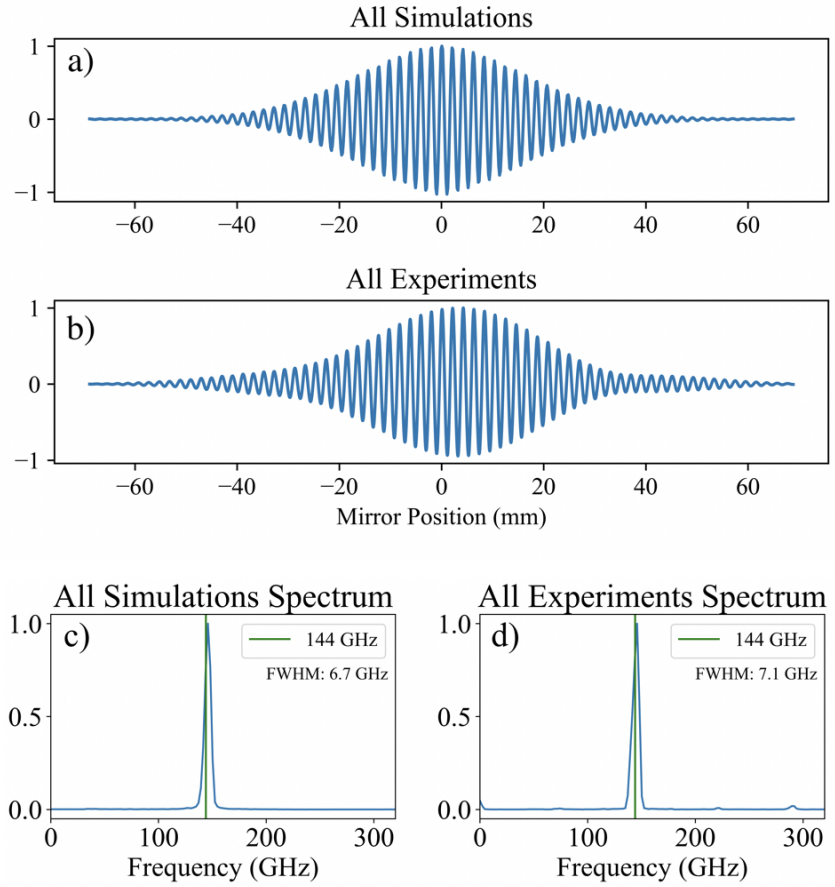


Figure 3.15: (a) and (b) are the sums of all simulated and experimental interferograms over 81 source positions, which approximate an extended source illuminating the full source plane. The interferograms are summed with the interferogram amplitude as the weight, which is also proportional to the location-dependent coupling efficiency. The FFTs of (a) and (b) generate the corresponding frequency spectra shown in (c) and (d). The FWHMs of the frequency peaks are the frequency resolutions of the simulation and data.

# CHAPTER 4

# GRAVITATIONAL LENSING ANALYSIS

## 4.1 Observation and data processing

### *4.1.1 CMB Observations*

The main SPT-3G survey field covers a 1500 $\mathrm{deg}^2$ patch of sky extending in right ascension from $20^{\mathrm{h}}40^{\mathrm{m}}0^{\mathrm{s}}$ to $3^{\mathrm{h}}20^{\mathrm{m}}0^{\mathrm{s}}$ and in declinations from $-42°$ to $-70°$. We chose the survey field to overlap with the BICEP Array survey to help remove lensing-induced contamination from BICEP Array data in search of inflationary B-modes. The survey field also overlaps with the Dark Energy Survey (DES) field, enabling cross-correlation measurements at optical wavelengths. We divide the observation of the full survey field into four subfields centered at $-44.75°$, $-52.25°$, $-59.75°$, and $-67.25°$ declinations to maintain a relatively stable optical loading and detector response for each subfield.

The telescope observes each subfield using a raster scanning strategy. It repetitively scans right and left at a constant elevation and then moves up in elevation by ∼12 arcmin until finishing the subfield. A left-going or right-going constant-elevation sweep is called a scan, and all scans covering a subfield constitute an observation. See Fig. 4.1 for the scanning pattern. The observations began at a set of different elevations called "dither steps" to better cover the gaps between the elevation steps. While the noise of an individual observation is high, we observed each subfield ∼150 times in 2018 to integrate the noise down. The observing efficiency is defind as the percentage of observing time spent on observing the CMB field and is close to 59%. During a 24 hr observing cycle, the telescope spends 4.3 hours re-condensing liquid helium in the helium absorption fridge and cooling the detectors, ∼0.8 hours doing calibration measurements, and the remaining time observing two of the four subfields three times each.

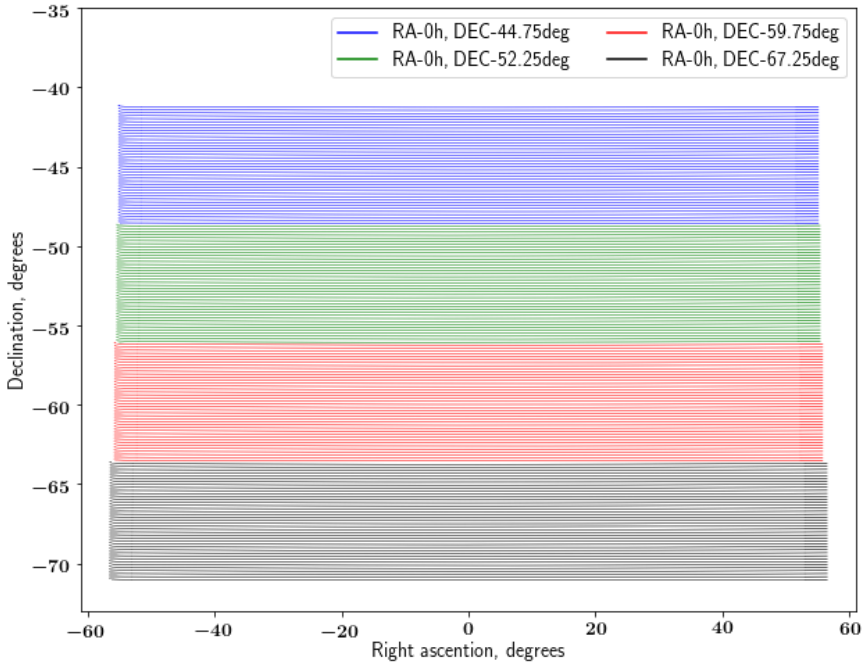


Figure 4.1: Telescope scanning patterns for the four subfields. For each subfield, the telescope starts to scan at one side of the field, sweep right and left at a constant elevation, step up in elevation (or step down in declination), and repeat the above steps until finishing a subfield. The elevation steps are on the left edge of the plot. To better sample the declination, we also apply small dither steps to offset individual subfield observations of the same sky area. The dither steps are less than the elevation step during the field observation and fill in the gap between elevation steps.

### *4.1.2 Data calibration*

The TES detectors used by SPT-3G convert received optical power into thermal power. The thermal power perturbation results in an equal amount of change of the measured electrical bias power in the high electrothermal feedback limit. The electrical bias power, or the current flowing through the detectors, is recorded as the measured signal. We conduct a suite of calibration measurements to relate the recorded electrical power change to differential CMB temperature on the sky. The main temperature calibration comes from observations of two galactic star-forming HII regions: RCW38 and MAT5a (NGC3576). We use RCW38

at declination $-47°30'39''$ to calibrate the two higher-declination subfields from $-56°$ to $-42°$ and MAT5a at declination $-61°21'44''$ to calibrate the two lower-declination subfields from $-70°$ to $-56°$. We compare the individual detector source maps in pW with Planck-calibrated SPT-SZ source maps in $\mathrm{K_{CMB}}$ to obtain a pW to $\mathrm{K_{CMB}}$ calibration factor for each detector.

We perform ten-minute-long (short) RCW38 or MAT5a observations over a small sky area where only a fraction of detectors observes the source during every observing cycle. We also take a longer and more extended source observation once a week where all detectors scan through the source. The more extended observations provide per-detector calibration factors, while the shorter ones monitor the daily atmosphere transmission changes per frequency band.

Another factor we include in the calibration is the current-to-power responsivity change of the detectors. In reality, the electrothermal feedback of the detectors is not infinite, and their responsivity can change as a function of time and the elevation-dependent optical loading. We measure all detectors' responses to a chopped thermal calibrator before each CMB observation or source observation at the corresponding elevation to calibrate the detector responses properly. Note that the response calibration is a relative calibration tied to the RCW38 or MAT5a calibration.

We can summarize the per-detector power-to-temperature calibration factor for an observation in the equation below:

$$\begin{aligned} C(\mathrm{obs}) &= \frac{\int P(\mathrm{HII},\mathrm{long})}{\int T(\mathrm{HII})} \, \frac{\int P(\mathrm{HII},\mathrm{short})/R(\mathrm{HII},\mathrm{short})}{\int P(\mathrm{HII},\mathrm{long})/R(\mathrm{HII},\mathrm{long})} \, \frac{R(\mathrm{obs})}{R(\mathrm{HII},\mathrm{long})} \\ &= \mathrm{pW/K(HII,long)} \times \mathrm{Atmosphere\,transmission\,change} \times \mathrm{Response\,ratio}\,. \end{aligned} \tag{4.1}$$

Here $\int P(\mathrm{HII},\mathrm{long})$ or $\int P(\mathrm{HII},\mathrm{short})$ is the integral of the HII region source map made in power unit (pW) from a long or short source observation, $\int T(\mathrm{HII})$ is the integral of Planck-calibrated SPT-SZ source map in temperature unit (K), $R(\mathrm{HII},\mathrm{long})$ or $R(\mathrm{HII},\mathrm{short})$

is the calibrator response corresponding to the long or short HII region observation, and $R$(obs) is the calibrator response corresponding to the observation we want to calibrate. The calibration in Eq. 4.1 can be decomposed into three parts: the per-detector power-to-temperature conversion factor for the long source observation, the per-band and per-subfield-observation atmosphere transmission change monitored by the short source observations, and the per-detector response ratio between the calibrator responses corresponding to the observation to be calibrated and the long source observation. The atmosphere transmission change is calculated for each of the three frequency bands using a subset of detectors that cover the source during the short source observations.

A further non-ideality can come from the demodulation process. We encode sky signal as amplitude modulations of a high-frequency sinusoidal carrier signal and then demodulate the carrier signal to get the sky signal. Ideally, all the sky signal is in the in-phase part of the carrier when the carrier's phase is perfectly known. A misaligned phase when demodulating the carrier signal can leak some sky signal into the out-of-phase part. To correct the phase misalignment, we scan the telescope through two degrees in elevation and measure the in-phase and out-of-phase drift of the demodulated sky signal. We then perform a phase rotation for the in- and out-of-phase signals so that all the optical signal is in the in-phase part. The phase rotation is done for every sky observation and happens before the power-to-temperature calibrations discussed above.

### *4.1.3 Time-ordered data filtering and data cuts*

The recorded data from the receiver after demodulation is the time-ordered data (TOD) of current flowing through the detector as a function of time. We sample the data at 152 Hz and downsample it by a factor of two to speed up the computing and compress the data for transmission while not losing the information within the signal band. We apply a series of filters at the TOD level to prevent low- and high-frequency noise from leaking into our

signal band. Note that the filtering scheme here is for the analysis of the 2018 data used for lensing reconstruction. The atmosphere and temperature drift do not affect large-scale polarizaiton as signficantly, and we are filtering more lightly for the B-mode analysis. The primary sources for low-frequency noise include atmosphere fluctuations and the detector wafer's temperature drift. To eliminate the low-frequency noise, we subtract a 19th-order Legendre polynomial and remove modes corresponding to multipoles less than 300 from the TOD for each constant-elevation scan. To further reject the low-frequency noise, we apply a common-mode filtering technique where we calculate the averaged signal across all detectors within the same wafer and frequency band and subtract the averaged signal from each detector's TOD for the corresponding detector group. The common-mode filtering removes temperature noise and signal on scales larger than $\ell$ of $\sim$500, which corresponds to a single wafer's field-of-view on the sky. To deal with higher-frequency noise, we low-pass filter the TOD on a by-scan basis at multiple of $\ell = 6600$ to avoid the aliasing of high-frequency noise beyond the spatial Nyquist frequency of our two-arcmin pixel size into the signal band. To avoid filtering wings around bright point sources, we mask the bright point sources detected at above 50 mJy at 150 GHz in the TOD before applying the above TOD filters.

We perform data quality checks and cut data on several levels: individual detectors of a scan or all observations, all data in a scan, and all data in a subfield observation. The data from a detector is cut from a scan if the detector data has sharp spikes or discontinuities in the TOD (glitch), low response less than S/N of 20 to a chopped thermal source, oscillations from unstable bolometer operation, or anomalously low variance. A detector is also cut if the bias point is not in the superconducting transition, or if the readout is beyond the dynamic range. While the above reasons make up most detector cuts, there are cuts due to technical reasons in data processing that cause a detector to have unphysical values or miss identifying information. After the filtering process, detector weights are calculated based on their noise in the frequency range between 1.0 Hz and 4.0 Hz, which roughly corresponds to

$500 < \ell < 2000$. We removed detectors with anomalously high or low weights beyond $3\sigma$ of the distribution center. We excluded some bolometers through the 2018 observing season because of their noisy behavior, fabrication defects, or readout issues. In particular, we cut a detector wafer because it has high noise lines at 1.0 Hz, 1.4 Hz (pulse tube fridge frequency), 10 Hz, and their harmonics. We also exclude the physically disconnected detectors due to a telescope mechanical issue earlier in 2018 that shook and broke the detector focal plane's mounting structure and some detectors. The issue was fixed in 2019 and later by limiting the telescope acceleration and installing a more stiff detector mounting structure. Besides detector-level cuts, a scan including all detectors' data is cut if fewer than 50% detectors survive the cuts or the telescope pointing range does not match the CMB field's range.

The data in this analysis typically uses 8340 detectors, after cuts, over a 3-month period in 2018. During the 2018 season, the number of observations was limited by mechanical damage to the focal plane, which also limited the number of detectors that could be renumbered after fixing the mechanical damage. All other detector cuts removed ∼20% detectors out of the operable detectors. We cut subfield observations without complete calibration information or detector mapping information and ended up with 569 observations out of the 602 subfield observations collected in 2018.

### *4.1.4 Map-making*

We convert TOD data into maps with detector pointing information, detector weights calculated from noise RMS, and detector polarization properties. The weight $w_i$ for detector $i$ is calculated by $(\gamma_i/n)^2$, where $\gamma_i$ is the polarization efficiency, and $n$ is the detector TOD noise level between 1.0 Hz and 4.0 Hz. We use one for the polarization efficiency and correct for the deviation from one during the polarization calibration step (discussed in Section 4.1.6). The Stokes T, Q, and U maps for the $i$th detector can be constructed with the weight $w_i$, detector $i$'s TOD data as a function of time $t$ $d_{ti}$, the pointing matrix $P_{ti\alpha}$ indicating when

detector $i$ points at pixel $\alpha$, the polarization efficiency $\gamma_i$, and the polarization angle $\theta_i$.

$$\begin{aligned}
\hat{T}^W_{i\alpha} &= \sum_t P_{ti\alpha} w_i d_{ti} \\
\hat{Q}^W_{i\alpha} &= \sum_t P_{ti\alpha} w_i \gamma_i \cos 2\theta_i d_{ti} \\
\hat{U}^W_{i\alpha} &= \sum_t P_{ti\alpha} w_i \gamma_i \sin 2\theta_i d_{ti}
\end{aligned} \tag{4.2}$$

Here, the detector polarization angle $\theta_i$ is the antenna's designed polarization angle from the CAD drawing propagated through the optical system into sky coordinates. The designed polarization angle agrees with the actual polarization angle measured by comparing individual detector's measurement of Centaurus A's polarized radio lobes to a template.

We construct a $3 \times 3$ weight matrix for each pixel encoding the weight and correlation between pixels [166]. We sum up the weight matrix and the weighted maps over detector number $i$ for each frequency bands and multiply the inversion of the weight matrix by the weighted per-pixel T, Q, and U map vectors to obtain the unweighted maps.

$$\{\hat{T}_\alpha,\ \hat{Q}_\alpha,\ \hat{U}_\alpha\} = {W_\alpha}^{-1}\{\hat{T}^W_\alpha,\ \hat{Q}^W_\alpha,\ \hat{U}^W_\alpha\} \tag{4.3}$$

For our analysis, we make maps in the oblique Lambert azimuthal equal-area projection with square one arcminute pixels and then rebin the maps into two-arcmin resolution with anti-alias filtering following methods in Section 4.2.2) before using the maps for lensing reconstruction. Since the Q and U angles for the initial maps are defined in a curved sky relative to longitudes and latitudes, we rotate the polarization angles by $\psi(\alpha)$ to redefine the angles relative to the x-y grid in flat-sky coordinates.

$$(Q' + iU') = e^{-i2\pi\psi(\alpha)}(Q + iU). \tag{4.4}$$

Here $\psi(\alpha)$ is the angle between the north direction along longitudinal lines in curved-sky

coordinates and the north direction in projected flat-sky coordinates.

Following the procedures above, we made 2018 CMB maps and show the 150 GHz CMB maps in Figs. 4.2. From top to bottom are temperature (T), Stokes Q, and Stokes U maps. The noise levels of the maps are 20.9/21.8/73.7 $\mu$K-arcmin in temperature and 27.8/20.3/77.4 $\mu$K-arcmin in polarization for the 95/150/220 GHz bands over the multipole range of $1000 < \ell < 3000$. The maps have two-arcmin resolution and contain effects from the map filterings discussed above. High spatial frequency features along the scanning direction are removed during the time-ordered data filtering step. Spatial anisotropies from the CMB are visible in the T, Q, and U maps. The bright dots in the temperature map are from point sources emitting at millimeter-wavelength, such as active galactic nuclei (AGNs). The curl-free polarization E modes dominate the signals in Q and U maps. As a result, the Q map's spatial patterns are preferentially along X or Y direction, while the U map's features are 45 degrees relative to the axes.

Finally, we convert the Q and U maps to coordinate-independent scalar and pseudoscalar fields E and B. The E-mode and B-mode are calculated by [10]:

$$\begin{aligned} E_{\boldsymbol{\ell}} &= Q_{\boldsymbol{\ell}} \cos 2\phi_{\boldsymbol{\ell}} + U_{\boldsymbol{\ell}} \sin 2\phi_{\boldsymbol{\ell}} \\ B_{\boldsymbol{\ell}} &= -Q_{\boldsymbol{\ell}} \sin 2\phi_{\boldsymbol{\ell}} + U_{\boldsymbol{\ell}} \cos 2\phi_{\boldsymbol{\ell}} \end{aligned} \tag{4.5}$$

where $\boldsymbol{\ell}$ can be related to the Fourier wavevector $\boldsymbol{u}$ by $\boldsymbol{\ell} = 2\pi\boldsymbol{u}$, and $\phi_{\boldsymbol{\ell}} = \arctan(-\ell_x/\ell_y)$. Note that $\phi_{\boldsymbol{\ell}}$ should be defined from north to east. Our map array is stored such that the increasing directions of $x$ and $y$ are along the west and north direction.

The inverse-variance filtering of the CMB fields (Section 4.2.2) requires a 2D noise spectrum in Fourier space. And we need to make CMB simulation with realistic noise realizations that are close to the data for estimating the lensing biases (Section 4.2.3). We generate the noise maps by differencing half-depth maps and dividing the difference map by two. For every observation, we make one CMB map with data taken when the telescope scans left-to-

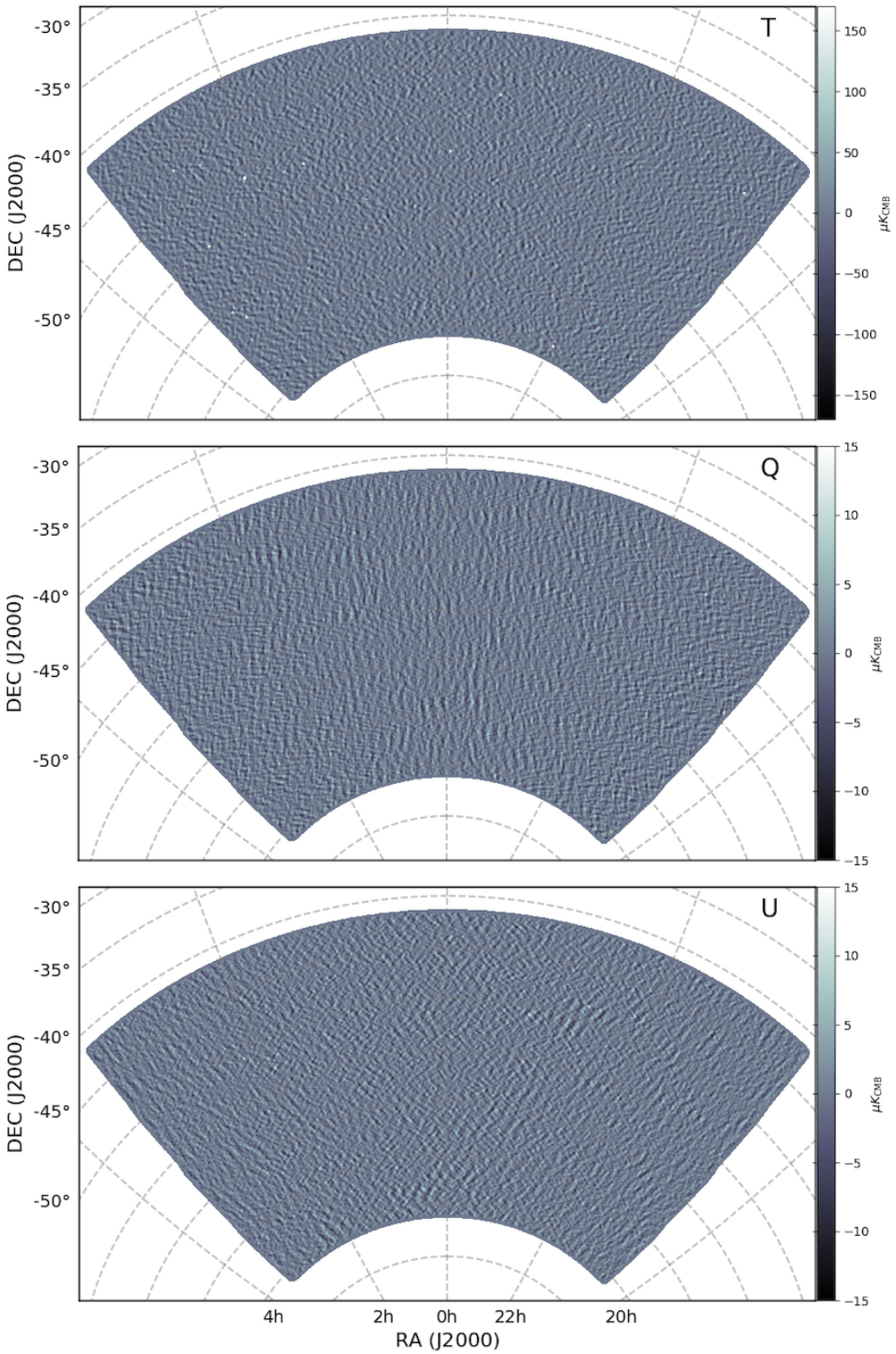


Figure 4.2: From top to bottom are temperature (T), Stokes Q, and Stokes U maps made with the SPT-3G 2018 150 GHz data. I have smoothed the maps with a 10 arcmin beam. The CMB maps are the inputs for the lensing analysis.

right and another map with the telescope scanning right-to-left. We subtract the right-going CMB map from the left-going map for every CMB subfield observation. The next step is to add the difference maps from all CMB observations with random sign flips. In total, 500 noise realizations were generated for the simulations in Section 4.2.3. We then calculated the 1D and 2D noise spectra averaged over all 500 noise realizations. The 1D noise curves are in Fig. 4.3. The 150 GHz band has the lowest noise level. The Q/U polarization noise power spectra are flatter vs. angular multipole compared to temperature because the polarization component is measured by differencing pairs of detectors with orthogonal polarization angles, so the common fluctuations cancel out. The high noise at low-frequency in 2018 data was known to be associated with microphonics heating, which improved with a redesigned focal plane structure in the following year. The 220 GHz band has the worst noise performance because of lower atmosphere transmission and worse instrument performance. I have also plotted the noise levels we use as white noise floors in the inverse-variance map filtering step (Section 4.2.2).

### *4.1.5 Beam*

The beam of the telescope can be measured by the response to a point source of the sky. To zeroth order, the optics design aims for a diffraction limited beam across the focal plane, however optical aberations and other non-idealities (e.g., scattering, reflections) in the optical design can cause additional features in the beam on the sky. The illuminated diameter of the primary dish is 8-meter for SPT-3G, and the corresponding Airy disk diameter is $\sim$1 arcmin at 150 GHz, which is close to the FWHM diameter of the beam at 150 GHz. The measured sky signal by the telescope is the convolution of the true sky signal and the beam response, and the beam $B_\ell$ needs to be divided out in Fourier space to recover the true sky signal. We measure the beam for 2018 using a combination of Mars observations and point sources in the CMB maps. Planets such as Mars can provide high signal-to-noise (S/N) beam response out

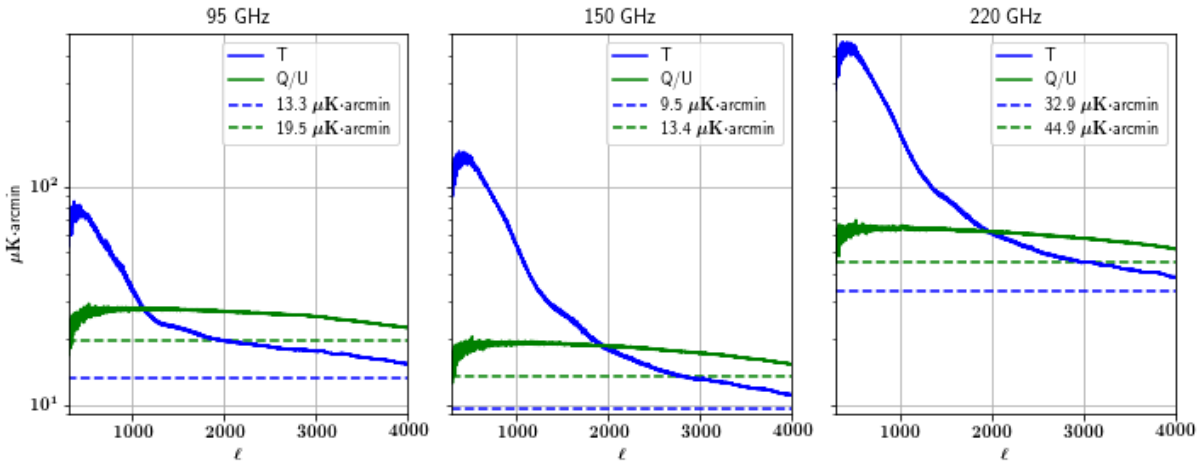


Figure 4.3: From left to right are the 2018 temperature and polarization noise curves for the 95, 150, and 220 GHz bands. The white noise floors used in the inverse-variance map filtering (Section 4.2.2) are overplotted in dashed lines. The white noise floors are lower than the average noise levels or noise curves. We include 2D scale-dependent noise beyond the noise floor in the anisotropic noise term. As discussed in more detail in Section 4.2.2, we have found that slightly varying the white noise floor does not change the map filtering results as long as the sum of the white noise floor and the anisotropic noise equals the total noise.

to a large angular diameter (∼1 deg) but cause the detector to saturate when the telescope points close to the planet. Point source observations do not saturate the detectors but do not have enough S/N to probe the beam out to large angular diamter (∼1 deg). We convolve the coadded point source profile with the planet disk (∼ 20″ diameter for Mars depending on the time) and convolve the planet map with the telescope pointing jitter to match up the two types of maps. Then we stitch the point source map and the planet map using an overlapped annulus where both maps have high S/N. The stitched hybrid beam contains large-scale (>∼5 arcmin) beam from the planet and small-scale beam from the point sources. Lastly, we subtract the CMB measured by Planck from the hybrid beam and correct the planet disk. For our analysis in Section 4.2.2, we want to characterize the 1-d response of our beam in Fourier space, $B_\ell$. To measure $B_\ell$, we start with measuring real-space beams, generate Fourier transforms of the real-space beams, and average the 2D Fourier modes within angular multipole annuli. The beam uncertainty is calculated by adding $B_\ell$ 's scatter

from individual point source observations and individual planet observations in quadrature.

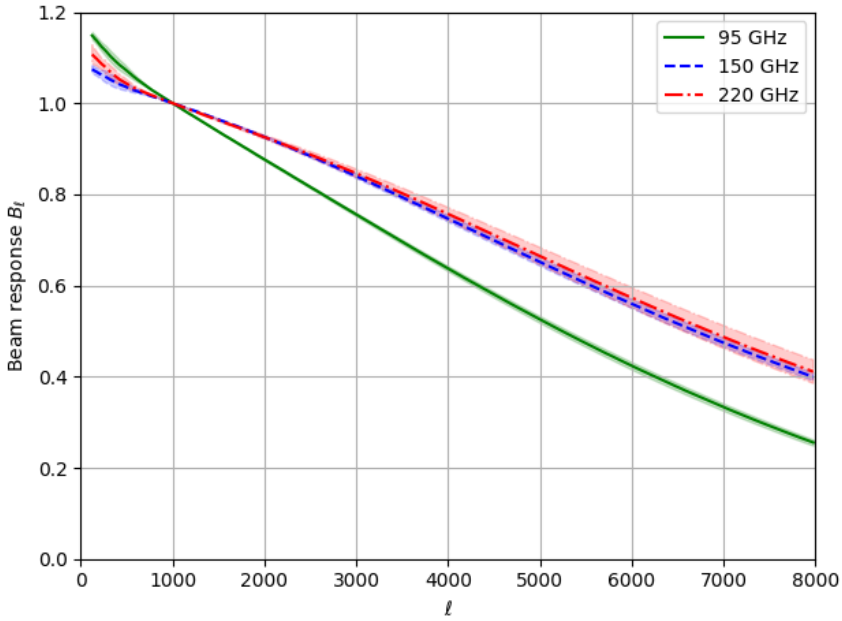


Figure 4.4: The beams of SPT-3G's 95, 150, and 220 GHz frequency bands. To generate the beam as a function of angular multipole, we measure the telescope's response to a point source in real space, Fourier transform the response into 2D Fourier space, and then average over annuli in Fourier space. The beams are normalized to one at $\ell = 1000$, and their absolute temperature calibration is discussed in Section 4.1.6. Figure made with code from Neil Goeckner-Wald.

### *4.1.6 Absolute temperature and polarization calibration*

Besides the calibration using the HII regions, we obtain the absolute temperature calibration of the coadded maps by comparing the SPT-3G 95, 150, and 220 GHz maps with 100, 143, and 217 GHz maps measured by the Planck satellite (PR3 dataset [167]) over the angular multipole range of $400 < \ell < 1500$. We compute the calibration factor $\eta^T$ by dividing the SPT-3G cross-spectra between two half-depth maps by the cross spectra between full-depth SPT-3G and Planck maps:

$$\eta^T B_\ell^{SPT} = \frac{\tilde{C}_\ell^{SPT_{1st} \times SPT_{2nd}}}{\tilde{C}_\ell^{SPT_{full} \times Planck}} B_\ell^{Planck}, \tag{4.6}$$

where $\tilde{C}_\ell$ is the power spectrum of the maps without de-biasing, $B_\ell^{SPT}$ is the SPT-3G beam, and $B_\ell^{Planck}$ is the Planck beam. We mock-observe the Planck maps in the same manner as we made the SPT-3G maps, with the same pointing, filtering, data cuts, and binning steps, so the mock-observed Planck maps have the same filter-transfer function and mode-coupling as the SPT-3G maps. With this processing, the bias to the power spectra from these effects divides out from the ratio. We estimate the uncertainty of the calibration factor using SPT-3G and Planck simulations of the same underlying sky. We generate noise realizations for SPT-3G simulations by adding individual observation maps with random sign flips, and we use FFP10 [167] simulations of Planck noise for the Planck simulations. We apply the approximate SPT-3G beam and Planck beam to the corresponding simulations and compute the $\eta^T$ and $\sigma(\eta^T)$ from these simulations. The calibration numbers are in Table 4.1. The maps calibrated by HII regions in Section 4.1.2 are scaled by the calibration factors in Table 4.1 on a per-subfield basis.

The absolute polarization calibration $\eta^P$ is computed by fitting a scaling factor that minimizes the chi-square between the EE power spectrum from the temperature-calibrated SPT-3G maps and the power spectrum from Planck 2018 best-fit ΛCDM cosmology. The uncertainties in $\eta^P$ come from the distribution of calibrations for different data subsets. The absolute polarization calibration is not subfield-dependent, because the relevant factors affecting the number, such as non-ideal detector polarization angle and polarization efficiency, do not change across subfields.

### *4.1.7 Temperature to polarization leakage*

The CMB temperature signal (T) can leak into the polarization signal (P) if the gains of the orthogonal-polarization detector pairs are mismatched, which creates a scaled copy of T in P (monopole leakage). Other factors, such as differential pointing of detector pairs, beam ellipticity, or common-mode filtering (Section 4.1.3), can induce higher-order leakage. We

| Type of calibration | (Sub)field | 95 GHz | 150 GHz | 220GHz |
|---|---|---|---|---|
| Absolute temperature | ra0hdec-44.75 | 1.086±0.004 | 1.050±0.003 | 1.016±0.011 |
| | ra0hdec-52.25 | 1.080±0.003 | 1.050±0.003 | 1.019±0.011 |
| | ra0hdec-59.75 | 1.101±0.004 | 1.034±0.002 | 1.046±0.010 |
| | ra0hdec-67.25 | 1.091±0.005 | 1.042±0.004 | 1.063±0.010 |
| Absolute polarization | All subfields | 1.02±0.01 | 1.05±0.01 | 1.12±0.05 |

Table 4.1: Temperture and polarization absolute calibration factors. We calculate the absolute temperature calibration on a per-subfield basis because different subfields are calibrated differently. The subfield label ra0hdec-67.25 indicates the subfield is centered at right ascension of 0h and declination of 67.25° The absolute polarization calibration is not dependent on subfields.

quantify the monopole leakage by fitting a combination of TT and TE spectra to the TQ, TU cross-spectra:

$$C_\ell^{TP} = \epsilon^P C_\ell^{TT} + \epsilon^{P,TE} C_\ell^{TE}, \tag{4.7}$$

where $P \in Q, U$ . We did not perform the same fitting of $C_\ell^{TP} = \epsilon^P C_\ell^{TT}$ as previous work [168, 27] because the (common-mode) filtering in our map-making induced strong TP and TE correlation as well. We found $\epsilon^Q$ to be {0.0061±0.0007, 0.0046±0.0005, 0.0090±0.0013} and $\epsilon^U$ to be {0.0080±0.0008, 0.0128±0.0007, 0.0133±0.0018} for the 95, 150, and 220 GHz bands, respectively. We calculate the spectra in Eq. 4.7 using cross-spectra between two half-depth maps to avoid noise biasing. The uncertainties come from the leakage distribution among ten pairs of simulations with different CMB, foreground, and half-depth noise realizations, which account for both the noise variance and sample variance. We deproject temperature leakage from polarization map using $\hat{P} = \tilde{P} - \epsilon^P \tilde{T}$, where $\tilde{T}$ and $\tilde{P}$ are uncalibrated temperature and polarization maps, and $\hat{P}$ is the polarization map after leakage correction. We can summarize the map calibration and leakage correction steps in two equations:

$$\begin{aligned} T &= \eta^T \tilde{T} \\ P &= \eta^T \eta^P (\tilde{P} - \epsilon^P \tilde{T}), \end{aligned} \tag{4.8}$$

where $T$ and $P$ are the calibrated and corrected temperature and polarization maps, $\eta^T$ is the absolute temperature calibration, $\eta^P$ is the absolute polarization calibration, and $\epsilon^P$ is the temperature-to-polarization leakage.

## 4.2 CMB-lensing analysis

### *4.2.1 Analysis overview*

Gravitational lensing from large-scale structure deflects CMB photons and induces correlations in CMB temperature and polarization modes. We can use these correlations to reconstruct the intervening matter distribution from CMB data maps. Before doing lensing reconstruction with the data, we need to clean contaminations in the maps that can mimic lensing. The map cleaning steps include inpainting map areas contaminated by bright point sources and clusters and anti-alias filtering that prevents higher-angular-frequency features from aliasing into our signal band. We also inverse-variance filter our maps to suppress non-CMB modes and maximize the signal-to-noise of lensing reconstruction. The map processing steps are in Section 4.2.2. Another critical ingredient for lensing analysis are simulations with similar statistical properties as the measured CMB maps. These simulations are useful for estimating the bias terms and normalizing the lensing reconstruction. We summarize the simulation generation steps in Section 4.2.3.

In Section 4.2.4, we introduce CMB lensing and derive the off-diagonal correlations induced by lensing to the CMB temperature field. The correlations allow us to build weight functions to weigh pairs of CMB modes and extract the lensing potential with minimum variance. We convolve the cleaned and filtered CMB maps with weight functions to get the 2D lensing potential (Section 4.2.5). The reconstructed lensing maps contain the weight function and map filtering effects and need a renormalization to recover the proper amplitude (Section 4.2.6). To reduce the noise, we combine the lensing maps from different

combinations of CMB fields into a minimum-variance combined (MV) map (Section 4.2.6). We then Fourier-transform the lensing map and multiply the Fourier transform by its conjugate to get the 2D lensing power spectrum. However, the lensing spectrum estimated this way contain biases. We can divide the biases into a map-level bias called the mean-field bias and spectrum-level biases proportional to the zeroth and first order of the lensing spectrum. We discuss the map-level bias in Section 4.2.5 and spectrum-level biases in Section 4.2.7. We estimate the bias terms with simulations and subtract the bias terms from the lensing reconstruction to get unbiased results. To reduce the lensing spectrum's variance, we can bin it into wider multipole annuli in Fourier space and get a 1D power spectrum.

The lensing reconstruction results from the simulations are presented in Section 4.2.9 and 4.2.10, and the results from SPT-3G measurements are in Section 4.2.11. We discuss forecasts of cosmological parameter constraints in Section 4.2.12.

### *4.2.2 Map processing and filtering*

We make our CMB data maps and mock-observed simulation maps at $1'$ resolution. To speed up the analysis, we rebin the maps into $2'$ resolution, which corresponds to a pixel Nyquist frequency corresponds to $\ell = 5400$. One problem with direct rebinning is the aliasing of small-scale modes at $\ell > 5400$ into $\ell < 5400$. Power aliasing is also the reason not to make 2 arcmin-resolution maps directly, which will have the same effect as direct rebinning. We reduce the aliasing by multiplying the $1'$ resolution maps in Fourier space by a cosine-tapered low-pass filter to remove modes beyond $\ell = 5200$ before rebinning into $2'$ resolution maps.

A second treatment we apply to the maps and mock-observed simulations before the lensing analysis is inpainting the point sources and galaxy clusters detected in the maps. The temperature gradient around point sources and galaxy clusters can mimick lensing and cause bias to our lensing maps and lensing spectra. We inpaint all detected sources and galaxy clusters. The inpainting radius is $10'$ for sources with 150 GHz flux $S$ >500 mJy,

$7'$ for sources with 150 GHz flux $50 < S < 500$ mJy, $3'$ for sources with 150 GHz flux $6.4 < S < 50$ mJy, and $1'$ for sources with 150 GHz flux below 6.4 mJy. We inpaint all sources detected at above S/N of 5 for any one of the three frequency bands. The S/N threshold roughly corresponds to the minimum fluxes of 2.7, 3.3, 12.0 mJy at 95, 150, and 220 GHz. Similarly, we inpaint clusters detected above S/N of 9 and below S/N of 9 with radiuses of $6'$ and $3'$, respectively. The inpainting method used here is similar to [169, 68, 170, 171]. We define two regions around the source or cluster center, $R \leq R_1$ and $R_1 < R \leq R_2$, where $R_1$ is the inpainting radius and $R_2$ is fixed to be $25'$. We fill values within $R_1$ based on values in the $R_1 < R \leq R_2$ annulus using constrained Gaussian realizations

$$\hat{T}_1 = \tilde{T}_1 + \hat{\boldsymbol{C}}_{12}\hat{\boldsymbol{C}}_{22}^{-1}(T_2 - \tilde{T}_2)\,, \tag{4.9}$$

where 1 indicates the $R \leq R_1$ region, 2 indicates the $R_1 < R \leq R_2$ region, $T$ is the original map, $\hat{T}$ is the inpainted map, $\tilde{T}$ is the simulated Gaussian map realization, and $\hat{\boldsymbol{C}}_{XY}$ is the covariance matrix of the CMB fields between two regions X, Y. We generate Gaussian realizations in a fixed $200' \times 200'$ box with the same CMB, foreground, noise spectra, and filter transfer function as the data to be inpainted. We estimate the covariance matrices $\hat{\boldsymbol{C}}_{12}$ and $\hat{\boldsymbol{C}}_{22}$ with 5000 Gaussian realizations following the method in [171]. During the inpainting process, small-scale noise can creep into larger scales of interest. Therefore, we low-pass filter the map region to be inpainted and the simulated maps for generating the covariance matrices below $\ell = 3000$. However, low-pass filtering a map region with a bright source can cause filtering wings around the source. To avoid filtering artifacts, we have adopted a two-step filtering method. We first fill the source region with some reasonable values by inpainting without a low-pass filter and then inpaint again with the low-pass filter turned on. We also found that inpainting a faint point source next to a bright one can contaminate the inpainted map. Our solution was to inpaint all sources and clusters from bright to faint. Some point sources could be close to the masking edge, but we can still

inpaint them because the CMB map around the masking edge still has sufficient signal-to-noise. See Fig. 4.5 for an inpainting example. The inpainting process does not change the power spectrum or Gaussian statistics of the original maps. However, the inpainted region has no lensing, resulting in reduced lensing power. We can correct the deficit of lensing power from inpainting using simulations inpainted the same way as the data. The same normalization that brings the simulation lensing reconstruction to the proper amplitude will work for the data too.

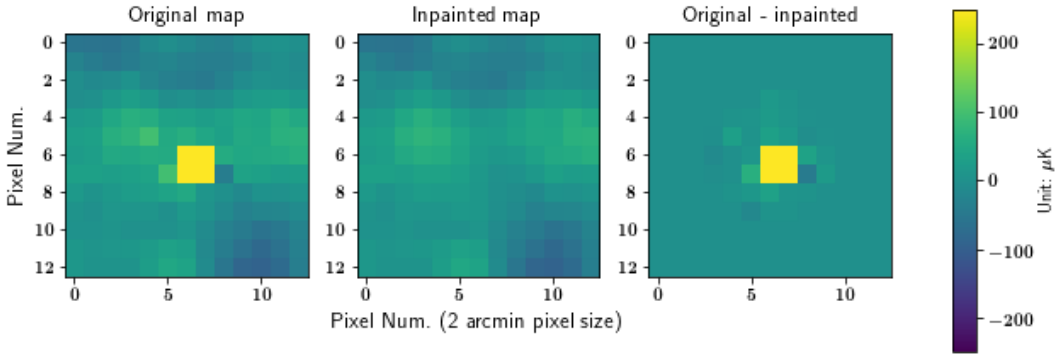


Figure 4.5: Original CMB temperature map before inpainting, inpainted map, and their difference. The original map contains a bright point source at the center, which is gone after inpainting. The inpainting process fills a map region with values that satisfies the same Gaussian statistics as the rest of the map.

We filter our maps to minimize the variance of lensing reconstruction. The inverse-variance filter consists of two parts: a Wiener filter that minimizes the expected residual between the estimated signal and the underlying signal given the noise level; and a weighting of the Wiener-filtered modes. The SPT-3G data map $d \in [T(\hat{\mathbf{n}}), Q(\hat{\mathbf{n}}), U(\hat{\mathbf{n}})]$ is a measurement of the underlying sky signal $X_{\boldsymbol{\ell}} \in [T(\boldsymbol{\ell}), E(\boldsymbol{\ell}), B(\boldsymbol{\ell})]$, and the data maps are related to the underlying sky signal by

$$d_j = \sum_{\boldsymbol{\ell}} P_{j\boldsymbol{\ell}} X_{\boldsymbol{\ell}} + \sum_{\boldsymbol{\ell}} P_{j\boldsymbol{\ell}} N_{\boldsymbol{\ell}} + n_j \,. \tag{4.10}$$

Here $P_{j\boldsymbol{\ell}}$ is a matrix operator that includes the transfer function, and TEB→TQU conversion. For temperature $T$, the operator is $P_{j\boldsymbol{\ell}} = e^{i\boldsymbol{\ell}\mathbf{x}_j} F_{\boldsymbol{\ell}}$, where $F_{\boldsymbol{\ell}}$ is the transfer function, which includes beam, pixelization effect, and timestream filtering. $\mathbf{x}_j$ is the position vector for pixel $j$. For $E$ and $B$ modes, this operator is $P_{j\boldsymbol{\ell}} = e^{i\boldsymbol{\ell}\mathbf{x}_j \pm 2i\phi_{\boldsymbol{\ell}}} F_{\boldsymbol{\ell}}$, which also includes the Fourier space angle $\phi_{\boldsymbol{\ell}}$ for $EB$ to $QU$ conversion (also see Section 4.1.4). $N_{\boldsymbol{\ell}}$ is the anisotropic sky noise that does not trace the CMB, such as atmosphere noise. $n_j$ is the map noise variance modeled as homogeneous white noise.

The inverse-variance filtered field $\bar{X}$ takes the form

$$\bar{X} = S^{-1}\hat{X} = S^{-1}[S^{-1} + P^\dagger n^{-1} P]^{-1} P^\dagger n^{-1} d\,, \tag{4.11}$$

where $S = C_{\boldsymbol{\ell}}^{XX} + C_{\boldsymbol{\ell}}^{NN}$ is the total signal covariance matrix including CMB, foregrounds, and anisotropic noise. $C_{\boldsymbol{\ell}}^{XX}$ is the sum of CMB and foreground spectra interpolated to 2D, and $C_{\boldsymbol{\ell}}^{NN}$ is the 2D anisotropic noise spectrum. The inverse-variance filtering includes a $S^{-1}$ multiplication and a Wiener-filter shown below

$$\hat{X} = [S^{-1} + P^\dagger n^{-1} P]^{-1} P^\dagger n^{-1} d\,. \tag{4.12}$$

Note that the Wiener filtering here optimizes for the total signal $S$, which includes CMB, foreground, and anisotropic noise. $n^{-1}$ is the inverse of map white noise multiplied by the map mask, so it also effectively removes the masked region in Eq. 4.12.

The full inverse-variance filtering effect is $\bar{X} = S^{-1}P^{-1}d = S^{-1}X$ in regions away from the masked area if we include the white noise $n$ into signal covariance $S$ and do the approximation of $n \to 0$ for Eq. 4.11. In our analysis, we use the same CMB and foreground spectra used for generating CMB simulations in Section 4.2.3 for $C_{\boldsymbol{\ell}}^{XX}$. We estimate our anisotropic noise with 500 independent noise realizations created following the method in Section 4.1.4. We average over 500 noise realizations to reduce the variance and subtract

the uncorrelated white noise floor $n$ from the averaged 2D noise spectrum to obtain $C_{\boldsymbol{\ell}}^{NN}$. The white noise floors and the transfer functions are discussed in Section 4.1.4 and 4.2.3, respectively. The white noise floors used for $n$ are in Fig. 4.3. After the filtering, we remove the modes at $\ell < 300$ and $\ell > 3000$, which are contaminated by low-frequency noise or contain higher foreground or noise than the CMB.

### *4.2.3 Simulation generation*

We use simulations to estimate the lensing map-level mean-field bias $\bar{\phi}_{\mathbf{L}}^{XY,\mathrm{MF}}$ (Section 4.2.5), corrections to the response function, uncertainty, and spectrum-level bias terms proportional to the zeroth and first order of the lensing spectra ($N_{\mathbf{L}}^{RD,0}$ and $N_{\mathbf{L}}^{1}$, see Section 4.2.7). The cosmology we use to generate the simulated CMB comes from the Planck best-fit results [29, 172]. We use CAMB [173] to generate theoretical CMB and lensing potential angular power spectra from Planck cosmology and HEALPix [174] to synthesize random spherical harmonics realizations $a_{lm}$ of the CMB and lensing potential that satisfy the power spectra statistics. We generate the lensed CMB by deflecting the unlensed CMB realizations by the lensing potential with Lenspix [175].

The measured millimeter-wave signals also contain foreground emissions or contaminations from the cosmic infrared background (CIB), thermal and kinetic Sunyaev-Zel'dovich effects (tSZ, kSZ), radio sources, and galactic dust. We model the diffuse foreground emissions as Gaussian realizations following the measured angular power spectra of these components. The measured foreground spectra come from [176]. The CIB in the simulation consists of a Poisson-distributed component with $D_\ell \propto \ell^2$ from faint dusty star-forming galaxies and a clustered part with $D_\ell \propto \ell^{0.8}$. Here $D_\ell$ is related to angular power spectrum $C_\ell$ by $D_\ell = \frac{1}{2\pi}\ell(\ell+1)C_\ell$. The spectral shape of the CIB is $\nu^\beta B_\nu(T_{\mathrm{dust}})$, where $B_\nu$ is the blackbody spectrum, $T_{\mathrm{dust}}$ is 12 K, and $\beta$ is $1.48\pm0.13$ for the Poisson term and $2.23\pm0.18$ for the clustered term. At 150 GHz and $\ell = 3000$, the amplitude of $D_\ell^{\mathrm{CIB}}$ is $D_{3000}^{\mathrm{CIB,P}} = 7.24\mu\mathrm{K}^2$ for

the Poisson term and $D_{3000}^{\mathrm{CIB,cl}} = 4.03\mu\mathrm{K}^2$ for the clustered term. The clustered term includes the contributions from one- and two-halo terms. The tSZ and kSZ angular power spectra shapes follow the tSZ template in [177] and the kSZ template in [178, 179]. The amplitude at 143 GHz and $\ell = 3000$ is $D_{3000}^{\mathrm{tSZ}} = 3.42\mu\mathrm{K}^2$ for tSZ and $D_{3000}^{\mathrm{kSZ}} = 3.0\mu\mathrm{K}^2$ for kSZ. The radio source component has a spectrum shape of $D_\ell \propto \ell^2$ and amplitude of $D_{3000}^{\mathrm{radio}} = 1.01\mu\mathrm{K}^2$ at 150 GHz. The frequency spectrum for radio sources is $\nu^{-0.76}$. Gaussian foregrounds in the simulation can model the contribution to the $N_{\mathbf{L}}^{RD,0}$ bias term, which is the largest bias to the lensing power spectrum. However, Gaussian modeling of the foregrounds cannot catch their four-point power contribution to the lensing measurements, since we do not include higher-order correlations in the simulations. The four-point power from foregrounds can be estimated and subtracted later.

Besides Gaussian foregrounds, the CMB maps also contain point sources and galaxy clusters. We found point sources and galaxy clusters from the CMB data maps using simplified methods similar to [180] and [181]. The point source fluxes and the galaxy clusters' peak amplitudes are accurate within 10% and not biased after checking against previous measurements. We included detected point sources and clusters in the detected positions with the detected amplitudes and profiles in the simulated maps for all three frequencies. Reichardt et al. [176] included contributions from fainter point sources and clusters' below their detection thresholds in the Gaussian foreground spectra. Since SPT-3G detection thresholds are lower than [176], we have populated some faint detected point sources and clusters below [176]'s detection thresholds in the simulated maps. Thus we need to subtract the contributions from these sources and galaxy clusters to the foreground spectra in [176]. The point sources and clusters are the same between the data and the simulation, which allows us to use the same masks and inpainting (Section 4.2.2) for both. The final component of the simulations is instrument and sky noise similar to the data, which is generated using the method in Section 4.1.4.

After combining all components, we convolve the simulated maps at the three frequency bands with the corresponding beams reported in Section 4.1.5. We then mock-observe the simulations using the same methods used for data processing, so the mock-observed simulations will have the same filter transfer function and mode-coupling as the data maps.

We generate five sets of simulations:

- A: 500 lensed simulations with foregrounds,
- B: 160 lensed simulations with no foregrounds,
- C: 160 lensed simulations with no foregrounds and with the same realizations of lensing potential as set B, but different CMB,
- D: 500 unlensed simulations with foregrounds and the same CMB power spectrum as the lensed CMB.

A simulation from Set A is shown in Fig. 4.6. The maps have random Gaussian realizations of the CMB that are different from the CMB measurements in Fig. 4.2. But the map-processing steps are identical, so they have the same statistical properties. The point sources are in the same spots as the data.

We use all simulations in A to estimate the $N_{\mathbf{L}}^{RD,0}$ bias term and 340 simulations in A to estimate the statistical uncertainty of the lensing power spectrum. We use 160 simulations in A to estimate the mean-field bias (Section 4.2.5), with 80 sims for each of the two lensing potential estimations that form the lensing spectrum (see Eq. 4.28). All of simulation set B and C are used to calculate the $N_{\mathbf{L}}^{1}$ bias term, which is proportional to the first order of lensing power and does not depend on the foregrounds. Simulation set D can check that the lensing pipeline returns zero lensing for the unlensed maps and quantify the probability of lensing detection against the no-lensing hypothesis. The number of simulations for estimating each term is chosen such that each term sufficient converges, to not bias the lensing spectrum estimation.

We can also use the simulations to estimate the transfer function, which contains the

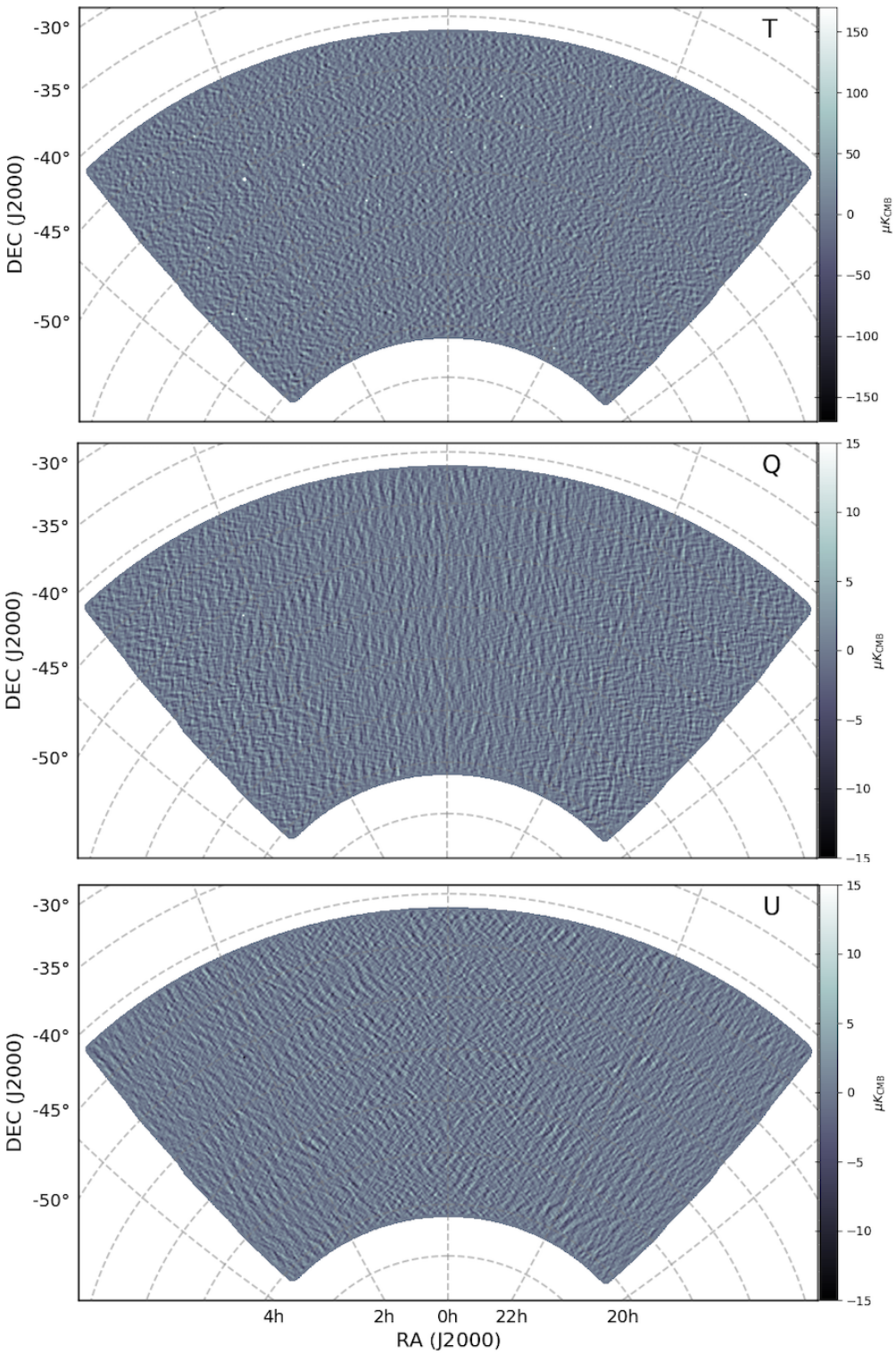


Figure 4.6: From top to bottom are the simulated temperature (T), Stokes Q, and Stokes U maps at 150 GHz. The simulated maps have the same foregrounds and noise statistics as the data. The map-making TOD filtering steps are also the same as the data. The detected point sources (bright dots in the maps) and galaxy clusters are in the same spots as the data.

filtering effects in the map-making process (Section 4.1.3). The filtering removes low and high-frequency modes along the telescope scanning direction, which causes anisotropic suppression of CMB modes at specific angular scales. We estimate the transfer function with mock-observed simulations. During a mock-observation, we have the detectors scan through a simulated map with identical pointing information as the actual observation. The simulated time-ordered-data then goes through the filtering steps in Section 4.1.3 and is made into mock-observed maps using the methods in Section 4.1.4. The transfer function is the ratio between the mock-observed map and the simulated map in Fourier space. The ratio will therefore contain filtering effects from map-making. We average the transfer functions from 160 simulations and smooth it in Fourier space to reduce the scatter. Fig. 4.7 shows the transfer functions for temperature and E-mode polarization. If the scanning (constant-declination) direction is the same as the x-direction, then high-pass filtering will generate a low-value stripe around $\ell_x = 0$. In our map projection, the scanning direction is not along the x-axis, which gives the filtering pattern in Fig. 4.7.

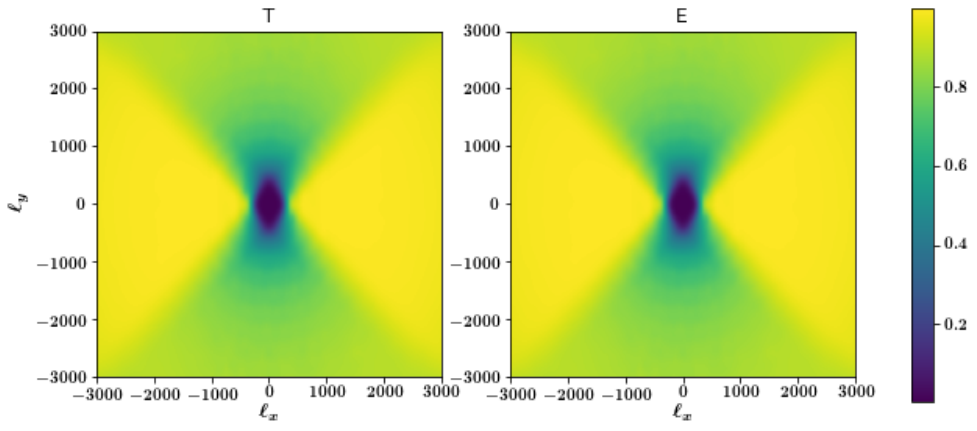


Figure 4.7: The 2D filter transfer function for temperature (T) and E-mode. The transfer function for B-mode is not shown because it's noisier and should be roughly the same as the E transfer function.

### 4.2.4 *Gravitational lensing of the CMB*

The 3D gravitational potential $\Psi$ from large scale structures deflects CMB photons as they travel through the universe. With Newtonian gauge and natural unit, the deflection angle $\boldsymbol{\alpha}$ is [182]:

$$\boldsymbol{\alpha} = -2\int_0^{\chi_*} d\chi \frac{\chi_* - \chi}{\chi_*} \nabla_\perp \Psi(\chi\hat{\mathbf{n}}; \eta_0 - \chi), \tag{4.13}$$

where $\chi$ is the comoving distance, $\chi_*$ is the source's comoving distance, and $\eta_0 - \chi$ is the conformal time when the photon was at position $\chi\hat{\mathbf{n}}$.

The lensing deflection angle can be expressed as the angular gradient of the 2D lensing potential $\phi$, $\boldsymbol{\alpha} = \nabla\phi(\hat{\mathbf{n}})$, with $\phi$ defined as:

$$\phi(\hat{\mathbf{n}}) = -2\int_0^{\chi_*} d\chi \frac{\chi_* - \chi}{\chi_*\chi} \Psi(\chi\hat{\mathbf{n}}; \eta_0 - \chi). \tag{4.14}$$

We assume weak lensing with small angular deflections, which is generally true for CMB lensing. Weak lensing remaps sources to image planes by deflecting the unlensed maps by the gradient of the projected lensing potential $\phi$. Below we take the temperature field as an example:

$$T(\hat{\mathbf{n}}) = \tilde{T}(\hat{\mathbf{n}} + \nabla\phi(\hat{\mathbf{n}})) = \tilde{T}(\hat{\mathbf{n}}) + \nabla_i\phi(\hat{\mathbf{n}})\nabla^i\tilde{T}(\hat{\mathbf{n}}) + \cdots . \tag{4.15}$$

Here $T$ is the lensed field, and $\tilde{T}$ is the unlensed field. We express Eq. 4.15 in Fourier space to gain intuition to the lensing process. $T(\hat{\mathbf{n}})$ and $\phi(\hat{\mathbf{n}})$ can be related to their Fourier transforms by:

$$\begin{aligned} T_{\boldsymbol{\ell}} &= \int d\hat{\mathbf{n}} T(\hat{\mathbf{n}}) e^{-i\boldsymbol{\ell}\hat{\mathbf{n}}} \\ \phi_{\boldsymbol{\ell}} &= \int d\hat{\mathbf{n}} \phi(\hat{\mathbf{n}}) e^{-i\boldsymbol{\ell}\hat{\mathbf{n}}} . \end{aligned} \tag{4.16}$$

We expand the lensed field $T(\ell)$ in Fourier space and only keep the first-order term in the

weak-lensing limit:

$$\begin{aligned} T_{\boldsymbol{\ell}} &= \int d\hat{\mathbf{n}} T(\hat{\mathbf{n}}) e^{-i\boldsymbol{\ell}\hat{\mathbf{n}}} \\ &\approx \int d\hat{\mathbf{n}} [\tilde{T}(\hat{\mathbf{n}}) + \nabla_i \phi(\hat{\mathbf{n}}) \nabla^i \tilde{T}(\hat{\mathbf{n}})] e^{-i\boldsymbol{\ell}\hat{\mathbf{n}}} \,, \\ &= \tilde{T}_{\boldsymbol{\ell}} - \int \frac{d\boldsymbol{\ell}_1}{2\pi} \boldsymbol{\ell}_1 (\boldsymbol{\ell} - \boldsymbol{\ell}_1) \tilde{T}_{\boldsymbol{\ell}-\boldsymbol{\ell}_1} \phi_{\boldsymbol{\ell}_1} \end{aligned} \tag{4.17}$$

which indicates that lensing can couple CMB modes at different angular scales and cause off-diagonal correlation in CMB band power covariance. The third line of Eq. 4.17 used integration by parts and the convolution theorem. The power spectrum of CMB temperature is $< \tilde{T}_{\boldsymbol{\ell}} \tilde{T}^*_{\boldsymbol{\ell}'} >_{\rm CMB} = (2\pi)^2 \delta(\boldsymbol{\ell} - \boldsymbol{\ell}') \tilde{C}^{TT}_{\ell}$. Combine with Eq. 4.17 and we have:

$$< T_{\boldsymbol{\ell}} T^*_{\boldsymbol{\ell}'} >_{\rm CMB} = [\tilde{C}^{TT}_{\ell}(\boldsymbol{\ell} \cdot \boldsymbol{L}) - \tilde{C}^{TT}_{\ell'}(\boldsymbol{\ell}' \cdot \boldsymbol{L})] \phi_{\boldsymbol{L}} = W_{\boldsymbol{\ell},\boldsymbol{\ell}'} \phi_{\boldsymbol{L}} \,, \tag{4.18}$$

where $W_{\boldsymbol{\ell},\boldsymbol{\ell}'} = \tilde{C}^{TT}_{\ell}(\boldsymbol{\ell} \cdot \boldsymbol{L}) - \tilde{C}^{TT}_{\ell'}(\boldsymbol{\ell}' \cdot \boldsymbol{L})$ and $\boldsymbol{L} = \boldsymbol{\ell} - \boldsymbol{\ell}'$ ($\boldsymbol{L} \neq \mathbf{0}$). We have used $\int g(\boldsymbol{\ell}') \delta(\boldsymbol{\ell} - \boldsymbol{\ell}') d\boldsymbol{\ell}' = g(\boldsymbol{\ell})$ in Eq. 4.18. The average is over CMB realizations and not over the large scale structure (LSS) that deflect the CMB, otherwise $\phi_{\boldsymbol{L}}$ would average to zero. Since lensing at angular scale $\boldsymbol{L}$ creates off-diagonal correlations between CMB modes differed by $\boldsymbol{L}$, we can define a weighting of the pair of CMB modes separated by $\boldsymbol{L}$ to extract the lensing potential at scale $\boldsymbol{L}$:

$$\hat{\phi}_{\boldsymbol{L}} = R^{-1}_{\boldsymbol{L}} \int \frac{d^2\boldsymbol{\ell}}{2\pi^2} F_{\boldsymbol{\ell},\boldsymbol{\ell}'} T_{\boldsymbol{\ell}} T^*_{\boldsymbol{\ell}'} \,, \tag{4.19}$$

Here $R^{-1}_{\mathbf{L}}$ is the normalization function chosen such that $< \hat{\phi}_{\boldsymbol{L}} >_{\rm CMB} = \phi_{\boldsymbol{L}}$. Hu and Okamoto [47] found the weighting $F_{\boldsymbol{l},\boldsymbol{l}'}$ that minimizes the variance $< \hat{\phi}^*_{\boldsymbol{L}} \hat{\phi}_{\boldsymbol{L}} > - < \hat{\phi}^*_{\boldsymbol{L}} >< \hat{\phi}_{\boldsymbol{L}} >$ to be $F_{\boldsymbol{l},\boldsymbol{l}'} = W_{\boldsymbol{l},\boldsymbol{l}'}/(2C^{TT}_{l} C^{TT}_{l'})$. Similarly, the minimum-variance weight functions between CMB TE, TB, EE, and EB modes can be derived [47]. Note that the primordial B-modes are small, and most of the B-modes come from lensed E-modes, so the above expansion in Eq. 4.17 do not apply to B-modes. In our lensing analysis, we include $C^{TT}_{l}$

and $C_{l'}^{TT}$ in the inverse-variance weighting $S^{-1}$ step of map-processing (Section 4.2.2) and convolve the filtered maps with the weight function $W$, which is noted as $f_\alpha(\boldsymbol{l}_1, \boldsymbol{l}_2)$ in [47]. We also use the lensed CMB spectra instead of unlensed CMB spectra in the weight function $W$ to reduce lensing bias [90].

### *4.2.5 Quadratic lensing estimation*

The unlensed CMB is a statistically isotropic Gaussian random field with zero off-diagonal covariance. Lensing breaks the statistical isotropy and introduces off-diagonal correlations across CMB temperature and polarization modes in Fourier space. Section 4.2.4 derived the covariance of CMB temperature fields with a fixed lensing field averaged over different CMB realizations. In the general case where $XY \in [TT, TE, EE, EB, TB]$, the covariance is

$$\langle X_{\boldsymbol{\ell}}\, Y^*_{\boldsymbol{\ell}'}\rangle_{\rm CMB} = \delta(\boldsymbol{\ell}-\boldsymbol{\ell}')C_l^{XY} + W^{XY}_{\boldsymbol{\ell},\boldsymbol{\ell}'}\,\phi_{\boldsymbol{\ell}-\boldsymbol{\ell}'} + \mathcal{O}(\phi^2)\,, \tag{4.20}$$

Using these off-diagonal correlations, we can estimate the inverse-variance weighted lensing potential at $\mathbf{L}$ by calculating the weighted sum of the inverse-variance filtered lensing modes separated by $\mathbf{L}$

$$\bar{\phi}^{XY}_{\mathbf{L}} = \int d^2\boldsymbol{\ell} W^{XY}_{\boldsymbol{\ell},\boldsymbol{\ell}-\mathbf{L}} \bar{X}_{\boldsymbol{\ell}}\, \bar{Y}^*_{\boldsymbol{\ell}-\mathbf{L}}\,, \tag{4.21}$$

where the weighting function is the same as $W^{XY}$ in Eq. 4.20 for minimum variance lensing estimation.

The lensing estimation contains biases from other statistically anisotropic sources unrelated to lensing, such as the map mask and anisotropic sky noise. To remove it, we estimate the mean-field (MF) bias $\bar{\phi}^{XY,\rm MF}_{\mathbf{L}}$ by averaging the lensing estimations of multiple simulations with different realizations of CMB, lensing potential, and noise.

$$\bar{\phi}^{XY,\rm MF}_{\mathbf{L}} = \int d^2\boldsymbol{\ell} W^{XY}_{\boldsymbol{\ell},\boldsymbol{\ell}-\mathbf{L}} \langle \bar{X}_{\boldsymbol{\ell}}\, \bar{Y}^*_{\boldsymbol{\ell}-\mathbf{L}}\rangle\,. \tag{4.22}$$

The lensing potentials from different simulations are independent and average zero, so the averaged lensing estimation only contains the MF bias from common non-lensing features shared among the simulations. We subtract the MF bias from $\bar{\phi}^{XY}_{\mathbf{L}}$.

### *4.2.6 Normalization and combination of lensing estimations*

We also normalize the lensing potential so they are unbiased in amplitude. The normalization function contains contributions from the weights ($W^{XY}$) used to convolve the filtered CMB fields, and the approximated inverse-variance filters $\mathcal{F}^X$ for the CMB fields. We also call the normalization function the lensing response because it is the Fisher matrix for the lensing potential estimation $\phi^{XY}_{\mathbf{L}}$. The analytical normalization function, or response, takes the form of

$$\mathcal{R}^{XY,\mathrm{Analytic}}_{\mathbf{L}} = \int d^2\boldsymbol{\ell}\, W^{XY}_{\boldsymbol{\ell},\boldsymbol{\ell}-\mathbf{L}} \times W^{XY}_{\boldsymbol{\ell},\boldsymbol{\ell}-\mathbf{L}} \mathcal{F}^X_{\boldsymbol{\ell}} \mathcal{F}^Y_{\boldsymbol{\ell}-\mathbf{L}}\,. \tag{4.23}$$

Here $\mathcal{F}^X_{\boldsymbol{\ell}} X_{\boldsymbol{\ell}} = [C^{XX}_{\boldsymbol{\ell}} + C^{NN}_{\boldsymbol{\ell}}]^{-1} X_{\boldsymbol{\ell}}$ is the approximation of the inverse-variance filtering (Section 4.2.2), and the approximation is accurate when $n = 0$ and $C^{NN}_{\boldsymbol{\ell}}$ captures all anisotropic noise. For the general case with anisotropic noise that $C^{NN}_{\boldsymbol{\ell}}$ does not capture or when $n \neq 0$, we apply an MC response correction $\mathcal{R}^{XY,\mathrm{MC}}_{\mathbf{L}}$ to account for the deviation from this approximation. We divide the cross-spectrum between the estimated lensing potential and the input lensing potential by the input auto-spectrum and average this ratio over many simulation realizations to get the MC response. MC here indicates the term is from the difference between the amplitude in simulations and the input.

$$\mathcal{R}^{XY,\mathrm{MC}}_{\mathbf{L}} = \frac{\langle \hat{\phi}^{XY'}_{\mathbf{L}}\, \phi^{I*}_{\mathbf{L}} \rangle}{\langle \phi^{I}_{\mathbf{L}} \phi^{I*}_{\mathbf{L}} \rangle} \tag{4.24}$$

Here $\phi^I$ is the input lensing potential, $\hat{\phi}^{XY'}_{\mathbf{L}}$ is the estimated lensing potential with mean-field subtraction and analytical response normalization:

$$\hat{\phi}^{XY'}_{\mathbf{L}} = \frac{1}{\mathcal{R}^{XY,\mathrm{Analytic}}_{\mathbf{L}}}(\bar{\phi}^{XY}_{\mathbf{L}} - \bar{\phi}^{XY,\mathrm{MF}}_{\mathbf{L}}) \tag{4.25}$$

We use a hat ($\hat{\phi}$) to denote debiased estimation, and a cross-bar ($\bar{\phi}$) to denote inverse-variance weighted estimation. We average over the analytical response within annuli in Fourier space to reduce the noise and get $\mathcal{R}^{XY,\mathrm{MC}}_{L} = \langle \mathcal{R}^{XY,\mathrm{MC}}_{\mathbf{L}} \rangle$. The full response is

$$\mathcal{R}^{XY}_{\mathbf{L}} = \mathcal{R}^{XY,\mathrm{MC}}_{L} \mathcal{R}^{XY,\mathrm{Analytic}}_{\mathbf{L}} \,, \tag{4.26}$$

and the lensing potential with the full correction is

$$\hat{\phi}^{XY}_{\mathbf{L}} = \frac{1}{\mathcal{R}^{XY}_{\mathbf{L}}}(\bar{\phi}^{XY}_{\mathbf{L}} - \bar{\phi}^{XY,\mathrm{MF}}_{\mathbf{L}}) \,. \tag{4.27}$$

To reduce the noise in individual lensing estimators, we add them with proper weighting to obtain minimum-variance (MV) lensing estimator and polarization-only (POL) estimator. The weight used to combine them is just the response function $\mathcal{R}^{XY}_{\mathbf{L}}$. Therefore, the weighted sum is the sum of inverse-variance weighted lensing estimators, which, with the mean-field subtraction, takes the form of $\sum_{XY}(\bar{\phi}^{XY}_{\mathbf{L}} - \bar{\phi}^{XY,\mathrm{MF}}_{\mathbf{L}})$, where $XY$ goes over TT, TE, EE, EB, and TB for the MV estimator. Note that we omitted the BB estimator because the primordial B-mode is very small, and the B-mode signal from the lensing of E-mode is linear in $\phi$, which makes the BB estimator weight function second-order in $\phi$ and thus negligible compared to other estimators. For the POL estimator, $XY$ includes EE and EB. We correct the weighted sum of all estimators first by the analytical response, which is the sum of individual estimators' analytic response functions: $R^{\mathrm{Analytic}}_{\mathbf{L}} = \sum_{XY}(R^{XY,\mathrm{Analytic}}_{\mathbf{L}})$. We then apply the MC response $R^{MC}_{L}$correction, which is calculated by crossing the combined lensing

estimation by the input lensing potential and dividing the input lensing auto-spectrum.

We plot the MV mean-field spectra for 95, 150, and 220 GHz in Fig. 4.8. The 150 GHz mean-field spectrum is lower than the theoretical lensing spectrum for most of the $L$ range we report. The 95 and 220 GHz mean-field spectra are higher than 150 GHz due to higher noise plus foreground.

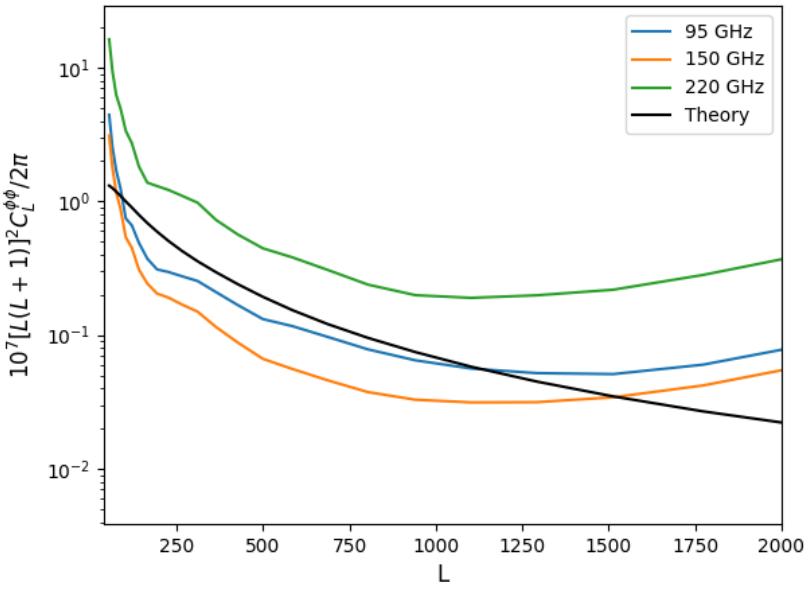


Figure 4.8: MV mean-field spectra for 95, 150, and 220 GHz. The solid line is the theoretical lensing spectrum.

### *4.2.7 Lensing power spectrum and its biases*

We can calculate the lensing power spectrum with the debiased lensing potentials $\hat{\phi}^{XY}$ and $\hat{\phi}^{UV}$, where $XY, UV \in [TT, TE, EE, EB, TB]$. The two lensing potentials can also be MV or POL combinations. Since we apply a border apodization and point source mask to the four $XYUV$ maps entering the lensing estimation, we need to divide out a masking factor

$f_{\rm Mask}$, which is the average of the mask applied to a single map to the fourth.

$$C_{\mathbf{L}}^{\hat{\phi}^{XY}\hat{\phi}^{UV}} = f_{\rm Mask}^{-1}\langle\hat{\phi}_{\mathbf{L}}^{XY}\ \hat{\phi}^{*}{}_{\mathbf{L}}^{UV}\rangle \tag{4.28}$$

However, the above lensing power spectrum is biased because the lensing spectrum is the integral of a four-point correlation function that includes spurious correlations among the CMB fields. According to Wick's theorem, a four-point correlation $\langle XYUV\rangle_{\rm CMB,LSS}$ averaged over CMB and large scale-structure (LSS) realizations includes three pairs of two-point contractions

$$\begin{aligned}\langle XYUV\rangle_{\rm CMB,LSS} =&\langle\langle XY\rangle_{\rm CMB}\langle UV\rangle_{\rm CMB}\rangle_{\rm LSS} + \langle\langle XU\rangle_{\rm CMB}\langle YV\rangle_{\rm CMB}\rangle_{\rm LSS}\\ &+ \langle\langle XV\rangle_{\rm CMB}\langle YU\rangle_{\rm CMB}\rangle_{\rm LSS}.\end{aligned} \tag{4.29}$$

Here the average over the CMB gives lensing-induced correlations, and the average over LSS yields the lensing spectrum. In our analysis, we only have one sky with one realization of CMB and LSS. Therefore, the results will contain sample variance. The sample variance will reduce at higher angular multipoles, where we have more modes to average into the 1D power spectrum. We can expand the two-point contractions similarly to Eq. 4.18 and neglect second order terms proportional to $\phi^2$. Only the first contraction $\langle\langle XY\rangle_{\rm CMB}\langle UV\rangle_{\rm CMB}\rangle_{\rm LSS}$ contains the unbiased lensing power spectrum $\hat{C}_L^{\phi\phi}$, and the other two contractions lead to biases. After expanding the two-point contractions in Taylor series of $\phi$, we can demonstrate that the latter two terms in Eq. 4.29 contain bias power to the zeroth order of lensing spectrum $N^0$ and the first order of lensing spectrum $N^1$. $N^0$ comes from the Gaussian (two-point) correlation in the input fields, while $N^1$ is from the four-point power. We can also expand Eq. 4.29 further to the second order in $\phi$ and estimate the $N^2$ bias to the second-order of the lensing spectrum. We reduce the $N^2$ bias by using the lensed CMB spectra in the lensing estimators [90] instead of the unlensed ones in [47]. Higher-order bias

terms are small and not considered.

We estimate the $N^0$ and $N^1$ bias terms with simulations. Since $N^0$ bias contains Gaussian correlations, we use simulations with CMB, foregrounds, and noise components that have the same Gaussian power spectrum as the data. $N^0$ is estimated using

$$N^0_{\mathbf{L}} = \left\langle C^{\hat{\phi}\hat{\phi}}_{\mathbf{L}}[\bar{X}_{\rm MC}, \bar{Y}_{\rm MC'}, \bar{U}_{\rm MC}, \bar{V}_{\rm MC'}] + C^{\hat{\phi}\hat{\phi}}_{\mathbf{L}}[\bar{X}_{\rm MC}, \bar{Y}_{\rm MC'}, \bar{U}_{\rm MC'}, \bar{V}_{\rm MC}] \right\rangle_{\rm MC,MC'}, \tag{4.30}$$

where $C^{\hat{\phi}\hat{\phi}}_{\mathbf{L}}[\bar{X}_{\rm MC}, \bar{Y}_{\rm MC'}, \bar{U}_{\rm MC}, \bar{V}_{\rm MC'}]$ is the lensing cross spectrum between two unbiased lensing potentials $\hat{\phi}^{XY}$ and $\hat{\phi}^{UV}$. $MC$ and $MC'$ denote simulations with different realizations of the CMB, foreground, and lensing potential. Therefore, in the above equation, only the Gaussian correlations between fields with the same subscript ($MC$ or $MC'$) are non-zero. The two terms in Eq. 4.30 correspond to Gaussian correlations in the latter two contractions in Eq. 4.29. The $N^0_{\mathbf{L}}$ estimated this way can be inaccurate, because the data may have slightly different Gaussian power from the simulations depending on the simulation modeling and realization. To reduce the bias caused by the difference, we adopt a realization-dependent $N^{RD,0}_{\mathbf{L}}$ [183] defined by

$$\begin{aligned} N^{RD,0}_{\mathbf{L}} = & \\ & \Big\langle + C^{\hat{\phi}\hat{\phi}}_{\mathbf{L}}[\bar{X}_{\rm d}, \bar{Y}_{\rm MC}, \bar{U}_{\rm d}, \bar{V}_{\rm MC}] + C^{\hat{\phi}\hat{\phi}}_{\mathbf{L}}[\bar{X}_{\rm MC}, \bar{Y}_{\rm d}, \bar{U}_{\rm d}, \bar{V}_{\rm MC}] \\ & + C^{\hat{\phi}\hat{\phi}}_{\mathbf{L}}[\bar{X}_{\rm d}, \bar{Y}_{\rm MC}, \bar{U}_{\rm MC}, \bar{V}_{\rm d}] + C^{\hat{\phi}\hat{\phi}}_{\mathbf{L}}[\bar{X}_{\rm MC}, \bar{Y}_{\rm d}, \bar{U}_{\rm MC}, \bar{V}_{\rm d}] \\ & - N^0_{\mathbf{L}} \Big\rangle_{\rm MC,MC'} \quad , \end{aligned} \tag{4.31}$$

where $d$ denotes the data. In $N^{RD,0}_{\mathbf{L}}$, we calculate the lensing spectra from lensing potentials estimated using both the data and simulation. We then subtract $N^0_{\mathbf{L}}$ bias defined in Eq. 4.30. This method also suppresses off-diagonal contributions to the covariance of the lensing power spectrum.

The $N^1_{\mathbf{L}}$ bias term is from connected contributions to the trispectrum and is estimated

using simulations with the same lensing field but different CMB realizations. $N^1_{\mathbf{L}}$ is

$$\begin{aligned} N^1_{\mathbf{L}} = & \\ & \Big\langle + C^{\hat{\phi}\hat{\phi}}_{\mathbf{L}}[\bar{U}_{\phi^1,\mathrm{MC}}, \bar{V}_{\phi^1,\mathrm{MC}'}, \bar{X}_{\phi^1,\mathrm{MC}}, \bar{Y}_{\phi^1,\mathrm{MC}'}] \\ & + C^{\hat{\phi}\hat{\phi}}_{\mathbf{L}}[\bar{U}_{\phi^1,\mathrm{MC}}, \bar{V}_{\phi^1,\mathrm{MC}'}, \bar{X}_{\phi^1,\mathrm{MC}'}, \bar{Y}_{\phi^1,\mathrm{MC}}] \\ & - N^0_{\mathbf{L}} \Big\rangle_{\mathrm{MC},\mathrm{MC}'} , \end{aligned} \tag{4.32}$$

where $\phi^1$ indicates that the simulations share the same lensing field. Fields with subscripts $MC$ and $MC'$ have different CMB realizations, and the correlation between them averages zero. The first two terms contain $N^0_{\mathbf{L}}$ bias from Gaussian power and the $N^1_{\mathbf{L}}$ bias from the shared lensing potential among the four fields. We subtract $N^0_{\mathbf{L}}$ bias from the first two terms to get the $N^1_{\mathbf{L}}$ bias.

The debiased lensing spectrum after N0 and N1 correction is

$$\hat{C}^{\phi\phi}_{\mathbf{L}} = C^{\hat{\phi}\hat{\phi}}_{\mathbf{L}} - N^{RD,0}_{\mathbf{L}} - N^1_{\mathbf{L}} \,. \tag{4.33}$$

We define another bias term called MC bias that includes any other corrections not considered yet. The MC bias is the difference between the averaged debiased lensing spectra from random simulation realizations and the input theory lensing power spectrum:

$$\Delta C^{\phi\phi}_{\mathbf{L},\mathrm{MC}} = \langle \hat{C}^{\phi\phi}_{\mathbf{L},\mathrm{MC}} \rangle - C^{\phi\phi}_{\mathbf{L},\mathrm{Theory}}. \tag{4.34}$$

The MC bias can be additive or multiplicative. Wu et al. [64] found their MC bias mostly come from higher-order coupling from the point source masks and have a multiplicative nature. However, our current dominant sources for MC bias are likely 4-point power from point sources, galaxy clusters, filtering wings, and low-frequency noise, which are additive. We treat our MC bias as an additive correction here and are currently investigating this term further. A more thorough study of the MC bias sources can lead to a more confident

lensing power spectrum measurement [64]. The MC bias is typically small compared to the measurement's error bars in other analyses [62] when the bias term modeling is accurate, and the contamination is low. In Fig. 4.9, our MC bias in 150 GHz is relatively insignificant. The MC bias at 95 GHz is slightly higher, and the MC bias at 220 GHz is fractionally large compared to the theory curve. We expect to reduce this term with better data processing and bias modeling discussed in Section 4.2.10.

We show the bias terms for 95, 150, and 220 GHz minimum-variance lensing measurements in Fig. 4.9. The bias terms we plot include the $N^{RD,0}_{\mathbf{L}}$, $N^{1}_{\mathbf{L}}$, and $\Delta C^{\phi\phi}_{\mathbf{L},\mathrm{MC}}$ (MC bias) defined above. We plot the theoretical lensing power spectrum in black for comparison. We also add individual bias terms and plot the total bias in green. The total bias is an estimate of the noise in the lensing measurements. We can measure per-mode lensing signal with larger-than-one signal-to-noise at the angular scales where the theory line is above the total bias (see [89] Eq. 24). From Fig. 4.9, the lensing modes have greater-than-unity signal-to-noise at $L \lesssim 120$ for 95 GHz and $L \lesssim 160$ for 150 GHz. These angular scales roughly correspond to 1.5 and 1.1 degrees . Therefore, with one-degree beam smoothing, the 95 and 150 GHz lensing maps in Fig. 4.17 are mostly lensing features with larger-than-unity signal-to-noise. All lensing modes in 220 GHz have less-than-unity signal-to-noise because the total bias is always higher than the theory curve for 220 GHz.

### *4.2.8 Power spectra binning*

Now we have the debiased lensing power spectrum in 2D Fourier space (or spherical harmonic space for curved sky coordinates), we need to bin it into larger angular multipole bins. To save disk space, we first bin the lensing spectra to 1D with a angular multipole space of $\Delta L = 1$ before saving the spectra. The first-stage binning averages the 2D Fourier modes within the $\Delta L = 1$ annuli to get a 1D power spectrum $\hat{C}^{\phi\phi}_{L}$, which has spectral values for each integer $L$. Then we calculate the averaged power spectrum values for a larger angular

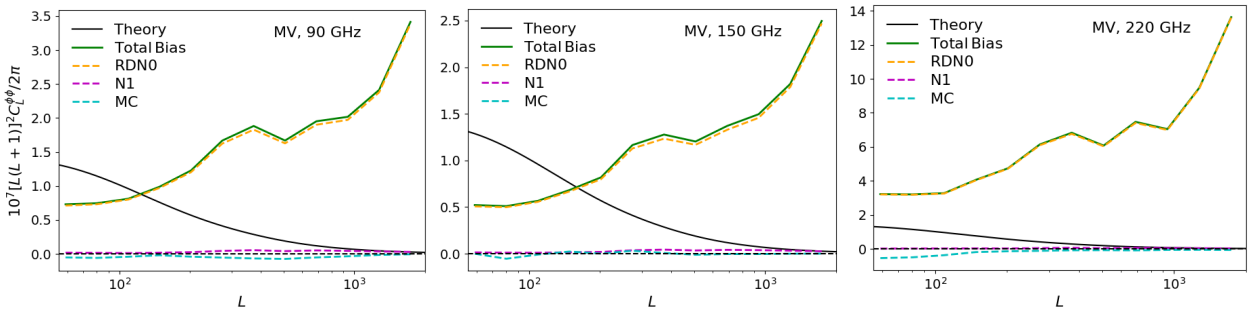


(a) 95 GHz (b) 150 GHz (c) 220 GHz

Figure 4.9: The lensing spectrum biases for 95, 150, and 220 GHz. We plot the $N_{\mathbf{L}}^{RD,0}$, $N_{\mathbf{L}}^{1}$, and MC biases, all of which are corrections terms subtracted from the raw lensing spectra. The $N_{\mathbf{L}}^{RD,0}$ bias term from the disconnected contribution to lensing four-point power dominates over other bias contributions. The $N_{\mathbf{L}}^{1}$ bias from connected term in lensing four-point power is much smaller in amplitude. We also plot the theory lensing spectrum in black for comparison. The sum of all bias terms is the total bias. Regions where the total bias is lower than the theory curve have larger-than-one per-mode signal-to-noise.

multipole bin $b$. A naive averaging is not optimal because the modes within each bin $b$ can have different signal-to-noise. We calculate the weighted average for each bin based on the variance:

$$C_b^{\phi\phi} \equiv \frac{\sum_{L\in b} w_L \hat{C}_L^{\phi\phi}}{\sum_{L\in b} w_L}, \tag{4.35}$$

where $w_L = C_{L,\mathrm{Theory}}^{\phi\phi}/\mathrm{Var}(\hat{\mathrm{C}}_{\mathrm{L}}^{\phi\phi})$. The variance for $\hat{C}_L^{\phi\phi}$ is from the distribution of simulation results with the same settings. We calculate the binned theory power $C_{b,\mathrm{Theory}}^{\phi\phi}$ also using Eq. 4.35 and define $C_b^{\phi\phi}/C_{b,\mathrm{Theory}}^{\phi\phi}$ as the lensing amplitude $A_b$ in bin $b$. The measured lensing power at the bin center $L_b$ is $\hat{C}_{L_b}^{\phi\phi} = A_b \hat{C}_{L_b,\mathrm{Theory}}^{\phi\phi}$, where $\hat{C}_{L_b,\mathrm{Theory}}^{\phi\phi}$ is the theory power at bin center $L_b$. The full dataset's lensing amplitude is defined the same way, with one single bin covering all the angular scales.

### *4.2.9 Lensing reconstructions from noiseless simulations*

We need to validate our lensing reconstruction pipeline on simulations before using it on the data. The first set of tests we did are on lensed CMB simulations without noise and

mock-observation. We first generate Gaussian realizations of unlensed CMB maps and large-scale structures following the power spectra from Planck 2015's `plikHM_TT_lowTEB_lensing` cosmology [184]. We then deflect the unlensed CMB with the large scale structure to form the lensed CMB. We run our lensing reconstruction pipeline on the lensed CMB and reconstruct the underlying large scale structure. The lensing reconstruction steps include inverse-variance filtering the maps and convolving the maps' filtered Fourier modes with the weight functions in Fourier space. We also performed mean-field bias correction and normalization. Fig. 4.10(a) and Fig. 4.10(b) are the simulated and reconstructed large-scale structure maps for one simulation realization. In the two figures, we plot the lensing convergence $\kappa$, the Laplacian of the lensing potential $\kappa = -1/2\,\nabla^2\phi$, which represents the projected 2D matter density in the universe. The two maps' features match well, indicating that our lensing reconstruction pipeline can recover the lensed CMB maps' underlying matter distribution.

We can quantify the agreement between the lensing reconstruction and the lensing input in the power spectrum space. Fig. 4.11 plots the minimum-variance combined (see Section 4.2.6) lensing power spectra extracted from 400 lensed CMB simulation realizations (gray lines). The lensing spectra are normalized by $\mathcal{R}_{\mathbf{L}}^{XY}$ following Section 4.2.6 and corrected for $N_{\mathbf{L}}^{RD,0}$ and $N_{\mathbf{L}}^{1}$ biases using the methods in Section 4.2.7 . We also overplot the simulation average (red dots) and the input theoretical lensing spectrum for generating the lensed CMBs (black line). The extension of gray curves in the background represents the statistical uncertainty among the simulations, which includes noise variance and sample variance in the lensing reconstruction. The averaged lensing spectrum of all simulations agrees with the theory input spectrum within 4%, which is well within the statistical uncertainty. To further improve the agreement, we can improve the convergence of the bias terms and normalization using more simulations. We can also explore ways to improve the accuracy of bias term estimations, such as using the cosmology that agrees with the data better to generate simulations used for estimating the bias terms. The tests performed here have demonstrated the lensing

analysis pipeline can reconstruct the lensing map and lensing spectrum that agrees with the input theory within the statistical uncertainty. However, the simulations used here does not contain noise and have different statistics from the actual CMB measurements. Therefore, we will test the pipeline further in the next section with mock-observed simulations that have more similar statistics to the CMB maps.

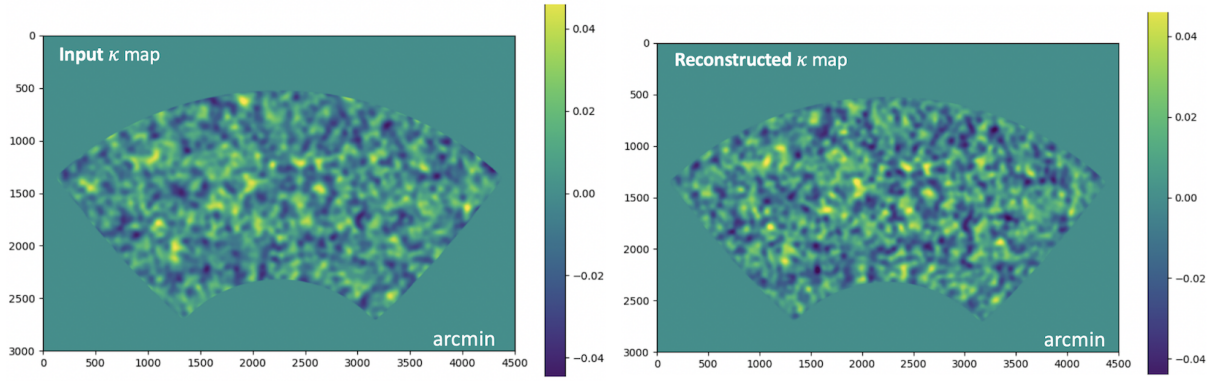


(a) Input $\kappa$ (b) Reconstructed $\kappa$

Figure 4.10: (a)Input $\kappa$ map for simulating the lensed CMB maps. (b) Reconstructed $\kappa$ map from the lensed CMB maps. The features in the two figures match well, which indicates our lensing reconstruction pipeline works.

### *4.2.10 Lensing reconstructions from mock-observed simulations*

We generate mock-observed simulations following the procedures in Section 4.2.3. These simulations have the same foregrounds, noise properties, and map-making filtering processes as the data, so they have the same statistical properties as the data maps. The statistical uncertainty and biases from lensing reconstructions of mock-observed simulations will inform us of the pipeline's performance on CMB data. We start by comparing the input lensing convergence $\kappa$ map and the reconstructed $\kappa$ map. Fig. 4.12 is the input $\kappa$ map, and Fig. 4.13 is the reconstructed minimum-variance combined $\kappa$ maps for the 95, 150, and 220 GHz frequency bands. We have smoothed all the maps with a 1 deg beam to show the large-scale modes at $L$ smaller than $\sim$180, where the per-mode signal-to-noise for 95 and 150 GHz is

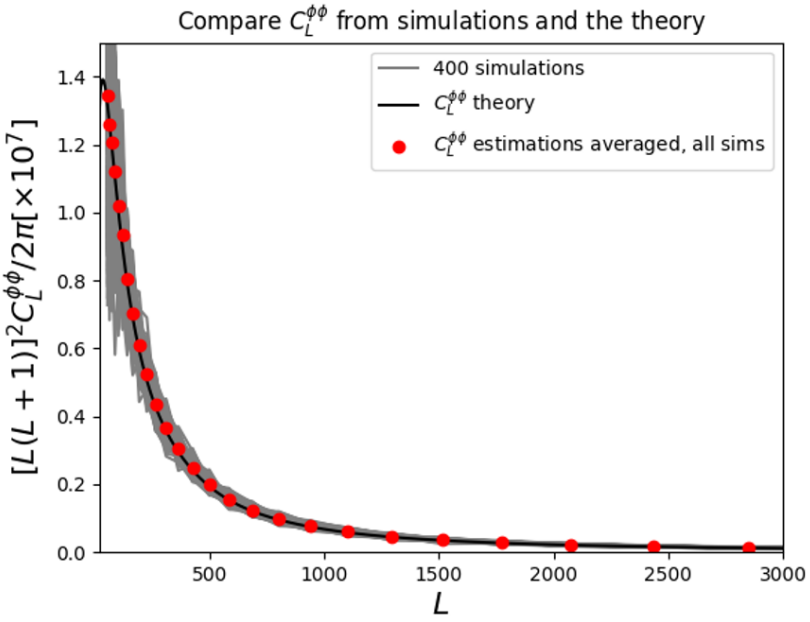


Figure 4.11: Reconstructed lensing spectra vs. theory lensing spectrum. Gray lines in the background are reconstructed lensing spectra from 400 lensed CMB simulations, and their average are the red dots. The theory lensing spectrum is in black. The averaged reconstructed lensing spectra agree well with the theory curve.

$\gtrsim 1$. The large-scale features in the input and reconstructed maps agree well. The 150 GHz reconstruction has the highest signal-to-noise due to lower map noise and follows the input lensing map more closely than the other two frequency bands. The 95 GHz map noise is slightly higher, and the 220 GHz map noise is much worse (Fig. 4.3). The $\kappa$ maps from the three frequency bands agree with each other visually, though different bands have different noise features. Despite of the high noise fluctuations in the 220 GHz reconstruction, we can see common lensing features shared between the input and the 220 GHz reconstruction. We quantify the lensing reconstruction's agreement with input theory and the lensing amplitude for the three frequency bands in power spectrum space.

The minimum-variance combined lensing spectra for the three frequency bands are in Fig. 4.14. The data points are the averaged lensing spectra reconstructed from 320 simulation realizations, and the statistical uncertainty is the standard deviation among 320 simulation

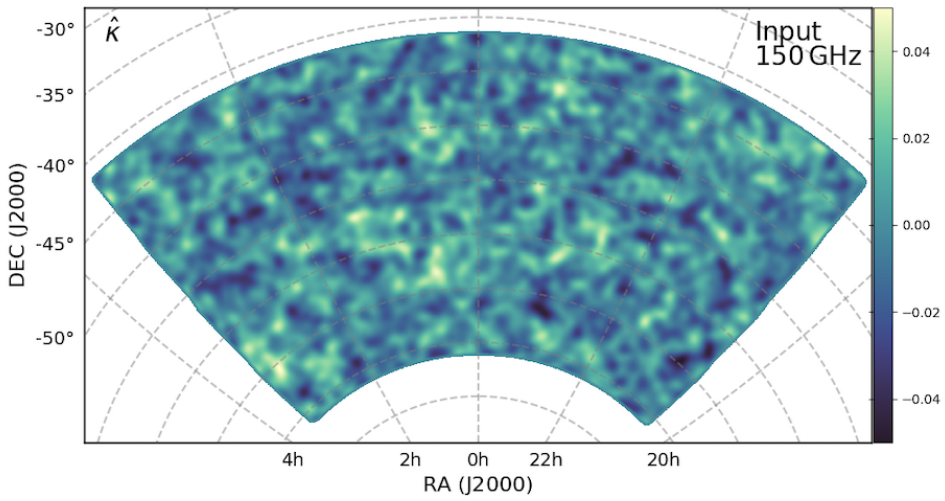


Figure 4.12: The input $\kappa$ map for generating the lensed CMB simulation.

reconstructions. The uncertainties contains both the sample and noise variances in the lensing reconstructions. We calculated the lensing amplitude using the method in Section 4.2.8. The black line is the theory lensing spectrum curve for generating the simulations, and the averaged lensing power reconstructed from the simulations should approximate the theory curve. The averaged 150 GHz spectrum is close to the input theory, while the 95 and 220 GHz spectra are biased more. The difference between averaged simulation spectra and the theory is the MC bias. Note that the lensing spectra in Fig. 4.14 is only corrected for $N_{\mathbf{L}}^{RD,0}$ and $N_{\mathbf{L}}^{1}$, and not corrected for the MC bias.

To locate the sources for the MC bias of 95 and 220 GHz spectra, we plot the mean-field maps for the three frequency bands. The mean-field is the lensing reconstruction averaged over many simulation realizations (see Section 4.2.5) so that the lensing features average out. The remaining structures in the mean-field map are from shared features in all simulations, such as gradients around the mask and filtering artifacts around the bright point sources. Regions with high inhomogeneous noise that do not average to a negligible level will also remain in the mean-field.

We have found several causes for the biases in the 95 and 220 GHz lensing spectra by studying their mean-fields and performing related tests. Fig. 4.15 shows the mean-fields for

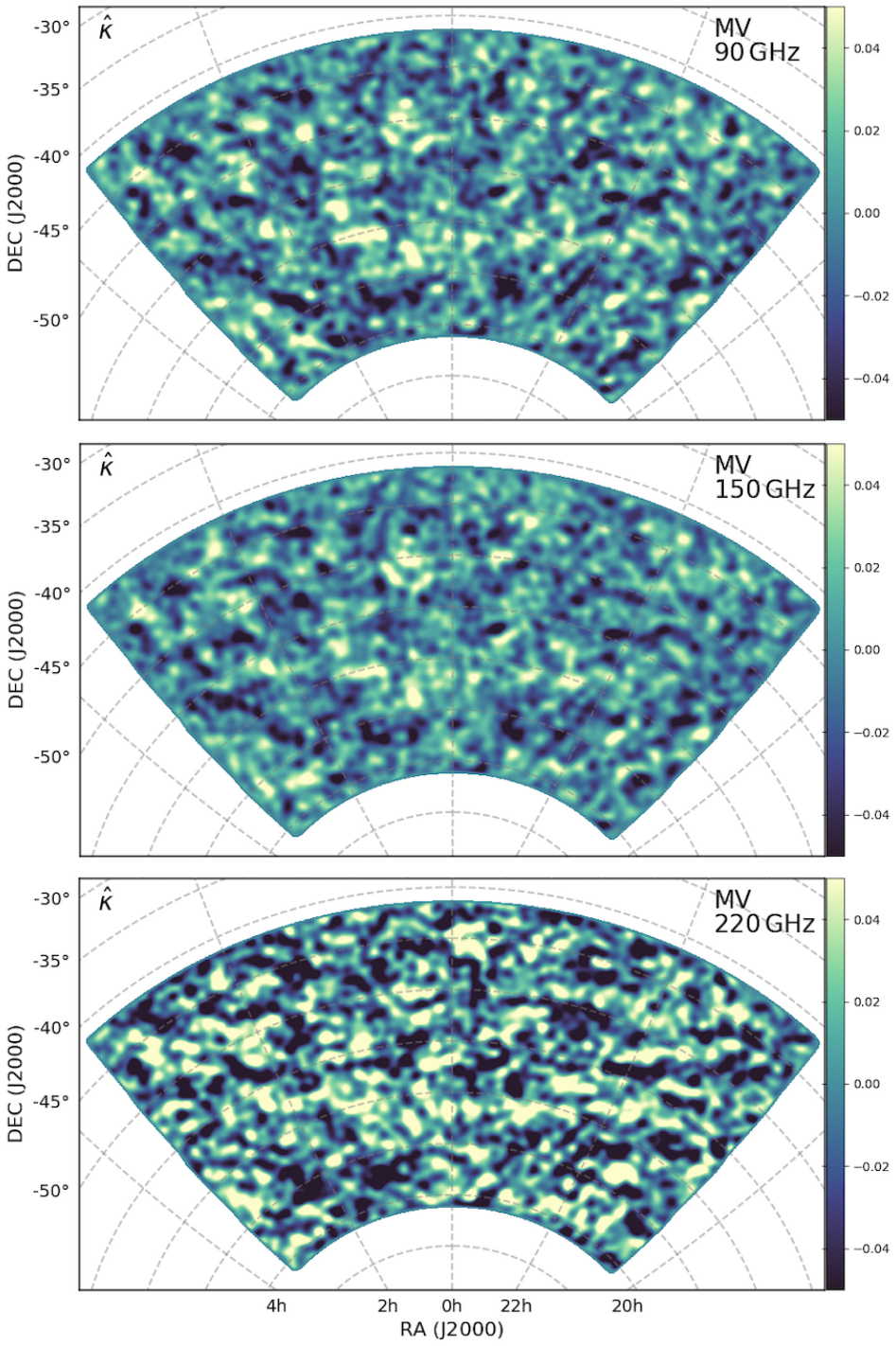


Figure 4.13: The reconstructed $\kappa$ maps from mock-observed CMB maps. From top to bottom are 95, 150, and 220 GHz reconstructions. 95 and 150 GHz $\kappa$ maps have similar noise levels. 220 GHz is much noisier than the other two bands.

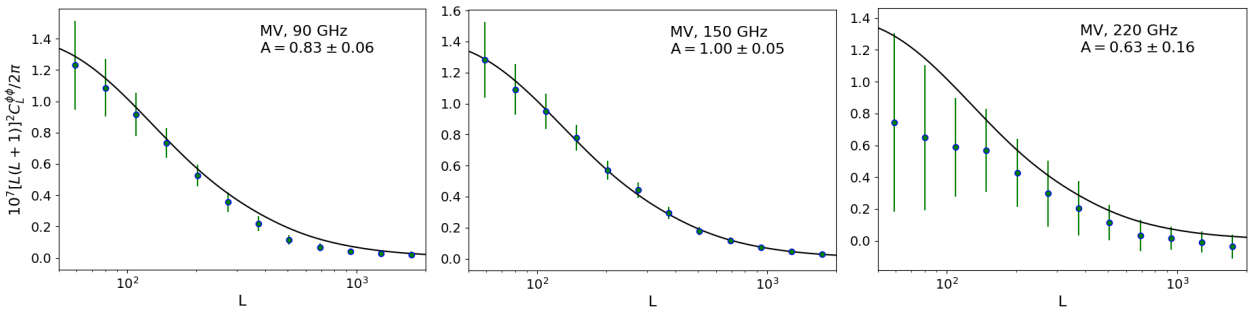


(a) 95 GHz (b) 150 GHz (c) 220 GHz

Figure 4.14: Reconstructed lensing spectra for 95, 150, and 220 GHz. The dots are averaged and binned spectra for 320 simulation realizations. The uncertainty comes from the standard deviation of the 320 simulations. 150 GHz spectrum is close to the theory curve, while 95 and 220 GHz spectra are more biased. The causes of the biases are discussed in this section.

the three frequency bands. The mean-field maps have structures around the point source masking holes, which generates gradients around the masking edges shared by all simulations. Two other prominent features are the bright short lines along the telescope scanning direction in the 95 GHz mean-field and the large-scale fluctuations in the 220 GHz mean-field. The bright lines in 95 GHz are from high-pass filtering around bright point sources or high significance clusters while making the maps. The solution is to mask out point sources and galaxy clusters during the time-ordered data filtering process. Our current masking threshold of 50 mJy source flux at 150 GHz is not enough, and we need to decrease this threshold. We can also mask or inpaint along the scanning direction around point sources and galaxy clusters to cover the filtering wings. However, this solution will unnecessarily inpaint or cut out too much map area and reduce the signal-to-noise. The current inpaint and mask area is $\sim 2\%$ of the field size. The filtering wings extend about ten times the source or cluster's diameter and cover $\sim 20\%$ of the field size. The large-scale features in 220 GHz are from low-frequency noise in the CMB maps that are not filtered away by the high-pass filter. The solution is to implement harsher filtering on time-ordered data or remove the noisy modes in Fourier space. Some fine-tuning of the filtering scheme is needed. The noisy structures are mostly along the scanning direction or constant-declination, but they are not along the

x-direction due to the projection distortion. One way to cut low-frequency noise modes along the scan direction is to reproject our map into the sinusoidal projection such that the noise features are along the x-axis in Fourier space. Then we can remove the low $\ell_x$ modes in Fourier space and project the cleaned map back to the original map projection. We can also try removing particularly noisy CMB observations from the coadded map.

We have performed several tests that indicate better treatments of the point sources, galaxy clusters, their filtering wings, and the low-frequency noise can help reduce the MC bias. We have found that removing the point source apodization mask increased the MC bias, which suggests that harsher source masking can help. We also tested harsher noise filtering by removing $\ell_x < 1000$ modes for 220 GHz and successfully reduced the MC bias level in 220 GHz lensing spectra. While these tests are not conclusive yet, they suggest the treatments mentioned above will likely reduce the MC bias.

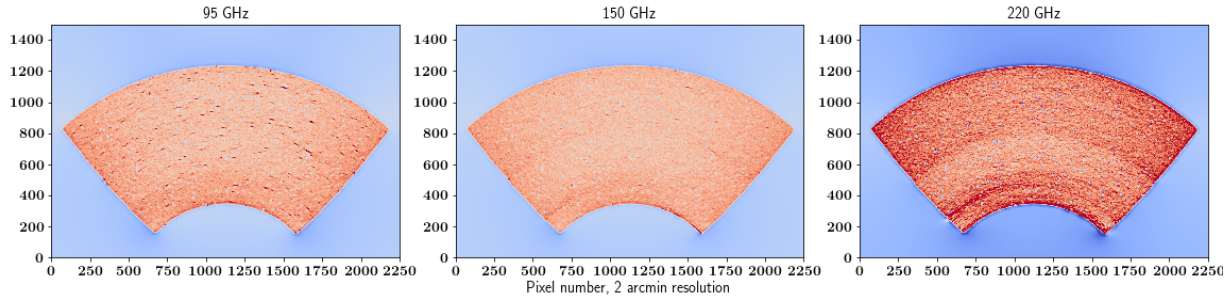


Figure 4.15: The mean-fields from the TT estimator for the 95, 150, and 220 GHz frequency bands. 150 GHz mean-field is the cleanest. 95 GHz is contaminated by high-pass filtering wings around point sources, and 220 GHz is contaminated by large-scale noise features that do not average down.

The 150 GHz mean-field is better-behaved because the low-frequency noise is not as high as in 220 GHz, and the point sources and galaxy clusters are fainter than 95 GHz. With lower bias sources, the reconstructed lensing power spectrum for 150 GHz is less biased (Fig. 4.14). Fixing the biases in lensing spectra is the next analysis step. For now, we assume the data and the simulation share the same additive (MC) bias and correct the data by the MC

bias.

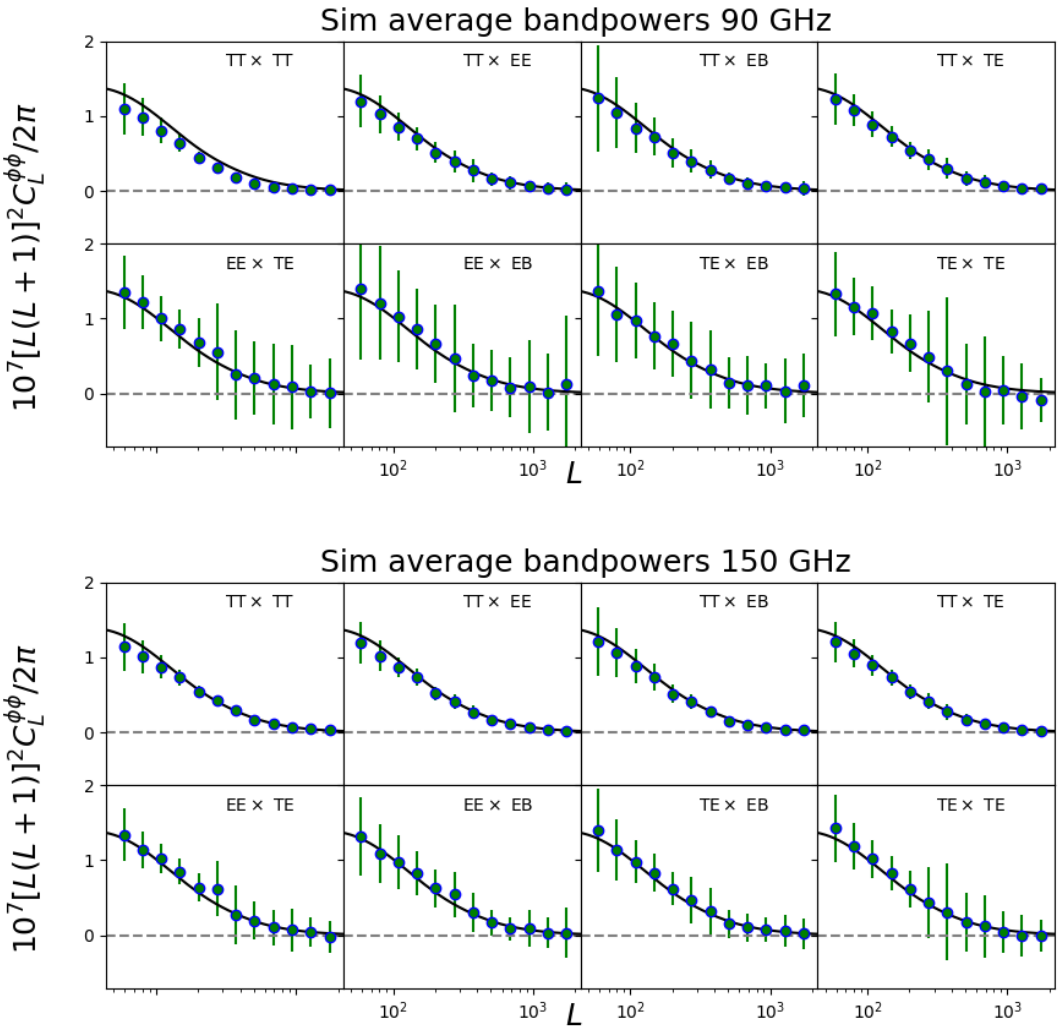


Figure 4.16: Top: 95 GHz lensing spectra from eight high signal-to-noise lensing estimators. Bottom: 150 GHz lensing spectra from eight high signal-to-noise lensing estimators. The 150 GHz estimators are less noisy and less biased, especially for the TT×TT estimator.

The lensing power spectrum is a four-point correlation function because we use two CMB fields to estimate the lensing potential and two lensing maps to estimate the lensing spectrum. The four CMB fields entering the lensing spectrum can be T, E, or B, forming many estimators. The complete list of lensing spectrum estimators is TT×TT, EE×EE, TE×TE, TB×TB, EB×EB, TT×EE, TT×EB, TT×TE, EE×TE, EE×EB, TE×EB, TT×TB, EE×TB,

EB×TB, and TE×TB. We neglect estimators containing BB because of the low signal level. The lensing spectra from individual lensing estimators can give insight into each estimator's signal-to-noise and the bias sources. Fig. 4.16 top and bottom are the lensing spectra from eight high-signal-to-noise estimators for 95 and 150 GHz. We do not show 220 GHz plots because they are noisy and do not contribute too much to the overall signal-to-noise. Most of the lensing signal-to-noise comes from the TT×TT estimator, and we need to reduce the bias in TT×TT by subtracting bias estimations or tuning the analysis steps using methods mentioned above. In the future, CMB polarization will dominate the signal-to-noise in lensing reconstruction, and the lensing bias from foregrounds and low-frequency noise will be less of a concern for CMB polarization.

### *4.2.11 Preliminary results from SPT-3G data*

From the simulation tests, we are confident about the lensing maps, while the spectrum results are preliminary because work is ongoing to understand and remove the sources of extra MC biases. The MC bias is small at 150 GHz (see Fig. 4.14), where we have the most precise lensing measurements. The MC bias is slightly higher at 95 GHz and more visible at 220 GHz. We have discussed the sources of the biases and their removal in Section 4.2.10. We report the significance of our lensing measurements from their statistical uncertainty here. We will report the lensing amplitudes of the data after all other sources of the MC biases are accounted for, and the correction from them is small for 95 GHz and 150 GHz.

Fig. 4.17 shows the minimum-variance lensing convergence $\kappa$ map extracted from the 95, 150, and 220 GHz CMB measurements. These maps are smoothed by a one-degree beam, which constitute the high S/N modes, and the fluctuations seen by-eye are dominated by the matter density. The 95 and 150 GHz lensing $\kappa$ maps have similar signal-to-noise and share common large-scale structures. The 220 GHz $\kappa$ map is noisier but still share common structures with the other two frequency bands. We can also compare the lensing maps

with previous lensing measurements, such as the SPTpol measurement in [64]. The SPTpol lensing measurement covers 500 deg$^2$ of the sky, while SPT-3G covers 1500 deg$^2$. The two lensing measurements agree well in the common sky area (Fig. 4.18). Fig. 4.18 top is the SPTpol lensing map and Fig. 4.18 bottom is the lensing map from this work. The SPTpol lensing $\kappa$ map is also overplotted as contour lines at [-0.048,-0.032,-0.016,0,0.016,0.032, 0.048] (unitless) to assist the visual check.

We also report lensing spectra measurements in logarithmically-spaced bins between $50 < \ell < 2000$. In Fig. 4.19, we show the minimum-variance combined lensing spectra for the 95, 150, and 220 GHz frequency bands. We have corrected the MC bias assuming the mock-observed simulations and the data have the same additive MC biases . The lensing amplitude uncertainties and the lensing spectra error bars are statistical uncertainties inferred from the distribution of mock-observed simulation results. The significance of the lensing amplitude is measured to be $18.4\sigma$ at 150 GHz and $14.5\sigma$ at 95 GHz data, relative to the Planck2018 best-fit cosmology in the `TTEEEE_lowl_lowE_lensing` dataset [29, 172]. The systematic uncertainty is yet to be estimated with the uncertainties from the beam, calibration, T$\rightarrow$P leakage, and foreground uncertainties in a similar way to [64]. The SPTpol measurement of the lensing amplitude is $0.946\pm0.058$(Stat.)$\pm0.025$(Sys.) [64] ($16.3\sigma$) relative to the Planck 2015 `plikHM_TT_lowTEB` cosmology dataset. Our 150 GHz lensing amplitude is consistent with the SPTpol number and has slightly smaller statistical uncertainty. The per-mode noise for SPT-3G 2018 measurement is higher than SPTpol, but SPT-3G covers three times of sky area, which reduces the sample variance and results in slightly tighter constraints. Note that we still need to perform systematic tests to validate the number and propagate systematic uncertainties to the lensing amplitude. Given the comparable noise level and similar calibration procedures, we expect our systematic uncertainty to be similar to the SPTpol measurement. The largest contribution to the SPTpol systematic uncertainty comes from data calibration. To improve the calibration, we can cross-calibrate the map with

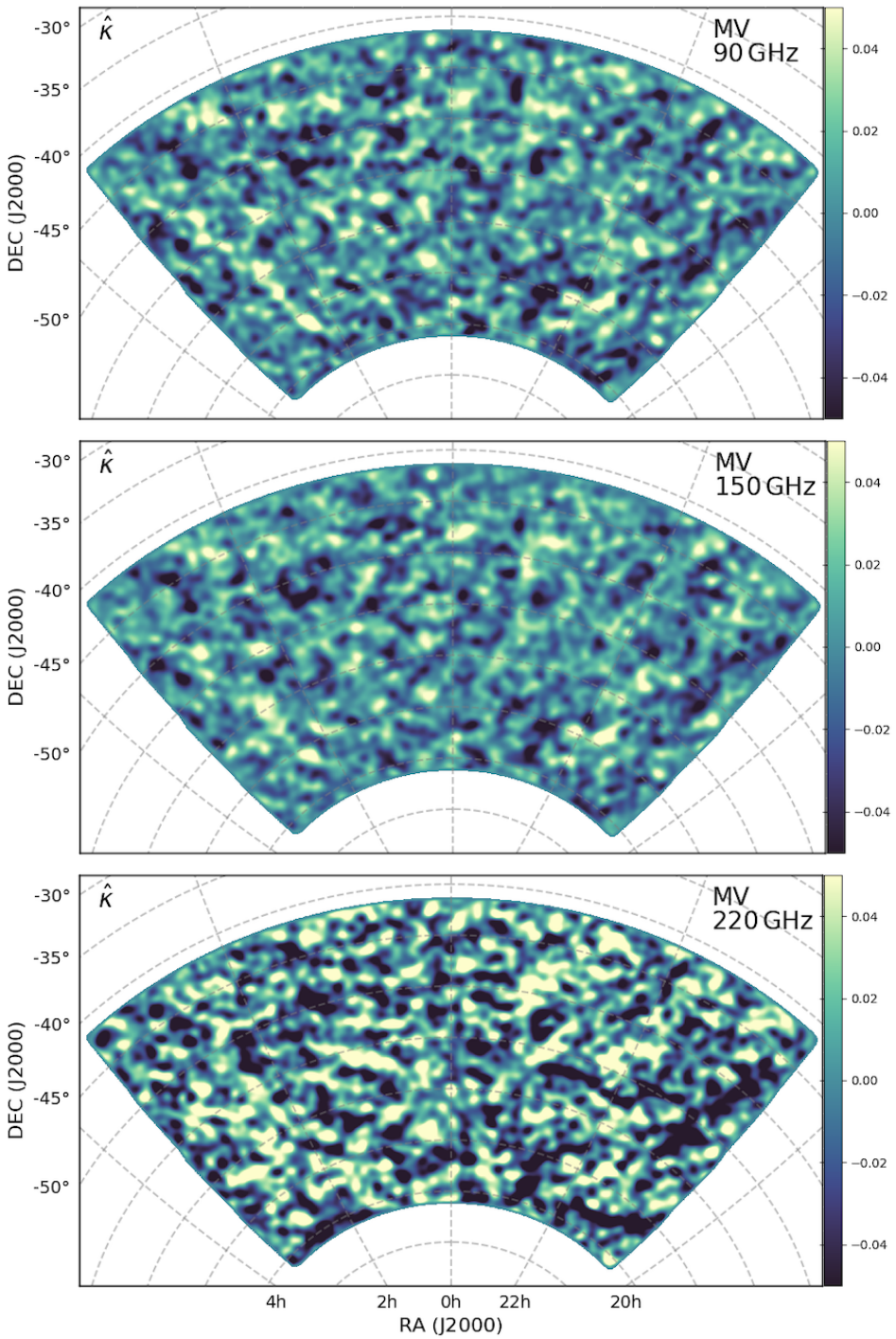


Figure 4.17: The reconstructed $\kappa$ maps using SPT-3G's 2018 data. From top to bottom are 95, 150, and 220 GHz reconstructions. All the lensing maps shown are smoothed with a 1 degree beam to show the signal-dominated modes. The three lensing maps share common large scale structures. 150 GHz has the highest signal-to-noise, followed by 95 and 220 GHz.

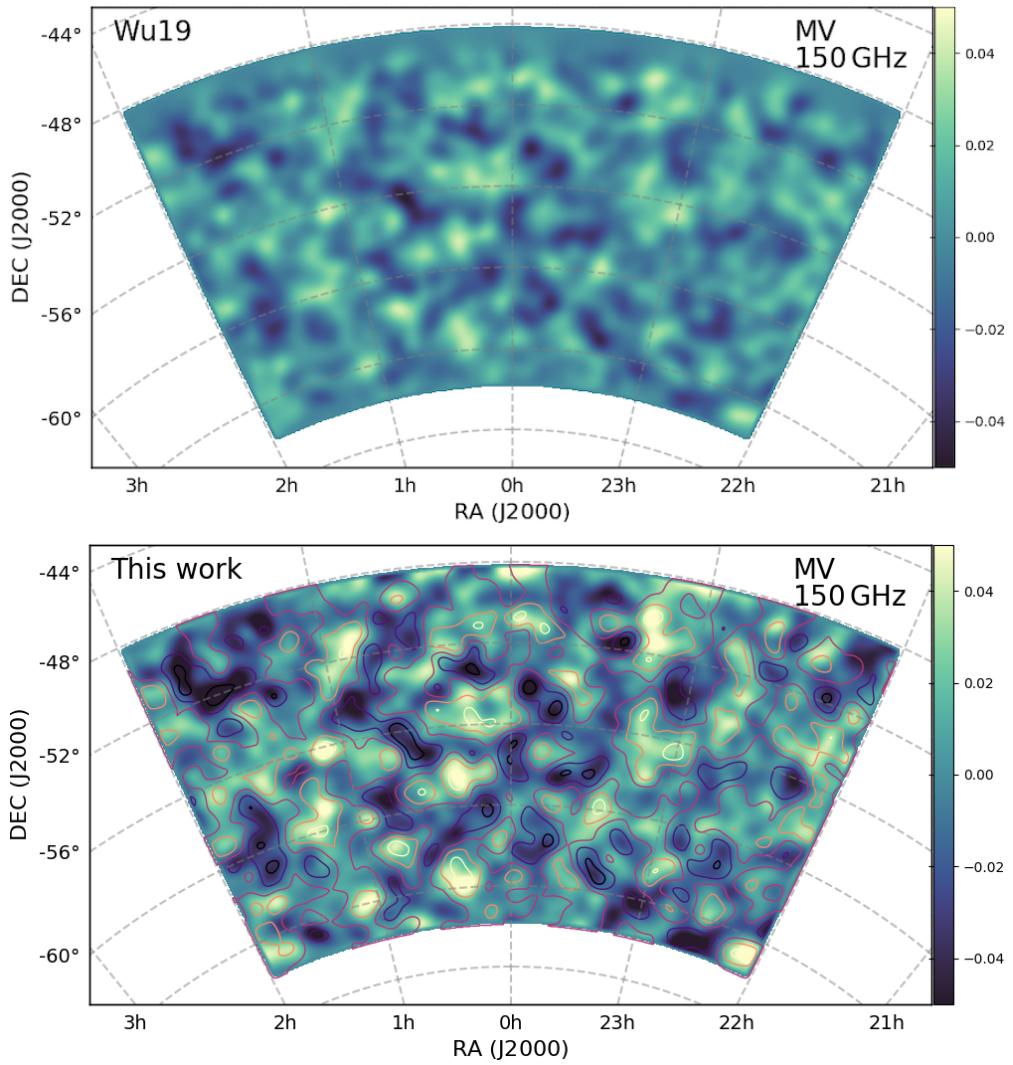


Figure 4.18: The SPT-3G $\kappa$ measurement vs. the SPTpol $\kappa$ measurement in the shared 500 deg$^2$ of sky. Top: the minimum-variance $\kappa$ map from SPTpol using 150 GHz data [64]. Bottom: the minimum-variance $\kappa$ map for the same patch of sky using SPT-3G 150 GHz data. The contour lines in the bottom plot are SPTpol measurements from the top plot. Both maps are smoothed with a 1 degree beam. The CMB datasets for the two measurements were taken with different receivers in different years. Their visual agreement serves as a consistency check.

external datasets with lower noise and more accurate calibrations. Another way is to use the measured data spectrum for one of the weight functions of the lensing response (Eq. 4.23), so the map calibration cancels out when dividing the lensing response[64].

The 95 GHz lensing power is biased low towards smaller angular scales. The bias is related

to higher tSZ and point source foregrounds and the associated filtering artifacts compared to 150 GHz. Our next step is to implement better masking, filtering and foreground bias estimation to reduce the bias in 95 GHz. The 220 GHz measurement is much noisier than the other two frequencies with larger error bars. The low $\ell$ or large angular scales of 220 GHz CMB maps are heavily contaminated by low-frequency map noise, which we will fix with better noise filtering or noisy map cuts. The detailed procedures for improving the 95 and 150 GHz reconstructions were discussed earlier in this section. The same improvements will also help with 150 GHz.

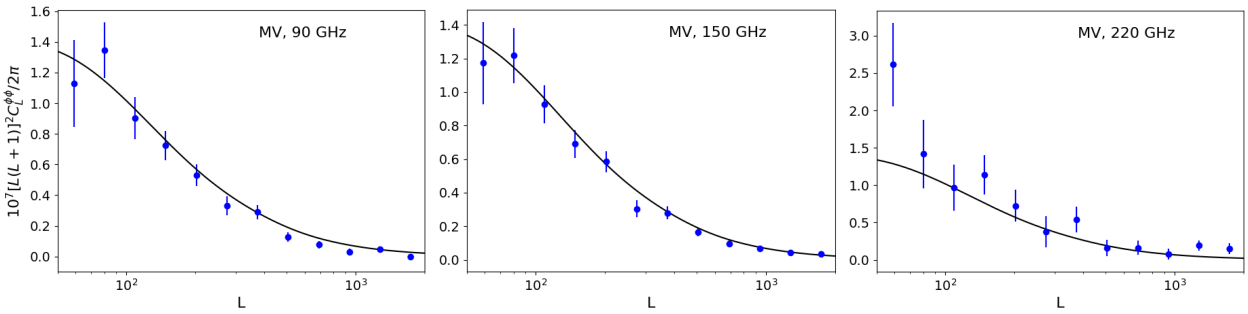


(a) 95 GHz (b) 150 GHz (c) 220 GHz

Figure 4.19: Reconstructed lensing spectra using the 95, 150, and 220 GHz CMB measurements by SPT-3G. The statistical uncertainty comes from the standard deviation of the 320 simulations. 150 GHz measurement has the lowest noise and matches the theory best. The 95 GHz lensing spectrum bias towards high $\ell$ is likely associated with stronger point sources, tSZ foregrounds, and the related filtering artifacts. The 220 GHz lensing spectrum have less than unity per-mode signal-to-noise through all angular scales and is contaminated by large-scale map noise more than the other two frequency bands. The solid lines are the theoretical lensing spectrum from Planck2018 best-fit cosmology in the `TTEEEE_lowl_lowE_lensing` dataset [29, 172].

### *4.2.12 Parameter constraint forecast*

While the lensing spectra need more systematic checks, we can forecast the cosmological parameter constraints with estimated SPT-3G 2018 lensing measurement uncertainties. We use the noise curves in Fig. 4.3 and theoretical CMB power spectrum to construct the $N^0_{\mathbf{L}}$ and $N^1_{\mathbf{L}}$ bias terms, which we use to estimate the expected lensing spectrum uncertainties

[89]. When estimating the lensing uncertainty, we remove the noise and theoretical CMB spectrum below $L < 300$ to approximate the treatment on SPT-3G data. The parameter estimation input is the lensing spectrum from Planck18 cosmology [29] combined with the SPT-3G lensing uncertainty estimated using the method above. We construct the CMB lensing likelihood following [185] and sample the parameter posteriors with the Markov Chain Monte Carlo CosmoMC code [186]. Fig. 4.20 shows the lensing-only constraints for $\Omega_m$ and $\sigma_8$. The constraint is in a well-defined band of $\sigma_8\Omega_m^{0.25} = \text{const}$. The colored contour area indicates how tight SPT-3G 2018 lensing constraint will be. Fig. 4.20(a) indicates that the lensing constraint from 95 GHz is comparable to 150 GHz and that combining the two frequencies in a minimum-variance (MV) manner improve the constraint. Both effects are expected, as can be seen in the simulations in Fig. 4.14 and the data constraints in Fig. 4.19, the lensing amplitude constraints from 95 and 150 GHz are similar. In addition, combining the 95 and 150 GHz data can shrink the error bar and tighten up the constraint. We are now working on combining the 95 and 150 GHz lensing reconstruction in map space instead of power spectrum space because the 95 and 150 GHz data is measuring the same structures in the sky, and there is significant correlated information between the two data sets. Fig. 4.20(b) illustrates the impact of large-scale lensing spectrum on the parameter constraints. Lensing measurements with large angular scale data ($L_{\text{min}} = 50$) do not have significantly better lensing-only parameter constraint compared to $L_{\text{min}} = 100$ because the measurement is sample variance limited there. Also included in Fig. 4.20(b) is the SPTpol parameter constraints, which are worse than the SPT-3G 2018 constraints.

The CMB lensing meaurements can be used with other data sets to place interesinting constraints on cosmology. One data set we consider is combing CMB lensing measurements with baryon acoustic oscillation (BAO) data. CMB lensing spectrum shape is sensitive to the $\ell_{\text{eq}} \equiv k_{\text{eq}}\chi_*$ and can constrain $\Omega_m^{0.6}h = \text{const}$ since $\ell_{\text{eq}} \propto \Omega_m^{0.6}h$ [188]. Here $k_{\text{eq}}$ is the wavenumber that passes the Hubble scale at matter-radiation equality, and $\chi_*$ is the

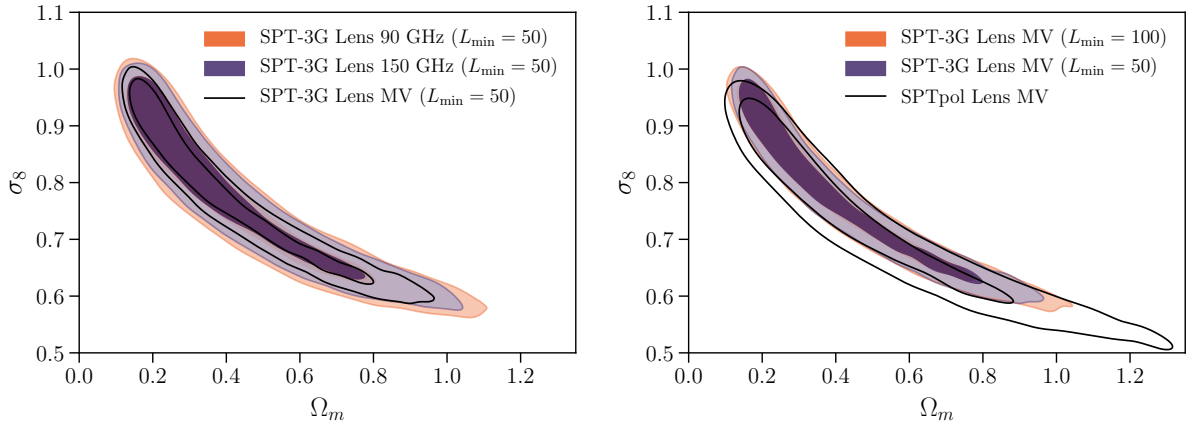


(a) Different frequency bands

(b) Different $L_{\rm min}$

Figure 4.20: (a)Lensing-only $\sigma_8$ and $\Omega_m$ constraints with SPT-3G 95 GHz, 150 GHz, and 95+150 GHz minimum-variance (MV) combined data. (b) 95+150 GHz parameter constraints with different $L_{\rm min}$ cuts. CMB modes below $L_{\rm min}$ are removed. We also overplot the SPTpol constraints. Plot made with code from Federico Bianchini [187].

distance to the CMB last-scattering surface. The BAO data prefers a correlation between $H_0$ and $\Omega_m$ and can break the parameter degeneracy from CMB lensing measurement, which prefers an anti-correlation between these two parameters. With BAO data, we can obtain a tighter constraint for $\sigma_8$ as well. Fig. 4.21 shows the expected constraints on $H_0$, $\sigma_8$, and $\Omega_m$ using SPTpol+BAO, SPT-3G 2018 data+BAO, SPT-3G full survey+BAO, and Planck+BAO. The SPT-3G 2018 constraints will be better than SPTpol. SPT-3G 2018 lensing measurements improves on SPTpol mostly on larger scales due to three times of sky coverage and smaller sample variance. The 5-year SPT-3G survey constraints will be better than Planck2018 [70] constraints.

We can also compare the $1\sigma$ constraints from different surveys quantitatively. With SPT-3G 2018 95+150 GHz lensing spectrum measured to $L_{\rm min} = 50$, our $1\sigma$ constraint on $\sigma_8\Omega_m^{0.25}$ is $^{+0.020}_{-0.018}$, compared to 0.025, 0.020, and $^{+0.012}_{-0.009}$ from SPTpol, Planck [185], and SPT-3G full survey, respectively. The parameter constraints from lensing+ BAO are summarized in Table 4.2.

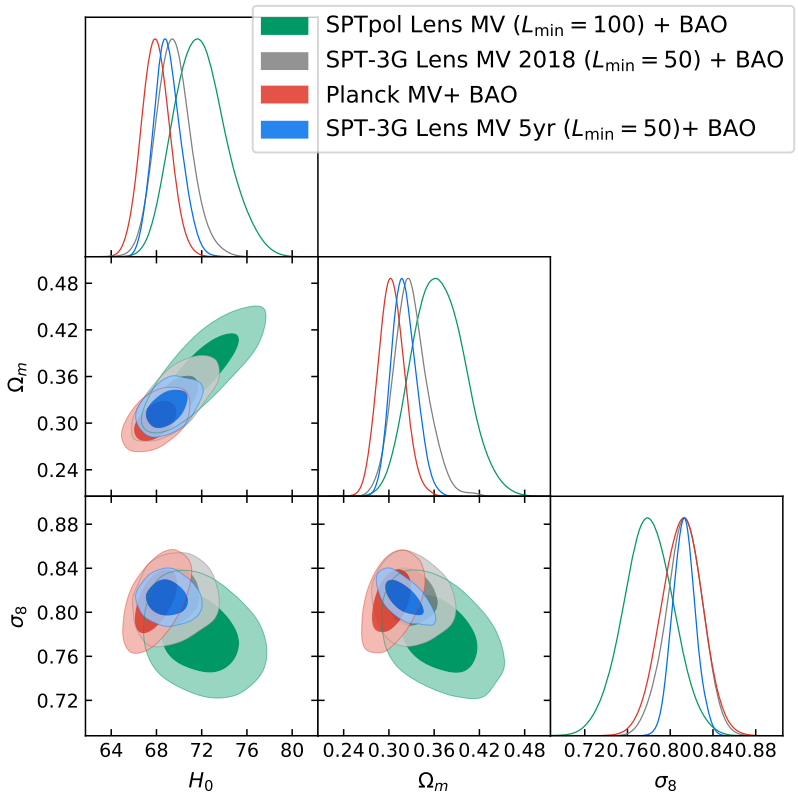


Figure 4.21: Constraints of $\Omega_m$, $H_0$, and $\sigma_8$ with CMB lensing and baryon acoustic oscillation (BAO) data. The constraints are tighter with BAO data. The green, gray, blue, and red contour are constraints for SPTpol, SPT-3G 2018 data, SPT-3G full survey, and Planck. The full 5-yr SPT-3G lensing+BAO constraints will be tighter than Planck lensing+BAO. Plot made with code from Federico Bianchini [187].

| Parameter | SPTpol | SPT-3G (2018) | SPT-3G (5yr) | Planck 2018 |
|---|---|---|---|---|
| $\sigma(\sigma_8)$ | 0.023 | $^{+0.018}_{-0.016}$ | 0.011 | 0.019 |
| $\sigma(\Omega_m)$ | $^{+0.031}_{-0.036}$ | $^{+0.025}_{-0.018}$ | $^{+0.015}_{-0.019}$ | $^{+0.016}_{-0.018}$ |
| $\sigma(H_0)$ | $^{+2.0}_{-2.5}$ | $^{+1.4}_{-1.6}$ | $^{+1.1}_{-1.3}$ | 1.2 |

Table 4.2: Table for $1\sigma$ constraints on $\sigma_8$, $\Omega_m$, and $H_0$ from different lensing measurements combined with BAO. $H_0$ is in unit of km s$^{-1}$Mpc$^{-1}$. The constraints are projected from Fig. 4.21.

# CHAPTER 5

# CONCLUSIONS

Precise measurements of the CMB are a cornerstone of modern cosmology and will continue to deepen our understanding of the universe. The CMB temperature anisotropy is at the $10^{-5}$ level, while the polarization anisotropy is an order of magnitude lower. The primordial polarization B-mode is predicted to be at a lower level, depending on the tensor-to-scalar ratio $r$. Additionally, the emerging discrepancies between CMB measurements and low-redshift surveys and between different CMB measurements[34, 35, 36] can be better understood through more sensitive measurements. There are a host of new measurements that can potentially weigh in from the current and future CMB experiments, including SPT-3G[4], ACTpol[37], Advanced ACTpol[38], Simons Array[39], BICEP3/ BICEP Array[40, 41], the Simons Observatory[42], and CMB-S4[43].

With the rapid advancing of detector and readout technologies, CMB detectors are now limited by background photon noise. The direction to increase receiver sensitivity is to increase the detector number. SPT-3G uses 16,000 polarization-sensitive sensors operating at 95, 150, and 220 GHz frequency bands. A crucial task for detector development is to ensure that the uniformity and performance meet our target. In Chapter 2, I have described the detector structure, characterization methods, and characterization results for SPT-3G. We measured the detector modules' optical efficiency with a temperature-controlled blackbody to be 81, 83, and 73% for the 95, 150, and 220 GHz bands. We designed a calibrator that can chop at different frequencies to probe the time constants of the detectors, which mostly fall between 0.5 and 10 ms. We measured the spectral bands of the detectors with a Fourier transform spectrometer (FTS) and validated their agreement with the simulate bands from Sonnet simulations. The electrothermal properties of the detectors, including the superconducting transition temperature, resistance, saturation power, thermal conductivity, also agree with the design targets. At the end of Chapter 2, I have summarized the readout

system for reading the detectors and the optical system that couples the detectors to the sky, which, together with the detector system, constitutes an optically efficient CMB receiver with low noise.

SPT-3G is at the geographic South Pole, where the atmosphere emission is low. However, even at the South Pole, the atmosphere emission is still stronger than the CMB and contributes to noise in the measurements. Moreover, the frequency-dependent atmosphere transmission limits the observation frequency bands, making CMB spectrum measurements challenging. A way to avoid these problems for CMB spectrum and anisotropy measurements is going to space. Previous space missions, including COBE [18, 19], WMAP [23], and Planck [29], have achieved several milestones in CMB measurements. The planned LiteBird [189] mission aims to measure CMB polarization over the entire sky and constrain the tensor-to-scalar ratio with $\sigma(r)$ <0.001. PIXIE is a proposed space mission to measure the primordial B-mode and the spectral distortion of the CMB [190, 5]. A compact Fourier transform spectrometer (FTS) is required to measure the yet unprobed CMB spectrum distortion from a perfect blackbody.

Chapter 3 has discussed a compact FTS operating at millimeter-wavelength, which is similar to the design of the PIXIE satellite instrument and was also used to characterize the spectral bands of SPT-3G detectors. A critical difference between the ground-based experiments like SPT-3G and PIXIE is that SPT-3G uses single-mode optics with 16,000 detectors while PIXIE uses multi-mode optics and only four detectors. To increase the number of modes and detection significance, the FTS needs to have a large throughput. Additional driving factors for the FTS design include high spectral resolution, compact size, and operational simplicity. These requirements are converted into instrument dimensions once the optical configuration is determined. Our optical configuration's unique features include the large solid angle of the beam, folded optical paths, and simple focusing optics milled on box walls. After designing and building, we characterized the optical properties of

the FTS carefully, out of which the most important ones are the frequency resolution and the frequency accuracy. We studied all effects limiting our frequency resolution, identifying decoherence to be the dominant factor. The frequency accuracy was dependent on the optical path and can be improved using a ray-tracing simulation.

We also developed a ray-trace based simulation for the FTS. The simulation tracks the polarization, path length, and intensity of the light rays through the FTS. These properties allowed us to study the transfer efficiency, non-idealities of the optics, and loss of interference. The simulation can be extended for FTS systems of other designs and can function as an assisting tool for FTS design and performance study.

SPT-3G instrument was quite successful and started its 1500 $\deg^2$ survey beginning in February 2018. Low-noise temperature and polarization CMB measurements have been going on since then. While the wealth of information in CMB temperature and polarization spectra has established the standard $\Lambda$CDM model, the statistical anisotropy in the CMB can be used to reconstruct the 2D matter distribution and probe the growth of structure over a large redshift range. I have presented a measurement of gravitational lensing using SPT-3G's 2018 data in Chapter 4. We have performed lensing reconstruction using 95, 150, and 220 GHz data from SPT-3G and made lensing maps that contain large-scale features highly consistent with the last-generation SPTpol lensing measurements. With our statistical uncertainty level, we estimate an $18.4\sigma$ measurement of the lensing amplitude relative to the Planck2018 best-fit cosmology in the `TTEEEE_lowl_lowE_lensing` dataset [29, 172] using SPT-3G 150 GHz data. The 90 GHz lensing amplitude measurement is estimated to be $14.5\sigma$, slightly worse than 150 GHz due to higher data noise. This measurement has a slightly higher significance than the SPTpol measurement with the best-fit lensing amplitude to be $0.946\pm0.058$(Stat.)$\pm0.025$(Sys.) [64] ($16.3\sigma$ measurement) relative to the Planck 2015 `plikHM_TT_lowTEB` cosmology dataset. The slightly higher significance here is due to three times of sky coverage than SPTpol despite slightly higher per-mode noise. The lensing

spectra from 150 GHz mock-observed simulations are generally consistent with the theoretical prediction given the error bars and consistent with a biased lensing amplitude of unity. The 95 and 220 GHz are more biased than 150 GHz compared to the theory curve. We have located the major bias sources to stronger point sources, galaxy clusters, and the associated filtering artifacts for 95 GHz. We attribute the bias at 220 GHz to high map noise at low spatial frequencies. To reduce the biases, we need to implement better time-ordered-data filtering, better source masking, and harsher noise filtering for low spatial frequencies, which are future work for this analysis. The systematic error budget will be estimated after the bias correction. With the current noise level, we will obtain tighter cosmological parameter constraints compared to SPTpol with better lensing measurements at larger scales. The SPT-3G 2018 $1\sigma$ constraint on $\sigma_8\Omega_m^{0.25}$ with lensing data only is $^{+0.020}_{-0.018}$, compared to 0.025 from SPTpol[185]. When combined with BAO, the SPT-3G 2018 constraints of $\sigma_8$, $\Omega_m$, and $H_0$ are $^{+0.018}_{-0.016}$ , $^{+0.025}_{-0.018}$, and $^{+1.4}_{-1.6}$, as compared to 0.023 , $^{+0.031}_{-0.036}$, and $^{+2.0}_{-2.5}$ from SPTpol [185].

The future of CMB lensing is promising with SPT-3G and other third- and fourth-generation experiments. Lensing estimators weigh pairs of CMB modes to reconstruct the lensing potential. SPT-3G data is the ideal dataset for lensing measurements because SPT-3G can provide a large number of low-noise modes, thanks to SPT-3G's unprecedented combination of high angular resolution and low-noise. The ten-meter dish gives the telescope 1.6, 1.2, and 1.0 arcmin resolution at 95, 150, and 220 GHz, respectively. A focal plane with 16,000 detectors will help the SPT-3G full survey reach low noise levels of 3.0, 2.2, and 8.8 $\mu$K-arcmin at 95, 150, and 220 GHz for a 1500 deg$^2$ patch of sky. The joint de-lensing with BICEP Array can help remove lensing-induced contaminations to the B-mode and enable a better constraint on the primordial B-mode. The constraint on tensor-to-scalar ratio, $\sigma(r)$, will be 0.003 with delensing and 0.006 without. Cross-correlation measurements are yet another frontier. SPT-3G full survey will measure lensing features with signal-to-noise larger than one for scales larger than 12 arcmin, compared to $\sim$1 degree for current experiments

[64]. The parameter constraints from the SPT-3G full survey will be better than Planck [70]. The lensing only $1\sigma$ constraint on $\sigma_8\Omega_m^{0.25}$ is 0.020 for Planck [185, 188] and will be $^{+0.012}_{-0.009}$ for the SPT-3G full survey. With lower noise, lensing signal-to-noise in future experiments will be dominated by polarization estimators, especially the EB estimator. Future lensing reconstruction will benefit from more optimal estimators, including the maximum-a-posteriori CMB lensing reconstruction [109] and the Bayesian delensing approach in [107, 108].

# References


[1] Z Pan, P. A.R. Ade, Z. Ahmed, A J Anderson, J. E. Austermann, J. S. Avva, R Basu Thakur, A. N. Bender, B A Benson, J E Carlstrom, F W Carter, T Cecil, C L Chang, J. F. Cliche, A. Cukierman, E. V. Denison, T. de Haan, J. Ding, M. A. Dobbs, D Dutcher, W Everett, A. Foster, R. N. Gannon, A. Gilbert, J. C. Groh, N W Halverson, A. H. Harke-Hosemann, N L Harrington, J. W. Henning, G. C. Hilton, W. L. Holzapfel, N. Huang, K D Irwin, O. B. Jeong, M. Jonas, T. Khaire, A M Kofman, M. Korman, D. Kubik, S. Kuhlmann, C. L. Kuo, A. T. Lee, A. E. Lowitz, S. S. Meyer, D. Michalik, J. Montgomery, A. Nadolski, T. Natoli, H. Nguyen, G. I. Noble, V. Novosad, S. Padin, J. Pearson, C. M. Posada, A. Rahlin, J. E. Ruhl, L. J. Saunders, J. T. Sayre, I. Shirley, E. Shirokoff, G Smecher, J. A. Sobrin, A. A. Stark, K. T. Story, A. Suzuki, Q. Y. Tang, K. L. Thompson, C. Tucker, L. R. Vale, K. Vanderlinde, J. D. Vieira, G. Wang, N. Whitehorn, V. Yefremenko, K. W. Yoon, and M. R. Young. Optical Characterization of the SPT-3G Camera. *Journal of Low Temperature Physics*, 193(3-4):305–313, 2018.

[2] Zhaodi Pan, Mira Liu, Ritoban Basu Thakur, Bradford A. Benson, Dale J. Fixsen, Hazal Goksu, Eleanor Rath, and Stephan S. Meyer. Compact millimeter-wavelength Fourier-transform spectrometer. *Applied Optics*, 58(23):6257, aug 2019.

[3] Mira Liu, Zhaodi Pan, Ritoban Basu Thakur, and Stephan Meyer. Simulation and Calibration of a Compact Millimeter-wavelength Fourier Transform Spectrometer. *Applied Optics*, 59(25):7726–7733, jul 2020.

[4] B A Benson, P A R Ade, Z Ahmed, S W Allen, K Arnold, J E Austermann, A. N. Bender, L. E. Bleem, J. E. Carlstrom, C. L. Chang, H. M. Cho, J. F. Cliche, T. M. Crawford, A. Cukierman, T. de Haan, M. A. Dobbs, D. Dutcher, W. Everett, A. Gilbert, N. W. Halverson, D. Hanson, N. L. Harrington, K. Hattori, J. W. Henning, G. C. Hilton, G. P. Holder, W. L. Holzapfel, K. D. Irwin, R. Keisler, L. Knox, D. Kubik, C. L. Kuo, A. T. Lee, E. M. Leitch, D. Li, M. McDonald, S. S. Meyer, J. Montgomery, M. Myers, T. Natoli, H. Nguyen, V. Novosad, S. Padin, Z. Pan, J. Pearson, C. Reichardt, J. E. Ruhl, B. R. Saliwanchik, G. Simard, G. Smecher, J. T. Sayre, E. Shirokoff, A. A. Stark, K. Story, A. Suzuki, K. L. Thompson, C. Tucker, K. Vanderlinde, J. D. Vieira, A. Vikhlinin, G. Wang, V. Yefremenko, and K. W. Yoon. SPT-3G: a next-generation cosmic microwave background polarization experiment on the South Pole telescope. In *Millimeter, Submillimeter, and Far-Infrared Detectors and Instrumentation for Astronomy VII*, volume 9153, page 91531P, 2014.

[5] Alan Kogut, David T. Chuss, Jessie Dotson, Dale J Fixsen, Mark Halpern, Gary F. Hinshaw, Stephan Meyer, S. Harvey Moseley, Michael D. Seiffert, David N. Spergel, and Edward J. Wollack. The Primordial Inflation Explorer (PIXIE). In *UV/Optical/IR Space Telescopes and Instruments: Innovative Technologies and Concepts V*, volume 8146, page 81460T, 2011.

[6] Joseph Silk. Cosmic Black-Body Radiation and Galaxy Formation. *The Astrophysical Journal*, 151:459, feb 1968.

[7] Asantha Cooray, Alessandro Melchiorri, and Joseph Silk. Is the cosmic microwave background circularly polarized? *Physics Letters, Section B: Nuclear, Elementary Particle and High-Energy Physics*, 554(1-2):1–6, feb 2003.

[8] J. M. Nagy, P. A. R. Ade, M. Amiri, S. J. Benton, A. S. Bergman, R. Bihary, J. J. Bock, J. R. Bond, S. A. Bryan, H. C. Chiang, C. R. Contaldi, O. Doré, A. J. Duivenvoorden, H. K. Eriksen, M. Farhang, J. P. Filippini, L. M. Fissel, A. A. Fraisse, K. Freese, M. Galloway, A. E. Gambrel, N. N. Gandilo, K. Ganga, J. E. Gudmundsson, M. Halpern, J. Hartley, M. Hasselfield, G. Hilton, W. Holmes, V. V. Hristov, Z. Huang, K. D. Irwin, W. C. Jones, C. L. Kuo, Z. D. Kermish, S. Li, P. V. Mason, K. Megerian, L. Moncelsi, T. A. Morford, C. B. Netterfield, M. Nolta, I. L. Padilla, B. Racine, A. S. Rahlin, C. Reintsema, J. E. Ruhl, M. C. Runyan, T. M. Ruud, J. A. Shariff, J. D. Soler, X. Song, A. Trangsrud, C. Tucker, R. S. Tucker, A. D. Turner, J. F. Van Der List, A. C. Weber, I. K. Wehus, D. V. Wiebe, and E. Y. Young. A New Limit on CMB Circular Polarization from SPIDER. *The Astrophysical Journal*, 844(2):151, 2017.

[9] Ivan L. Padilla, Joseph R. Eimer, Yunyang Li, Graeme E. Addison, Aamir Ali, John W. Appel, Charles L. Bennett, Ricardo Bustos, Michael K. Brewer, Manwei Chan, David T. Chuss, Joseph Cleary, Jullianna Couto, Sumit Dahal, Kevin Denis, Rolando Dünner, Thomas Essinger-Hileman, Pedro Fluxá, Dominik Gothe, Saianeesh K. Haridas, Kathleen Harrington, Jeffrey Iuliano, John Karakla, Tobias A. Marriage, Nathan J. Miller, Carolina Núñez, Lucas Parker, Matthew A. Petroff, Rodrigo Reeves, Karwan Rostem, Robert W. Stevens, Deniz Augusto Nunes Valle, Duncan J. Watts, Janet L. Weiland, Edward J. Wollack, and Zhilei Xu. Two-year Cosmology Large Angular Scale Surveyor (CLASS) Observations: A Measurement of Circular Polarization at 40 GHz. *The Astrophysical Journal*, 889(2):105, jan 2020.

[10] M. Zaldarriaga. Nature of the E-B decomposition of CMB polarization. *Physical Review D - Particles, Fields, Gravitation and Cosmology*, 64(10):1030011–1030018, 2001.

[11] Uroš Seljak and Matias Zaldarriaga. Signature of gravity waves in the polarization of the microwave background. *Physical Review Letters*, 78(11):2054–2057, 1997.

[12] Nabila Aghanim, Subhabrata Majumdar, and Joseph Silk. Secondary anisotropies of the CMB. *Reports on Progress in Physics*, 71(6), 2008.

[13] R. K. Sachs and A. M. Wolfe. Perturbations of a Cosmological Model and Angular Variations of the Microwave Background. *The Astrophysical Journal*, 147:73, jan 1967.

[14] M. J. Rees and D. W. Sciama. Large-scale density inhomogeneities in the universe. *Nature*, 217(5128):511–516, 1968.

[15] R. A. Sunyaev and Ya. B. Zel'dovich. The Spectrum of Primordial Radiation, its Distortions and their Significance. *Comments on Astrophysics and Space Physics*, 2:66, 1970.

[16] R.˜A. Sunyaev and Y.˜B. Zeldovich. The Observations of Relic Radiation as a Test of the Nature of X-Ray Radiation from the Clusters of Galaxies. *Comments on Astrophysics and Space Physics*, 4:173, 1972.

[17] A. A. Penzias and R. W. Wilson. A Measurement of Excess Antenna Temperature at 4080 Mc/s. *The Astrophysical Journal*, 142:419, jul 1965.

[18] J. C. Mather, E. S. Cheng, Jr. Eplee, R. E., R. B. Isaacman, S. S. Meyer, R. A. Shafer, R. Weiss, E. L. Wright, C. L. Bennett, N. W. Boggess, E. Dwek, S. Gulkis, M. G. Hauser, M. Janssen, T. Kelsall, P. M. Lubin, Jr. Moseley, S. H., T. L. Murdock, R. F. Silverberg, G. F. Smoot, and D. T. Wilkinson. A preliminary measurement of the cosmic microwave background spectrum by the Cosmic Background Explorer (COBE) satellite. *The Astrophysical Journal*, 354:L37, may 1990.

[19] E. L. Wright, S. S. Meyer, C. L. Bennett, N. W. Boggess, E. S. Cheng, M. G. Hauser, A. Kogut, C. Lineweaver, J. C. Mather, G. F. Smoot, R. Weiss, S. Gulkis, G. Hinshaw, M. Janssen, T. Kelsall, P. M. Lubin, Jr. Moseley, S. H., T. L. Murdock, R. A. Shafer, R. F. Silverberg, and D. T. Wilkinson. Interpretation of the cosmic microwave background radiation anisotropy detected by the COBE Differential Microwave Radiometer. *The Astrophysical Journal*, 396:L13, sep 1992.

[20] P. De Bernardis, P. A.R. Ade, J. J. Bock, J. R. Bond, J. Borrill, A. Boscaleri, K. Coble, B. P. Crill, G. De Gasperis, P. C. Farese, P. G. Ferreira, K. Ganga, M. Giacometti, E. Hivon, V. V. Hristov, A. Iacoangell, A. H. Jaffe, A. E. Lange, L. Martinis, S. Masi, P. V. Mason, P. D. Mauskopf, A. Melchiorri, L. Miglio, T. Montroy, C. B. Netterfield, E. Pascale, F. Placentini, D. Pogosyan, S. Prunet, S. Rao, G. Romeo, J. E. Ruhl, F. Scaramuzzi, D. Sforna, and N. Vittorio. A flat Universe from high-resolution maps of the cosmic microwave background radiation. *Nature*, 404(6781):955–959, apr 2000.

[21] A. Balbi, P. Ade, J. Bock, J. Borrill, A. Boscaleri, P. De Bernardis, P. G. Ferreira, S. Hanany, V. Hristov, A. H. Jaffe, A. T. Lee, S. Oh, E. Pascale, B. Rabii, P. L. Richards, G. F. Smoot, R. Stompor, C. D. Winant, and J. H. P. Wu. Constraints on Cosmological Parameters from MAXIMA-1. *The Astrophysical Journal*, 545(1):L1–L4, dec 2000.

[22] N. W. Halverson, E. M. Leitch, C. Pryke, J. Kovac, J. E. Carlstrom, W. L. Holzapfel, M. Dragovan, J. K. Cartwright, B. S. Mason, S. Padin, T. J. Pearson, A. C. S. Readhead, and M. C. Shepherd. Degree Angular Scale Interferometer First Results: A Measurement of the Cosmic Microwave Background Angular Power Spectrum. *The Astrophysical Journal*, 568(1):38–45, mar 2002.

[23] D. N. Spergel, L. Verde, H. V. Peiris, E. Komatsu, M. R. Nolta, C. L. Bennett, M. Halpern, G. Hinshaw, N. Jarosik, A. Kogut, M. Limon, S. S. Meyer, L. Page, G. S. Tucker, J. L. Weiland, E. Wollack, and E. L. Wright. First-Year Wilkinson Microwave Anisotropy Probe ( WMAP ) Observations: Determination of Cosmological Parameters. *The Astrophysical Journal Supplement Series*, 148(1):175–194, sep 2003.

[24] J. M. Kovac, E. M. Leitch, C. Pryke, J. E. Carlstrom, N. W. Halverson, and W. L. Holzapfel. Detection of polarization in the cosmic microwave background using DASI. *Nature*, 420(6917):772–787, dec 2002.

[25] D. Hanson, S. Hoover, A. Crites, P. A.R. Ade, K. A. Aird, J. E. Austermann, J. A. Beall, A. N. Bender, B. A. Benson, L. E. Bleem, J. J. Bock, J. E. Carlstrom, C. L. Chang, H. C. Chiang, H. M. Cho, A. Conley, T. M. Crawford, T. De Haan, M. A. Dobbs, W. Everett, J. Gallicchio, J. Gao, E. M. George, N. W. Halverson, N. Harrington, J. W. Henning, G. C. Hilton, G. P. Holder, W. L. Holzapfel, J. D. Hrubes, N. Huang, J. Hubmayr, K. D. Irwin, R. Keisler, L. Knox, A. T. Lee, E. Leitch, D. Li, C. Liang, D. Luong-Van, G. Marsden, J. J. McMahon, J. Mehl, S. S. Meyer, L. Mocanu, T. E. Montroy, T. Natoli, J. P. Nibarger, V. Novosad, S. Padin, C. Pryke, C. L. Reichardt, J. E. Ruhl, B. R. Saliwanchik, J. T. Sayre, K. K. Schaffer, B. Schulz, G. Smecher, A. A. Stark, K. T. Story, C. Tucker, K. Vanderlinde, J. D. Vieira, M. P. Viero, G. Wang, V. Yefremenko, O. Zahn, and M. Zemcov. Detection of B-mode polarization in the cosmic microwave background with data from the south pole telescope. *Physical Review Letters*, 111(14):141301, sep 2013.

[26] P. A.R. Ade, R. W. Aikin, D. Barkats, S. J. Benton, C. A. Bischoff, J. J. Bock, J. A. Brevik, I. Buder, E. Bullock, C. D. Dowell, L. Duband, J. P. Filippini, S. Fliescher, S. R. Golwala, M. Halpern, M. Hasselfield, S. R. Hildebrandt, G. C. Hilton, V. V. Hristov, K. D. Irwin, K. S. Karkare, J. P. Kaufman, B. G. Keating, S. A. Kernasovskiy, J. M. Kovac, C. L. Kuo, E. M. Leitch, M. Lueker, P. Mason, C. B. Netterfield, H. T. Nguyen, R. O'Brient, R. W. Ogburn IV, A. Orlando, C. Pryke, C. D. Reintsema, S. Richter, R. Schwarz, C. D. Sheehy, Z. K. Staniszewski, R. V. Sudiwala, G. P. Teply, J. E. Tolan, A. D. Turner, A. G. Vieregg, C. L. Wong, and K. W. Yoon. Detection of B -mode polarization at degree angular scales by BICEP2. *Physical Review Letters*, 112(24):1–25, 2014.

[27] J. W. Henning, J. T. Sayre, C. L. Reichardt, P. A. R. Ade, A. J. Anderson, J. E. Austermann, J. A. Beall, A. N. Bender, B. A. Benson, L. E. Bleem, J. E. Carlstrom, C. L. Chang, H. C. Chiang, H-M. Cho, R. Citron, C. Corbett Moran, T. M. Crawford, A. T. Crites, T. de Haan, M. A. Dobbs, W. Everett, J. Gallicchio, E. M. George, A. Gilbert, N. W. Halverson, N. Harrington, G. C. Hilton, G. P. Holder, W. L. Holzapfel, S. Hoover, Z. Hou, J. D. Hrubes, N. Huang, J. Hubmayr, K. D. Irwin, R. Keisler, L. Knox, A. T. Lee, E. M. Leitch, D. Li, A. Lowitz, A. Manzotti, J. J. McMahon, S. S. Meyer, L. Mocanu, J. Montgomery, A. Nadolski, T. Natoli, J. P. Nibarger, V. Novosad, S. Padin, C. Pryke, J. E. Ruhl, B. R. Saliwanchik, K. K. Schaffer, C. Sievers, G. Smecher, A. A. Stark, K. T. Story, C. Tucker, K. Vanderlinde, T. Veach,

J. D. Vieira, G. Wang, N. Whitehorn, W. L. K. Wu, and V. Yefremenko. Measurements of the Temperature and E-mode Polarization of the CMB from 500 Square Degrees of SPTpol Data. *The Astrophysical Journal*, 852(2):97, 2018.

[28] P. A.R. Ade, Z. Ahmed, R. W. Aikin, K. D. Alexander, D. Barkats, S. J. Benton, C. A. Bischoff, J. J. Bock, R. Bowens-Rubin, J. A. Brevik, I. Buder, E. Bullock, V. Buza, J. Connors, J. Cornelison, B. P. Crill, M. Crumrine, M. Dierickx, L. Duband, C. Dvorkin, J. P. Filippini, S. Fliescher, J. Grayson, G. Hall, M. Halpern, S. Harrison, S. R. Hildebrandt, G. C. Hilton, H. Hui, K. D. Irwin, J. Kang, K. S. Karkare, E. Karpel, J. P. Kaufman, B. G. Keating, S. Kefeli, S. A. Kernasovskiy, J. M. Kovac, C. L. Kuo, N. A. Larsen, K. Lau, E. M. Leitch, M. Lueker, K. G. Megerian, L. Moncelsi, T. Namikawa, C. B. Netterfield, H. T. Nguyen, R. O'Brient, R. W. Ogburn, S. Palladino, C. Pryke, B. Racine, S. Richter, A. Schillaci, R. Schwarz, C. D. Sheehy, A. Soliman, T. St Germaine, Z. K. Staniszewski, B. Steinbach, R. V. Sudiwala, G. P. Teply, K. L. Thompson, J. E. Tolan, C. Tucker, A. D. Turner, C. Umiltà, A. G. Vieregg, A. Wandui, A. C. Weber, D. V. Wiebe, J. Willmert, C. L. Wong, W. L.K. Wu, H. Yang, K. W. Yoon, and C. Zhang. Constraints on Primordial Gravitational Waves Using Planck, WMAP, and New BICEP2/ Keck Observations through the 2015 Season. *Physical Review Letters*, 121(22):221301, nov 2018.

[29] Planck Collaboration, N. Aghanim, Y. Akrami, M. Ashdown, J. Aumont, C. Baccigalupi, M. Ballardini, A. J. Banday, R. B. Barreiro, N. Bartolo, S. Basak, R. Battye, K. Benabed, J. P. Bernard, M. Bersanelli, P. Bielewicz, J. J. Bock, J. R. Bond, J. Borrill, F. R. Bouchet, F. Boulanger, M. Bucher, C. Burigana, R. C. Butler, E. Calabrese, J. F. Cardoso, J. Carron, A. Challinor, H. C. Chiang, J. Chluba, L. P. L. Colombo, C. Combet, D. Contreras, B. P. Crill, F. Cuttaia, P. de Bernardis, G. de Zotti, J. Delabrouille, J. M. Delouis, E. Di Valentino, J. M. Diego, O. Doré, M. Douspis, A. Ducout, X. Dupac, S. Dusini, G. Efstathiou, F. Elsner, T. A. Enßlin, H. K. Eriksen, Y. Fantaye, M. Farhang, J. Fergusson, R. Fernandez-Cobos, F. Finelli, F. Forastieri, M. Frailis, A. A. Fraisse, E. Franceschi, A. Frolov, S. Galeotta, S. Galli, K. Ganga, R. T. Génova-Santos, M. Gerbino, T. Ghosh, J. González-Nuevo, K. M. Górski, S. Gratton, A. Gruppuso, J. E. Gudmundsson, J. Hamann, W. Handley, F. K. Hansen, D. Herranz, S. R. Hildebrandt, E. Hivon, Z. Huang, A. H. Jaffe, W. C. Jones, A. Karakci, E. Keihänen, R. Keskitalo, K. Kiiveri, J. Kim, T. S. Kisner, L. Knox, N. Krachmalnicoff, M. Kunz, H. Kurki-Suonio, G. Lagache, J. M. Lamarre, A. Lasenby, M. Lattanzi, C. R. Lawrence, M. Le Jeune, P. Lemos, J. Lesgourgues, F. Levrier, A. Lewis, M. Liguori, P. B. Lilje, M. Lilley, V. Lindholm, M. López-Caniego, P. M. Lubin, Y. Z. Ma, J. F. Macías-Pérez, G. Maggio, D. Maino, N. Mandolesi, A. Mangilli, A. Marcos-Caballero, M. Maris, P. G. Martin, M. Martinelli, E. Martínez-González, S. Matarrese, N. Mauri, J. D. McEwen, P. R. Meinhold, A. Melchiorri, A. Mennella, M. Migliaccio, M. Millea, S. Mitra, M. A. Miville-Deschênes, D. Molinari, L. Montier, G. Morgante, A. Moss, P. Natoli, H. U. Nørgaard-Nielsen, L. Pagano, D. Paoletti, B. Partridge, G. Patanchon, H. V. Peiris, F. Perrotta, V. Pettorino, F. Piacentini, L. Polastri, G. Polenta, J. L. Puget, J. P. Rachen, M. Reinecke, M. Remazeilles, A. Renzi, G. Rocha, C. Rosset,

G. Roudier, J. A. Rubiño-Martín, B. Ruiz-Granados, L. Salvati, M. Sandri, M. Savelainen, D. Scott, E. P. S. Shellard, C. Sirignano, G. Sirri, L. D. Spencer, R. Sunyaev, A. S. Suur-Uski, J. A. Tauber, D. Tavagnacco, M. Tenti, L. Toffolatti, M. Tomasi, T. Trombetti, L. Valenziano, J. Valiviita, B. Van Tent, L. Vibert, P. Vielva, F. Villa, N. Vittorio, B. D. Wandelt, I. K. Wehus, M. White, S. D. M. White, A. Zacchei, and A. Zonca. Planck 2018 results. VI. Cosmological parameters. 2018.

[30] Steve K Choi, Matthew Hasselfield, Shuay-pwu Patty Ho, Brian Koopman, Marius Lungu, Maximilian H Abitbol, Graeme E Addison, Peter A R Ade, Simone Aiola, David Alonso, Mandana Amiri, Stefania Amodeo, Elio Angile, Jason E Austermann, Taylor Baildon, Nick Battaglia, James A Beall, Rachel Bean, Daniel T Becker, J Richard Bond, Sarah Marie Bruno, Erminia Calabrese, Victoria Calafut, Luis E Campusano, Felipe Carrero, Grace E Chesmore, Hsiao-mei Cho., Susan E Clark, Nicholas F Cothard, Devin Crichton, Kevin T Crowley, Omar Darwish, Rahul Datta, Edward V Denison, Mark J Devlin, Cody J Duell, Shannon M Duff, Adriaan J. Duivenvoorden, Jo Dunkley, Rolando Dünner, Thomas Essinger-Hileman, Max Fankhanel, Simone Ferraro, Anna E Fox, Brittany Fuzia, Patricio A Gallardo, Vera Gluscevic, Joseph E Golec, Emily Grace, Megan Gralla, Yilun Guan, Kirsten Hall, Mark Halpern, Dongwon Han, Peter Hargrave, Shawn Henderson, Brandon Hensley, J Colin Hill, Gene C. Hilton, Matt Hilton, Adam D. Hincks, Renée Hložek, Johannes Hubmayr, Kevin M. Huffenberger, John P. Hughes, Leopoldo Infante, Kent Irwin, Rebecca Jackson, Jeff Klein, Kenda Knowles, Arthur Kosowsky, Vincent Lakey, Dale Li, Yaqiong Li, Zack Li, Martine Lokken, Thibaut Louis, Amanda MacInnis, Mathew Madhavacheril, Felipe Maldonado, Maya Mallaby-Kay, Danica Marsden, Loïc Maurin, Jeff McMahon, Felipe Menanteau, Kavilan Moodley, Tim Morton, Sigurd Naess, Toshiya Namikawa, Federico Nati, Laura Newburgh, John P Nibarger, Andrina Nicola, Michael D. Niemack, Michael R. Nolta, John Orlowski-Sherer, Lyman A. Page, Christine G Pappas, Bruce Partridge, Phumlani Phakathi, Heather Prince, Roberto Puddu, Frank J. Qu, Jesus Rivera, Naomi Robertson, Felipe Rojas, Maria Salatino, Emmanuel Schaan, Alessandro Schillaci, Benjamin L. Schmitt, Neelima Sehgal, Blake D. Sherwin, Carlos Sierra, Jon Sievers, Cristobal Sifon, Precious Sikhosana, Sara Simon, David N Spergel, Suzanne T. Staggs, Jason Stevens, Emilie Storer, Dhaneshwar D. Sunder, Eric R. Switzer, Ben Thorne, Robert Thornton, Hy Trac, Jesse Treu, Carole Tucker, Leila R Vale, Alexander Van Engelen, Jeff Van Lanen, Eve M Vavagiakis, Kasey Wagoner, Yuhan Wang, Jonathan T Ward, Edward J Wollack, Zhilei Xu, Fernando Zago, and Ningfeng Zhu. The Atacama Cosmology Telescope: A Measurement of the Cosmic Microwave Background Power Spectra at 98 and 150 GHz. pages 1–42, 2020.

[31] J. T. Sayre, C. L. Reichardt, J. W. Henning, P. A.R. Ade, A. J. Anderson, J. E. Austermann, J. S. Avva, J. A. Beall, A. N. Bender, B. A. Benson, F. Bianchini, L. E. Bleem, J. E. Carlstrom, C. L. Chang, P. Chaubal, H. C. Chiang, R. Citron, C. Corbett Moran, T. M. Crawford, A. T. Crites, T. De Haan, M. A. Dobbs, W. Everett, J. Gallicchio, E. M. George, A. Gilbert, N. Gupta, N. W. Halverson, N. Harrington, G. C. Hilton, G. P. Holder, W. L. Holzapfel, J. D. Hrubes, N. Huang, J. Hubmayr,

K. D. Irwin, L. Knox, A. T. Lee, D. Li, A. Lowitz, J. J. Mcmahon, S. S. Meyer, L. M. Mocanu, J. Montgomery, A. Nadolski, T. Natoli, J. P. Nibarger, G. Noble, V. Novosad, S. Padin, S. Patil, C. Pryke, J. E. Ruhl, B. R. Saliwanchik, K. K. Schaffer, C. Sievers, G. Smecher, A. A. Stark, C. Tucker, K. Vanderlinde, T. Veach, J. D. Vieira, G. Wang, N. Whitehorn, W. L.K. Wu, and V. Yefremenko. Measurements of b -mode polarization of the cosmic microwave background from 500 square degrees of sptpol data. *Physical Review D*, 101(12):122003, jun 2020.

[32] S. Adachi, M. A. O. Aguilar Faúndez, K. Arnold, C. Baccigalupi, D. Barron, D. Beck, F. Bianchini, S. Chapman, K. Cheung, Y. Chinone, K. Crowley, M. Dobbs, H. El Bouhargani, T. Elleflot, J. Errard, G. Fabbian, C. Feng, T. Fujino, N. Galitzki, N. Goeckner-Wald, J. Groh, G. Hall, M. Hasegawa, M. Hazumi, H. Hirose, A. H. Jaffe, O. Jeong, D. Kaneko, N. Katayama, B. Keating, S. Kikuchi, T. Kisner, A. Kusaka, A. T. Lee, D. Leon, E. Linder, L. N. Lowry, F. Matsuda, T. Matsumura, Y. Minami, M. Navaroli, H. Nishino, A. T. P. Pham, D. Poletti, C. L. Reichardt, Y. Segawa, P. Siritanasak, O. Tajima, S. Takakura, S. Takatori, D. Tanabe, G. P. Teply, C. Tsai, C. Vergès, B. Westbrook, and Y. Zhou. A measurement of the CMB E-mode angular power spectrum at subdegree scales from 670 square degrees of POLARBEAR data. may 2020.

[33] S. Adachi, M. A. O. Aguilar Faúndez, K. Arnold, C. Baccigalupi, D. Barron, D. Beck, S. Beckman, F. Bianchini, D. Boettger, J. Borrill, J. Carron, S. Chapman, K. Cheung, Y. Chinone, K. Crowley, A. Cukierman, M. Dobbs, H. El Bouhargani, T. Elleflot, J. Errard, G. Fabbian, C. Feng, T. Fujino, N. Galitzki, N. Goeckner-Wald, J. Groh, G. Hall, N. Halverson, T. Hamada, M. Hasegawa, M. Hazumi, C. A. Hill, L. Howe, Y. Inoue, G. Jaehnig, O. Jeong, D. Kaneko, N. Katayama, B. Keating, R. Keskitalo, S. Kikuchi, T. Kisner, N. Krachmalnicoff, A. Kusaka, A. T. Lee, D. Leon, E. Linder, L. N. Lowry, A. Mangu, F. Matsuda, Y. Minami, M. Navaroli, H. Nishino, A. T. P. Pham, D. Poletti, G. Puglisi, C. L. Reichardt, Y. Segawa, M. Silva-Feaver, P. Siritanasak, N. Stebor, R. Stompor, A. Suzuki, O. Tajima, S. Takakura, S. Takatori, D. Tanabe, G. P. Teply, C. Tsai, C. Verges, B. Westbrook, and Y. Zhou. A Measurement of the Degree Scale CMB B-mode Angular Power Spectrum with POLARBEAR. *The Astrophysical Journal*, 897(1):55, jul 2019.

[34] Wendy L. Freedman. Cosmology at a crossroads, mar 2017.

[35] Licia Verde, Tommaso Treu, and Adam G. Riess. Tensions between the early and late Universe. In *Nature Astronomy*, volume 3, pages 891–895, 2019.

[36] K. Aylor, Z. Hou, L. Knox, K. T. Story, B. A. Benson, L. E. Bleem, J. E. Carlstrom, C. L. Chang, H-M. Cho, R. Chown, T. M. Crawford, A. T. Crites, T. de Haan, M. A. Dobbs, W. B. Everett, E. M. George, N. W. Halverson, N. L. Harrington, G. P. Holder, W. L. Holzapfel, J. D. Hrubes, R. Keisler, A. T. Lee, E. M. Leitch, D. Luong-Van, D. P. Marrone, J. J. McMahon, S. S. Meyer, M. Millea, L. M. Mocanu, J. J. Mohr, T. Natoli, Y. Omori, S. Padin, C. Pryke, C. L. Reichardt, J. E. Ruhl, J. T. Sayre, K. K.

Schaffer, E. Shirokoff, Z. Staniszewski, A. A. Stark, K. Vanderlinde, J. D. Vieira, and R. Williamson. A Comparison of Cosmological Parameters Determined from CMB Temperature Power Spectra from the South Pole Telescope and the Planck Satellite. *The Astrophysical Journal*, 850(1):101, nov 2017.

[37] M D Niemack, P A R Ade, J Aguirre, F Barrientos, J A Beall, J R Bond, J Britton, H M Cho, S Das, M J Devlin, S Dicker, J Dunkley, R. Dünner, J. W. Fowler, A. Hajian, M. Halpern, M. Hasselfield, G. C. Hilton, M. Hilton, J Hubmayr, J P Hughes, L Infante, K D Irwin, N Jarosik, J Klein, A Kosowsky, T. A. Marriage, J. McMahon, F. Menanteau, K. Moodley, J. P. Nibarger, M. R. Nolta, L. A. Page, B. Partridge, E. D. Reese, J. Sievers, D. N. Spergel, S. T. Staggs, R. Thornton, C. Tucker, E. Wollack, and K. W. Yoon. ACTPol: a polarization-sensitive receiver for the Atacama Cosmology Telescope. In *Millimeter, Submillimeter, and Far-Infrared Detectors and Instrumentation for Astronomy V*, volume 7741, page 77411S, 2010.

[38] S. W. Henderson, R. Allison, J. Austermann, T. Baildon, N. Battaglia, J. A. Beall, D. Becker, F. De Bernardis, J. R. Bond, E. Calabrese, S. K. Choi, K. P. Coughlin, K. T. Crowley, R. Datta, M. J. Devlin, S. M. Duff, J. Dunkley, R. Dünner, A. van Engelen, P. A. Gallardo, E. Grace, M. Hasselfield, F. Hills, G. C. Hilton, A. D. Hincks, R. Hlozek, S. P. Ho, J. Hubmayr, K. Huffenberger, J. P. Hughes, K. D. Irwin, B. J. Koopman, A. B. Kosowsky, D. Li, J. McMahon, C. Munson, F. Nati, L. Newburgh, M. D. Niemack, P. Niraula, L. A. Page, C. G. Pappas, M. Salatino, A. Schillaci, B. L. Schmitt, N. Sehgal, B. D. Sherwin, J. L. Sievers, S. M. Simon, D. N. Spergel, S. T. Staggs, J. R. Stevens, R. Thornton, J. Van Lanen, E. M. Vavagiakis, J. T. Ward, and E. J. Wollack. Advanced ACTPol Cryogenic Detector Arrays and Readout. *Journal of Low Temperature Physics*, 184(3-4):772–779, aug 2016.

[39] A. Suzuki, P. Ade, Y. Akiba, C. Aleman, K. Arnold, C. Baccigalupi, B. Barch, D. Barron, A. Bender, D. Boettger, J. Borrill, S. Chapman, Y. Chinone, A. Cukierman, M. Dobbs, A. Ducout, R. Dunner, T. Elleflot, J. Errard, G. Fabbian, S. Feeney, C. Feng, T. Fujino, G. Fuller, A. Gilbert, N. Goeckner-Wald, J. Groh, T. De Haan, G. Hall, N. Halverson, T. Hamada, M. Hasegawa, K. Hattori, M. Hazumi, C. Hill, W. Holzapfel, Y. Hori, L. Howe, Y. Inoue, F. Irie, G. Jaehnig, A. Jaffe, O. Jeong, N. Katayama, J. Kaufman, K. Kazemzadeh, B. Keating, Z. Kermish, R. Keskitalo, T. Kisner, A. Kusaka, M. Le Jeune, A. Lee, D. Leon, E. Linder, L. Lowry, F. Matsuda, T. Matsumura, N. Miller, K. Mizukami, J. Montgomery, M. Navaroli, H. Nishino, J. Peloton, D. Poletti, G. Puglisi, G. Rebeiz, C. Raum, C. Reichardt, P. Richards, C. Ross, K. Rotermund, Y. Segawa, B. Sherwin, I. Shirley, P. Siritanasak, N. Stebor, R. Stompor, J. Suzuki, O. Tajima, S. Takada, S. Takakura, S. Takatori, A. Tikhomirov, T. Tomaru, B. Westbrook, N. Whitehorn, T. Yamashita, A. Zahn, and O. Zahn. The Polarbear-2 and the Simons Array Experiments. *Journal of Low Temperature Physics*, 184(3-4):805–810, aug 2016.

[40] J. A. Grayson, P. A. R. Ade, Z. Ahmed, K. D. Alexander, M. Amiri, D. Barkats, S. J. Benton, C. A. Bischoff, J. J. Bock, H. Boenish, R. Bowens-Rubin, I. Buder,

E. Bullock, V. Buza, J. Connors, J. P. Filippini, S. Fliescher, M. Halpern, S. Harrison, G. C. Hilton, V. V. Hristov, H. Hui, K. D. Irwin, J. Kang, K. S. Karkare, E. Karpel, S. Kefeli, S. A. Kernasovskiy, J. M. Kovac, C. L. Kuo, E. M. Leitch, M. Lueker, K. G. Megerian, V. Monticue, T. Namikawa, C. B. Netterfield, H. T. Nguyen, R. O'Brient, R. W. Ogburn, C. Pryke, C. D. Reintsema, S. Richter, R. Schwarz, C. Sorenson, C. D. Sheehy, Z. K. Staniszewski, B. Steinbach, G. P. Teply, K. L. Thompson, J. E. Tolan, C. Tucker, A. D. Turner, A. G. Vieregg, A. Wandui, A. C. Weber, D. V. Wiebe, J. Willmert, W. L. K. Wu, and K. W. Yoon. BICEP3 performance overview and planned Keck Array upgrade. In Wayne S. Holland and Jonas Zmuidzinas, editors, *Millimeter, Submillimeter, and Far-Infrared Detectors and Instrumentation for Astronomy VIII*, volume 9914, page 99140S. SPIE, jul 2016.

[41] Howard Hui, P. A. R. Ade, Zeeshan Ahmed, Randol Aikin, Kate D. Alexander, Denis Barkats, Steve J. Benton, Colin A. Bischoff, James J. Bock, Rachel Bowens-Rubin, Justus A. Brevik, Immanuel Buder, Eric Bullock, Victor Buza, Jake Connors, James Cornelison, Brendan Crill, Michael Crumrine, Marion Dierickx, Lionel Duband, Cora Dvorkin, Jeff P. Filippini, Stefan Fliescher, James A. Grayson, Grantland Hall, Mark Halpern, Sam A. Harrison, Sergi Hildebrandt, Gene C. Hilton, Kent D. Irwin, Jae Hwan Kang, Kirit S. Karkare, Ethan Karpel, Jonathan Kaufman, Brian G. Keating, Sinan Kefeli, Sarah A. Kernasovskiy, J. M. Kovac, Chao-Lin Kuo, Nicole Larson, King Lau, Erik M. Leitch, Martin Lueker, K. G. Megerian, Lorenzo Moncelsi, Toshiya Namikawa, C. B. Netterfield, H. T. Nguyen, Roger O'brient, R. Walt Ogburn IV, Stephen Palladino, Clement Pryke, Benjamin Racine, Steffen Richter, Alessandro Schillaci, Robert Schwarz, Chris D. Sheehy, Ahmed Soliman, Tyler St Germaine, Zachary K. Staniszewski, Bryan Steinbach, Rashmi Sudiwala, Grant P. Teply, Keith L. Thompson, James E. Tolan, Carole Tucker, Anthony D. Turner, Caterina Umiltà, Abigail G. Vieregg, Albert Wandui, Alexis C. Weber, Don Wiebe, Justin Willmert, Chin Lin Wong, Wai Ling K. Wu, Eric Yang, Ki Won Yoon, and Cheng Zheng. BICEP Array: a multi-frequency degree-scale CMB polarimeter. In Jonas Zmuidzinas and Jian-Rong Gao, editors, *Millimeter, Submillimeter, and Far-Infrared Detectors and Instrumentation for Astronomy IX*, volume 10708, page 49. SPIE, jul 2018.

[42] Peter Ade, James Aguirre, Zeeshan Ahmed, Simone Aiola, Aamir Ali, David Alonso, Marcelo A. Alvarez, Kam Arnold, Peter Ashton, Jason Austermann, Humna Awan, Carlo Baccigalupi, Taylor Baildon, Darcy Barron, Nick Battaglia, Richard Battye, Eric Baxter, Andrew Bazarko, James A. Beall, Rachel Bean, Dominic Beck, Shawn Beckman, Benjamin Beringue, Federico Bianchini, Steven Boada, David Boettger, J. Richard Bond, Julian Borrill, Michael L. Brown, Sarah Marie Bruno, Sean Bryan, Erminia Calabrese, Victoria Calafut, Paolo Calisse, Julien Carron, Anthony Challinor, Grace Chesmore, Yuji Chinone, Jens Chluba, Hsiao Mei Sherry Cho, Steve Choi, Gabriele Coppi, Nicholas F. Cothard, Kevin Coughlin, Devin Crichton, Kevin D. Crowley, Kevin T. Crowley, Ari Cukierman, John M. D'Ewart, Rolando Dünner, Tijmen De Haan, Mark Devlin, Simon Dicker, Joy Didier, Matt Dobbs, Bradley Dober, Cody J.

Duell, Shannon Duff, Adri Duivenvoorden, Jo Dunkley, John Dusatko, Josquin Errard, Giulio Fabbian, Stephen Feeney, Simone Ferraro, Pedro Fluxà, Katherine Freese, Josef C. Frisch, Andrei Frolov, George Fuller, Brittany Fuzia, Nicholas Galitzki, Patricio A. Gallardo, Jose Tomas Galvez Ghersi, Jiansong Gao, Eric Gawiser, Martina Gerbino, Vera Gluscevic, Neil Goeckner-Wald, Joseph Golec, Sam Gordon, Megan Gralla, Daniel Green, Arpi Grigorian, John Groh, Chris Groppi, Yilun Guan, Jon E. Gudmundsson, Dongwon Han, Peter Hargrave, Masaya Hasegawa, Matthew Hasselfield, Makoto Hattori, Victor Haynes, Masashi Hazumi, Yizhou He, Erin Healy, Shawn W. Henderson, Carlos Hervias-Caimapo, Charles A. Hill, J. Colin Hill, Gene Hilton, Matt Hilton, Adam D. Hincks, Gary Hinshaw, Renée Hložek, Shirley Ho, Shuay Pwu Patty Ho, Logan Howe, Zhiqi Huang, Johannes Hubmayr, Kevin Huffenberger, John P. Hughes, Anna Ijjas, Margaret Ikape, Kent Irwin, Andrew H. Jaffe, Bhuvnesh Jain, Oliver Jeong, Daisuke Kaneko, Ethan D. Karpel, Nobuhiko Katayama, Brian Keating, Sarah S. Kernasovskiy, Reijo Keskitalo, Theodore Kisner, Kenji Kiuchi, Jeff Klein, Kenda Knowles, Brian Koopman, Arthur Kosowsky, Nicoletta Krachmalnicoff, Stephen E. Kuenstner, Chao Lin Kuo, Akito Kusaka, Jacob Lashner, Adrian Lee, Eunseong Lee, David Leon, Jason S.Y. Leung, Antony Lewis, Yaqiong Li, Zack Li, Michele Limon, Eric Linder, Carlos Lopez-Caraballo, Thibaut Louis, Lindsay Lowry, Marius Lungu, Mathew Madhavacheril, Daisy Mak, Felipe Maldonado, Hamdi Mani, Ben Mates, Frederick Matsuda, Loïc Maurin, Phil Mauskopf, Andrew May, Nialh McCallum, Chris McKenney, Jeff McMahon, P. Daniel Meerburg, Joel Meyers, Amber Miller, Mark Mirmelstein, Kavilan Moodley, Moritz Munchmeyer, Charles Munson, Sigurd Naess, Federico Nati, Martin Navaroli, Laura Newburgh, Ho Nam Nguyen, Michael Niemack, Haruki Nishino, John Orlowski-Scherer, Lyman Page, Bruce Partridge, Julien Peloton, Francesca Perrotta, Lucio Piccirillo, Giampaolo Pisano, Davide Poletti, Roberto Puddu, Giuseppe Puglisi, Chris Raum, Christian L. Reichardt, Mathieu Remazeilles, Yoel Rephaeli, Dominik Riechers, Felipe Rojas, Anirban Roy, Sharon Sadeh, Yuki Sakurai, Maria Salatino, Mayuri Sathyanarayana Rao, Emmanuel Schaan, Marcel Schmittfull, Neelima Sehgal, Joseph Seibert, Uros Seljak, Blake Sherwin, Meir Shimon, Carlos Sierra, Jonathan Sievers, Precious Sikhosana, Maximiliano Silva-Feaver, Sara M. Simon, Adrian Sinclair, Praween Siritanasak, Kendrick Smith, Stephen R. Smith, David Spergel, Suzanne T. Staggs, George Stein, Jason R. Stevens, Radek Stompor, Aritoki Suzuki, Osamu Tajima, Satoru Takakura, Grant Teply, Daniel B. Thomas, Ben Thorne, Robert Thornton, Hy Trac, Calvin Tsai, Carole Tucker, Joel Ullom, Sunny Vagnozzi, Alexander Van Engelen, Jeff Van Lanen, Daniel D.Van Winkle, Eve M. Vavagiakis, Clara Vergès, Michael Vissers, Kasey Wagoner, Samantha Walker, Jon Ward, Ben Westbrook, Nathan Whitehorn, Jason Williams, Joel Williams, Edward J. Wollack, Zhilei Xu, Byeonghee Yu, Cyndia Yu, Fernando Zago, Hezi Zhang, and Ningfeng Zhu. The Simons Observatory: Science goals and forecasts. *Journal of Cosmology and Astroparticle Physics*, 2019(2):056, feb 2019.

[43] Kevork N. Abazajian, Peter Adshead, Zeeshan Ahmed, Steven W. Allen, David Alonso, Kam S. Arnold, Carlo Baccigalupi, James G. Bartlett, Nicholas Battaglia, Bradford A.

Benson, Colin A. Bischoff, Julian Borrill, Victor Buza, Erminia Calabrese, Robert Caldwell, John E. Carlstrom, Clarence L. Chang, Thomas M. Crawford, Francis-Yan Cyr-Racine, Francesco De Bernardis, Tijmen de Haan, Sperello di Serego Alighieri, Joanna Dunkley, Cora Dvorkin, Josquin Errard, Giulio Fabbian, Stephen Feeney, Simone Ferraro, Jeffrey P. Filippini, Raphael Flauger, George M. Fuller, Vera Gluscevic, Daniel Green, Daniel Grin, Evan Grohs, Jason W. Henning, J. Colin Hill, Renee Hlozek, Gilbert Holder, William Holzapfel, Wayne Hu, Kevin M. Huffenberger, Reijo Keskitalo, Lloyd Knox, Arthur Kosowsky, John Kovac, Ely D. Kovetz, Chao-Lin Kuo, Akito Kusaka, Maude Le Jeune, Adrian T. Lee, Marc Lilley, Marilena Loverde, Mathew S. Madhavacheril, Adam Mantz, David J. E. Marsh, Jeffrey McMahon, Pieter Daniel Meerburg, Joel Meyers, Amber D. Miller, Julian B. Munoz, Ho Nam Nguyen, Michael D. Niemack, Marco Peloso, Julien Peloton, Levon Pogosian, Clement Pryke, Marco Raveri, Christian L. Reichardt, Graca Rocha, Aditya Rotti, Emmanuel Schaan, Marcel M. Schmittfull, Douglas Scott, Neelima Sehgal, Sarah Shandera, Blake D. Sherwin, Tristan L. Smith, Lorenzo Sorbo, Glenn D. Starkman, Kyle T. Story, Alexander van Engelen, Joaquin D. Vieira, Scott Watson, Nathan Whitehorn, and W. L. Kimmy Wu. CMB-S4 Science Book, First Edition. oct 2016.

[44] Wayne Hu. http://background.uchicago.edu/˜whu/.

[45] Wayne Hu and Gilbert P Holder. Model-independent reionization observables in the CMB. *Physical Review D*, 68(2):1–4, 2003.

[46] Zhen Hou, Ryan Keisler, Lloyd Knox, Marius Millea, and Christian Reichardt. How massless neutrinos affect the cosmic microwave background damping tail. *Physical Review D - Particles, Fields, Gravitation and Cosmology*, 87(8):1–11, 2013.

[47] Wayne Hu and Takemi Okamoto. Mass Reconstruction with Cosmic Microwave Background Polarization. *The Astrophysical Journal*, 574(2):566–574, 2002.

[48] F. Bianchini, W. L. K. Wu, P. A. R. Ade, A. J. Anderson, J. E. Austermann, J. S. Avva, J. A. Beall, A. N. Bender, B. A. Benson, L. E. Bleem, J. E. Carlstrom, C. L. Chang, P. Chaubal, H. C. Chiang, R. Citron, C. Corbett Moran, T. M. Crawford, A. T. Crites, T. de Haan, M. A. Dobbs, W. Everett, J. Gallicchio, E. M. George, A. Gilbert, N. Gupta, N. W. Halverson, N. Harrington, J. W. Henning, G. C. Hilton, G. P. Holder, W. L. Holzapfel, J. D. Hrubes, N. Huang, J. Hubmayr, K. D. Irwin, L. Knox, A. T. Lee, D. Li, A. Lowitz, A. Manzotti, J. J. McMahon, S. S. Meyer, M. Millea, L. M. Mocanu, J. Montgomery, A. Nadolski, T. Natoli, J. P. Nibarger, G. Noble, V. Novosad, Y. Omori, S. Padin, S. Patil, C. Pryke, C. L. Reichardt, J. E. Ruhl, B. R. Saliwanchik, J. T. Sayre, K. K. Schaffer, C. Sievers, G. Simard, G. Smecher, A. A. Stark, K. T. Story, C. Tucker, K. Vanderlinde, T. Veach, J. D. Vieira, G. Wang, N. Whitehorn, and V. Yefremenko. Constraints on Cosmological Parameters from the 500 deg 2 SPTPOL Lensing Power Spectrum. *The Astrophysical Journal*, 888(2):119, jan 2020.

[49] Julien Lesgourgues, Laurence Perotto, Sergio Pastor, and Michel Piat. Probing neutrino masses with CMB lensing extraction. *Physical Review D - Particles, Fields, Gravitation and Cosmology*, 73(4):1–13, 2006.

[50] Julien Lesgourgues and Sergio Pastor. Massive neutrinos and cosmology. *Physics Reports*, 429(6):307–379, mar 2006.

[51] Roland De Putter, Oliver Zahn, and Eric V Linder. CMB lensing constraints on neutrinos and dark energy. *Physical Review D - Particles, Fields, Gravitation and Cosmology*, 79(6):1–18, 2009.

[52] Aoife Boyle. Understanding the neutrino mass constraints achievable by combining CMB lensing and spectroscopic galaxy surveys. *Journal of Cosmology and Astroparticle Physics*, 2019(4):038, apr 2019.

[53] Blake D. Sherwin, Joanna Dunkley, Sudeep Das, John W. Appel, J. Richard Bond, C. Sofia Carvalho, Mark J. Devlin, Rolando Dünner, Thomas Essinger-Hileman, Joseph W. Fowler, Amir Hajian, Mark Halpern, Matthew Hasselfield, Adam D. Hincks, Renée Hlozek, John P. Hughes, Kent D. Irwin, Jeff Klein, Arthur Kosowsky, Tobias A. Marriage, Danica Marsden, Kavilan Moodley, Felipe Menanteau, Michael D. Niemack, Michael R. Nolta, Lyman A. Page, Lucas Parker, Erik D. Reese, Benjamin L. Schmitt, Neelima Sehgal, Jon Sievers, David N. Spergel, Suzanne T. Staggs, Daniel S. Swetz, Eric R. Switzer, Robert Thornton, Katerina Visnjic, and Ed Wollack. Evidence for dark energy from the cosmic microwave background alone using the atacama cosmology telescope lensing measurements. *Physical Review Letters*, 107(2):021302, jul 2011.

[54] Toshiya Namikawa, François R. Bouchet, and Atsushi Taruya. CMB lensing bispectrum as a probe of modified gravity theories. *Physical Review D*, 98(4):43530, 2018.

[55] Sukhdeep Singh, Shadab Alam, Rachel Mandelbaum, Uroš Seljak, Sergio Rodriguez-Torres, and Shirley Ho. Probing gravity with a joint analysis of galaxy and CMB lensing and SDSS spectroscopy. *Monthly Notices of the Royal Astronomical Society*, 482(1):785–806, jan 2019.

[56] Yucheng Zhang, Anthony R Pullen, Shadab Alam, Sukhdeep Singh, Etienne Burtin, Chia-hsun Chuang, Jiamin Hou, Brad W Lyke, Adam D Myers, Richard Neveux, Ashley J Ross, Graziano Rossi, and Cheng Zhao. Testing General Relativity on cosmological scales at redshift 1.5 with quasar and CMB lensing. 15(July):1–15, 2020.

[57] Uros Seljak. Gravitational Lensing Effect on Cosmic Microwave Background Anisotropies: A Power Spectrum Approach. *The Astrophysical Journal*, 463:1, 1996.

[58] K T Story, C L Reichardt, Z Hou, R Keisler, K A Aird, B A Benson, L E Bleem, J E Carlstrom, C L Chang, H. M. Cho, T M Crawford, A T Crites, T. De Haan, M A Dobbs, J. Dudley, B. Follin, E. M. George, N. W. Halverson, G. P. Holder, W. L. Holzapfel, S. Hoover, J. D. Hrubes, M. Joy, L. Knox, A. T. Lee, E. M. Leitch,

M. Lueker, D. Luong-Van, J. J. McMahon, J. Mehl, S. S. Meyer, M. Millea, J. J. Mohr, T. E. Montroy, S. Padin, T. Plagge, C. Pryke, J. E. Ruhl, J. T. Sayre, K. K. Schaffer, L. Shaw, E. Shirokoff, H. G. Spieler, Z. Staniszewski, A. A. Stark, A. Van Engelen, K. Vanderlinde, J. D. Vieira, R. Williamson, and O. Zahn. A measurement of the cosmic microwave background damping tail from the 2500-square-degree SPT-SZ survey. *Astrophysical Journal*, 779(1), 2013.

[59] Simone Aiola, Erminia Calabrese, Sigurd Naess, Benjamin L Schmitt, Max Abitbol, Graeme Addison, Peter A R Ade, David Alonso, Mandana Amiri, Stefania Amodeo, Elio Angile, Jason Austermann, Taylor Baildon, Nick Battaglia, James A Beall, Rachel Bean, Felipe Carrero, Grace E Chesmore, Hsiao-mei Cho, Steve K Choi, Susan E Clark, Nicholas F Cothard, Kevin Coughlin, Devin Crichton, Kevin T Crowley, Omar Darwish, Rahul Datta, Mark J Devlin, Brad Dober, Cody J Duell, Shannon M Duff, Thomas Essinger-hileman, Max Fankhanel, Simone Ferraro, Anna E Fox, Brittany Fuzia, Patricio A Gallardo, Vera Gluscevic, Joey Golec, Peter Hargrave, Matthew Hasselfield, Shawn Henderson, Brandon Hensley, J Colin Hill, Shuay-pwu Patty Ho, Johannes Hubmayr, Kevin M Huffenberger, John P Hughes, Leopoldo Infante, Kent Irwin, Toshiya Namikawa, Federico Nati, Laura Newburgh, John Nibarger, Andrina Nicola, Bruce Partridge, Phumlani Phakathi, Heather Prince, Roberto Puddu, Frank J Qu, Jesus Rivera, Neelima Sehgal, Blake D Sherwin, Carlos Sierra, Jon Sievers, Cristobal Sifon, Precious Sikhosana, Dhaneshwar D Sunder, Eric R Switzer, Ben Thorne, Robert Thornton, Hy Trac, Jesse Treu, Carole Tucker, Leila Vale, Alexander Van Engelen, Eve M Vavagiakis, Kasey Wagoner, Yuhan Wang, Jonathan T Ward, Edward J Wollack, Zhilei Xu, Fernando Zago, and Ningfeng Zhu. THE ATACAMA COSMOLOGY TELESCOPE : DR4 MAPS AND COSMOLOGICAL RESULTS We present new arcminute-resolution maps of the Cosmic Microwave Background temperature and polarization anisotropy from the Atacama Cosmology Telescope , using data taken from 2013 – 201. pages 1–30, 2020.

[60] Uroš Seljak. Reconstructing projected matter density power spectrum from cosmic microwave background. *Physical Review D - Particles, Fields, Gravitation and Cosmology*, 59(12):1–15, 1999.

[61] A. Van Engelen, R. Keisler, O. Zahn, K. A. Aird, B. A. Benson, L. E. Bleem, J. E. Carlstrom, C. L. Chang, H. M. Cho, T. M. Crawford, A. T. Crites, T. De Haan, M. A. Dobbs, J. Dudley, E. M. George, N. W. Halverson, G. P. Holder, W. L. Holzapfel, S. Hoover, Z. Hou, J. D. Hrubes, M. Joy, L. Knox, A. T. Lee, E. M. Leitch, M. Lueker, D. Luong-Van, J. J. McMahon, J. Mehl, S. S. Meyer, M. Millea, J. J. Mohr, T. E. Montroy, T. Natoli, S. Padin, T. Plagge, C. Pryke, C. L. Reichardt, J. E. Ruhl, J. T. Sayre, K. K. Schaffer, L. Shaw, E. Shirokoff, H. G. Spieler, Z. Staniszewski, A. A. Stark, K. Story, K. Vanderlinde, J. D. Vieira, and R. Williamson. A measurement of gravitational lensing of the microwave background using south pole telescope data. *Astrophysical Journal*, 756(2), 2012.

[62] K. T. Story, D. Hanson, P. A.R. Ade, K. A. Aird, J. E. Austermann, J. A. Beall, A. N.

Bender, B. A. Benson, L. E. Bleem, J. E. Carlstrom, C. L. Chang, H. C. Chiang, H. M. Cho, R. Citron, T. M. Crawford, A. T. Crites, T. De Haan, M. A. Dobbs, W. Everett, J. Gallicchio, J. Gao, E. M. George, A. Gilbert, N. W. Halverson, N. Harrington, J. W. Henning, G. C. Hilton, G. P. Holder, W. L. Holzapfel, S. Hoover, Z. Hou, J. D. Hrubes, N. Huang, J. Hubmayr, K. D. Irwin, R. Keisler, L. Knox, A. T. Lee, E. M. Leitch, D. Li, C. Liang, D. Luong-Van, J. J. McMahon, J. Mehl, S. S. Meyer, L. Mocanu, T. E. Montroy, T. Natoli, J. P. Nibarger, V. Novosad, S. Padin, C. Pryke, C. L. Reichardt, J. E. Ruhl, B. R. Saliwanchik, J. T. Sayre, K. K. Schaffer, G. Smecher, A. A. Stark, C. Tucker, K. Vanderlinde, J. D. Vieira, G. Wang, N. Whitehorn, V. Yefremenko, and O. Zahn. a Measurement of the Cosmic Microwave Background Gravitational Lensing Potential From 100 Square Degrees of Sptpol Data. *Astrophysical Journal*, 810(1), 2015.

[63] Y. Omori, R. Chown, G. Simard, K. T. Story, K. Aylor, E. J. Baxter, B. A. Benson, L. E. Bleem, J. E. Carlstrom, C. L. Chang, H-M. Cho, T. M. Crawford, A. T. Crites, T. de Haan, M. A. Dobbs, W. B. Everett, E. M. George, N. W. Halverson, N. L. Harrington, G. P. Holder, Z. Hou, W. L. Holzapfel, J. D. Hrubes, L. Knox, A. T. Lee, E. M. Leitch, D. Luong-Van, A. Manzotti, D. P. Marrone, J. J. McMahon, S. S. Meyer, L. M. Mocanu, J. J. Mohr, T. Natoli, S. Padin, C. Pryke, C. L. Reichardt, J. E. Ruhl, J. T. Sayre, K. K. Schaffer, E. Shirokoff, Z. Staniszewski, A. A. Stark, K. Vanderlinde, J. D. Vieira, R. Williamson, and O. Zahn. A 2500 deg 2 CMB Lensing Map from Combined South Pole Telescope and Planck Data . *The Astrophysical Journal*, 849(2):124, 2017.

[64] W L K Wu, L M Mocanu, P A R Ade, A J Anderson, J E Austermann, J S Avva, J A Beall, A N Bender, B A Benson, F Bianchini, L E Bleem, J E Carlstrom, C L Chang, H C Chiang, R Citron, C Corbett Moran, T M Crawford, A T Crites, T De Haan, M A Dobbs, W Everett, J Gallicchio, E M George, A Gilbert, N Gupta, N W Halverson, N Harrington, J W Henning, G C Hilton, G P Holder, W L Holzapfel, Z Hou, J D Hrubes, N Huang, J Hubmayr, K D Irwin, L Knox, A T Lee, D Li, A Lowitz, A Manzotti, J. J. McMahon, S S Meyer, M Millea, J Montgomery, A Nadolski, T Natoli, J P Nibarger, G I Noble, V Novosad, Y Omori, S Padin, S Patil, C Pryke, C L Reichardt, J E Ruhl, B R Saliwanchik, J T Sayre, K K Schaffer, C Sievers, G Simard, G Smecher, A A Stark, K T Story, C Tucker, K Vanderlinde, T Veach, J D Vieira, G Wang, N Whitehorn, and V Yefremenko. A Measurement of the Cosmic Microwave Background Lensing Potential and Power Spectrum from 500 deg 2 of SPTpol Temperature and Polarization Data. *The Astrophysical Journal*, 884(1):70, 2019.

[65] Sudeep Das, Blake D Sherwin, Paula Aguirre, John W Appel, J Richard Bond, C Sofia Carvalho, Mark J Devlin, Joanna Dunkley, Rolando Dünner, Thomas Essinger-Hileman, Joseph W Fowler, Amir Hajian, Mark Halpern, Matthew Hasselfield, Adam D Hincks, Renée Hlozek, Kevin M. Huffenberger, John P Hughes, Kent D Irwin, Jeff Klein, Arthur Kosowsky, Robert H Lupton, Tobias A Marriage, Danica Marsden, Felipe Menanteau, Kavilan Moodley, Michael D Niemack, Michael R Nolta, Lyman A Page, Lucas Parker, Erik D Reese, Benjamin L Schmitt, Neelima Sehgal, Jon Sievers,

David N Spergel, Suzanne T Staggs, Daniel S Swetz, Eric R Switzer, Robert Thornton, Katerina Visnjic, and Ed Wollack. Detection of the power spectrum of cosmic microwave background lensing by the atacama cosmology telescope. *Physical Review Letters*, 107(2):1–5, 2011.

[66] Blake D. Sherwin, Alexander Van Engelen, Neelima Sehgal, Mathew Madhavacheril, Graeme E. Addison, Simone Aiola, Rupert Allison, Nicholas Battaglia, Daniel T. Becker, James A. Beall, J. Richard Bond, Erminia Calabrese, Rahul Datta, Mark J. Devlin, Rolando Dünner, Joanna Dunkley, Anna E. Fox, Patricio Gallardo, Mark Halpern, Matthew Hasselfield, Shawn Henderson, J. Colin Hill, Gene C. Hilton, Johannes Hubmayr, John P. Hughes, Adam D. Hincks, Renée Hlozek, Kevin M. Huffenberger, Brian Koopman, Arthur Kosowsky, Thibaut Louis, Loïc Maurin, Jeff McMahon, Kavilan Moodley, Sigurd Naess, Federico Nati, Laura Newburgh, Michael D. Niemack, Lyman A. Page, Jonathan Sievers, David N. Spergel, Suzanne T. Staggs, Robert J. Thornton, Jeff Van Lanen, Eve Vavagiakis, and Edward J. Wollack. Two-season Atacama Cosmology Telescope polarimeter lensing power spectrum. *Physical Review D*, 95(12):1–17, 2017.

[67] Omar Darwish, Mathew S. Madhavacheril, Blake Sherwin, Simone Aiola, Nicholas Battaglia, James A. Beall, Daniel T. Becker, J. Richard Bond, Erminia Calabrese, Steve Choi, Mark J. Devlin, Jo Dunkley, Rolando Dünner, Simone Ferraro, Anna E. Fox, Patricio A. Gallardo, Yilun Guan, Mark Halpern, Dongwon Han, Matthew Hasselfield, J. Colin Hill, Gene C. Hilton, Matt Hilton, Adam D. Hincks, Shuay-Pwu Patty Ho, J. Hubmayr, John P. Hughes, Brian J. Koopman, Arthur Kosowsky, J. Van Lanen, Thibaut Louis, Marius Lungu, Amanda MacInnis, Loïc Maurin, Jeffrey McMahon, Kavilan Moodley, Sigurd Naess, Toshiya Namikawa, Laura Newburgh, John P. Nibarger, Micheal D. Niemack, Lyman A. Page, Bruce Partridge, Frank J. Qu, Naomi Robertson, Benjamin Schmitt, Neelima Sehgal, Cristóbal Sifón, David N. Spergel, Suzanne Staggs, Emilie Storer, Alexander van Engelen, and Edward J. Wollack. The Atacama Cosmology Telescope: A CMB lensing mass map over 2100 square degrees of sky and its cross-correlation with BOSS-CMASS galaxies. 2020.

[68] P. A.R. Ade, N. Aghanim, C. Armitage-Caplan, M. Arnaud, M. Ashdown, F. Atrio-Barandela, J. Aumont, C. Baccigalupi, A. J. Banday, R. B. Barreiro, J. G. Bartlett, S. Basak, E. Battaner, K. Benabed, A. Benoît, A. Benoit-Lévy, J. P. Bernard, M. Bersanelli, P. Bielewicz, J. Bobin, J. J. Bock, A. Bonaldi, L. Bonavera, J. R. Bond, J. Borrill, F. R. Bouchet, M. Bridges, M. Bucher, C. Burigana, R. C. Butler, J. F. Cardoso, A. Catalano, A. Challinor, A. Chamballu, H. C. Chiang, L. Y. Chiang, P. R. Christensen, S. Church, D. L. Clements, S. Colombi, L. P.L. Colombo, F. Couchot, A. Coulais, B. P. Crill, A. Curto, F. Cuttaia, L. Danese, R. D. Davies, R. J. Davis, P. De Bernardis, A. De Rosa, G. De Zotti, T. Déchelette, J. Delabrouille, J. M. Delouis, F. X. Désert, C. Dickinson, J. M. Diego, H. Dole, S. Donzelli, O. Doré, M. Douspis, J. Dunkley, X. Dupac, G. Efstathiou, T. A. Enßlin, H. K. Eriksen, F. Finelli, O. Forni, M. Frailis, E. Franceschi, S. Galeotta, K. Ganga, M. Giard, G. Giardino, Y. Giraud-Héraud, J. González-Nuevo, K. M. Górski, S. Gratton, A. Gregorio,

A. Gruppuso, J. E. Gudmundsson, F. K. Hansen, D. Hanson, D. Harrison, S. Henrot-Versillé, C. Hernández-Monteagudo, D. Herranz, S. R. Hildebrandt, E. Hivon, S. Ho, M. Hobson, W. A. Holmes, A. Hornstrup, W. Hovest, K. M. Huffenberger, A. H. Jaffe, T. R. Jaffe, W. C. Jones, M. Juvela, E. Keihänen, R. Keskitalo, T. S. Kisner, R. Kneissl, J. Knoche, L. Knox, M. Kunz, H. Kurki-Suonio, G. Lagache, A. Lähteenmäki, J. M. Lamarre, A. Lasenby, R. J. Laureijs, A. Lavabre, C. R. Lawrence, J. P. Leahy, R. Leonardi, J. León-Tavares, J. Lesgourgues, A. Lewis, M. Liguori, P. B. Lilje, M. Linden-Vørnle, M. López-Caniego, P. M. Lubin, J. F. Maciás-Pérez, B. Maffei, D. Maino, N. Mandolesi, A. Mangilli, M. Maris, D. J. Marshall, P. G. Martin, E. Martínez-González, S. Masi, M. Massardi, S. Matarrese, F. Matthai, P. Mazzotta, A. Melchiorri, L. Mendes, A. Mennella, M. Migliaccio, S. Mitra, M. A. Miville-Deschênes, A. Moneti, L. Montier, G. Morgante, D. Mortlock, A. Moss, D. Munshi, J. A. Murphy, P. Naselsky, F. Nati, P. Natoli, C. B. Netterfield, H. U. Nørgaard-Nielsen, F. Noviello, D. Novikov, I. Novikov, S. Osborne, C. A. Oxborrow, F. Paci, L. Pagano, F. Pajot, D. Paoletti, B. Partridge, F. Pasian, G. Patanchon, O. Perdereau, L. Perotto, F. Perrotta, F. Piacentini, M. Piat, E. Pierpaoli, D. Pietrobon, S. Plaszczynski, E. Pointecouteau, G. Polenta, N. Ponthieu, L. Popa, T. Poutanen, G. W. Pratt, G. Prézeau, S. Prunet, J. L. Puget, A. R. Pullen, J. P. Rachen, R. Rebolo, M. Reinecke, M. Remazeilles, C. Renault, S. Ricciardi, T. Riller, I. Ristorcelli, G. Rocha, C. Rosset, G. Roudier, M. Rowan-Robinson, J. A. Rubinõ-Martín, B. Rusholme, M. Sandri, D. Santos, G. Savini, D. Scott, M. D. Seiffert, E. P.S. Shellard, K. Smith, L. D. Spencer, J. L. Starck, V. Stolyarov, R. Stompor, R. Sudiwala, R. Sunyaev, F. Sureau, D. Sutton, A. S. Suur-Uski, J. F. Sygnet, J. A. Tauber, D. Tavagnacco, L. Terenzi, L. Toffolatti, M. Tomasi, M. Tristram, M. Tucci, J. Tuovinen, G. Umana, L. Valenziano, J. Valiviita, B. Van Tent, P. Vielva, F. Villa, N. Vittorio, L. A. Wade, B. D. Wandelt, M. White, S. D.M. White, D. Yvon, A. Zacchei, and A. Zonca. Planck 2013 results. XVII. Gravitational lensing by large-scale structure. *Astronomy and Astrophysics*, 571:A17, nov 2014.

[69] Planck Collaboration, P. A. R. Ade, N. Aghanim, M. Arnaud, M. Ashdown, J. Aumont, C. Baccigalupi, A. J. Banday, R. B. Barreiro, J. G. Bartlett, N. Bartolo, S. Basak, E. Battaner, K. Benabed, A. Benoît, A. Benoit-Lévy, J. P. Bernard, M. Bersanelli, P. Bielewicz, J. J. Bock, A. Bonaldi, L. Bonavera, J. R. Bond, J. Borrill, F. R. Bouchet, F. Boulanger, M. Bucher, C. Burigana, R. C. Butler, E. Calabrese, J. F. Cardoso, A. Catalano, A. Challinor, A. Chamballu, H. C. Chiang, P. R. Christensen, S. Church, D. L. Clements, S. Colombi, L. P. L. Colombo, C. Combet, F. Couchot, A. Coulais, B. P. Crill, A. Curto, F. Cuttaia, L. Danese, R. D. Davies, R. J. Davis, P. de Bernardis, A. de Rosa, G. de Zotti, J. Delabrouille, F. X. Désert, J. M. Diego, H. Dole, S. Donzelli, O. Doré, M. Douspis, A. Ducout, J. Dunkley, X. Dupac, G. Efstathiou, F. Elsner, T. A. Enßlin, H. K. Eriksen, J. Fergusson, F. Finelli, O. Forni, M. Frailis, A. A. Fraisse, E. Franceschi, A. Frejsel, S. Galeotta, S. Galli, K. Ganga, M. Giard, Y. Giraud-Héraud, E. Gjerløw, J. González-Nuevo, K. M. Górski, S. Gratton, A. Gregorio, A. Gruppuso, J. E. Gudmundsson, F. K. Hansen, D. Hanson, D. L. Harrison, S. Henrot-Versillé, C. Hernández-Monteagudo, D. Herranz, S. R.

Hildebrandt, E. Hivon, M. Hobson, W. A. Holmes, A. Hornstrup, W. Hovest, K. M. Huffenberger, G. Hurier, A. H. Jaffe, T. R. Jaffe, W. C. Jones, M. Juvela, E. Keihänen, R. Keskitalo, T. S. Kisner, R. Kneissl, J. Knoche, M. Kunz, H. Kurki-Suonio, G. Lagache, A. Lähteenmäki, J. M. Lamarre, A. Lasenby, M. Lattanzi, C. R. Lawrence, R. Leonardi, J. Lesgourgues, F. Levrier, A. Lewis, M. Liguori, P. B. Lilje, M. Linden-Vørnle, M. López-Caniego, P. M. Lubin, J. F. Macías-Pérez, G. Maggio, D. Maino, N. Mandolesi, A. Mangilli, M. Maris, P. G. Martin, E. Martínez-González, S. Masi, S. Matarrese, P. McGehee, P. R. Meinhold, A. Melchiorri, L. Mendes, A. Mennella, M. Migliaccio, S. Mitra, M. A. Miville-Deschênes, A. Moneti, L. Montier, G. Morgante, D. Mortlock, A. Moss, D. Munshi, J. A. Murphy, P. Naselsky, F. Nati, P. Natoli, C. B. Netterfield, H. U. Nørgaard-Nielsen, F. Noviello, D. Novikov, I. Novikov, C. A. Oxborrow, F. Paci, L. Pagano, F. Pajot, D. Paoletti, F. Pasian, G. Patanchon, O. Perdereau, L. Perotto, F. Perrotta, V. Pettorino, F. Piacentini, M. Piat, E. Pierpaoli, D. Pietrobon, S. Plaszczynski, E. Pointecouteau, G. Polenta, L. Popa, G. W. Pratt, G. Prézeau, S. Prunet, J. L. Puget, J. P. Rachen, W. T. Reach, R. Rebolo, M. Reinecke, M. Remazeilles, C. Renault, A. Renzi, I. Ristorcelli, G. Rocha, C. Rosset, M. Rossetti, G. Roudier, M. Rowan-Robinson, J. A. Rubiño-Martín, B. Rusholme, M. Sandri, D. Santos, M. Savelainen, G. Savini, D. Scott, M. D. Seiffert, E. P. S. Shellard, L. D. Spencer, V. Stolyarov, R. Stompor, R. Sudiwala, R. Sunyaev, D. Sutton, A. S. Suur-Uski, J. F. Sygnet, J. A. Tauber, L. Terenzi, L. Toffolatti, M. Tomasi, M. Tristram, M. Tucci, J. Tuovinen, L. Valenziano, J. Valiviita, B. Van Tent, P. Vielva, F. Villa, L. A. Wade, B. D. Wandelt, I. K. Wehus, M. White, D. Yvon, A. Zacchei, and A. Zonca. Planck 2015 results. XV. Gravitational lensing. 2015.

[70] Planck Collaboration, N. Aghanim, Y. Akrami, M. Ashdown, J. Aumont, C. Baccigalupi, M. Ballardini, A. J. Banday, R. B. Barreiro, N. Bartolo, S. Basak, K. Benabed, J. P. Bernard, M. Bersanelli, P. Bielewicz, J. J. Bock, J. R. Bond, J. Borrill, F. R. Bouchet, F. Boulanger, M. Bucher, C. Burigana, E. Calabrese, J. F. Cardoso, J. Carron, A. Challinor, H. C. Chiang, L. P. L. Colombo, C. Combet, B. P. Crill, F. Cuttaia, P. de Bernardis, G. de Zotti, J. Delabrouille, E. Di Valentino, J. M. Diego, O. Doré, M. Douspis, A. Ducout, X. Dupac, G. Efstathiou, F. Elsner, T. A. Enßlin, H. K. Eriksen, Y. Fantaye, R. Fernandez-Cobos, F. Forastieri, M. Frailis, A. A. Fraisse, E. Franceschi, A. Frolov, S. Galeotta, S. Galli, K. Ganga, R. T. Génova-Santos, M. Gerbino, T. Ghosh, J. González-Nuevo, K. M. Górski, S. Gratton, A. Gruppuso, J. E. Gudmundsson, J. Hamann, W. Handley, F. K. Hansen, D. Herranz, E. Hivon, Z. Huang, A. H. Jaffe, W. C. Jones, A. Karakci, E. Keihänen, R. Keskitalo, K. Kiiveri, J. Kim, L. Knox, N. Krachmalnicoff, M. Kunz, H. Kurki-Suonio, G. Lagache, J. M. Lamarre, A. Lasenby, M. Lattanzi, C. R. Lawrence, M. Le Jeune, F. Levrier, A. Lewis, M. Liguori, P. B. Lilje, V. Lindholm, M. López-Caniego, P. M. Lubin, Y. Z. Ma, J. F. Macías-Pérez, G. Maggio, D. Maino, N. Mandolesi, A. Mangilli, A. Marcos-Caballero, M. Maris, P. G. Martin, E. Martínez-González, S. Matarrese, N. Mauri, J. D. McEwen, A. Melchiorri, A. Mennella, M. Migliaccio, M. A. Miville-Deschênes, D. Molinari, A. Moneti, L. Montier, G. Morgante, A. Moss, P. Natoli, L. Pagano, D. Paoletti, B. Partridge, G. Patanchon, F. Perrotta, V. Pettorino, F. Piacentini, L. Polastri, G. Po-

lenta, J. L. Puget, J. P. Rachen, M. Reinecke, M. Remazeilles, A. Renzi, G. Rocha, C. Rosset, G. Roudier, J. A. Rubiño-Martín, B. Ruiz-Granados, L. Salvati, M. Sandri, M. Savelainen, D. Scott, C. Sirignano, R. Sunyaev, A. S. Suur-Uski, J. A. Tauber, D. Tavagnacco, M. Tenti, L. Toffolatti, M. Tomasi, T. Trombetti, J. Valiviita, B. Van Tent, P. Vielva, F. Villa, N. Vittorio, B. D. Wandelt, I. K. Wehus, M. White, S. D. M. White, A. Zacchei, and A. Zonca. Planck 2018 results. VIII. Gravitational lensing. 2018.

[71] Planck Collaboration P A R Ade, N Aghanim, M Arnaud, M Ashdown, and J Aumont. Planck 2013 results. XVII. Gravitational lensing by large-scale structure. *Astronomy & Astrophysics*, 24, 2014.

[72] P A R Ade, Z Ahmed, R W Aikin, K D Alexander, D Barkats, S J Benton, C A Bischoff, J J Bock, R Bowens-Rubin, J A Brevik, I Buder, E Bullock, V Buza, J Connors, B P Crill, L Duband, C Dvorkin, J P Filippini, S Fliescher, J Grayson, M Halpern, S Harrison, S R Hildebrandt, G C Hilton, H Hui, K D Irwin, J Kang, K S Karkare, E Karpel, J P Kaufman, B G Keating, S Kefeli, S A Kernasovskiy, J M Kovac, C L Kuo, E M Leitch, M Lueker, K G Megerian, T Namikawa, C B Netterfield, H T Nguyen, R. O'Brient, R. W. Ogburn IV, A Orlando, C Pryke, S Richter, R Schwarz, C D Sheehy, Z K Staniszewski, B Steinbach, R V Sudiwala, G P Teply, K L Thompson, J E Tolan, C Tucker, A D Turner, A G Vieregg, A C Weber, D V Wiebe, J Willmert, C L Wong, W L K Wu, and K W Yoon. Bicep2/ KECK ARRAY VIII: MEASUREMENT OF GRAVITATIONAL LENSING FROM LARGE-SCALE B -MODE POLARIZATION. *The Astrophysical Journal*, 833(2):228, dec 2016.

[73] SPT-3G collaboration. SPT-3G Operations and Management Proposal, 2018.

[74] Emmanuel Schaan, Elisabeth Krause, Tim Eifler, Olivier Doré, Hironao Miyatake, Jason Rhodes, and David N Spergel. Looking through the same lens: Shear calibration for LSST, Euclid, and WFIRST with stage 4 CMB lensing. *Physical Review D*, 95(12):1–23, 2017.

[75] Marcel Schmittfull and Uroš Seljak. Parameter constraints from cross-correlation of CMB lensing with galaxy clustering. *Physical Review D*, 97(12):1–33, 2018.

[76] T. Giannantonio, P. Fosalba, R. Cawthon, Y. Omori, M. Crocce, F. Elsner, B. Leistedt, S. Dodelson, A. Benoit-Lévy, E. Gaztañaga, G. Holder, H. V. Peiris, W. J. Percival, D. Kirk, A. H. Bauer, B. A. Benson, G. M. Bernstein, J. Carretero, T. M. Crawford, R. Crittenden, D. Huterer, B. Jain, E. Krause, C. L. Reichardt, A. J. Ross, G. Simard, B. Soergel, A. Stark, K. T. Story, J. D. Vieira, J. Weller, T. Abbott, F. B. Abdalla, S. Allam, R. Armstrong, M. Banerji, R. A. Bernstein, E. Bertin, D. Brooks, E. Buckley-Geer, D. L. Burke, D. Capozzi, J. E. Carlstrom, A. Carnero Rosell, M. Carrasco Kind, F. J. Castander, C. L. Chang, C. E. Cunha, L. N. da Costa, C. B. D'Andrea, D. L. DePoy, S. Desai, H. T. Diehl, J. P. Dietrich, P. Doel, T. F. Eifler, A. E. Evrard, A. Fausti Neto, E. Fernandez, D. A. Finley, B. Flaugher, J. Frieman, D. Gerdes,

D. Gruen, R. A. Gruendl, G. Gutierrez, W. L. Holzapfel, K. Honscheid, D. J. James, K. Kuehn, N. Kuropatkin, O. Lahav, T. S. Li, M. Lima, M. March, J. L. Marshall, P. Martini, P. Melchior, R. Miquel, J. J. Mohr, R. C. Nichol, B. Nord, R. Ogando, A. A. Plazas, A. K. Romer, A. Roodman, E. S. Rykoff, M. Sako, B. R. Saliwanchik, E. Sanchez, M. Schubnell, I. Sevilla-Noarbe, R. C. Smith, M. Soares-Santos, F. Sobreira, E. Suchyta, M. E.C. Swanson, G. Tarle, J. Thaler, D. Thomas, V. Vikram, A. R. Walker, R. H. Wechsler, and J. Zuntz. CMB lensing tomography with the DES Science Verification galaxies. *Monthly Notices of the Royal Astronomical Society*, 456(3):3213–3244, mar 2016.

[77] Gabriela A. Marques and Armando Bernui. Tomographic analyses of the CMB lensing and galaxy clustering to probe the linear structure growth. *Journal of Cosmology and Astroparticle Physics*, 2020(5), aug 2020.

[78] Y. Omori, Y. Omori, T. Giannantonio, A. Porredon, E. J. Baxter, C. Chang, M. Crocce, P. Fosalba, A. Alarcon, N. Banik, J. Blazek, L. E. Bleem, S. L. Bridle, R. Cawthon, A. Choi, R. Chown, T. Crawford, S. Dodelson, A. Drlica-Wagner, T. F. Eifler, J. Elvin-Poole, O. Friedrich, D. Gruen, G. P. Holder, D. Huterer, B. Jain, M. Jarvis, D. Kirk, N. Kokron, E. Krause, N. Maccrann, J. Muir, J. Prat, C. L. Reichardt, A. J. Ross, E. Rozo, E. S. Rykoff, C. Sánchez, L. F. Secco, G. Simard, R. H. Wechsler, J. Zuntz, T. M.C. Abbott, F. B. Abdalla, S. Allam, S. Avila, K. Aylor, B. A. Benson, G. M. Bernstein, E. Bertin, F. Bianchini, D. Brooks, E. Buckley-Geer, D. L. Burke, J. E. Carlstrom, A. Carnero Rosell, M. Carrasco Kind, J. Carretero, F. J. Castander, C. L. Chang, H. M. Cho, A. T. Crites, C. E. Cunha, L. N. Da Costa, T. De Haan, C. Davis, J. De Vicente, S. Desai, H. T. Diehl, J. P. Dietrich, M. A. Dobbs, W. B. Everett, P. Doel, J. Estrada, B. Flaugher, J. Frieman, J. García-Bellido, E. Gaztanaga, D. W. Gerdes, E. M. George, R. A. Gruendl, J. Gschwend, G. Gutierrez, N. W. Halverson, N. L. Harrington, W. G. Hartley, D. L. Hollowood, W. L. Holzapfel, K. Honscheid, Z. Hou, B. Hoyle, J. D. Hrubes, D. J. James, T. Jeltema, K. Kuehn, N. Kuropatkin, A. T. Lee, E. M. Leitch, M. Lima, D. Luong-Van, A. Manzotti, D. P. Marrone, J. L. Marshall, J. J. McMahon, P. Melchior, F. Menanteau, S. S. Meyer, C. J. Miller, R. Miquel, L. M. Mocanu, J. J. Mohr, T. Natoli, S. Padin, A. A. Plazas, C. Pryke, A. K. Romer, A. Roodman, J. E. Ruhl, E. Sanchez, V. Scarpine, K. K. Schaffer, M. Schubnell, S. Serrano, I. Sevilla-Noarbe, E. Shirokoff, M. Smith, M. Soares-Santos, F. Sobreira, Z. Staniszewski, A. A. Stark, K. T. Story, E. Suchyta, M. E.C. Swanson, G. Tarle, D. Thomas, M. A. Troxel, K. Vanderlinde, J. D. Vieira, A. R. Walker, W. L.K. Wu, and O. Zahn. Dark Energy Survey Year 1 Results: Tomographic cross-correlations between Dark Energy Survey galaxies and CMB lensing from South Pole Telescope+Planck. *Physical Review D*, 100(4):043501, aug 2019.

[79] Alex Krolewski, Simone Ferraro, Edward F. Schlafly, and Martin White. UnWISE tomography of Planck CMB lensing. *Journal of Cosmology and Astroparticle Physics*, 2020(5):047, may 2020.

[80] Kendrick M Smith, Oliver Zahn, and Olivier Doré. Detection of gravitational lensing in

the cosmic microwave background. *Physical Review D - Particles, Fields, Gravitation and Cosmology*, 76(4):1–28, 2007.

[81] D. Kirk, Y. Omori, A. Benoit-Lévy, R. Cawthon, C. Chang, P. Larsen, A. Amara, D. Bacon, T. M. Crawford, S. Dodelson, P. Fosalba, T. Giannantonio, G. Holder, B. Jain, T. Kacprzak, O. Lahav, N. MacCrann, A. Nicola, A. Refregier, E. Sheldon, K. T. Story, M. A. Troxel, J. D. Vieira, V. Vikram, J. Zuntz, T. M.C. Abbott, F. B. Abdalla, M. R. Becker, B. A. Benson, G. M. Bernstein, R. A. Bernstein, L. E. Bleem, C. Bonnett, S. L. Bridle, D. Brooks, E. Buckley-Geer, D. L. Burke, D. Capozzi, J. E. Carlstrom, A. Carnero Rosell, M. Carrasco Kind, J. Carretero, M. Crocce, C. E. Cunha, C. B. D'Andrea, L. N. Da Costa, S. Desai, H. T. Diehl, J. P. Dietrich, P. Doel, T. F. Eifler, A. E. Evrard, B. Flaugher, J. Frieman, D. W. Gerdes, D. A. Goldstein, D. Gruen, R. A. Gruendl, K. Honscheid, D. J. James, M. Jarvis, S. Kent, K. Kuehn, N. Kuropatkin, M. Lima, M. March, P. Martini, P. Melchior, C. J. Miller, R. Miquel, R. C. Nichol, R. Ogando, A. A. Plazas, C. L. Reichardt, A. Roodman, E. Rozo, E. S. Rykoff, M. Sako, E. Sanchez, V. Scarpine, M. Schubnell, I. Sevilla-Noarbe, G. Simard, R. C. Smith, M. Soares-Santos, F. Sobreira, E. Suchyta, M. E.C. Swanson, G. Tarle, D. Thomas, R. H. Wechsler, and J. Weller. Cross-correlation of gravitational lensing from DES Science Verification data with SPT and Planck lensing. *Monthly Notices of the Royal Astronomical Society*, 459(1):21–34, jun 2016.

[82] E. Baxter, J. Clampitt, T. Giannantonio, S. Dodelson, B. Jain, D. Huterer, L. Bleem, T. Crawford, G. Efstathiou, P. Fosalba, D. Kirk, J. Kwan, C. Śanchez, K. Story, M. A. Troxel, T. M.C. Abbott, F. B. Abdalla, R. Armstrong, A. Benoit-Lévy, B. Benson, G. M. Bernstein, R. A. Bernstein, E. Bertin, D. Brooks, J. Carlstrom, A. Carnero Rosell, M. Carrasco Kind, J. Carretero, R. Chown, M. Crocce, C. E. Cunha, L. N. da Costa, S. Desai, H. T. Diehl, J. P. Dietrich, P. Doel, A. E. Evrard, A. Fausti Neto, B. Flaugher, J. Frieman, D. Gruen, R. A. Gruendl, G. Gutierrez, T. de Haan, G. Holder, K. Honscheid, Z. Hou, D. J. James, K. Kuehn, N. Kuropatkin, M. Lima, M. March, J. L. Marshall, P. Martini, P. Melchior, C. J. Miller, R. Miquel, J. J. Mohr, B. Nord, Y. Omori, A. A. Plazas, C. Reichardt, A. K. Romer, E. S. Rykoff, E. Sanchez, I. Sevilla-Noarbe, E. Sheldon, R. C. Smith, M. Soares-Santos, F. Sobreira, E. Suchyta, A. Stark, M. E.C. Swanson, G. Tarle, D. Thomas, A. R. Walker, and R. H. Wechsler. Joint measurement of lensing-galaxy correlations using SPT and DES SV data. *Monthly Notices of the Royal Astronomical Society*, 461(4):4099–4114, oct 2016.

[83] Sukhdeep Singh, Rachel Mandelbaum, and Joel R. Brownstein. Cross-correlating Planck CMB lensing with SDSS: Lensing-lensing and galaxy-lensing cross-correlations. *Monthly Notices of the Royal Astronomical Society*, 464(2):2120–2138, jan 2017.

[84] Gabriela A Marques, Jia Liu, Kevin M Huffenberger, and J Colin Hill. Cross-correlation between Subaru Hyper Suprime-Cam Galaxy Weak Lensing and Planck Cosmic Microwave Background Lensing. 2020.

[85] Ye Cao, Yan Gong, Chang Feng, Asantha Cooray, Gong Cheng, and Xuelei Chen.

Cross-Correlation of Far-Infrared Background Anisotropies and CMB Lensing form Herschel and Planck satellites. pages 1–13, 2019.

[86] F. Bianchini, P. Bielewicz, A. Lapi, J. Gonzalez-Nuevo, C. Baccigalupi, G. De Zotti, L. Danese, N. Bourne, A. Cooray, L. Dunne, S. Dye, S. Eales, R. Ivison, S. Maddox, M. Negrello, D. Scott, M. W.L. Smith, and E. Valiante. Cross-correlation between the CMB lensing potential measured by Planck and high-z submillimeter galaxies detected by the Herschel-atlas survey. *Astrophysical Journal*, 802(1):64, mar 2015.

[87] M. Aguilar Faúndez, K. Arnold, C. Baccigalupi, D. Barron, D. Beck, F. Bianchini, D. Boettger, J. Borrill, J. Carron, K. Cheung, Y. Chinone, H. El Bouhargani, T. Elleflot, J. Errard, G. Fabbian, C. Feng, N. Galitzki, N. Goeckner-Wald, M. Hasegawa, M. Hazumi, L. Howe, D. Kaneko, N. Katayama, B. Keating, N. Krachmalnicoff, A. Kusaka, A. T. Lee, D. Leon, E. Linder, L. N. Lowry, F. Matsuda, Y. Minami, M. Navaroli, H. Nishino, A. T. P. Pham, D. Poletti, G. Puglisi, C. L. Reichardt, B. D. Sherwin, M. Silva-Feaver, R. Stompor, A. Suzuki, O. Tajima, S. Takakura, S. Takatori, G. P. Teply, C. Tsai, and C. Vergès. Cross-correlation of CMB Polarization Lensing with High- z Submillimeter Herschel -ATLAS Galaxies. *The Astrophysical Journal*, 886(1):38, nov 2019.

[88] G. Hurier, P. Singh, and C. Hernández-Monteagudo. First measurement of the cross-correlation between CMB weak lensing and X-ray emission. *Astronomy and Astrophysics*, 625:L4, may 2019.

[89] Michael Kesden, Asantha Cooray, and Marc Kamionkowski. Lensing reconstruction with CMB temperature and polarization. *Physical Review D - Particles, Fields, Gravitation and Cosmology*, 67(12):1–15, 2003.

[90] Duncan Hanson, Anthony Challinor, George Efstathiou, and Pawel Bielewicz. CMB temperature lensing power reconstruction. *Physical Review D - Particles, Fields, Gravitation and Cosmology*, 83(4):1–17, 2011.

[91] Dominic Beck, Josquin Errard, and Radek Stompor. Impact of polarized galactic foreground emission on CMB lensing reconstruction and delensing of B-modes. *Journal of Cosmology and Astroparticle Physics*, 2020(6), 2020.

[92] A. Van Engelen, S. Bhattacharya, N. Sehgal, G. P. Holder, O. Zahn, and D. Nagai. CMB lensing power spectrum biases from galaxies and clusters using high-angular resolution temperature maps. *Astrophysical Journal*, 786(1):13, may 2014.

[93] Stephen J Osborne, Duncan Hanson, and Olivier Doré. Extragalactic foreground contamination in temperature-based CMB lens reconstruction, 2014.

[94] Vanessa Böhm, Marcel Schmittfull, and Blake D Sherwin. Bias to CMB lensing measurements from the bispectrum of large-scale structure. *Physical Review D*, 94(4):1–31, 2016.

[95] Vanessa Böhm, Blake D Sherwin, Jia Liu, J Colin Hill, Marcel Schmittfull, and Toshiya Namikawa. Effect of non-Gaussian lensing deflections on CMB lensing measurements. *Physical Review D*, 98(12):123510, 2018.

[96] Giovanni Marozzi, Giuseppe Fanizza, Enea Di Dio, and Ruth Durrer. CMB-lensing beyond the Born approximation. *Journal of Cosmology and Astroparticle Physics*, 2016(9), may 2016.

[97] Geraint Pratten and Antony Lewis. Impact of post-Born lensing on the CMB. *Journal of Cosmology and Astroparticle Physics*, 2016(8), may 2016.

[98] Giulio Fabbian, Matteo Calabrese, and Carmelita Carbone. CMB weak-lensing beyond the Born approximation: A numerical approach, feb 2018.

[99] Dominic Beck, Giulio Fabbian, and Josquin Errard. Lensing reconstruction in post-Born cosmic microwave background weak lensing. *Physical Review D*, 98(4):43512, 2018.

[100] Alexandre Barthelemy, Sandrine Codis, and Francis Bernardeau. Post-Born corrections to the one-point statistics of (CMB) lensing convergence obtained via large deviation theory. *Monthly Notices of the Royal Astronomical Society*, 494(3):3368–3382, may 2020.

[101] Nishant Mishra and Emmanuel Schaan. Bias to CMB lensing from lensed foregrounds. *Physical Review D*, 100(12):123504, 2019.

[102] Eegene Chung, Simon Foreman, and Alexander Van Engelen. Baryonic effects on CMB lensing and neutrino mass constraints. *Physical Review D*, 101(6):63534, 2020.

[103] E. J. Baxter, Y. Omori, C. Chang, T. Giannantonio, D. Kirk, E. Krause, J. Blazek, L. Bleem, A. Choi, T. M. Crawford, S. Dodelson, T. F. Eifler, O. Friedrich, D. Gruen, G. P. Holder, B. Jain, M. Jarvis, N. Maccrann, A. Nicola, S. Pandey, J. Prat, C. L. Reichardt, S. Samuroff, C. Sánchez, L. F. Secco, E. Sheldon, M. A. Troxel, J. Zuntz, T. M.C. Abbott, F. B. Abdalla, J. Annis, S. Avila, K. Bechtol, B. A. Benson, E. Bertin, D. Brooks, E. Buckley-Geer, D. L. Burke, A. Carnero Rosell, M. Carrasco Kind, J. Carretero, F. J. Castander, R. Cawthon, C. E. Cunha, C. B. D'Andrea, L. N. Da Costa, C. Davis, J. De Vicente, D. L. Depoy, H. T. Diehl, P. Doel, J. Estrada, A. E. Evrard, B. Flaugher, P. Fosalba, J. Frieman, J. García-Bellido, E. Gaztanaga, D. W. Gerdes, R. A. Gruendl, J. Gschwend, G. Gutierrez, W. G. Hartley, D. Hollowood, B. Hoyle, D. J. James, S. Kent, K. Kuehn, N. Kuropatkin, O. Lahav, M. Lima, M. A.G. Maia, M. March, J. L. Marshall, P. Melchior, F. Menanteau, R. Miquel, A. A. Plazas, A. Roodman, E. S. Rykoff, E. Sanchez, R. Schindler, M. Schubnell, I. Sevilla-Noarbe, M. Smith, R. C. Smith, M. Soares-Santos, F. Sobreira, E. Suchyta, M. E.C. Swanson, G. Tarle, A. R. Walker, W. L.K. Wu, and J. Weller. Dark Energy Survey Year 1 results: Methodology and projections for joint analysis of galaxy clustering, galaxy lensing, and CMB lensing two-point functions. *Physical Review D*, 99(2):23508, 2019.

[104] Emmanuel Schaan and Simone Ferraro. Foreground-Immune Cosmic Microwave Background Lensing with Shear-Only Reconstruction. *Physical Review Letters*, 122(18):181301, 2019.

[105] Mathew S. Madhavacheril and J. Colin Hill. Mitigating foreground biases in CMB lensing reconstruction using cleaned gradients. *Physical Review D*, 98(2):1–12, 2018.

[106] Christopher M Hirata and Uroš Seljak. Analyzing weak lensing of the cosmic microwave background using the likelihood function. *Physical Review D - Particles, Fields, Gravitation and Cosmology*, 67(4):1–19, 2003.

[107] Marius Millea, Ethan Anderes, and Benjamin D Wandelt. Bayesian delensing of CMB temperature and polarization. *Physical Review D*, 100(2):23509, 2019.

[108] Marius Millea, Ethan Anderes, and Benjamin D. Wandelt. Bayesian delensing delight: sampling-based inference of the primordial CMB and gravitational lensing. 2020.

[109] Julien Carron and Antony Lewis. Maximum a posteriori CMB lensing reconstruction. *Physical Review D*, 96(6):1–21, 2017.

[110] Boryana Hadzhiyska, Blake D Sherwin, Mathew Madhavacheril, and Simone Ferraro. Improving small-scale CMB lensing reconstruction. *Physical Review D*, 100(2):23547, 2019.

[111] P. A.R. Ade, Y Akiba, A E Anthony, K Arnold, M Atlas, D Barron, D. Boettger, J. Borrill, S. Chapman, Y. Chinone, M. Dobbs, T. Elleflot, J. Errard, G. Fabbian, C. Feng, D. Flanigan, A. Gilbert, W. Grainger, N. W. Halverson, M. Hasegawa, K. Hattori, M. Hazumi, W. L. Holzapfel, Y. Hori, J. Howard, P. Hyland, Y. Inoue, G. C. Jaehnig, A. H. Jaffe, B. Keating, Z. Kermish, R. Keskitalo, T. Kisner, M. Le Jeune, A. T. Lee, E. M. Leitch, E. Linder, M. Lungu, F. Matsuda, T. Matsumura, X. Meng, N. J. Miller, H. Morii, S. Moyerman, M. J. Myers, M. Navaroli, H. Nishino, A. Orlando, H. Paar, J. Peloton, D. Poletti, E. Quealy, G. Rebeiz, C. L. Reichardt, P. L. Richards, C. Ross, I. Schanning, D. E. Schenck, B. D. Sherwin, A. Shimizu, C. Shimmin, M. Shimon, P. Siritanasak, G. Smecher, H. Spieler, N. Stebor, B. Steinbach, R. Stompor, A. Suzuki, S. Takakura, T. Tomaru, B. Wilson, A. Yadav, and O. Zahn. A measurement of the cosmic microwave background B-mode polarization power spectrum at sub-degree scales with Polarbear. *Astrophysical Journal*, 794(2), 2014.

[112] R. Keisler, S. Hoover, N. Harrington, J. W. Henning, P. A.R. Ade, K. A. Aird, J. E. Austermann, J. A. Beall, A. N. Bender, B. A. Benson, L. E. Bleem, J. E. Carlstrom, C. L. Chang, H. C. Chiang, H. M. Cho, R. Citron, T. M. Crawford, A. T. Crites, T. De Haan, M. A. Dobbs, W. Everett, J. Gallicchio, J. Gao, E. M. George, A. Gilbert, N. W. Halverson, D. Hanson, G. C. Hilton, G. P. Holder, W. L. Holzapfel, Z. Hou, J. D. Hrubes, N. Huang, J. Hubmayr, K. D. Irwin, L. Knox, A. T. Lee, E. M. Leitch, D. Li, D. Luong-Van, D. P. Marrone, J. J. McMahon, J. Mehl, S. S. Meyer, L. Mocanu, T. Natoli, J. P. Nibarger, V. Novosad, S. Padin, C. Pryke, C. L. Reichardt, J. E.

Ruhl, B. R. Saliwanchik, J. T. Sayre, K. K. Schaffer, E. Shirokoff, G. Smecher, A. A. Stark, K. T. Story, C. Tucker, K. Vanderlinde, J. D. Vieira, G. Wang, N. Whitehorn, V. Yefremenko, and O. Zahn. Measurements of Sub-Degree B-Mode Polarization in the Cosmic Microwave Background From 100 Square Degrees of Sptpol Data. *Astrophysical Journal*, 807(2), 2015.

[113] A. Manzotti, K. T. Story, W. L. K. Wu, J. E. Austermann, J. A. Beall, A. N. Bender, B. A. Benson, L. E. Bleem, J. J. Bock, J. E. Carlstrom, C. L. Chang, H. C. Chiang, H-M. Cho, R. Citron, A. Conley, T. M. Crawford, A. T. Crites, T. de Haan, M. A. Dobbs, S. Dodelson, W. Everett, J. Gallicchio, E. M. George, A. Gilbert, N. W. Halverson, N. Harrington, J. W. Henning, G. C. Hilton, G. P. Holder, W. L. Holzapfel, S. Hoover, Z. Hou, J. D. Hrubes, N. Huang, J. Hubmayr, K. D. Irwin, R. Keisler, L. Knox, A. T. Lee, E. M. Leitch, D. Li, J. J. McMahon, S. S. Meyer, L. M. Mocanu, T. Natoli, J. P. Nibarger, V. Novosad, S. Padin, C. Pryke, C. L. Reichardt, J. E. Ruhl, B. R. Saliwanchik, J. T. Sayre, K. K. Schaffer, G. Smecher, A. A. Stark, K. Vanderlinde, J. D. Vieira, M. P. Viero, G. Wang, N. Whitehorn, V. Yefremenko, and M. Zemcov. CMB Polarization B-mode Delensing with SPTpol and Herschel. 2017.

[114] Byeonghee Yu, J Colin Hill, and Blake D Sherwin. Multitracer CMB delensing maps from Planck and WISE data. *Physical Review D*, 96(12):1–11, 2017.

[115] A. Manzotti. Future cosmic microwave background delensing with galaxy surveys. *Physical Review D*, 97(4):43527, 2018.

[116] John Ruhl, Peter A. R. Ade, John E. Carlstrom, Hsiao-Mei Cho, Thomas Crawford, Matt Dobbs, Chris H. Greer, Nils w. Halverson, William L. Holzapfel, Trevor M. Lanting, Adrian T. Lee, Erik M. Leitch, Jon Leong, Wenyang Lu, Martin Lueker, Jared Mehl, Stephan S. Meyer, Joe J. Mohr, Steve Padin, T. Plagge, Clem Pryke, Marcus C. Runyan, Dan Schwan, M. K. Sharp, Helmuth Spieler, Zak Staniszewski, and Antony A. Stark. The South Pole Telescope. In Jonas Zmuidzinas, Wayne S. Holland, and Stafford Withington, editors, *Millimeter and Submillimeter Detectors for Astronomy II*, volume 5498, page 11. SPIE, oct 2004.

[117] J. E. Carlstrom, P. A. R. Ade, K. A. Aird, B. A. Benson, L. E. Bleem, S. Busetti, C. L. Chang, E. Chauvin, H.-M. Cho, T. M. Crawford, A. T. Crites, M. A. Dobbs, N. W. Halverson, S. Heimsath, W. L. Holzapfel, J. D. Hrubes, M. Joy, R. Keisler, T. M. Lanting, A. T. Lee, E. M. Leitch, J. Leong, W. Lu, M. Lueker, D. Luong-Van, J. J. McMahon, J. Mehl, S. S. Meyer, J. J. Mohr, T. E. Montroy, S. Padin, T. Plagge, C. Pryke, J. E. Ruhl, K. K. Schaffer, D. Schwan, E. Shirokoff, H. G. Spieler, Z. Staniszewski, A. A. Stark, C. Tucker, K. Vanderlinde, J. D. Vieira, and R. Williamson. The 10 Meter South Pole Telescope. *Publications of the Astronomical Society of the Pacific*, 123(903):568–581, 2011.

[118] Richard A. Chamberlin. South Pole submillimeter sky opacity and correlations with radiosonde observations. *Journal of Geophysical Research: Atmospheres*, 106(D17):20101–20113, sep 2001.

[119] R S Bussmann, W L Holzapfel, and C L Kuo. Millimeter Wavelength Brightness Fluctuations of the Atmosphere above the South Pole. *The Astrophysical Journal*, 622(2):1343–1355, 2005.

[120] H. Yang, C A Kulesa, C K Walker, N F H Tothill, J Yang, M C B Ashley, X Cui, L Feng, J S Lawrence, D M Luong-Van, M. J. McCaughrean, J W V Storey, L Wang, X Zhou, and Z. Zhu. Exceptional Terahertz Transparency and Stability above Dome A, Antarctica. *Publications of the Astronomical Society of the Pacific*, 122(890):490–494, 2010.

[121] Simon J. E. Radford. Observing Conditions for Submillimeter Astronomy. *Revista Mexicana de Astronomia y Astrofisica: Serie de Conferencias*, 41:87–90, jul 2011.

[122] R. A. Chamberlin and E. N. Grossman. The wintertime South Pole tropospheric water vapor column: Comparisons of radiosonde and recent terahertz radiometry, use of the saturated column as a proxy measurement, and inference of decadal trends. *Journal of Geophysical Research: Atmospheres*, 117(D13):n/a–n/a, jul 2012.

[123] Simon J.E. Radford and Jeffery B Peterson. Submillimeter atmospheric transparency at Maunakea, at the South Pole, and at Chajnantor. *Publications of the Astronomical Society of the Pacific*, 128(965), 2016.

[124] Chao-Lin Kuo. Assessments of Ali, Dome A, and Summit Camp for mm-wave Observations Using MERRA-2 Reanalysis. *The Astrophysical Journal*, 848(1):64, oct 2017.

[125] S. Padin, Z. Staniszewski, R. Keisler, M. Joy, A. A. Stark, P. A.R. Ade, K. A. Aird, B. A. Benson, L. E. Bleem, J. E. Carlstrom, C. L. Chang, T. M. Crawford, A. T. Crites, M. A. Dobbs, N. W. Halverson, S. Heimsath, R. E. Hills, W. L. Holzapfel, C. Lawrie, A. T. Lee, E. M. Leitch, J. Leong, W. Lu, M. Lueker, J. J. McMahon, S. S. Meyer, J. J. Mohr, T. E. Montroy, T. Plagge, C. Pryke, J. E. Ruhl, K. K. Schaffer, E. Shirokoff, H. G. Spieler, and J. D. Vieira. South Pole Telescope optics. *Applied Optics*, 47(24):4418–4428, aug 2008.

[126] K T Story, C L Reichardt, Z Hou, R Keisler, K A Aird, B A Benson, L E Bleem, J E Carlstrom, C L Chang, H. M. Cho, T M Crawford, A T Crites, T De Haan, M A Dobbs, J Dudley, B Follin, E M George, N W Halverson, G P Holder, W L Holzapfel, S Hoover, J D Hrubes, M Joy, L Knox, A T Lee, E M Leitch, M Lueker, D Luong-Van, J. J. McMahon, J Mehl, S S Meyer, M Millea, J J Mohr, T E Montroy, S Padin, T Plagge, C Pryke, J E Ruhl, J T Sayre, K K Schaffer, L Shaw, E Shirokoff, H G Spieler, Z Staniszewski, A A Stark, A Van Engelen, K Vanderlinde, J D Vieira, R Williamson, and O Zahn. A measurement of the cosmic microwave background damping tail from the 2500-square-degree SPT-SZ survey. *Astrophysical Journal*, 779(1):86, 2013.

[127] L. E. Bleem, B. Stalder, T. De Haan, K. A. Aird, S. W. Allen, D. E. Applegate, M. L.N. Ashby, M. Bautz, M. Bayliss, B. A. Benson, S. Bocquet, M. Brodwin, J. E. Carlstrom, C. L. Chang, I. Chiu, H. M. Cho, A. Clocchiatti, T. M. Crawford, A. T. Crites,

S. Desai, J. P. Dietrich, M. A. Dobbs, R. J. Foley, W. R. Forman, E. M. George, M. D. Gladders, A. H. Gonzalez, N. W. Halverson, C. Hennig, H. Hoekstra, G. P. Holder, W. L. Holzapfel, J. D. Hrubes, C. Jones, R. Keisler, L. Knox, A. T. Lee, E. M. Leitch, J. Liu, M. Lueker, D. Luong-Van, A. Mantz, D. P. Marrone, M. McDonald, J. J. McMahon, S. S. Meyer, L. Mocanu, J. J. Mohr, S. S. Murray, S. Padin, C. Pryke, C. L. Reichardt, A. Rest, J. Ruel, J. E. Ruhl, B. R. Saliwanchik, A. Saro, J. T. Sayre, K. K. Schaffer, T. Schrabback, E. Shirokoff, J. Song, H. G. Spieler, S. A. Stanford, Z. Staniszewski, A. A. Stark, K. T. Story, C. W. Stubbs, K. Vanderlinde, J. D. Vieira, A. Vikhlinin, R. Williamson, O. Zahn, and A. Zenteno. Galaxy clusters discovered via the sunyaev-zel'dovich effect in the 2500-square-degree spt-sz survey. *Astrophysical Journal, Supplement Series*, 216(2), 2015.

[128] J. E. Austermann, K. A. Aird, J. A. Beall, D Becker, A Bender, B. A. Benson, L. E. Bleem, J Britton, J. E. Carlstrom, C. L. Chang, H. C. Chiang, H-m Cho, T. M. Crawford, A. T. Crites, A Datesman, T de Haan, M. A. Dobbs, E. M. George, N. W. Halverson, N Harrington, J. W. Henning, G. C. Hilton, G. P. Holder, W. L. Holzapfel, S Hoover, N Huang, J Hubmayr, K. D. Irwin, R Keisler, J Kennedy, L Knox, A. T. Lee, E Leitch, D Li, M Lueker, D. P. Marrone, J. J. McMahon, J Mehl, S. S. Meyer, T. E. Montroy, T Natoli, J. P. Nibarger, M. D. Niemack, V Novosad, S Padin, C Pryke, C. L. Reichardt, J. E. Ruhl, B. R. Saliwanchik, J. T. Sayre, K. K. Schaffer, E Shirokoff, A. A. Stark, K Story, K Vanderlinde, J. D. Vieira, G Wang, R Williamson, V Yefremenko, K W Yoon, and O Zahn. SPTpol: an instrument for CMB polarization measurements with the South Pole Telescope. In *Millimeter, Submillimeter, and Far-Infrared Detectors and Instrumentation for Astronomy VI*, volume 8452, page 84521E, 2012.

[129] J W Henning, P Ade, K A Aird, J E Austermann, J A Beall, D Becker, B. A. Benson, L. E. Bleem, J. Britton, J. E. Carlstrom, C. L. Chang, H.-M. Cho, T. M. Crawford, A. T. Crites, A. Datesman, T. de Haan, M A. Dobbs, W. Everett, A. Ewall-Wice, E. M. George, N. W. Halverson, N. Harrington, G. C. Hilton, W. L. Holzapfel, J. Hubmayr, K. D. Irwin, M. Karfunkle, R. Keisler, J. Kennedy, A. T. Lee, E. Leitch, D. Li, M. Lueker, D. P. Marrone, J. J. McMahon, J. Mehl, S. S. Meyer, J. Montgomery, T. E. Montroy, J. Nagy, T. Natoli, J. P. Nibarger, M. D. Niemack, V. Novosad, S. Padin, C. Pryke, C. L. Reichardt, J. E. Ruhl, B. R. Saliwanchik, J. T. Sayre, K. K. Schaffer, E. Shirokoff, K. Story, C. Tucker, K. Vanderlinde, J. D. Vieira, G. Wang, R. Williamson, V. Yefremenko, K. W. Yoon, and E. Young. Feedhorn-coupled TES polarimeter camera modules at 150 GHz for CMB polarization measurements with SPTpol. In *Millimeter, Submillimeter, and Far-Infrared Detectors and Instrumentation for Astronomy VI*, volume 8452, page 84523A, 2012.

[130] A. Orlando, R W Aikin, M Amiri, J J Bock, J A Bonetti, J A Brevik, B Burger, G. Chattopadthyay, P K Day, J P Filippini, S R Golwala, M Halpern, M Hasselfield, G. C. Hilton, K D Irwin, M Kenyon, J M Kovac, C L Kuo, A E Lange, H. G. LeDuc, N Llombart, H T Nguyen, R W Ogburn, C D Reintsema, M C Runyan, Z. Staniszewski, R Sudiwala, G Teply, A R Trangsrud, A D Turner, and P Wilson. Antenna-coupled

TES bolometer arrays for BICEP2/Keck and SPIDER. In *Millimeter, Submillimeter, and Far-Infrared Detectors and Instrumentation for Astronomy V*, volume 7741, page 77410H, 2010.

[131] Shawn W Henderson, Zeeshan Ahmed, David Brown, Saptarshi Chaudhuri, Hsiao-mei Sherry Cho, John M. D'Ewart, Bradley Dober, John E Dusatko, Sofia Fatigoni, Josef C Frisch, Mark Halpern, Gene C Hilton, Johannes Hubmayr, Kent D Irwin, Ethan D Karpel, Sarah S Kernasovskiy, Stephen E Kuenstner, Chao-lin Kuo, Dale Li, John A. B. Mates, Stephen R. Smith, Joel Ullom, Leila R. Vale, Daniel D. Van Winkle, Cyndia Yu, Jason E. Austermann, Daniel Becker, Douglas A. Bennett, Shannon M Duff, Jonathon D Gard, Carl D. Reintsema, and Michael Vissers. Highly-multiplexed microwave SQUID readout using the SLAC Microresonator Radio Frequency (SMuRF) electronics for future CMB and sub-millimeter surveys. In Jonas Zmuidzinas and Jian-Rong Gao, editors, *Millimeter, Submillimeter, and Far-Infrared Detectors and Instrumentation for Astronomy IX*, page 43. SPIE, jul 2018.

[132] F W Carter, P. A.R. Ade, Z. Ahmed, A J Anderson, J. E. Austermann, J. S. Avva, R Basu Thakur, A. N. Bender, B A Benson, J E Carlstrom, T Cecil, C L Chang, J. F. Cliche, A. Cukierman, E. V. Denison, T. de Haan, J. Ding, R. Divan, M. A. Dobbs, D Dutcher, W. Everett, A. Foster, R. N. Gannon, A. Gilbert, J. C. Groh, N W Halverson, A. H. Harke-Hosemann, N L Harrington, J. W. Henning, G. C. Hilton, W. L. Holzapfel, N. Huang, K D Irwin, O. B. Jeong, M. Jonas, T. Khaire, A M Kofman, M. Korman, D. Kubik, S. Kuhlmann, C. L. Kuo, V. Kutepova, A. T. Lee, A. E. Lowitz, S. S. Meyer, D. Michalik, C. S. Miller, J. Montgomery, A. Nadolski, T. Natoli, H. Nguyen, G. I. Noble, V. Novosad, S. Padin, Z. Pan, J. Pearson, C. M. Posada, A. Rahlin, J. E. Ruhl, L. J. Saunders, J. T. Sayre, I. Shirley, E. Shirokoff, G. Smecher, J. A. Sobrin, L. Stan, A. A. Stark, K. T. Story, A. Suzuki, Q. Y. Tang, K. L. Thompson, C. Tucker, L. R. Vale, K. Vanderlinde, J. D. Vieira, G. Wang, N. Whitehorn, V. Yefremenko, K. W. Yoon, and M. R. Young. Tuning SPT-3G Transition-Edge-Sensor Electrical Properties with a Four-Layer Ti–Au–Ti–Au Thin-Film Stack. *Journal of Low Temperature Physics*, 193(5-6):695–702, 2018.

[133] K. D. Irwin and G. C. Hilton. Transition-edge sensors. *Topics in Applied Physics*, 99:63–152, jul 2005.

[134] Jennifer M. Edwards, Roger O'Brient, Adrian T. Lee, and Gabriel M. Rebeiz. Dual-polarized sinuous antennas on extended hemispherical silicon lenses. *IEEE Transactions on Antennas and Propagation*, 60(9):4082–4091, 2012.

[135] C. M. Posada, P. A.R. Ade, Z. Ahmed, K. Arnold, J. E. Austermann, A. N. Bender, L. E. Bleem, B. A. Benson, K. Byrum, J. E. Carlstrom, C. L. Chang, H. M. Cho, S. T. Ciocys, J. F. Cliche, T. M. Crawford, A. Cukierman, D. Czaplewski, J. Ding, R. Divan, T. De Haan, M. A. Dobbs, D. Dutcher, W. Everett, A. Gilbert, N. W. Halverson, N. L. Harrington, K. Hattori, J. W. Henning, G. C. Hilton, W. L. Holzapfel, J. Hubmayr, K. D. Irwin, O. Jeong, R. Keisler, D. Kubik, C. L. Kuo, A. T. Lee, E. M.

Leitch, S. Lendinez, S. S. Meyer, C. S. Miller, J. Montgomery, M. Myers, A. Nadolski, T. Natoli, H. Nguyen, V. Novosad, S. Padin, Z. Pan, J. Pearson, J. E. Ruhl, B. R. Saliwanchik, G. Smecher, J. T. Sayre, E. Shirokoff, L. Stan, A. A. Stark, J. Sobrin, K. Story, A. Suzuki, K. L. Thompson, C. Tucker, K. Vanderlinde, J. D. Vieira, G. Wang, N. Whitehorn, V. Yefremenko, K. W. Yoon, and K. E. Ziegler. Fabrication of large dual-polarized multichroic TES bolometer arrays for CMB measurements with the SPT-3G camera. *Superconductor Science and Technology*, 28(9), 2015.

[136] C. M. Posada, P. A.R. Ade, Z. Ahmed, A J Anderson, J. E. Austermann, J. S. Avva, R Basu Thakur, A. N. Bender, B A Benson, J E Carlstrom, F W Carter, T. Cecil, C. L. Chang, J. F. Cliche, A. Cukierman, E. V. Denison, T. de Haan, J. Ding, R. Divan, M. A. Dobbs, D Dutcher, W. Everett, A. Foster, R. N. Gannon, A. Gilbert, J. C. Groh, N. W. Halverson, A. H. Harke-Hosemann, N. L. Harrington, J. W. Henning, G. C. Hilton, W. L. Holzapfel, N. Huang, K. D. Irwin, O. B. Jeong, M. Jonas, T. Khaire, A M Kofman, M. Korman, D. Kubik, S. Kuhlmann, C. L. Kuo, A. T. Lee, A. E. Lowitz, S. S. Meyer, D. Michalik, C. S. Miller, J. Montgomery, A. Nadolski, T. Natoli, H. Nguyen, G. I. Noble, V. Novosad, S. Padin, Z. Pan, J. Pearson, A. Rahlin, J. E. Ruhl, L. J. Saunders, J. T. Sayre, I. Shirley, E. Shirokoff, G Smecher, J. A. Sobrin, L. Stan, A. A. Stark, K. T. Story, A. Suzuki, Q. Y. Tang, K. L. Thompson, C. Tucker, L. R. Vale, K. Vanderlinde, J. D. Vieira, G. Wang, N. Whitehorn, V. Yefremenko, K. W. Yoon, and M. R. Young. Fabrication of Detector Arrays for the SPT-3G Receiver. *Journal of Low Temperature Physics*, 193(5-6):703–711, 2018.

[137] Junjia Ding, P. A.R. Ade, A. J. Anderson, J. Avva, Z. Ahmed, K. Arnold, J. E. Austermann, A. N. Bender, B. A. Benson, L. E. Bleem, K. Byrum, J. E. Carlstrom, F. W. Carter, C. L. Chang, H. M. Cho, J. F. Clich, A. Cukierman, D. Czaplewski, R. Divan, T. De Haan, M. A. Dobbs, D. Dutcher, W. Everett, A. Gilbert, R. Gannon, R. Guyser, N. W. Halverson, N. L. Harrington, K. Hattori, J. W. Henning, G. C. Hilton, W. L. Holzapfel, J. Hubmayr, N. Huang, K. D. Irwin, O. Jeong, T. Khaire, D. Kubik, C. L. Kuo, A. T. Lee, E. M. Leitch, S. S. Meyer, C. S. Miller, J. Montgomery, A. Nadolski, T. Natoli, H. Nguyen, V. Novosad, S. Padin, Z. Pan, J. Pearson, C. M. Posada, A. Rahlin, C. L. Reichardt, J. E. Ruhl, B. R. Saliwanchik, J. T. Sayre, J. A. Shariff, I. Shirley, E. Shirokoff, G. Smecher, J. Sobrin, L. Stan, A. A. Stark, K. Story, A. Suzuki, Q. Y. Tang, R. B. Thakur, K. L. Thompson, C. Tucker, K. Vanderlinde, J. D. Vieira, G. Wang, N. Whitehorn, W. L.K. Wu, V. Yefremenko, and K. W. Yoon. Optimization of Transition Edge Sensor Arrays for Cosmic Microwave Background Observations with the South Pole Telescope. *IEEE Transactions on Applied Superconductivity*, 27(4), jun 2017.

[138] Martin Lueker. *Measurements of Secondary Cosmic Microwave Background Anisotropies with the South Pole Telescope*. PhD thesis, University of California, Berkeley, 2010.

[139] John C. Mather. Bolometer noise: nonequilibrium theory. *Applied Optics*, 21(6):1125, mar 1982.

[140] Herbert Kroemer and Charles Kittel. *Thermal physics*. WH Freeman, 1980.

[141] P. L. Richards. Bolometers for infrared and millimeter waves. *Journal of Applied Physics*, 76(1):1–24, jul 1994.

[142] J. M. Lamarre. Photon noise in photometric instruments at far-infrared and submillimeter wavelengths. *Applied Optics*, 25(6):870, mar 1986.

[143] H. Nyquist. Thermal agitation of electric charge in conductors. *Physical Review*, 32(1):110–113, jul 1928.

[144] Tijmen de Haan, Graeme Smecher, and Matt Dobbs. Improved performance of TES bolometers using digital feedback. In Wayne S. Holland, editor, *Millimeter, Submillimeter, and Far-Infrared Detectors and Instrumentation for Astronomy VI*, volume 8452, page 84520E. SPIE, sep 2012.

[145] A J Anderson, P. A.R. Ade, Z. Ahmed, J. E. Austermann, J. S. Avva, P. S. Barry, R. Basu Thakur, A. N. Bender, B. A. Benson, L. E. Bleem, K. Byrum, J. E. Carlstrom, F. W. Carter, T. Cecil, C. L. Chang, H. M. Cho, J. F. Cliche, T. M. Crawford, A. Cukierman, E. V. Denison, T. de Haan, J. Ding, M. A. Dobbs, D. Dutcher, W. Everett, A. Foster, R. N. Gannon, A. Gilbert, J. C. Groh, N. W. Halverson, A. H. Harke-Hosemann, N. L. Harrington, J. W. Henning, G. C. Hilton, G. P. Holder, W. L. Holzapfel, N. Huang, K. D. Irwin, O. B. Jeong, M. Jonas, T. Khaire, L. Knox, A. M. Kofman, M. Korman, D. Kubik, S. Kuhlmann, N. Kuklev, C. L. Kuo, A. T. Lee, E. M. Leitch, A. E. Lowitz, S. S. Meyer, D. Michalik, J. Montgomery, A. Nadolski, T. Natoli, H. Nguyen, G. I. Noble, V. Novosad, S. Padin, Z. Pan, J. Pearson, C. M. Posada, A. Rahlin, C. L. Reichardt, J. E. Ruhl, L. J. Saunders, J. T. Sayre, I. Shirley, E. Shirokoff, G. Smecher, J. A. Sobrin, A. A. Stark, K. T. Story, A. Suzuki, Q. Y. Tang, K. L. Thompson, C. Tucker, L. R. Vale, K. Vanderlinde, J. D. Vieira, G. Wang, N. Whitehorn, V. Yefremenko, K. W. Yoon, and M. R. Young. SPT-3G: A Multichroic Receiver for the South Pole Telescope. *Journal of Low Temperature Physics*, 193(5-6):1057–1065, 2018.

[146] Radar absorbing material, Thomas Keating, http://www.terahertz.co.uk/tk-instruments/products/tesselatingterahertzram, accessed July-19-2020, 2020.

[147] A J Anderson, P. A.R. Ade, Z. Ahmed, J. S. Avva, P. S. Barry, R. Basu Thakur, A. N. Bender, B. A. Benson, L. Bryant, K. Byrum, J. E. Carlstrom, F. W. Carter, T. W. Cecil, C. L. Chang, H. M. Cho, J. F. Cliche, A. Cukierman, T. de Haan, E. V. Denison, J. Ding, M. A. Dobbs, D. Dutcher, W. Everett, K. R. Ferguson, A. Foster, J. Fu, J. Gallicchio, A. E. Gambrel, R. W. Gardner, A. Gilbert, J. C. Groh, S. T. Guns, R. Guyser, N. W. Halverson, A. H. Harke-Hosemann, N. L. Harrington, J. W. Henning, G. C. Hilton, W. L. Holzapfel, D. Howe, N. Huang, K. D. Irwin, O. B. Jeong, M. Jonas, A. Jones, T. S. Khaire, A. M. Kofman, M. Korman, D. L. Kubik, S. Kuhlmann, C. L. Kuo, A. T. Lee, E. M. Leitch, A. E. Lowitz, S. S. Meyer, D. Michalik, J. Montgomery, A. Nadolski, T. Natoli, H. Nguyen, G. I. Noble, V. Novosad, S. Padin, Z. Pan,

P. Paschos, J. Pearson, C. M. Posada, W. Quan, A. Rahlin, D. Riebel, J. E. Ruhl, J. T. Sayre, E. Shirokoff, G. Smecher, J. A. Sobrin, A. A. Stark, J. Stephen, K. T. Story, A. Suzuki, K. L. Thompson, C. Tucker, L. R. Vale, K. Vanderlinde, J. D. Vieira, G. Wang, N. Whitehorn, V. Yefremenko, K. W. Yoon, and M. R. Young. Performance of Al–Mn Transition-Edge Sensor Bolometers in SPT-3G. *Journal of Low Temperature Physics*, 199(1-2):320–329, 2020.

[148] SPT-3G collaboration. SPT-3G Instrument Paper.

[149] A N Bender, A. J. Anderson, J. S. Avva, P. A.R. Ade, Z. Ahmed, P. S. Barry, R. Basu Thakur, B. A. Benson, L. Bryant, K. Byrum, J. E. Carlstrom, F. W. Carter, T. W. Cecil, C. L. Chang, H. M. Cho, J. F. Cliche, A. Cukierman, T. de Haan, E. V. Denison, J. Ding, M. A. Dobbs, D. Dutcher, W. Everett, K. R. Ferguson, A. Foster, J. Fu, J. Gallicchio, A. E. Gambrel, R. W. Gardner, A. Gilbert, J. C. Groh, S. Guns, R. Guyser, N. W. Halverson, A. H. Harke-Hosemann, N. L. Harrington, J. W. Henning, G. C. Hilton, W. L. Holzapfel, D. Howe, N. Huang, K. D. Irwin, O. B. Jeong, M. Jonas, A. Jones, T. S. Khaire, A. M. Kofman, M. Korman, D. L. Kubik, S. Kuhlmann, C. L. Kuo, A. T. Lee, E. M. Leitch, A. E. Lowitz, S. S. Meyer, D. Michalik, J. Montgomery, A. Nadolski, T. Natoli, H. Nguyen, G. I. Noble, V. Novosad, S. Padin, Z. Pan, P. Paschos, J. Pearson, C. M. Posada, W. Quan, A. Rahlin, D. Riebel, J. E. Ruhl, J. T. Sayre, E. Shirokoff, G. Smecher, J. A. Sobrin, A. A. Stark, J. Stephen, K. T. Story, A. Suzuki, K. L. Thompson, C. Tucker, L. R. Vale, K. Vanderlinde, J. D. Vieira, G. Wang, N. Whitehorn, V. Yefremenko, K. W. Yoon, and M. R. Young. On-Sky Performance of the SPT-3G Frequency-Domain Multiplexed Readout. *Journal of Low Temperature Physics*, 199(1-2):182–191, 2020.

[150] A. Nadolski, J. D. Vieira, J. A. Sobrin, A. M. Kofman, P. A. R. Ade, Z. Ahmed, A. J. Anderson, J. S. Avva, R. Basu Thakur, A. N. Bender, B. A. Benson, L. Bryant, J. E. Carlstrom, F. W. Carter, T. W. Cecil, C. L. Chang, J. R. Cheshire, G. E. Chesmore, J. F. Cliche, A. Cukierman, T. de Haan, M. Dierickx, J. Ding, D. Dutcher, W. Everett, J. Farwick, K. R. Ferguson, L. Florez, A. Foster, J. Fu, J. Gallicchio, A. E. Gambrel, R. W. Gardner, J. C. Groh, S. Guns, R. Guyser, N. W. Halverson, A. H. Harke-Hosemann, N. L. Harrington, R. J. Harris, J. W. Henning, W. L. Holzapfel, D. Howe, N. Huang, K. D. Irwin, O. Jeong, M. Jonas, A. Jones, M. Korman, J. Kovac, D. L. Kubik, S. Kuhlmann, C.-L. Kuo, A. T. Lee, A. E. Lowitz, J. McMahon, J. Meier, S. S. Meyer, D. Michalik, J. Montgomery, T. Natoli, H. Nguyen, G. I. Noble, V. Novosad, S. Padin, Z. Pan, P. Paschos, J. Pearson, C. M. Posada, W. Quan, A. Rahlin, D. Riebel, J. E. Ruhl, J. T. Sayre, E. Shirokoff, G. Smecher, A. A. Stark, J. Stephen, K. T. Story, A. Suzuki, C. Tandoi, K. L. Thompson, C. Tucker, K. Vanderlinde, G. Wang, N. Whitehorn, V. Yefremenko, K. W. Yoon, and M. R. Young. Broadband, millimeter-wave antireflection coatings for large-format, cryogenic aluminum oxide optics. *Applied Optics*, 59(10):3285, apr 2020.

[151] T. R. Ayres and L. Testerman. Fourier Transform Spectrometer observations of solar

carbon monoxide. I - The fundamental and first overtone bands in the quiet sun. *The Astrophysical Journal*, 245:1124, may 1981.

[152] B. Klein, S. D. Philipp, I. Krämer, C. Kasemann, R. Güsten, and K. M. Menten. The APEX digital fast fourier transform spectrometer. *Astronomy and Astrophysics*, 454(2):L29–L32, aug 2006.

[153] Akihiko Kuze, Hiroshi Suto, Masakatsu Nakajima, and Takashi Hamazaki. Thermal and near infrared sensor for carbon observation Fourier-transform spectrometer on the Greenhouse Gases Observing Satellite for greenhouse gases monitoring. *Applied Optics*, 48(35):6716–6733, dec 2009.

[154] A P Thorne, C J Harris, I Wynne-Jones, R. C.M. Learner, and G Cox. A Fourier transform spectrometer for the vacuum ultraviolet: Design and performance. *Journal of Physics E: Scientific Instruments*, 20(1):54–60, jan 1987.

[155] T. J. Balle and W. H. Flygare. Fabry-Perot cavity pulsed Fourier transform microwave spectrometer with a pulsed nozzle particle source. *Review of Scientific Instruments*, 52(1):33–45, jan 1981.

[156] J. U. Grabow and W. Stahl. A Pulsed 'Molecular Beam Microwave Fourier Transform Spectrometer with Parallel Molecular Beam and Resonator Axes, aug 1990.

[157] D. H. Martin and E. Puplett. Polarised interferometric spectrometry for the millimetre and submillimetre spectrum. *Infrared Physics*, 10(2):105–109, jun 1970.

[158] John Chamberlain. *The Principles of Interferometric Spectroscopy*. A Wiley-Interscience Publication, 1979.

[159] Zaber Technology, T-LSM, https://www.zaber.com/products/product_detail.php?detail=T-LSM050B; accessed 12-Jul-2020.

[160] Emerson and Cuming Microwave. Eccosorb HR, http://www.eccosorb.com/products-eccosorb-hr.htm; accessed 12-Jul-2020, 2020.

[161] P. M. Downey, A. D. Jeffries, S. S. Meyer, R. Weiss, F. J. Bachner, J. P. Donnelly, W. T. Lindley, R. W. Mountain, and D. J. Silversmith. Monolithic silicon bolometers. *Applied Optics*, 23(6):910, mar 1984.

[162] John E. Carlstrom, Richard L. Plambeck, and D. D. Thornton. CONTINUOUSLY TUNABLE 65-115-GHZ GUNN OSCILLATOR. *IEEE Transactions on Microwave Theory and Techniques*, MTT-33(7):610–619, jul 1985.

[163] David Hopkins Shoemaker. *A Fourier transform spectrometer for millimeter and submillimeter wavelengths*. PhD thesis, Massachusetts Institute of Technology, 1980.

[164] Control software, available at https://github.com/panzhaodi/FTS_software.git; accessed 12-Jul-2020, 2020.

[165] M J Persky. A review of spaceborne infrared Fourier transform spectrometers for remote sensing. *Review of Scientific Instruments*, 66(10):4763–4797, 1995.

[166] R. Keisler, S. Hoover, N. Harrington, J. W. Henning, P. A.R. Ade, K. A. Aird, J. E. Austermann, J. A. Beall, A. N. Bender, B. A. Benson, L. E. Bleem, J. E. Carlstrom, C. L. Chang, H. C. Chiang, H. M. Cho, R. Citron, T. M. Crawford, A. T. Crites, T. De Haan, M. A. Dobbs, W. Everett, J. Gallicchio, J. Gao, E. M. George, A. Gilbert, N. W. Halverson, D. Hanson, G. C. Hilton, G. P. Holder, W. L. Holzapfel, Z. Hou, J. D. Hrubes, N. Huang, J. Hubmayr, K. D. Irwin, L. Knox, A. T. Lee, E. M. Leitch, D. Li, D. Luong-Van, D. P. Marrone, J. J. McMahon, J. Mehl, S. S. Meyer, L. Mocanu, T. Natoli, J. P. Nibarger, V. Novosad, S. Padin, C. Pryke, C. L. Reichardt, J. E. Ruhl, B. R. Saliwanchik, J. T. Sayre, K. K. Schaffer, E. Shirokoff, G. Smecher, A. A. Stark, K. T. Story, C. Tucker, K. Vanderlinde, J. D. Vieira, G. Wang, N. Whitehorn, V. Yefremenko, and O. Zahn. Measurements of Sub-Degree B-Mode Polarization in the Cosmic Microwave Background From 100 Square Degrees of Sptpol Data. *Astrophysical Journal*, 807(2), 2015.

[167] Planck Collaboration. Planck Legacy Archive, https://pla.esac.esa.int.

[168] A. T. Crites, J. W. Henning, P. A.R. Ade, K. A. Aird, J. E. Austermann, J. A. Beall, A. N. Bender, B. A. Benson, L. E. Bleem, J. E. Carlstrom, C. L. Chang, H. C. Chiang, H. M. Cho, R. Citron, T. M. Crawford, T. De Haan, M. A. Dobbs, W. Everett, J. Gallicchio, J. Gao, E. M. George, A. Gilbert, N. W. Halverson, D. Hanson, N. Harrington, G. C. Hilton, G. P. Holder, W. L. Holzapfel, S. Hoover, Z. Hou, J. D. Hrubes, N. Huang, J. Hubmayr, K. D. Irwin, R. Keisler, L. Knox, A. T. Lee, E. M. Leitch, D. Li, C. Liang, D. Luong-Van, J. J. McMahon, J. Mehl, S. S. Meyer, L. Mocanu, T. E. Montroy, T. Natoli, J. P. Nibarger, V. Novosad, S. Padin, C. Pryke, C. L. Reichardt, J. E. Ruhl, B. R. Saliwanchik, J. T. Sayre, K. K. Schaffer, G. Smecher, A. A. Stark, K. T. Story, C. Tucker, K. Vanderlinde, J. D. Vieira, G. Wang, N. Whitehorn, V. Yefremenko, and O. Zahn. Measurements of E-Mode Polarization and Temperature-E-Mode Correlation in the Cosmic Microwave Background From 100 Square Degrees of Sptpol Data. *Astrophysical Journal*, 805(1), 2015.

[169] Yehuda Hoffman and Erez Ribak. Constrained realizations of Gaussian fields - A simple algorithm. *The Astrophysical Journal*, 380:L5, oct 1991.

[170] Y. Omori, R. Chown, G. Simard, K. T. Story, K. Aylor, E. J. Baxter, B. A. Benson, L. E. Bleem, J. E. Carlstrom, C. L. Chang, H-M. Cho, T. M. Crawford, A. T. Crites, T. de Haan, M. A. Dobbs, W. B. Everett, E. M. George, N. W. Halverson, N. L. Harrington, G. P. Holder, Z. Hou, W. L. Holzapfel, J. D. Hrubes, L. Knox, A. T. Lee, E. M. Leitch, D. Luong-Van, A. Manzotti, D. P. Marrone, J. J. McMahon, S. S. Meyer, L. M. Mocanu, J. J. Mohr, T. Natoli, S. Padin, C. Pryke, C. L. Reichardt, J. E. Ruhl, J. T. Sayre, K. K. Schaffer, E. Shirokoff, Z. Staniszewski, A. A. Stark, K. Vanderlinde, J. D. Vieira, R. Williamson, and O. Zahn. A 2500 deg 2 CMB Lensing Map from Combined South Pole Telescope and Planck Data. *The Astrophysical Journal*, 849(2):124, nov 2017.

[171] Srinivasan Raghunathan, Gilbert P. Holder, James G. Bartlett, Sanjay Kumar Patil, Christian L. Reichardt, and Nathan Whitehorn. An inpainting approach to tackle the kinematic and thermal SZ induced biases in CMB-cluster lensing estimators. *Journal of Cosmology and Astroparticle Physics*, 2019(11), 2019.

[172] Planck Collaboration. Planck Legacy Archive, https://www.cosmos.esa.int/web/planck/pla, 2018.

[173] Antony Lewis and Anthony Challinor. CAMB: Code for Anisotropies in the Microwave Background. *Astrophysics Source Code Library*, page ascl:1102.026, 2011.

[174] K. M. Gorski, E Hivon, A J Banday, B D Wandelt, F K Hansen, M Reinecke, and M Bartelmann. HEALPix: A Framework for High-Resolution Discretization and Fast Analysis of Data Distributed on the Sphere. *The Astrophysical Journal*, 622(2):759–771, 2005.

[175] Antony Lewis. Lensed CMB simulation and parameter estimation. *Physical Review D - Particles, Fields, Gravitation and Cosmology*, 71(8):1–9, 2005.

[176] C. L. Reichardt, S. Patil, P. A. R. Ade, A. J. Anderson, J. E. Austermann, J. S. Avva, E. Baxter, J. A. Beall, A. N. Bender, B. A. Benson, F. Bianchini, L. E. Bleem, J. E. Carlstrom, C. L. Chang, P. Chaubal, H. C. Chiang, T. L. Chou, R. Citron, C. Corbett Moran, T. M. Crawford, A. T. Crites, T. de Haan, M. A. Dobbs, W. Everett, J. Gallicchio, E. M. George, A. Gilbert, N. Gupta, N. W. Halverson, N. Harrington, J. W. Henning, G. C. Hilton, G. P. Holder, W. L. Holzapfel, J. D. Hrubes, N. Huang, J. Hubmayr, K. D. Irwin, L. Knox, A. T. Lee, D. Li, A. Lowitz, D. Luong-Van, J. J. McMahon, J. Mehl, S. S. Meyer, M. Millea, L. M. Mocanu, J. J. Mohr, J. Montgomery, A. Nadolski, T. Natoli, J. P. Nibarger, G. Noble, V. Novosad, Y. Omori, S. Padin, C. Pryke, J. E. Ruhl, B. R. Saliwanchik, J. T. Sayre, K. K. Schaffer, E. Shirokoff, C. Sievers, G. Smecher, H. G. Spieler, Z. Staniszewski, A. A. Stark, C. Tucker, K. Vanderlinde, T. Veach, J. D. Vieira, G. Wang, N. Whitehorn, R. Williamson, W. L. K. Wu, and V. Yefremenko. An Improved Measurement of the Secondary Cosmic Microwave Background Anisotropies from the SPT-SZ + SPTpol Surveys. pages 1–16, feb 2020.

[177] Laurie D. Shaw, Daisuke Nagai, Suman Bhattacharya, and Erwin T. Lau. Impact of cluster physics on the Sunyaev-Zel'dovich power spectrum. *Astrophysical Journal*, 725(2):1452–1465, dec 2010.

[178] Laurie D. Shaw, Douglas H. Rudd, and Daisuke Nagai. Deconstructing the kinetic SZ power spectrum. *Astrophysical Journal*, 756(1):15, 2012.

[179] O. Zahn, C. L. Reichardt, L. Shaw, A. Lidz, K. A. Aird, B. A. Benson, L. E. Bleem, J. E. Carlstrom, C. L. Chang, H. M. Cho, T. M. Crawford, A. T. Crites, T. De Haan, M. A. Dobbs, O. Doré, J. Dudley, E. M. George, N. W. Halverson, G. P. Holder, W. L. Holzapfel, S. Hoover, Z. Hou, J. D. Hrubes, M. Joy, R. Keisler, L. Knox, A. T. Lee, E. M. Leitch, M. Lueker, D. Luong-Van, J. J. McMahon, J. Mehl, S. S. Meyer,

M. Millea, J. J. Mohr, T. E. Montroy, T. Natoli, S. Padin, T. Plagge, C. Pryke, J. E. Ruhl, K. K. Schaffer, E. Shirokoff, H. G. Spieler, Z. Staniszewski, A. A. Stark, K. Story, A. Vanengelen, K. Vanderlinde, J. D. Vieira, and R. Williamson. Cosmic microwave background constraints on the duration and timing of reionization from the south pole telescope. *Astrophysical Journal*, 756(1):65, 2012.

[180] W. B. Everett, L. Zhang, T. M. Crawford, J. D. Vieira, M. Aravena, M. A. Archipley, J. E. Austermann, B. A. Benson, L. E. Bleem, J. E. Carlstrom, C. L. Chang, S. Chapman, A. T. Crites, T. de Haan, M. A. Dobbs, E. M. George, N. W. Halverson, N. Harrington, G. P. Holder, W. L. Holzapfel, J. D. Hrubes, L. Knox, A. T. Lee, D. Luong-Van, A. C. Mangian, D. P. Marrone, J. J. McMahon, S. S. Meyer, L. M. Mocanu, J. J. Mohr, T. Natoli, S. Padin, C. Pryke, C. L. Reichardt, C. A. Reuter, J. E. Ruhl, J. T. Sayre, K. K. Schaffer, E. Shirokoff, J. S. Spilker, B. Stalder, Z. Staniszewski, A. A. Stark, K. T. Story, E. R. Switzer, K. Vanderlinde, A. Weiss, and R. Williamson. Millimeter-wave Point Sources from the 2500-square-degree SPT-SZ Survey: Catalog and Population Statistics. pages 1–43, mar 2020.

[181] L. E. Bleem, B. Stalder, T. De Haan, K. A. Aird, S. W. Allen, D. E. Applegate, M. L.N. Ashby, M. Bautz, M. Bayliss, B. A. Benson, S. Bocquet, M. Brodwin, J. E. Carlstrom, C. L. Chang, I. Chiu, H. M. Cho, A. Clocchiatti, T. M. Crawford, A. T. Crites, S. Desai, J. P. Dietrich, M. A. Dobbs, R. J. Foley, W. R. Forman, E. M. George, M. D. Gladders, A. H. Gonzalez, N. W. Halverson, C. Hennig, H. Hoekstra, G. P. Holder, W. L. Holzapfel, J. D. Hrubes, C. Jones, R. Keisler, L. Knox, A. T. Lee, E. M. Leitch, J. Liu, M. Lueker, D. Luong-Van, A. Mantz, D. P. Marrone, M. McDonald, J. J. McMahon, S. S. Meyer, L. Mocanu, J. J. Mohr, S. S. Murray, S. Padin, C. Pryke, C. L. Reichardt, A. Rest, J. Ruel, J. E. Ruhl, B. R. Saliwanchik, A. Saro, J. T. Sayre, K. K. Schaffer, T. Schrabback, E. Shirokoff, J. Song, H. G. Spieler, S. A. Stanford, Z. Staniszewski, A. A. Stark, K. T. Story, C. W. Stubbs, K. Vanderlinde, J. D. Vieira, A. Vikhlinin, R. Williamson, O. Zahn, and A. Zenteno. Galaxy clusters discovered via the sunyaev-zel'dovich effect in the 2500-square-degree spt-sz survey. *Astrophysical Journal, Supplement Series*, 216(2):27, feb 2015.

[182] Antony Lewis and Anthony Challinor. Weak gravitational lensing of the CMB, jun 2006.

[183] Toshiya Namikawa, Duncan Hanson, and Ryuichi Takahashi. Bias-hardened CMB lensing. *Monthly Notices of the Royal Astronomical Society*, 431(1):609–620, may 2013.

[184] P. A.R. Ade, N. Aghanim, M. Arnaud, M. Ashdown, J. Aumont, C. Baccigalupi, A. J. Banday, R. B. Barreiro, J. G. Bartlett, N. Bartolo, E. Battaner, R. Battye, K. Benabed, A. Benoît, A. Benoit-Lévy, J. P. Bernard, M. Bersanelli, P. Bielewicz, J. J. Bock, A. Bonaldi, L. Bonavera, J. R. Bond, J. Borrill, F. R. Bouchet, F. Boulanger, M. Bucher, C. Burigana, R. C. Butler, E. Calabrese, J. F. Cardoso, A. Catalano, A. Challinor, A. Chamballu, R. R. Chary, H. C. Chiang, J. Chluba, P. R. Christensen, S. Church, D. L. Clements, S. Colombi, L. P.L. Colombo, C. Combet, A. Coulais, B. P.

Crill, A. Curto, F. Cuttaia, L. Danese, R. D. Davies, R. J. Davis, P. De Bernardis, A. De Rosa, G. De Zotti, J. Delabrouille, F. X. Désert, E. Di Valentino, C. Dickinson, J. M. Diego, K. Dolag, H. Dole, S. Donzelli, O. Doré, M. Douspis, A. Ducout, J. Dunkley, X. Dupac, G. Efstathiou, F. Elsner, T. A. Enßlin, H. K. Eriksen, M. Farhang, J. Fergusson, F. Finelli, O. Forni, M. Frailis, A. A. Fraisse, E. Franceschi, A. Frejsel, S. Galeotta, S. Galli, K. Ganga, C. Gauthier, M. Gerbino, T. Ghosh, M. Giard, Y. Giraud-Héraud, E. Giusarma, E. Gjerløw, J. González-Nuevo, K. M. Górski, S. Gratton, A. Gregorio, A. Gruppuso, J. E. Gudmundsson, J. Hamann, F. K. Hansen, D. Hanson, D. L. Harrison, G. Helou, S. Henrot-Versillé, C. Hernández-Monteagudo, D. Herranz, S. R. Hildebrandt, E. Hivon, M. Hobson, W. A. Holmes, A. Hornstrup, W. Hovest, Z. Huang, K. M. Huffenberger, G. Hurier, A. H. Jaffe, T. R. Jaffe, W. C. Jones, M. Juvela, E. Keihänen, R. Keskitalo, T. S. Kisner, R. Kneissl, J. Knoche, L. Knox, M. Kunz, H. Kurki-Suonio, G. Lagache, A. Lähteenmäki, J. M. Lamarre, A. Lasenby, M. Lattanzi, C. R. Lawrence, J. P. Leahy, R. Leonardi, J. Lesgourgues, F. Levrier, A. Lewis, M. Liguori, P. B. Lilje, M. Linden-Vørnle, M. López-Caniego, P. M. Lubin, J. F. Maciás-Pérez, G. Maggio, D. Maino, N. Mandolesi, A. Mangilli, A. Marchini, M. Maris, P. G. Martin, M. Martinelli, E. Martínez-González, S. Masi, S. Matarrese, P. Mcgehee, P. R. Meinhold, A. Melchiorri, J. B. Melin, L. Mendes, A. Mennella, M. Migliaccio, M. Millea, S. Mitra, M. A. Miville-Deschênes, A. Moneti, L. Montier, G. Morgante, D. Mortlock, A. Moss, D. Munshi, J. A. Murphy, P. Naselsky, F. Nati, P. Natoli, C. B. Netterfield, H. U. Nørgaard-Nielsen, F. Noviello, D. Novikov, I. Novikov, C. A. Oxborrow, F. Paci, L. Pagano, F. Pajot, R. Paladini, D. Paoletti, B. Partridge, F. Pasian, G. Patanchon, T. J. Pearson, O. Perdereau, L. Perotto, F. Perrotta, V. Pettorino, F. Piacentini, M. Piat, E. Pierpaoli, D. Pietrobon, S. Plaszczynski, E. Pointecouteau, G. Polenta, L. Popa, G. W. Pratt, G. Prézeau, S. Prunet, J. L. Puget, J. P. Rachen, W. T. Reach, R. Rebolo, M. Reinecke, M. Remazeilles, C. Renault, A. Renzi, I. Ristorcelli, G. Rocha, C. Rosset, M. Rossetti, G. Roudier, B. Rouillé D'orfeuil, M. Rowan-Robinson, J. A. Rubinõ-Martín, B. Rusholme, N. Said, V. Salvatelli, L. Salvati, M. Sandri, D. Santos, M. Savelainen, G. Savini, D. Scott, M. D. Seiffert, P. Serra, E. P.S. Shellard, L. D. Spencer, M. Spinelli, V. Stolyarov, R. Stompor, R. Sudiwala, R. Sunyaev, D. Sutton, A. S. Suur-Uski, J. F. Sygnet, J. A. Tauber, L. Terenzi, L. Toffolatti, M. Tomasi, M. Tristram, T. Trombetti, M. Tucci, J. Tuovinen, M. Türler, G. Umana, L. Valenziano, J. Valiviita, F. Van Tent, P. Vielva, F. Villa, L. A. Wade, B. D. Wandelt, I. K. Wehus, M. White, S. D.M. White, A. Wilkinson, D. Yvon, A. Zacchei, and A. Zonca. Planck 2015 results: XIII. Cosmological parameters. *Astronomy and Astrophysics*, 594:A13, oct 2016.

[185] F. Bianchini, W. L. K. Wu, P. A. R. Ade, A. J. Anderson, J. E. Austermann, J. S. Avva, J. A. Beall, A. N. Bender, B. A. Benson, L. E. Bleem, J. E. Carlstrom, C. L. Chang, P. Chaubal, H. C. Chiang, R. Citron, C. Corbett Moran, T. M. Crawford, A. T. Crites, T. de Haan, M. A. Dobbs, W. Everett, J. Gallicchio, E. M. George, A. Gilbert, N. Gupta, N. W. Halverson, N. Harrington, J. W. Henning, G. C. Hilton, G. P. Holder, W. L. Holzapfel, J. D. Hrubes, N. Huang, J. Hubmayr, K. D. Irwin, L. Knox, A. T. Lee, D. Li, A. Lowitz, A. Manzotti, J. J. McMahon, S. S. Meyer, M. Millea, L. M.

Mocanu, J. Montgomery, A. Nadolski, T. Natoli, J. P. Nibarger, G. Noble, V. Novosad, Y. Omori, S. Padin, S. Patil, C. Pryke, C. L. Reichardt, J. E. Ruhl, B. R. Saliwanchik, J. T. Sayre, K. K. Schaffer, C. Sievers, G. Simard, G. Smecher, A. A. Stark, K. T. Story, C. Tucker, K. Vanderlinde, T. Veach, J. D. Vieira, G. Wang, N. Whitehorn, and V. Yefremenko. Constraints on Cosmological Parameters from the 500 deg 2 SPTPOL Lensing Power Spectrum . *The Astrophysical Journal*, 888(2):119, 2020.

[186] Sarah Bridle. Cosmological parameters from CMB and other data: A Monte Carlo approach. *Physical Review D - Particles, Fields, Gravitation and Cosmology*, 66(10):1–16, 2002.

[187] Federico Bianchini and Zhaodi Pan. Forecasts on Cosmological Parameter Constraints from the 1500 deg2 SPT3G Lensing Power Spectrum, internal memo, 2020.

[188] P. A.R. Ade, N. Aghanim, M. Arnaud, M. Ashdown, J. Aumont, C. Baccigalupi, A. J. Banday, R. B. Barreiro, J. G. Bartlett, N. Bartolo, S. Basak, E. Battaner, K. Benabed, A. Benoît, A. Benoit-Lévy, J. P. Bernard, M. Bersanelli, P. Bielewicz, J. J. Bock, A. Bonaldi, L. Bonavera, J. R. Bond, J. Borrill, F. R. Bouchet, F. Boulanger, M. Bucher, C. Burigana, R. C. Butler, E. Calabrese, J. F. Cardoso, A. Catalano, A. Challinor, A. Chamballu, H. C. Chiang, P. R. Christensen, S. Church, D. L. Clements, S. Colombi, L. P.L. Colombo, C. Combet, F. Couchot, A. Coulais, B. P. Crill, A. Curto, F. Cuttaia, L. Danese, R. D. Davies, R. J. Davis, P. De Bernardis, A. De Rosa, G. De Zotti, J. Delabrouille, F. X. Désert, J. M. Diego, H. Dole, S. Donzelli, O. Doré, M. Douspis, A. Ducout, J. Dunkley, X. Dupac, G. Efstathiou, F. Elsner, T. A. Enßlin, H. K. Eriksen, J. Fergusson, F. Finelli, O. Forni, M. Frailis, A. A. Fraisse, E. Franceschi, A. Frejsel, S. Galeotta, S. Galli, K. Ganga, M. Giard, Y. Giraud-Héraud, E. Gjerløw, J. González-Nuevo, K. M. Górski, S. Gratton, A. Gregorio, A. Gruppuso, J. E. Gudmundsson, F. K. Hansen, D. Hanson, D. L. Harrison, S. Henrot-Versillé, C. Hernández-Monteagudo, D. Herranz, S. R. Hildebrandt, E. Hivon, M. Hobson, W. A. Holmes, A. Hornstrup, W. Hovest, K. M. Huffenberger, G. Hurier, A. H. Jaffe, T. R. Jaffe, W. C. Jones, M. Juvela, E. Keihänen, R. Keskitalo, T. S. Kisner, R. Kneissl, J. Knoche, M. Kunz, H. Kurki-Suonio, G. Lagache, A. Lähteenmäki, J. M. Lamarre, A. Lasenby, M. Lattanzi, C. R. Lawrence, R. Leonardi, J. Lesgourgues, F. Levrier, A. Lewis, M. Liguori, P. B. Lilje, M. Linden-Vørnle, M. López-Caniego, P. M. Lubin, J. F. Maciás-Pérez, G. Maggio, D. Maino, N. Mandolesi, A. Mangilli, M. Maris, P. G. Martin, E. Martínez-González, S. Masi, S. Matarrese, P. Mcgehee, P. R. Meinhold, A. Melchiorri, L. Mendes, A. Mennella, M. Migliaccio, S. Mitra, M. A. Miville-Deschênes, A. Moneti, L. Montier, G. Morgante, D. Mortlock, A. Moss, D. Munshi, J. A. Murphy, P. Naselsky, F. Nati, P. Natoli, C. B. Netterfield, H. U. Nørgaard-Nielsen, F. Noviello, D. Novikov, I. Novikov, C. A. Oxborrow, F. Paci, L. Pagano, F. Pajot, D. Paoletti, F. Pasian, G. Patanchon, O. Perdereau, L. Perotto, F. Perrotta, V. Pettorino, F. Piacentini, M. Piat, E. Pierpaoli, D. Pietrobon, S. Plaszczynski, E. Pointecouteau, G. Polenta, L. Popa, G. W. Pratt, G. Prézeau, S. Prunet, J. L. Puget, J. P. Rachen, W. T. Reach, R. Rebolo, M. Reinecke, M. Remazeilles, C. Renault, A. Renzi, I. Ristorcelli, G. Rocha, C. Rosset, M. Rossetti, G. Roudier, M. Rowan-Robinson,

J. A. Rubinõ-Martín, B. Rusholme, M. Sandri, D. Santos, M. Savelainen, G. Savini, D. Scott, M. D. Seiffert, E. P.S. Shellard, L. D. Spencer, V. Stolyarov, R. Stompor, R. Sudiwala, R. Sunyaev, D. Sutton, A. S. Suur-Uski, J. F. Sygnet, J. A. Tauber, L. Terenzi, L. Toffolatti, M. Tomasi, M. Tristram, M. Tucci, J. Tuovinen, L. Valenziano, J. Valiviita, B. Van Tent, P. Vielva, F. Villa, L. A. Wade, B. D. Wandelt, I. K. Wehus, M. White, D. Yvon, A. Zacchei, and A. Zonca. Planck 2015 results: XV. Gravitational lensing. *Astronomy and Astrophysics*, 594:A15, oct 2016.

[189] T. Matsumura, Y. Akiba, J. Borrill, Y. Chinone, M. Dobbs, H. Fuke, A. Ghribi, M. Hasegawa, K. Hattori, M. Hattori, M. Hazumi, W. Holzapfel, Y. Inoue, K. Ishidoshiro, H. Ishino, H. Ishitsuka, K. Karatsu, N. Katayama, I. Kawano, A. Kibayashi, Y. Kibe, K. Kimura, N. Kimura, K. Koga, M. Kozu, E. Komatsu, A. Lee, H. Matsuhara, S. Mima, K. Mitsuda, K. Mizukami, H. Morii, T. Morishima, S. Murayama, M. Nagai, R. Nagata, S. Nakamura, M. Naruse, K. Natsume, T. Nishibori, H. Nishino, A. Noda, T. Noguchi, H. Ogawa, S. Oguri, I. Ohta, C. Otani, P. Richards, S. Sakai, N. Sato, Y. Sato, Y. Sekimoto, A. Shimizu, K. Shinozaki, H. Sugita, T. Suzuki, A. Suzuki, O. Tajima, S. Takada, S. Takakura, Y. Takei, T. Tomaru, Y. Uzawa, T. Wada, H. Watanabe, M. Yoshida, N. Yamasaki, T. Yoshida, and K. Yotsumoto. Mission design of LiteBIRD. *Journal of Low Temperature Physics*, 176(5-6):733–740, jan 2014.

[190] A. Kogut, D. J. Fixsen, D. T. Chuss, J. Dotson, E. Dwek, M. Halpern, G. F. Hinshaw, S. M. Meyer, S. H. Moseley, M. D. Seiffert, D. N. Spergel, and E. J. Wollack. The Primordial Inflation Explorer (PIXIE): A nulling polarimeter for cosmic microwave background observations. *Journal of Cosmology and Astroparticle Physics*, 2011(7), 2011.

[191] Thomas Crawford. SPT effective band centers, internal memo, 2015.

[192] E. M. George, C. L. Reichardt, K. A. Aird, B. A. Benson, L. E. Bleem, J. E. Carlstrom, C. L. Chang, H. M. Cho, T. M. Crawford, A. T. Crites, T. De Haan, M. A. Dobbs, J. Dudley, N. W. Halverson, N. L. Harrington, G. P. Holder, W. L. Holzapfel, Z. Hou, J. D. Hrubes, R. Keisler, L. Knox, A. T. Lee, E. M. Leitch, M. Lueker, D. Luong-Van, J. J. Mcmahon, J. Mehl, S. S. Meyer, M. Millea, L. M. Mocanu, J. J. Mohr, T. E. Montroy, S. Padin, T. Plagge, C. Pryke, J. E. Ruhl, K. K. Schaffer, L. Shaw, E. Shirokoff, H. G. Spieler, Z. Staniszewski, A. A. Stark, K. T. Story, A. Van Engelen, K. Vanderlinde, J. D. Vieira, R. Williamson, and O. Zahn. A measurement of secondary cosmic microwave background anisotropies from the 2500 square-degree SPT-SZ survey. *Astrophysical Journal*, 799(2), 2015.

# APPENDIX A

# EFFECTIVE FREQUENCY BAND CENTERS FOR SPT-3G

The framework here is based on Tom Crawford's internal collaboration note [191]. The frequency bands for a CMB detector usually extends over several tens of GHz. It is useful to define an effective frequency center for each frequency band that can be used to calculate a source's temperature calibrated against the CMB. The effective frequency center depends on the source spectrum. We calculate the effective frequency centers for radio sources, dusty sources, and tSZ in this note.

We define $\nu$ to be the frequency, $B_\nu(\nu, T)$ to be the frequency spectrum of the blackbody, $T_{\rm cmb}$ to be the CMB temperature (2.725 K), $I(\nu)$ to be the source spectrum, $t(\nu)$ to be the detector frequency band (not including the detector throughput $A\Omega$). To simplify the equations, define $B'_\nu(\nu)$ to be the partial derivative of $B_\nu(\nu, T)$ relative to $T$ at $T_{\rm cmb}$, define $f(\nu)$ to be the frequency-dependent part of $I(\nu)$, where $I(\nu) = I_0\, f(\nu)$, and $\nu_{\rm eff}$ to be the effective frequency of a frequency band. $\nu_{\rm eff}$ satisfies $I(\nu_{\rm eff}) = B'_\nu(\nu_{\rm eff})\Delta T_s$, here $\Delta T_s$ is the temperature of the source calibrated against the CMB temperature at the same frequency band.

The effective frequency satisfies the following equation:

$$\Delta T_s = \frac{I(\nu_{\rm eff})}{B'_\nu(\nu_{\rm eff})} = \frac{\int A\Omega I(\nu) t(\nu) d\nu}{\int A\Omega B'_\nu(\nu) t(\nu) d\nu} \tag{A.1}$$

where I have used $I(\nu) = I_0\, f(\nu)$. The sources are assumed to be beam-filling with the same $A\Omega$ as the CMB.

The frequency-dependent part of the source spectrum is $f(\nu) = \nu^{-0.5}$ for radio sources and $f(\nu) = \nu^{3.5}$ for dusty sources. The frequency-dependence of tSZ is $f(\nu) = B'_\nu g(\nu)$, where $g(\nu) = (x\frac{e^x+1}{e^x-1} - 4)(1 + \delta_{\rm SZE}(x, T_e))$ is the frequency-dependent part of $\Delta T_{\rm SZE}/T_{\rm cmb}$. Here $x = h\nu/k_B T_{\rm cmb}$ and $\delta_{\rm SZE}(x, T_e))$ is the relativistic correction (neglected in the following

calculations).

Using the above formulas, dusty source effective frequencies for the SPT-3G 95/ 150/ 220 GHz frequency bands are 95.96/150.01/222.76 GHz, radio source effective frequencies are 93.52/ 145.92/ 213.34 GHz, and tSZ effective frequencies are 95.69/148.85/220.15 GHz.

If we want to convert a source map in CMB unit measured by SPT-SZ to a SPT-3G map, we need to calculate the scaling ratio based on their effective frequencies for the corresponding bands. Define $\nu_{\text{eff1}}$ to be the effective frequency for SPT-3G, and define $\nu_{\text{eff2}}$ to be the effective frequency for SPT-SZ. The effective frequencies for SPT-SZ ($\nu_{\text{eff2}}$) comes from [192]. The conversion factor from a source temperature measured in SPT-SZ to SPT-3G is

$$Conv = \frac{\Delta T_{SPT-3G}}{\Delta T_{SPT-SZ}} = \frac{I(\nu_{\text{eff1}})/B'_{\nu}(\nu_{\text{eff1}})}{I(\nu_{\text{eff2}})/B'_{\nu}(\nu_{\text{eff2}})} \tag{A.2}$$